

LOOKING FOR BEYOND THE STANDARD MODEL PHYSICS IN DIJET-PLUS-LEPTON
FINAL-STATE EVENTS COLLECTED WITH THE ATLAS DETECTOR

by

Vincent R. Pascuzzi

A thesis submitted in conformity with the requirements
for the degree of Doctor of Philosophy
Graduate Department of Physics
University of Toronto

Abstract

Looking for Beyond the Standard Model Physics in Dijet-Plus-Lepton Final-State Events Collected with the ATLAS Detector

Vincent R. Pascuzzi
Doctor of Philosophy
Graduate Department of Physics
University of Toronto
2019

A search for a new resonant state decaying exclusively to two quarks in events with at least two jets and one isolated charged lepton using 139 fb^{-1} of proton-proton collision data collected by the ATLAS detector at $\sqrt{s} = 13 \text{ TeV}$ is presented. Requiring a charged lepton in dijet final states provides sensitivity to extensions of the Standard Model which predict the production of dijet resonances in association with leptonically-decaying vector bosons or top quarks. Whereas inclusive searches are limited to resonance masses greater than 1 TeV due to jet-based triggers which have a minimum jet transverse momentum of about 400 GeV, lepton triggers can be as low as 24 GeV, thereby permitting access to resonance masses of order 100 GeV.

The search presented in this thesis considers a dijet invariant mass range between 0.22–6.3 TeV. The largest deviation between the number of observed events and the Standard Model background estimate was found at a dijet invariant mass $m_{jj} = 1.3 \text{ TeV}$ with a global statistical significance of 0.5 standard deviations. In the absence of a statistically significant deviation of the data from the background expectation, exclusion limits are set at a 95% confidence level on the presence of generic Gaussian-shaped signals of different masses and widths. Such signals are excluded with cross sections ranging from 40–0.03 fb between 0.25–6.0 TeV. Limits are also set in the context of a Technicolor model and a Simplified Dark Matter model. A follow-up search using a machine learning approach is discussed last.

To Jules, Lala and Dora (and Ada).

Acknowledgements

A special “thanks” first to my supervisor, Peter Krieger, for taking me on as a graduate student and getting me into this mess I’m currently in. (If it were not for PK, I may have been stuck doing cosmology or astrophysics at another institution, or worse – have a “real” job by now.) One thing I especially appreciated were the many opportunities I was given as your student: spending nearly two years at CERN, and all of the travelling you allowed me to do for workshops, conferences, and “collaboration weeks”. I’m a strong believer in networking, and these opportunities let me interact with some people I regard as being true experts in the field. Even more, the infinite patience he had while reading and re-reading (and re-re-reading) the dozens of drafts of this thesis that has ultimately resulted in what I consider to be a “fine” dissertation. To my PhD committee members, Pekka Sinervo and Michael Luke: thanks for your help getting me here.

“Thanks” to the other ATLAS folks I’ve had the pleasure of working with as an ATLAS graduate student, namely Sergei Chekanov, John Chapman, Zach Marshall, Heather Grey, Emmanuel Monnier, Martin Aleksa, Nikiforos Nikiforou, and Tommaso Lari (and the more than two dozen others). You’ve all been pivotal in helping advance my career in ATLAS, and can’t help but think I wouldn’t be where I am today without your support and guidance. Cheers also to the awesome people in the ATLAS Simulation and JDM groups, as well as the LAr Calorimeter Operations team – it’s been a hell of a good time!

I’d like to also give a special shout-out to Osama “Uncle Hass” AbouZeid for being a great friend since almost the beginning of my studies in Toronto, and for being the godfather of my second daughter. To the rest of ATLAS Toronto: it’s really been a pleasure getting to know you and to work with you. I sincerely wish you all the best.

I need to of course also thank my family – the Pascuzzis, Edens, and Angers – for always showing interest in my work and supporting me (emotionally and sometimes financially) through what seems like a career as a professional student. Dad, you taught me how to be a man, and have always demonstrated the qualities of an incredible father and role model. Ma, you taught me how to love unconditionally, and that it’s OK to constantly worry about your kids (no matter how old they are). Nicky P., you taught me what brotherhood and true friendship is all about. I love you all.

Last, but not least, I thank my beloved and devoted wife, Julie Marie Carmelle Pascuzzi, who has put up with more than anyone could ever imagine (sorry, Ma!). You’ve loved me, always supported me, and took care of me through all of this – no matter what. You gave me the two (three) most important things in my life, our daughters Carmella and Doralie (and puppy, Ada), and have shown me what true love is. We’ve been through so much together over the past decade, and I can’t wait to experience whatever our future together has in store. I hope we all enjoy California!

Much love,

Vince (aka Vinny P., aka vrp)

Contents

Abstract	ii
Contents	v
1 Introduction	1
2 Some aspects of particle physics	3
2.1 A brief introduction to the Standard Model	4
2.1.1 Fundamental particles and forces	4
2.1.2 Symmetries and gauge theories	5
2.1.3 Spontaneous symmetry breaking (aka “hidden” symmetries)	8
2.1.4 Quantum chromodynamics	12
2.2 Physics beyond the Standard Model	14
2.2.1 The hierarchy and fine-tuning problems	14
2.2.2 Dark Matter	15
2.2.3 The Technicolor Model	16
2.2.4 The Simplified Dark Matter Model	17
2.3 Proton-proton collisions	18
2.3.1 Anatomy of a collision	18
2.3.2 Hard-scattering	20
2.3.3 Hadronisation	22
3 The Large Hadron Collider	25
3.1 Machine operation	25
3.2 The accelerator chain	26
4 The ATLAS Experiment	32
4.1 Physics and detector requirements	33
4.2 Magnet system and magnetic field	35
4.2.1 Central solenoid magnet	35
4.2.2 Toroid magnets	36
4.3 Inner detector	36
4.3.1 Pixel detector	37
4.3.2 Semiconductor Tracker	39
4.3.3 Transition Radiation Tracker	39

4.3.4	Beam Conditions Monitor	40
4.4	Calorimetry	41
4.4.1	Electromagnetic calorimeters	42
4.4.2	Hadronic calorimeters	45
4.4.3	LAr signal and readout methodology	49
4.5	Muon Spectrometer	50
4.5.1	Monitored Drift Tubes	51
4.5.2	Cathode Strip Chambers	52
4.5.3	Resistive Plate Chambers	52
4.5.4	Thin Gap Chambers	53
4.6	The LUCID detector	54
4.6.1	Detector design and algorithms	54
4.6.2	Calibration transfer for final luminosity determination	55
4.7	Trigger and data acquisition	56
5	Dataset and object reconstruction	58
5.1	Dataset and data quality	58
5.1.1	Dataset	58
5.1.2	Data quality	59
5.1.3	Pile-up	60
5.2	Clustering algorithms	62
5.2.1	Sliding-window calorimeter clustering	62
5.2.2	Topological calorimeter clustering	63
5.2.3	Adaptation of the 4-2-0 method for electrons	63
5.2.4	Superclusters	64
5.3	Object reconstruction and calibration	65
5.3.1	Tracks	65
5.3.2	Electrons	67
5.3.3	Muons	70
5.3.4	Jets	73
6	The dijet+lepton analysis	79
6.1	Introduction	79
6.2	Analysis strategy	82
6.2.1	Background estimate performance metrics	83
6.3	Standard Model backgrounds	85
6.3.1	Multijet background	85
6.3.2	Top quark background	85
6.3.3	W + jets background	86
6.4	Monte Carlo simulations and physics modelling	86
6.4.1	Event generation	87
6.4.2	Simulating the ATLAS detector	88
6.4.3	Background Monte Carlo	89
6.4.4	Signal modelling and Monte Carlo	90

6.5	Event selection	92
6.5.1	Triggering events	92
6.5.2	Object definitions and event preselection	94
6.6	Final selection and definitions of analysis regions	100
6.6.1	Signal leptons	100
6.6.2	Signal jets and determining the minimum m_{jj}	100
6.6.3	Signal region definition	102
6.6.4	Control region definition	103
6.7	Signal and control region kinematics	105
6.7.1	Signal region kinematics	105
6.7.2	Loose-lepton control region	105
6.8	Describing the SM background	107
6.8.1	Background hypothesis I: dijet function	108
6.8.2	Background hypothesis II: sliding window fit	110
6.8.3	Resolution-based binning of the dijet invariant mass spectrum	111
6.8.4	Background modelling using Monte Carlo	111
6.8.5	Modelling the LL-CR	112
6.9	Robustness of the background estimates	116
6.9.1	Signal injection test	117
6.9.2	Spurious signal test	119
6.10	Search phase	120
6.10.1	Search strategy	120
6.10.2	Describing the SR using f_{5p}	121
6.10.3	Robustness tests of f_{5p} in the SR	122
6.10.4	Results	124
6.11	Systematic uncertainties	129
6.11.1	Background estimate uncertainties	129
6.11.2	Jet energy scale and resolution	130
6.11.3	Lepton uncertainties	133
6.11.4	Systematic uncertainties from triggers	134
6.11.5	Luminosity uncertainty	134
6.11.6	Scale uncertainties	134
6.11.7	PDF uncertainty	135
6.11.8	Gaussian signal shape uncertainties	135
6.11.9	Summary of uncertainties	136
6.12	Limit setting	136
6.12.1	Statistical background	137
6.12.2	Credible intervals and upper limits	139
6.12.3	Efficiency calculations	139
6.12.4	Results	141

7 Conclusion	145
7.1 The future	146
7.1.1 Machine learning for signal identification	146
7.1.2 Machine learning for fitting smooth backgrounds	146
Appendix A Contributions to the ATLAS Experiment	149
Bibliography	151

Chapter 1

Introduction

Learn from yesterday, live for today, hope for tomorrow.

The important thing is not to stop questioning.

- Albert Einstein

Particle physics deals with the fundamental constituents of Nature and the forces through which they interact. The mathematical framework of particle physics is provided by the Standard Model (SM). The SM has so far provided an excellent description of elementary particles that interact amongst each other through three of the four known forces in Nature – the strong, electromagnetic, and weak forces. For over forty years, physicists have concocted experiments, small and large, to test the accuracy and consistency of the SM; to date, no significant deviations from its theoretical predictions have been observed. Despite the theory’s remarkable success, the SM does not paint a complete picture of fundamental physics.

Arguably the most obvious missing feature of the SM is a quantum field theoretic description of the fourth known force of Nature – gravity. Perhaps less familiar to people outside the high-energy physics community is the apparent conflict between the *observed* Higgs boson mass and *calculated* mass (following radiative corrections, as well as those from self-interactions); a conflict resolved only if there exists some new physics before the Planck scale, or otherwise requiring an extremely coincidental cancellation of large terms in precise calculations of its mass. Moreover, galactic- and cosmological-scale observations suggest the presence of a so-called “Dark Matter” – whose existence as a particle, while unconfirmed, is nonetheless not manifest in the SM.

The list goes on... so while the SM is a *theory of most things*, it is not a *theory of everything*.

The Large Hadron Collider (LHC), a proton-proton (pp) and heavy-ion collider located near Geneva, Switzerland, was designed to reach energies of up to $\sqrt{s} = 14$ TeV in order to probe the high-energy regime at which the SM electroweak sector could have broken down. The ATLAS detector, one of the general-purpose particle physics experiments stationed along the LHC ring, was designed to discover the Higgs boson, test the SM, and search for what else may exist in our Universe. ATLAS has been collecting pp collision data since 2009, and while the first two of its missions have so far been successful, no new physics beyond the SM (BSM) has been observed to date. However, with about 20 more years of data taking foreseen, and many LHC and detector upgrades to be made along the way, it is too soon to rule out all BSM physics at the TeV scale.

The analysis presented in this thesis is a search for a new strongly-interacting particle using the

ATLAS full Run-2 pp collision dataset, recorded between 2015–2018, at a centre-of-mass collision energy of 13 TeV. The search is performed on events with at least two jets (*dijet*) and one charged lepton¹ to look for signatures of a new particle produced in strong interactions. A new heavy object decaying into a pair of coloured particles (quarks or gluons) would appear as an excess (“bump”) around the region of the heavy object’s mass when compared to SM predictions. In the absence of a statistically significant deviation of data from prediction, limits on the production of such resonances are set in several contexts: generic Gaussian-shaped signals and two models proposed to be extensions of the SM.

Being a hadron collider, the most abundantly produced physics objects in pp collisions at the LHC are jets: collimated sprays of highly-energetic charged and neutral particles resulting from the initial interactions between quarks and gluons in collisions. The high production rate of jets means substantial statistics for searches involving them, and their nature provides a handle to investigate new strongly interacting physics processes. While leptons are not produced as copiously as jets at the LHC, they can be used for multijet background rejection to flesh out signatures of BSM physics.

This thesis is organised as follows. Chapter 2 provides a theoretical background to the SM, its limitations, and how the dijet+lepton analysis aims to address some of the most pressing issues. An overview of the LHC is given in Chap. 3 and ATLAS experiment in Chap. 4. The dataset used in this analysis and a description of jet, muon, and electron reconstruction in ATLAS are provided in Chap. 5. Chapter 6 presents the dijet+lepton analysis: the strategy used to construct the final discriminant, the evaluation of systematic uncertainties, and the mass limits. Chapter 7 concludes this thesis, and provides a brief overview of a machine learning approach for the next iteration of the dijet+lepton analysis.

¹Hence, colloquially referred to herein as the “dijet+lepton” analysis.

Chapter 2

Some aspects of particle physics

Knees collapsing...

We bow in it's aura.

- Veil of Maya, *We Bow in It's Aura*

The fundamental constituents of matter are widely accepted to be structureless, point-like objects, that constitute the building blocks of our Universe. As far as it is known, there are 12 flavours of such objects: six spin-1/2 quarks and six spin-1/2 leptons, collectively referred to as *fermions*.

Interactions between identical and different species of particles are mediated by *bosons*, carriers of the four fundamental forces of Nature: the strong and weak nuclear forces, the electromagnetic (EM), and gravitational force. These forces are responsible for multi-particle bound-states (*e.g.* protons, neutrons, and atomic nuclei in the case of the strong force, and atoms, molecules and proteins in the case of EM), particle decays (*e.g.* the weak force permits massive particles to decay into lighter ones), as well as the formation of galaxies (*e.g.* gravity). The theories of the strong, weak and EM forces are described by the SM of particle physics; gravity is not included, and anyways introduces complications in regards to renormalisation and its relative weakness at low energies. Moreover, the weak and electromagnetic forces have been unified into a single force – the electroweak interaction.

Despite missing elements, the SM has so far held up to all experimental tests for more than 50 years, providing a consistent and accurate description of Nature over a broad range of energies. However, as made readily apparent, and also has been known for quite some time [1], the SM is an incomplete theory, expected to be effective only at energies of order 1 TeV. The LHC, discussed in Chap. 3, has been colliding hadrons at a centre-of-mass energy of 13 TeV for several years and no significant deviation from theory have been observed.

This chapter provides an overview of particle physics in the context of the analysis presented herein. It is by no means representative of the accomplishments of the those who helped to build the field as it stands today, but aims to give sufficient detail so as to set the proverbial stage for the material that follows. Some theoretical aspects of particle physics are presented first in Sec. 2.1, including a brief description of SM particles and forces, gauge theories, the Higgs mechanism, and QCD. To motivate searches for new physics, some limitations of the SM are presented in Sec. 2.2, and potential candidates to address the issues raised are discussed. Lastly, Sec. 2.3 provides a discussion on hadron-hadron collision phenomenology.

2.1 A brief introduction to the Standard Model

This section gives an overview of Standard Model (SM) physics, its particle content, and gauge theories. Spontaneous symmetry breaking is discussed, as well as the Higgs mechanism. The theory of strong interactions, Quantum Chromodynamics, is presented last.

2.1.1 Fundamental particles and forces

The SM is a quantum field theory that describes the basic building blocks of our universe and three of the four fundamental forces of Nature through which they interact.

The SM is a $SU(3)_C \otimes SU(2)_L \otimes U(1)_Y$ locally (gauge) invariant theory. The generators of each group correspond to the spin-1 particles that mediate the associated force. Strong interactions, described by Quantum Chromodynamics (QCD), demonstrate invariance under local transformations of the $SU(3)_C$ symmetry group, where “ C ” indicates “colour”, the charge of the strong force. There are eight $(N^2 - 1)$ $SU(3)_C$ generators, corresponding to eight colour-charged gluons.

The combination of weak and EM interactions exhibit local invariance under $SU(2)_L \otimes U(1)_Y$ transformations, where “ L ” indicates only *left-handed* fermion interactions are allowed and “ Y ” is the weak hypercharge. The four generators of the electroweak group are related to the four physical gauge bosons of the electroweak theory, W^\pm , Z and γ , through linear combinations of the fields that transform under this group. The electric charge Q can be determined by a combination of the $U(1)$ weak hypercharge and the third component of weak isospin: $Q = T_3 + Y/2$. The weak bosons are endowed with mass through a spontaneous symmetry breaking mechanism, described later in this section, whereas the photon remains massless.

A photon, being electrically neutral, does not interact directly with other photons. On the other hand, as will be shown, the W^\pm and Z bosons can couple directly to each other, as can gluons. Table 2.1 summarises the force carriers included in the SM.

Force	Relative strength	Range [m]	Carrier(s)	Charge
Strong	1	10^{-15}	g	Colour
Electromagnetic	10^{-2}	∞	γ	–
Weak	10^{-6}	10^{-17}	W^\pm Z	Weak, Electromagnetic Weak

Table 2.1: The three fundamental forces and spin-1 bosons included in the SM. Relative strengths are approximate and given with respect to the strong force within an atomic nucleus.

Bosons and fermions are distinguished by their spin statistics. Bosons are particles with integer spin that have symmetric, commuting wave functions; there is no cancellation under permutations of their fields in a given Lagrangian. On the other hand, fermions are half-integer spin particles that obey Fermi-Dirac statistics; their wave functions are antisymmetric (anti-commute), and therefore no two identical fermions can occupy the same state.

The fundamental SM fermions consist of two general types, quarks and leptons, each of which are divided into three *generations* or *families*. The three generations of leptons are the electrically charged electron (e), muon (μ) and tau (τ), along with their associated electric-charge-neutral neutrinos (ν_e , ν_μ ,

ν_τ):

$$\begin{pmatrix} \nu_e \\ e \end{pmatrix}, \quad \begin{pmatrix} \nu_\mu \\ \mu \end{pmatrix}, \quad \begin{pmatrix} \nu_\tau \\ \tau \end{pmatrix}. \quad (2.1)$$

There are six distinct *flavours* of quarks – up (u), down (d), charm (c), strange (s), top (t), bottom (b):

$$\begin{pmatrix} u \\ d \end{pmatrix}, \quad \begin{pmatrix} c \\ s \end{pmatrix}, \quad \begin{pmatrix} t \\ b \end{pmatrix}, \quad (2.2)$$

categorised as *up*-type and *down*-type by their electric charge, Q , where the top row (up-type) in Eq. 2.2 has $Q = +\frac{2}{3}$ and the bottom (down-type) has $Q = -\frac{1}{3}$. Each fermion, f , has a corresponding anti-particle, \bar{f} , with identical mass but opposite quantum numbers (*e.g.* electric charge). All fermions have weak isospin (\mathbf{T}) and hypercharge (Y), therefore all participate in weak interactions, whereas those with only electric or colour charge interact electromagnetically or strongly, respectively. A summary of the fundamental fermions is presented in Table 2.2.

	Generation			Quantum number			
	1 st	2 nd	3 rd	T_3	Y	Q	C
Quarks	u_L	c_L	t_L	$+1/2$	$+1/3$	$+2/3$	(r, g, b)
	d_L	s_L	b_L	$-1/2$	$+1/3$	$-1/3$	(r, g, b)
	u_R	c_R	t_R	0	$+4/3$	$+2/3$	(r, g, b)
	d_R	s_R	b_R	0	$-2/3$	$-1/3$	(r, g, b)
Leptons	$\nu_{e,L}$	$\nu_{\mu,L}$	$\nu_{\tau,L}$	$+1/2$	-1	0	$-$
	e_L	μ_L	τ_L	$-1/2$	-1	-1	$-$
	e_R	μ_R	τ_R	0	-2	-1	$-$

Table 2.2: The fermions of the SM along with their quantum numbers. Each row contains particles with different masses (mass increases with generations), but are otherwise identical. The left-handed fermions transform as doublets under $SU(2)$, while the right-handed are singlets under $U(1)$. Interactions between right-handed neutrinos and SM particles have yet to be experimentally observed.

The last piece of the SM is the electrically neutral Higgs boson, a scalar particle with both weak isospin and weak hypercharge. Therefore, the Higgs, like the fermions, couples directly to weak vector bosons. However, the unique characteristic of the Higgs (field) is that it endows fundamental particles with mass. As a result, it couples to all massive fermions and gauge bosons. While the Yukawa coupling to a fermion is proportional the fermion’s mass, the coupling to a massive vector boson is proportional to the boson’s squared-mass.

2.1.2 Symmetries and gauge theories

The concept of symmetry plays a crucial role in understanding the development of the SM. Since quantum field theory was born of the marriage between quantum mechanics and special relativity, it is necessary that both unitarity and causality are respected. Therefore, all fundamental interactions are associated with local (gauge) symmetries which give rise to force-mediating particles.

Noether’s theorem states that for every continuous symmetry transformation under which a Lagrangian is invariant, there is a corresponding conserved quantity. Typical examples are (geometrical)

spacetime invariance, leading to conservation of four-momentum, and (internal) isospin symmetry. The typical programme followed to construct a gauge theory consists of writing down a Lagrangian, introducing a gauge-covariant derivative (that couples gauge fields to matter), and then constructing a field-strength tensor (*i.e.* a kinetic term) for the gauge fields. To see this in action, it is instructive to consider a non-Abelian field theory since it is a generalisation of the Abelian (*e.g.* electromagnetism) case.

Disregarding the electromagnetic force, the proton and neutron can be placed on equal footing; the near degeneracy of their masses and charge-independence of the strong force means the distinction between the proton and neutron is an entirely arbitrary convention. That is, in the absence of electromagnetism, the proton and neutron can be regarded as elementary particles with common mass, m . The free-nucleon Lagrangian,

$$\mathcal{L} = \bar{\psi}(i\gamma^\mu \partial_\mu - m)\psi, \quad (2.3)$$

written in terms of composite fermion fields,

$$\psi \equiv \begin{pmatrix} p \\ n \end{pmatrix}, \quad (2.4)$$

is invariant under *global* $SU(2)$ rotations in isospin space,

$$\psi \rightarrow \exp\left(\frac{i\boldsymbol{\tau}\cdot\boldsymbol{\omega}}{2}\right)\psi, \quad (2.5)$$

where $\boldsymbol{\tau} = (\tau_1, \tau_2, \tau_3)$ are the usual 2×2 Pauli isospin matrices, and $\boldsymbol{\omega} = (\omega_1, \omega_2, \omega_3)$ is an arbitrary constant (*i.e.* spacetime-independent) parameter of the transformation. A global transformation is one that subjects the spinor ψ to the same rotation throughout spacetime; once the proton and neutron are labeled at a point in spacetime, the convention must be respected everywhere.

A continuous transformation can be built up from infinitesimal ones,

$$\psi(x) \rightarrow \psi(x) + \delta\psi(x). \quad (2.6)$$

and so in the case of isospin rotations,

$$\psi(x) \rightarrow \psi(x) + \frac{i}{2}\boldsymbol{\tau} \cdot \boldsymbol{\omega}\psi(x). \quad (2.7)$$

For the Lagrangian in Eq. 2.3 to be invariant under such a transformation requires

$$\delta\mathcal{L} = 0, \quad (2.8)$$

and results in a conserved Noether current,

$$\mathbf{J}^\mu = \bar{\psi}\gamma^\mu \frac{\boldsymbol{\tau}}{2}\psi, \quad (2.9)$$

namely, the *conserved isospin current*.

The theory of Yang and Mills [2] – that exploits the utility of gauge invariance of electromagnetism

– promotes the global isospin symmetry to a local one,

$$\psi(x) \rightarrow \psi'(x) = G(x)\psi(x) \quad (2.10)$$

where $G(x)$ can be, for example,

$$U(1): \quad G_{\text{QED}}(x) \equiv \exp(iQ\alpha(x)) \quad (2.11)$$

$$SU(2): \quad G_{\text{iso}}(x) \equiv \exp\left(\frac{i\boldsymbol{\tau} \cdot \boldsymbol{\omega}(x)}{2}\right) \quad (2.12)$$

and $\boldsymbol{\omega}(x)$ is now a function of spacetime. To ensure local gauge invariance, a gauge-covariant derivative is introduced,

$$D_\mu \equiv \partial_\mu + \frac{ig}{2}\boldsymbol{\tau} \cdot \mathbf{w}_\mu, \quad (2.13)$$

requiring three gauge fields, $\mathbf{w}_\mu = (w_1, w_2, w_3)$, and with g playing the role of the strong interaction coupling constant. The modified, now locally gauge invariant, Lagrangian is given by

$$\mathcal{L} = \bar{\psi}(i\gamma^\mu D_\mu - m)\psi \quad (2.14)$$

$$= \mathcal{L}_0 - g\mathbf{w}_\mu \cdot \underbrace{\bar{\psi}\gamma^\mu \frac{\boldsymbol{\tau}}{2}\psi}_{\text{conserved isospin current}}, \quad (2.15)$$

a free Lagrangian plus an interaction term that couples the \mathbf{w}_μ gauge fields to the conserved isospin current of the nucleons (Eq. 2.9). With inspiration from electromagnetism, the gauge-invariant isospin kinetic term can be envisaged,

$$\mathcal{L}_{\text{gauge}} = \left(\frac{1}{2}\mathbf{F}_{\mu\nu} \cdot \boldsymbol{\tau}\right) \left(-\frac{1}{2}\mathbf{F}^{\mu\nu} \cdot \boldsymbol{\tau}\right) \quad (2.16)$$

$$= -\frac{1}{4}F_{\mu\nu}^a \tau^a F_b^{\mu\nu} \tau_b \quad (2.17)$$

$$= -\frac{1}{2}\text{tr}(F_{\mu\nu}F^{\mu\nu}) \quad (2.18)$$

where the last equality comes from the identity $\text{tr}(\tau^a \tau^b) = 2\delta^{ab}$, and the field-strength tensor $F_{\mu\nu}$ must transform under local gauge transformations G as

$$F'_{\mu\nu} = GF_{\mu\nu}G^{-1}. \quad (2.19)$$

In analogy with electromagnetism, the $F_{\mu\nu}$ can be written

$$F_{\mu\nu} = -\frac{i}{g}[D_\nu, D_\mu] \quad (2.20)$$

$$= \partial_\nu W_\mu - \partial_\mu W_\nu + ig[W_\nu, W_\mu], \quad (2.21)$$

with

$$W_\mu = \frac{1}{2}\tau^a w_\mu^a = \frac{1}{2} \begin{bmatrix} w_\mu^3 & w_\mu^1 - iw_\mu^2 \\ w_\mu^1 + iw_\mu^2 & -w_\mu^3 \end{bmatrix} \quad (2.22)$$

where w_μ are the three gauge fields. For the Abelian $U(1)_Y$ case, the commutator vanishes giving the electromagnetic field-strength tensor (with $W_\mu \rightarrow A_\mu$). In addition to the bilinear terms, the non-Abelian structure of $SU(2)$ results in trilinear and quadrilinear terms, meaning even without fermion sources there are still interactions among gauge bosons.

It can be shown through explicit calculation [3] that Eq. 2.20 has exactly the desired behaviour under local gauge transformations (Eq. 2.19). The locally gauge invariant Yang-Mills Lagrangian is given by

$$\mathcal{L}_{\text{YM}} = \bar{\psi}(i\gamma^\mu D_\mu - m)\psi - \frac{1}{2}\text{tr}(F_{\mu\nu}F^{\mu\nu}). \quad (2.23)$$

As in electromagnetism, adding in an *ad hoc* way a mass term for the \mathbf{w}_μ gauge fields breaks local gauge invariance. However, it is known that the nuclear force involves exchange of massive pseudoscalar and vector mesons, so this theory of isospin (or *flavour*) invariance cannot be the true description of the nuclear force; an extension from which mediators are endowed with mass is necessary.

2.1.3 Spontaneous symmetry breaking (aka “hidden” symmetries)

It was shown earlier that it is not possible to add a mass term to the gauge bosons of the Yang-Mills theory of isospin. Whereas adding explicit mass terms to $SU(3)_C$ theory gauge invariance is retained, the $SU(2)_L \otimes U(1)_Y$ electroweak symmetry of the SM breaks; adding a mass term of the form $M^2 B_\mu B^\mu$ for the known-to-be massive weak force bosons is incompatible with local gauge invariance. Moreover, introducing a mass term for fermions,

$$\begin{aligned} -m_\psi \bar{\psi}\psi &= -m_\psi \bar{\psi} \left[\frac{1}{2}(1 - \gamma^5) + \frac{1}{2}(1 + \gamma^5) \right] \psi \\ &= -m_\psi \bar{\psi} \left[\frac{1}{2}(1 - \gamma^5)\psi_L + \frac{1}{2}(1 + \gamma^5)\psi_R \right] \\ &= -m_\psi (\bar{\psi}_R \psi_L + \bar{\psi}_L \psi_R), \end{aligned} \quad (2.24)$$

is manifestly non-invariant under local isospin transformations since ψ_L is part of a weak isospin doublet and ψ_R a singlet; these two objects have different transformation properties, and therefore their coupling spoils gauge symmetry.

To generate gauge boson and fermion masses while, at the same time, maintain the $SU(2)_L \otimes U(1)_Y$ electroweak gauge symmetry, the Higgs(-Brout-Englart-Guralnik-Hagen-Kibble) mechanism of spontaneous symmetry breaking [4–8] (SSB) is needed¹.

The Goldstone theorem

Before diving into the Higgs mechanism, it is important to understand the consequences of SSB using a simple model, first investigated by Goldstone [9]. The Lagrangian for this model is based on two real scalar fields, ϕ_1 and ϕ_2 ,

$$\mathcal{L} = \frac{1}{2} \sum_{i=1}^2 \partial_\mu \phi_i \partial^\mu \phi_i - V(\Phi^2), \quad V(\Phi^2) = \frac{1}{2}\mu^2 \Phi^2 + \frac{1}{4}|\lambda|(\Phi^2)^2. \quad (2.25)$$

where $\Phi^2 = \phi_1^2 + \phi_2^2$. The quadratic term in V is reminiscent of the mass term in scalar field theory. Powers greater than the fourth are omitted to ensure renormalisability. The Lagrangian in Eqn. 2.25 is invariant under the group $SO(2)$ of rotations in the (ϕ_1, ϕ_2) internal symmetry space,

$$\Phi \equiv \begin{pmatrix} \phi_1 \\ \phi_2 \end{pmatrix} \rightarrow R(\theta) \begin{pmatrix} \phi_1 \\ \phi_2 \end{pmatrix}, \quad (2.26)$$

¹ The canonical example of spontaneous symmetry breaking is that of the Heisenberg (infinite) ferromagnet, as described in [3], p.73.

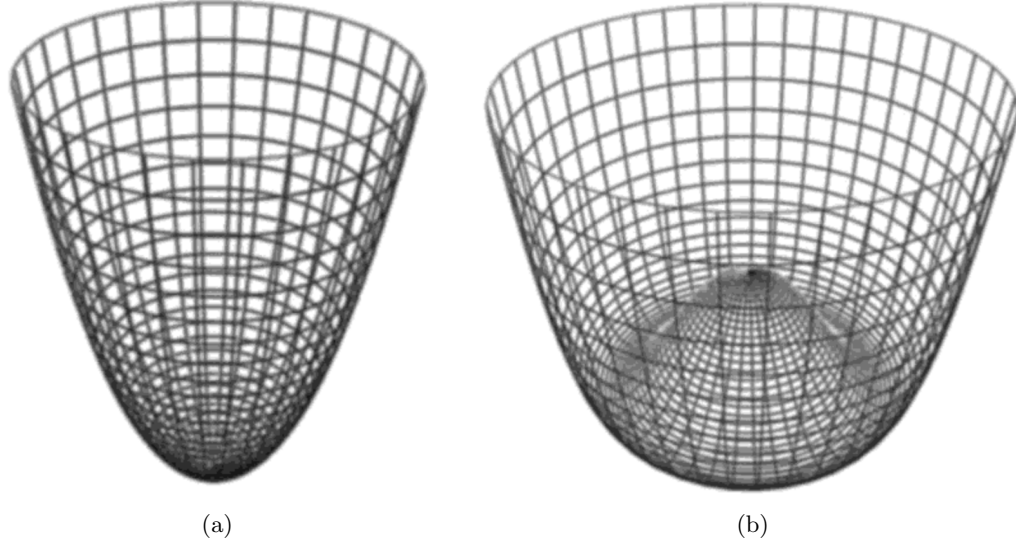


Figure 2.1: Potential in Eqn. 2.25 with (a) a unique minimum at $\phi_1 = \phi_2 = 0$ ($\mu^2 > 0$), and with (b) a degenerate vacuum at $\phi_1 = \phi_2 \neq 0$ ($\mu^2 < 0$) [3].

where $R(\theta)$ is a 2×2 orthogonal matrix with $\det(R) = 1$, as per $SO(2)$.

Two cases exist which correspond to either manifest or spontaneously broken (or hidden) $SO(2)$ symmetry. If the parameter $\mu^2 > 0$, the potential in Eq. 2.25 has a unique minimum at $\phi_1 = \phi_2 = 0$ (Fig. 2.1a), corresponding to a single, unique vacuum (ground) state,

$$\langle \Phi \rangle_0 = \begin{pmatrix} 0 \\ 0 \end{pmatrix}. \quad (2.27)$$

Disregarding quartic interaction terms (*i.e.* for small oscillations), the Lagrangian is

$$\mathcal{L}_{\text{SO}} = \frac{1}{2} \sum_{i=1}^2 [\partial_\mu \phi_i \partial^\mu \phi_i - \mu^2 \phi_i^2], \quad (2.28)$$

representing two free scalar fields with a common mass μ , and invariance under $SO(2)$. The generated mass can be thought of as resulting from the restoring force of the potential against small oscillations about the minimum potential.

Things get interesting if the parameter $\mu^2 < 0$. In this case, no unique minimum exists, as shown in Fig. 2.1b, and the field Φ acquires a continuum of distinct states of non-zero vacuum expectation value (vev). These states are degenerate in energy,

$$\langle \Phi^2 \rangle_0 \equiv \langle \phi_i^2 \rangle_0 = -\mu^2 / |\lambda| \equiv v^2, \quad (2.29)$$

owing to the $SO(2)$ symmetry of the potential. While the Lagrangian (Eqn. 2.25) is invariant under $SO(2)$ rotations, the vacuum state is not – it will be *spontaneously broken*, secret, or hidden, by a choice of vev that takes on a preferred direction in (ϕ_1, ϕ_2) -space. Choosing the vacuum state to be purely in

the ϕ_2 -direction,

$$\langle \Phi \rangle_0 = \begin{pmatrix} 0 \\ v \end{pmatrix} \quad (2.30)$$

and expanding around the vacuum configuration by defining

$$\Phi' \equiv \Phi - \langle \Phi \rangle \equiv \begin{pmatrix} \theta \\ \eta \end{pmatrix}, \quad (2.31)$$

the Lagrangian (2.25) can be written, with terms up to third-order in the fields, as

$$\begin{aligned} \mathcal{L} = & \frac{1}{2}(\partial_\mu \eta \partial^\mu \eta + 2\mu^2 \eta^2) + \frac{1}{2}(\partial_\mu \theta \partial^\mu \theta) \\ & - |\lambda| v \eta^3 - |\lambda| v \eta \theta^2 + \mathcal{O}(\Phi^4). \end{aligned} \quad (2.32)$$

The $SO(2)$ rotational symmetry is hidden/broken by the terms in the second line which are trilinear in the fields. It can be seen that there are two particles, one massive η particle with mass $m^2 = -2\mu^2 > 0$, and a massless θ . As before, the non-zero mass of the η can be attributed to the potential's restoring force in the radial direction. The masslessness of the θ is a consequence of $SO(2)$ invariance in that there is no angular restoring force; θ appears in Eq. 2.32 only through its derivatives.

This is exemplary of the Goldstone theorem [9–12]: for every spontaneously broken (or hidden/secret) continuous symmetry, a massless spin-0 particle called a “Goldstone boson” arises. That is, the cardinality of Goldstone bosons is the number of broken generators.

The Higgs mechanism

The same exercise as previously presented can be made for a complex doublet of scalar fields,

$$\Phi \equiv \begin{pmatrix} \phi^+ \\ \phi^0 \end{pmatrix} = \frac{1}{2} \begin{pmatrix} \phi_1 - i\phi_2 \\ \phi_3 - i\phi_4 \end{pmatrix} \quad (2.33)$$

with the invariant now being $\phi^\dagger \phi = \frac{1}{2} \sum_{i=0}^3 \phi_i^2 = \frac{1}{2} \phi_i \phi^i$. For the non-Abelian case of the electroweak sector of the SM, at least three degrees of freedom are needed, one for each of the weak gauge bosons; as defined, Φ has four. This is handy since $SU(2)_L \otimes U(1)_Y$ has four generators – three for the weak and one for the EM interaction.

The electroweak (ignoring the strong interaction) Lagrangian of the SM is given by [13]

$$\mathcal{L}_{\text{EW}} = -\frac{1}{4}(W_{\mu\nu}W^{\mu\nu} - B_{\mu\nu}B^{\mu\nu}) + i(\bar{\Psi}_L D_\mu \gamma^\mu \Psi_L + \bar{\psi}_R D_\mu \gamma^\mu \psi_R) + \dots, \quad (2.34)$$

where $L(R)$ represents the left (right) chiral projections, $\psi_{L(R)} = (1 \mp \gamma_5)\psi/2$, of fermions,

$$\Psi_L = \begin{pmatrix} u \\ d \end{pmatrix}_L, \quad \begin{pmatrix} \nu_\ell \\ \ell \end{pmatrix}_L, \quad (2.35)$$

and the right-handed singlet fields are

$$\psi_R = u_R, \, d_R, \, \ell_R. \quad (2.36)$$

The $SU(2)_L \otimes U(1)_Y$ gauge transformations transform the fields as

$$\Psi_L \rightarrow \Psi'_L = e^{iY_L\alpha(x)} G_{\text{iso}} \Psi_L \quad (2.37)$$

$$\psi_R \rightarrow \psi'_R = e^{iY_R\alpha(x)} \psi_R \quad (2.38)$$

where $G_{\text{iso}}(x)$ is given by Eqn. 2.12,

$$G_{\text{iso}}(x) \equiv \exp\left(\frac{i\tau \cdot \omega(x)}{2}\right). \quad (2.12)$$

The gauge-covariant derivatives of the W_μ and B_μ fields are

$$D_\mu \Psi_L = (\partial_\mu + igW_\mu + ig'Y_L B_\mu) \Psi_L, \quad (2.39)$$

$$D_\mu \phi_R = (\partial_\mu + ig'Y_R B_\mu) \psi_R. \quad (2.40)$$

with field-strength tensors

$$W_\mu \rightarrow G_{\text{iso}} W_\mu G_{\text{iso}}^\dagger + \frac{1}{g} (\partial_\mu G_{\text{iso}}) G_{\text{iso}}^\dagger, \quad (2.41)$$

$$B_\mu \rightarrow B_\mu - \frac{1}{g'} \partial_\mu \alpha. \quad (2.42)$$

In the spirit of the potential in Eqn. 2.25, a scalar Higgs Lagrangian can be constructed from the complex doublet (2.33),

$$\mathcal{L}_{\text{Higgs}} = (D^\mu \Phi)^\dagger (D_\mu \Phi) - \mu^2 \Phi^\dagger \Phi - |\lambda| (\Phi^\dagger \Phi)^2, \quad (2.43)$$

with weak hypercharge $Y_\Phi = +1$ fixed by the requirement of having correct couplings between Φ and A_μ .

Again $\mu^2 < 0$ results in a non-zero vev. Judicious assignment of the vev is needed now, since, in order to conserve electric charge, the vev cannot be in the charged direction of Φ . Therefore, the neutral component of Φ develops an infinite set of degenerate states,

$$\langle \Phi \rangle_0 = \begin{pmatrix} 0 \\ \frac{v}{\sqrt{2}} \end{pmatrix}, \quad v = \sqrt{\frac{-\mu^2}{|\lambda|}}, \quad (2.44)$$

and breaks the $SU(2)_L \otimes U(1)_Y$ gauge symmetry down to $U(1)_{\text{EM}}$, which is still a true symmetry of the vacuum. Following the same prescription as before, the field Φ can be parameterised in terms of four real fields,

$$\Phi \rightarrow \exp[-i\theta_a(x)\tau^a] \Phi = \frac{1}{\sqrt{2}} \begin{pmatrix} 0 \\ v + h(x) \end{pmatrix}, \quad (2.45)$$

where the right-hand side is written in the unitary gauge (*i.e.* $\theta(x) = 0$), and the replacement $\eta \rightarrow h$ is made to emphasise the Higgs particle. The three would-be Goldstone bosons are “gauged away” as a result of the $SU(2)$ invariance of the Lagrangian. Finally, expanding the kinetic term of Eqn. 2.43 reveals the four fields [13],

$$W_\mu^\pm = \frac{1}{2}(W_\mu^1 \mp iW_\mu^2), \quad Z_\mu = \frac{g_2 W_\mu^3 - g_1 B_\mu}{\sqrt{g_1^2 + g_2^2}}, \quad A_\mu = \frac{g_2 W_\mu^3 + g_1 B_\mu}{\sqrt{g_1^2 + g_2^2}} \quad (2.46)$$

with bilinear terms $M_W^2 W_\mu^+ W^{-\mu}$ and $M_Z^2 Z_\mu Z^\mu$, *i.e.* they have acquired mass.

For fermions, a $SU(2)_L \otimes U(1)_Y$ invariant Yukawa Lagrangian [14]

$$\mathcal{L}_F = -|\lambda_F| \bar{\Psi}_L \Phi \psi_R + h.c. \quad (2.47)$$

is introduced, and the same procedure as presented above is repeated. Fermion masses are then identified as the constant coefficients,

$$m_F = \frac{|\lambda_F| v}{\sqrt{2}} \quad (2.48)$$

where λ_F is the Yukawa coupling, proportional to m_F . In contrast to massive vector bosons, for which the coupling with the Higgs is proportional to M_V^2 , it can be seen that the coupling between the Higgs and fermions is proportional to the fermion mass.

It is crucial to know that while the total Lagrangian, $\mathcal{L} = \mathcal{L}_{EW} + \mathcal{L}_{\text{Higgs}}$, is invariant under gauge transformations, there is no *a priori* reason that the ground/vacuum state must respect the same invariance. The vacuum, or state of lowest energy, can suddenly fall to a specific fixed configuration, breaking the once-was $SU(2)_L \otimes U(1)_Y$ symmetry of the Lagrangian to $U(1)_{\text{QED}}$. In this case, the three broken generators of the broken gauge group give rise to three Goldstone bosons that are ultimately eliminated due to the underlying, hidden gauge symmetry. By switching to the unitary gauge, the W_μ^\pm and Z_μ become massive after absorbing, or “swallowing”, the Goldstone bosons, each gaining an additional (longitudinal) degree of freedom. On the other hand, A_μ remains massless since $U(1)_{\text{QED}}$ is an unbroken symmetry.

The Higgs boson

Nearly 50 years after having been hypothesised, a particle consistent with SM Higgs boson was observed by the ATLAS [15] and CMS [16] experiments with a mass $m_h \approx 125$ GeV. The Higgs is electrically neutral with positive parity, and carries both weak isospin ($T_3 = -1/2$) and hypercharge ($Y = +1$). While a triumphant moment for both experiments, the measured m_h appears to fall just short of the narrow range $m_h \in (130, 180)$ GeV for which the SM would survive at all energy scales up to the Planck scale [17]. This implies the Universe is possibly in a *metastable* and that its physics could eventually be reconstituted into new fundamental structures and forces different from what we know today. Finding only a Higgs at the TeV scale and nothing else is therefore considered to be a ‘maximal conceivable disaster’ [18]. On the other hand, such a ‘maximal conceivable disaster’ could be considered by some to be a blessing; it means the SM is likely only an effective theory, and therefore more physics exists to discover and understand somewhere between the electroweak and Planck scales.

2.1.4 Quantum chromodynamics

The theory that describes the strong interaction between coloured partons, *i.e.* quarks and gluons, is quantum chromodynamics (QCD). The $SU(3)_C$ component of the SM gauge group corresponds the invariance of QCD under rotations in “colour-space”. While Gell-Mann’s (and Zweig’s) quark model hypothesis [19] had already gained traction in 1964, and was supported by results from deep inelastic scattering experiments [20], skepticism remained. Quarks are required to have half-integer spin to account for the spins of observed hadrons – baryons, comprising three quarks, and mesons, comprising a quark and anti-quark. An immediate problem is evident then when considering spin-3/2 baryons with

three of the same flavour quarks (*e.g.* the Δ^{++}), namely, their wave functions are totally symmetric.

Around the same time the quark model was hypothesised, colour was introduced by Greenberg [21] to rectify this issue which directly contradicts Fermi-Dirac statistics; by including a colour degree of freedom with three possible values, indexed in what follows by $a = 1, 2, 3$ (red, green, or blue), baryon wave functions can be made totally anti-symmetric. The idea of confinement – that only colour singlet (*i.e.* colour-neutral) states can exist in Nature – remedied the implication of a multitude of new states as a result of the colour hypothesis. Quantum chromodynamics was widely accepted as the only candidate theory of the strong interactions after the discovery of charm quark in 1974 at Brookhaven National Laboratory’s alternating-gradient synchrotron [22] and the Stanford Linear Accelerator [23], and the gluon in 1979 [24] at the Deutsches Elektronen-Synchrotron.

Three coloured quarks $q_a, a = 1, 2, 3$ of each quark flavour form a triplet in the fundamental representation of $SU(3)_C$, and eight gluons form an octet in the adjoint representation. Mesons and baryons are colour-singlet states that can be represented by $q_a \bar{q}^a$ and $\epsilon^{abc} q_a q_b q_c$, respectively, where ϵ^{abc} is the total antisymmetric tensor. Following the general structure of a Yang-Mills theory (see Eqn. 2.23), the QCD Lagrangian is given by

$$\mathcal{L} = -\frac{1}{4} F_{a\mu\nu} F_a^{\mu\nu} + \sum_q \bar{q}_j (i\gamma^\mu \partial_\mu \delta_{jk} - g_s \gamma^\mu (T_a)_{jk} G_{a\mu} - M_j \delta_{jk}) q_k, \quad (2.49)$$

where the colour indices $a = 1, \dots, 8$ and $j, k = 1, 2, 3$, G_a^μ are the gluon fields, and T_a are the $SU(3)$ generators provided by the Hermitian and traceless Gell-Mann matrices, $T_a = 1/2\lambda_a$. The coupling g_s is related to the *strong coupling constant*, α_s , through the relation

$$\alpha_s = \frac{g_s^2}{4\pi}; \quad (2.50)$$

g_s and the quark masses are the fundamental parameters of QCD. The gluon field tensor is

$$F_a^{\mu\nu} = \partial_\mu G_a^\nu - \partial_\nu G_a^\mu - g_s f_{abc} G_b^\mu G_c^\nu, \quad (2.51)$$

with f_{abc} being the $SU(3)$ structure constants, defined by the commutation of the generators

$$[T_a, T_b] = i f_{abc} T_c. \quad (2.52)$$

The QCD Lagrangian is invariant under the infinitesimal gauge transformations

$$q(x) \rightarrow [1 - ig\alpha_a(x)T_a]q(x), \quad (2.53)$$

$$G_a^\mu(x) \rightarrow G_a^\mu(x) + \partial^\mu \alpha_a(x) + g_s f_{abc} \alpha_b(x) G_c^\mu(x), \quad (2.54)$$

Asymptotic freedom, confinement, and the not-so-constant coupling

The gluon field tensor in Eqn. 2.51 describes $q\bar{q}g$ and ggg vertices, proportional to the coupling g_s , and four-gluon vertices, proportional to g_s^2 ; the latter two couplings are due to the non-Abelian structure of the gauge group, analogous to the W self-interactions in the $SU(2)$ case. Gluons interact amongst one another due to the fact that they carry one unit of colour and one unit of anticolour charge. These self-interactions have important implications for QCD.

At short distances (large momentum transfers), the self-couplings result in a charge “anti-screening” effect², resulting in the weakening of α_s . As a result, when hadrons are probed at energies $\gtrsim 1$ GeV, constituent quarks behave essentially as free particles – a property called *asymptotic freedom*. Asymptotic freedom permits perturbative calculations in QCD, and therefore arrive at quantitative predictions for hard-scattering cross sections of hadronic collisions. On the other hand, at large distances (*i.e.* energies below about 1 GeV), α_s becomes large and leads to the *confinement* of quarks; the separation of quarks comprising a hadronic (colourless) bound state requires an amount of energy sufficient for the creation of additional quark-antiquark pairs. These newly-created pairs of quarks subsequently combine with the original quarks to form colourless states, a process called *hadronisation*.

In light of the strong coupling constant energy dependence, predictions for observables made using the framework of QCD are expressed in terms of a renormalised coupling, $\alpha_s(\mu_R^2)$, a function of the renormalisation scale, μ_R . When μ_R is taken to be close to the scale of the momentum transfer, Q , of a given process, then $\alpha_s(\mu_R^2 \simeq Q^2)$ is indicative of the effective strength of the strong coupling in that process. Parameterised as a function of Q , α_s can be expressed, at leading order, as

$$\alpha_s(Q^2) = \frac{g_s^2(Q^2)}{4\pi} \quad (2.55)$$

$$= \frac{1}{b_0 \ln \frac{Q^2}{\Lambda^2}} = \frac{12\pi}{(11C_A - 4n_f T_R) \ln \frac{Q^2}{\Lambda^2}}, \quad (2.56)$$

where b_0 is referred to as the 1-loop β -function coefficient, $C_F \equiv (N_C^2 - 1)/(2N_C) = 4/3$, $C_A = N_C = 3$, $T_R = 1/2$; Λ is an arbitrary energy scale for which α_s is assumed to be known. The positive integer n_f corresponds to the number of quark flavours whose masses are considered light (*i.e.* $m_q \ll Q$).

It can be seen in Eqn. 2.55 that if $n_f \leq 16$, then as $Q \rightarrow \infty$, the coupling strength approaches zero – quarks are asymptotically free. On the other hand, as Q decreases, α_s increases and eventually becomes greater than unity. Accordingly, confinement sets in and perturbative expansion in the coupling is no longer possible. The typical scale at which α_s is determined is $Q^2 = M_Z^2$, the squared-mass of the Z boson; the current (2016) world average, which was extracted using a number of results at different energy scales Q , is $\alpha_s(M_Z^2) = 0.1181 \pm 0.0011$ [25]. A summary of these measurements, demonstrating the running of the coupling, is given in Fig. 2.2.

2.2 Physics beyond the Standard Model

While the SM has been so far incredibly successful in describing the fundamental particles and the interactions between them, as already alluded to in the previous section, it appears that the SM is an incomplete theory.

While numerous limitations to the theory exist, two are described below to motivate the search presented in this analysis.

2.2.1 The hierarchy and fine-tuning problems

There is a large range in the intrinsic energy scales of the SM, $\mathcal{O}(100)$ GeV, and the Planck scale, $M_{\text{Pl}} \sim (10^{19})$ GeV, at which the gravitational force becomes significant. As such, unification of General

² Because photons do not carry electric charge, they do not couple to one another (hence the Abelian $U(1)$ theory of EM) and therefore the opposite effect occurs, *i.e.* charge is *screened*, and the fine-structure constant α increases.

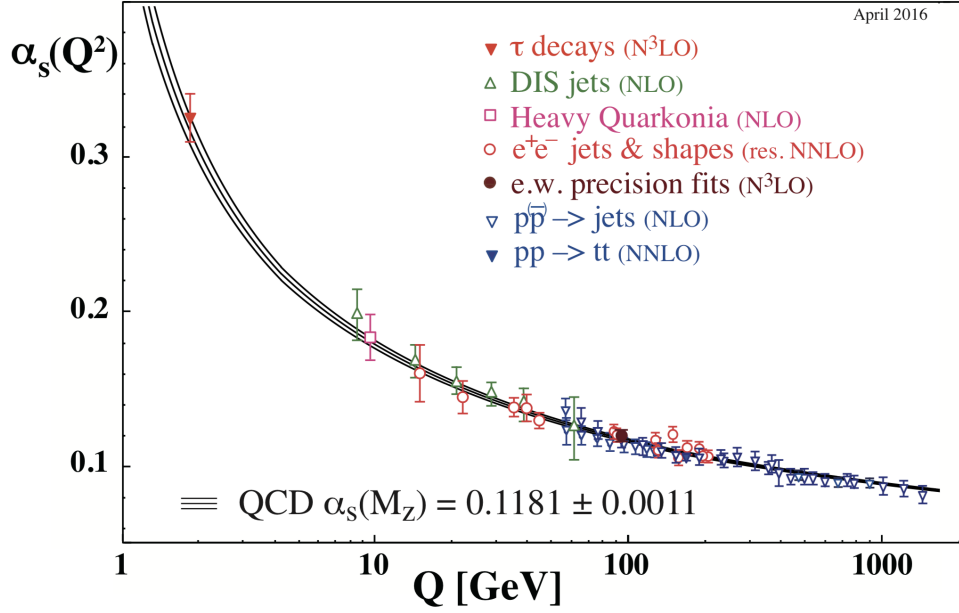


Figure 2.2: Summary of measurements of α_s as a function of energy scale Q , demonstrating the energy dependence of the coupling constant [25].

Relativity and the SM is difficult to achieve without resorting to an extraordinary level of fine-tuning of the mass of the Higgs boson.

The Higgs mass is directly related to its coupling in the SM Lagrangian via $m_h^2 = 2\mu^2$, but also receives higher order (perturbative) corrections to its mass, of which larger contributions come from more massive particles. The physical mass of the Higgs is $m_h^2 = m_{h0}^2 + \Delta m_h^2$, where m_{h0} is the tree-level (bare) mass. The quantum corrections to the mass, resulting from loop-level diagrams, is,

$$\Delta m_h^2 \sim \frac{\lambda^2}{16\pi^2} \Lambda_{UV}^2, \quad (2.57)$$

where λ is a dimensionless coupling, and Λ_{UV} is an ultraviolet cutoff scale. If the SM is expected to remain valid up to the Planck scale, then $\Lambda_{UV} \sim 10^{19}$ GeV, resulting in corrections to the Higgs mass of order $\sim 10^{17}$ larger than its observed mass. If the bare mass of the Higgs is to cancel out the large loop corrections, resulting in its experimentally observed physical mass, the bare mass and corrections would need to match at a precision of one part in 10^{36} – a highly coincidental result.

The hierarchy problem is eliminated if instead there is some $\Lambda_{NP} \sim 1$ TeV, a scale at which new physics exists. For example, the Higgs itself could be composite, held together by some new strong force around the weak scale.

2.2.2 Dark Matter

Measurements of galactic rotation curves – *i.e.* angular velocities of stars and gas as a function of their distance from a galactic center – provide some of the most convincing evidence [26] for additional mass in the Universe; simply put, most galaxies rotate much faster than expected should they follow Newtonian dynamics. These observations, as well as the anomolous observations of gravitational lensing [27], suggest the existence of some form of unknown, non-luminous matter is present in the Universe – clustered

predominantly around galaxies – that is invisible to telescopes.

More recent, and perhaps most convincing, evidence [28] for the so-called *Dark Matter* (DM) come from measurements of the cosmic microwave background (CMB), which provide a means to calculate the density of DM in the Universe rather than simply at a galactic scale. Measurements of observed CMB anisotropies are used to test cosmological models and place stringent constraints on model parameters. The European Space Agency’s Planck satellite [29] provided data to a set measurements of the dark matter and baryon densities, $\Omega_c h^2 = 0.129 \pm 0.001$ and $\Omega_b h^2 = 0.0224 \pm 0.0001$, respectively, indicating that there is nearly six times as much DM than ordinary matter in the Universe [30].

From studies of galaxy surveys, it was thought that every galaxy contained DM, and that it essential ingredient for galaxy formation, and therefore the DM *halo* and total stellar mass of a galaxy couple to one another. However, in 2018 a team of researchers discovered NGC1052-DF2, a galaxy almost completely devoid of DM [31, 32]. Again in 2019, another galaxy, NGC1052-DF4, was determined to contain little-to-no DM within it [33]. This apparent absence of DM demonstrates that DM is not always coupled with baryonic matter on galactic scales, and therefore DM exists independently of normal matter.

There is currently no appropriate candidate particle for DM in the SM, and so a new particle beyond the SM is expected to exist. It does not have direct couplings to photons, hence “dark”, and therefore is not directly observable by astronomical experiments. Furthermore, if DM had strong force couplings, it would make its detection more likely, however, since such particles have not been experimentally observed, models with DM-parton couplings are mostly disfavoured. These constraints then motivate *Weakly Interacting Massive Particles* (WIMPs), a general term including sterile neutrinos, Kaluza-Klein states, and others. Of particular interest to searches performed by LHC experiments are simplified DM models [34]. Such models propose extensions to the SM that include an additional gauge boson that couples to both DM and SM particles with potentially observable decays to SM partons.

Many theories beyond the SM model exist that attempt to explain, or provide solutions to, its shortcomings. The analysis presented in this thesis considers two such models that hypothesise new particles decaying to a pair of jets.

2.2.3 The Technicolor Model

Before the observation made in 2012 by the ATLAS and CMS experiments of a new particle with a mass around 125 GeV, technicolor (TC) theories were among those competing for an explanation of electroweak symmetry breaking (EWSB) in the Standard Model (SM). Measurements of Higgs boson couplings, spin, and parity have since been in good agreement with SM predictions. As a result, many physicists believe that the SM Higgs boson, h , has been discovered, thus excluding naive TC models and their interpretation of h as the lightest spin-0, positive parity bound state of technifermions. Recent developments in TC, namely extended TC (ETC), aim to reconcile the hierarchy problem associated with the SM Higgs, as well as address its dynamical origin.

The analysis presented in this thesis considers a generic strong ETC [35] as one of the signal models, herein denoted as the “ ρ -model”. In the ρ -model, the Higgs is a composite particle bound by strong interactions well above the electroweak scale, $\Lambda \gg \Lambda_{EW} \sim 100$ GeV, where Λ is the energy scale of the new dynamics or particles stabilising the Higgs mass, m_h . As in the SM and TC, fermions transform as left-handed doublets and right-handed singlets under $SU(2)_L \otimes U(1)_Y$. Furthermore, ETC is presumed to

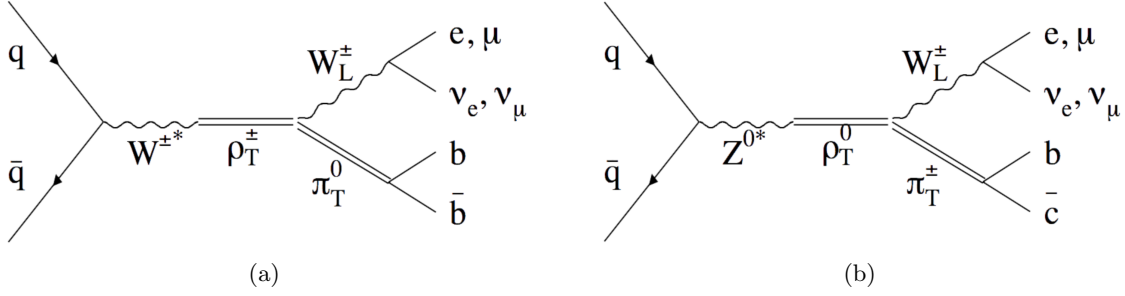


Figure 2.3: The Feynman diagrams for the (a) charged ρ_{TC}^\pm and (b) neutral ρ_{TC}^0 decays to a SM W vector boson and a π_{TC} technimeson, followed by the leptonic and hadronic decays of the W and π_{TC} , respectively.

be the source of electroweak symmetry breaking when its interaction strength exceeds a “critical value”. Beyond this critical value, non-zero top quark and technifermion masses, m_t and m_T , respectively, are generated. Although these masses are typically of order $\Lambda = \Lambda_{ETC} \sim 100$ TeV, the ETC coupling can be tuned to within $\mathcal{O}(m_t^2/\Lambda^2)$ of its critical value, thereby substantially reducing $m_t \sim 100$ GeV. Extended TC then generates a complex composite electroweak doublet for a scalar h with a vev $v = \mathcal{O}(m_t)$ plus three Goldstone bosons, specifically the longitudinal components of the SM W^\pm and Z vector bosons. The scalar has a mass $m_h = \mathcal{O}(m_t)$ and a large Yukawa coupling $g_t \simeq m_t/v$ to the top quark, consistent with SM measurements.

The primary motivation for the ρ -model is that the need for fine-tuning of SM couplings or masses is eliminated, meaning naturalness is manifest; the quadratically divergent terms contributing to m_h are removed by the condition that m_t and m_T are much less than Λ .

The ρ -model assumes that a heavy resonance, ρ_{TC} , is produced via the s -channel and decays to a SM W boson and a technimeson, π_{TC} , where the W and π_{TC} subsequently decay into leptons and jets, respectively:

$$\rho_{TC}^\pm \rightarrow W_L^\pm \pi_{TC}^0 \rightarrow (\ell^\pm \nu)(jj) \quad (2.58)$$

$$\rho_{TC}^0 \rightarrow W_L^\pm \pi_{TC}^\mp \rightarrow (\ell^\pm \nu)(jj). \quad (2.59)$$

The leading-order Feynman diagrams for these processes are shown in Figure 2.3.

2.2.4 The Simplified Dark Matter Model

Simplified models should provide an accurate description of the physics scale at which an accelerator probes, and introduce a limited number of additional free states and parameters [34]. Simplified DM models typically contain a dark sector comprising of one or more stable, long-lived DM particles, along with an unstable mediator particle that mediates the interaction between DM and SM particles.

The simplified DM model considered here contains a single spin-1 mediator, created through the addition of a new $U(1)$ gauge symmetry to the SM. The spin-1 mediator (Z') can have either vector or

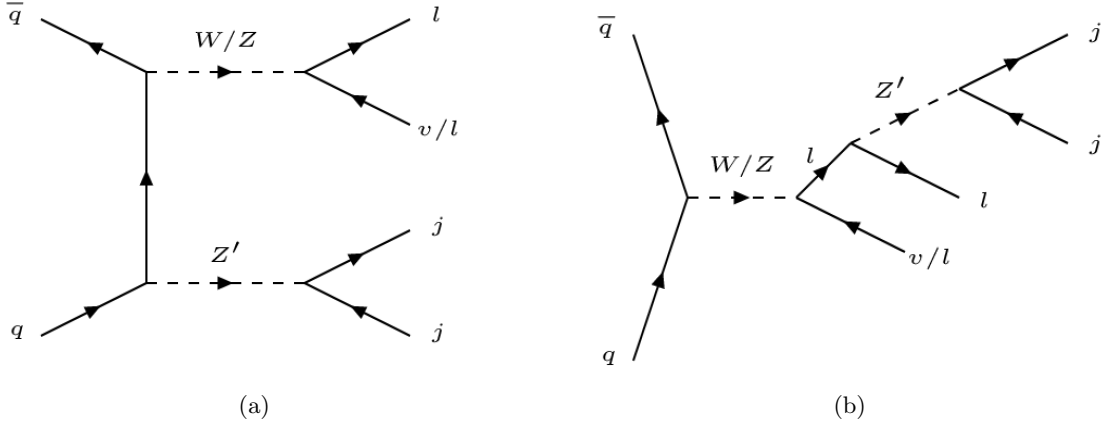


Figure 2.4: Feynman diagrams for the (a) t -channel production and (b) s -channel production of a Z' resonance in the context of the considered simplified DM model.

axial-vector couplings described with the following interaction Lagrangians [36]:

$$\mathcal{L}_{\text{vector}} = -g_{\text{DM}} Z'_\mu \bar{\chi} \gamma^\mu \chi - g_q \sum_{q=u,d,s,c,b,t} Z'_\mu \bar{q} \gamma^\mu q - g_\ell \sum_{\ell=e,\mu,\tau} Z'_\mu \bar{\ell} \gamma^\mu \ell \quad (2.60)$$

$$\mathcal{L}_{\text{axial-vector}} = -g_{\text{DM}} Z'_\mu \bar{\chi} \gamma^\mu \gamma_5 \chi - g_q \sum_{q=u,d,s,c,b,t} Z'_\mu \bar{q} \gamma^\mu \gamma_5 q - g_\ell \sum_{\ell=e,\mu,\tau} Z'_\mu \bar{\ell} \gamma^\mu \gamma_5 \ell \quad (2.61)$$

This model contains five free parameters; g_{DM} is the coupling of Z' to the long-lived DM fermion; g_q is the coupling of Z' to SM quarks, and g_ℓ is its coupling to SM leptons; M_{med} is the mass of Z' ; and M_χ is the mass of the DM particle. Figure 2.4 shows the two main resonant decay processes involving Z' decays to partons in association with one or two final-state charged leptons.

2.3 Proton-proton collisions

The compositeness of hadrons – or more specifically, protons – makes collisions between them a fair bit more complicated than those between *e.g.* electrons which are at present considered to be truly fundamental particles. A proton comprises two u and one d quarks which carry its electric charge and baryon quantum numbers; these *valence* quarks are held together by the strong force, *i.e.* through the exchange of gluons. Because these gluons can split into quark-antiquark pairs or additional gluons, the proton actually consists of a *sea* of quarks and gluons (collectively referred to as partons) in addition to the valence partons.

2.3.1 Anatomy of a collision

A result of splitting, and subsequent annihilation of sea quark-antiquark pairs, is that a number of different processes take place in a single pp collision at different squared momentum transfers, Q^2 . The complete interaction between two colliding protons can be decomposed into three separate parts: the *hard-scatter* (HS), *underlying event* (UE), and *hadronisation*.

Figure 2.5 shows a simulated pp collision – wherein the incoming protons dissociate, a so-called “inelastic” collision – illustrating the various interactions. In the upper hemisphere of this figure, the

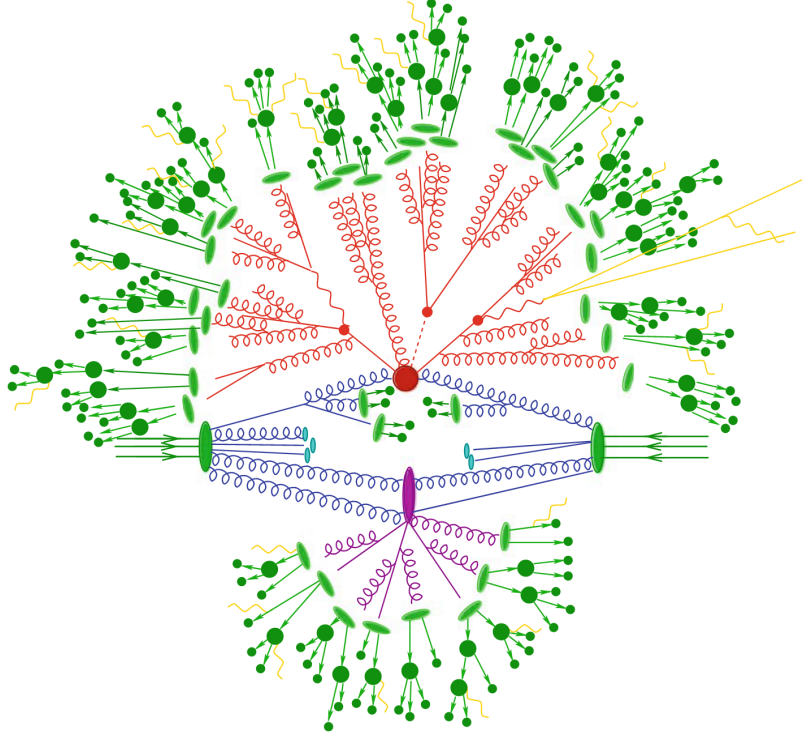


Figure 2.5: Illustration of a simulated pp collision [37]. Details can be found in the main text.

incoming protons are indicated by two green ellipses, each with three green arrows representing their direction of travel. The HS process between two partons (one from each incoming proton) is depicted by the large red circle near the centre of the figure. This is a high-energy interaction that permits perturbatively calculable observables, *e.g.* cross sections. Both partons involved in the HS are gluons (curly blue lines) in this example, which undergo initial-state radiation (*i.e.* they split before interacting), resulting in additional quark (straight blue line) and gluon final states.

The outgoing particles from the HS (red lines, representing here two top quarks and a Higgs boson) decay (red circles), and all coloured partons in the shower eventually hadronise (light green ellipses) into colourless states (large dark green circles). The behaviour of outgoing partons in the low momentum-transfer, long-distance regime are dominated by non-perturbative effects that are described using *hadronisation models*. Unstable hadrons decay into stable particles (small dark green circles). Collinear sets of stable hadrons finally form *jets*, objects whose kinematics can be measured by detectors.

The lower hemisphere of Fig. 2.5 illustrates the UE (purple ellipse): secondary interactions between the incoming protons' remnants that do not partake in the HS process. As in the HS, parton showers are produced and evolve to form stable, final-state hadrons. However, the UE is typically much softer (lower Q^2) than the HS, as are the interactions between beam remnants (violet ellipse), and are therefore non-perturbative; such processes are included in cross section calculations through *parton distribution functions*.

Electromagnetic radiation (yellow lines) from electrically charged particles can occur at any time.

2.3.2 Hard-scattering

In a typical pp collision, one parton from each proton participates in a HS process. However, constituent partons carry only a fraction of the total pp centre-of-mass energy, \sqrt{s} , *i.e.* the partonic centre-of-mass energy, $\sqrt{\hat{s}}$, which is related to the proton beam energy via $\hat{s} = x_1 x_2 s$. Here x_1 and x_2 are the *Bjorken* x -variables [38], which can be interpreted as the fraction of the total proton momentum carried by the interacting partons.

Parton distributions and evolution

The probability to find a parton of type i with a specific momentum fraction x at a given momentum transfer Q^2 is given by a parton distribution function (PDF)³, $f_i(x, Q^2)$.

Parton distribution functions are necessarily determined from experimental data – historically from lepton-nucleon deep inelastic scattering, and more recently collider experiments – since QCD cannot predict the structure of the proton. However, the energy dependence of PDFs can be calculated from the celebrated (Dokshitzer-)Gribov-Lipatov-Altarelli-Parisi (DGLAP) renormalisation group equations [39–42]:

$$\frac{\partial}{\partial t} q_i(x, t) = \frac{\alpha_s(t)}{2\pi} \int_x^1 \frac{d\xi}{\xi} \left[\sum_{j=1}^{2f} P_{q_i q_j} \left(\frac{x}{\xi}, \alpha_s(t) \right) q_j(\xi, t) + P_{q_i g} \left(\frac{x}{\xi}, \alpha_s(t) \right) g(\xi, t) \right], \quad (2.62)$$

$$\frac{\partial}{\partial t} g(x, t) = \frac{\alpha_s(t)}{2\pi} \int_x^1 \frac{d\xi}{\xi} \left[\sum_{j=1}^{2f} P_{g q_j} \left(\frac{x}{\xi}, \alpha_s(t) \right) q_j(\xi, t) + P_{gg} \left(\frac{x}{\xi}, \alpha_s(t) \right) g(\xi, t) \right], \quad (2.63)$$

where $t = \mu^2/\Lambda$ for a scale Λ , and the indices i and j run over all quark flavours. The $q_i(\xi, t)$ and $g(\xi, t)$ are respectively the quark and gluon PDFs, and P_{ab} are the *splitting functions* (or ‘evolution kernels’) which describe the probability distribution for a parton to radiate another parton (parton shower) [43]:

$$\begin{aligned} P_{q_i q_j}(z, \alpha_s) &= \delta_{ij} P_{qq}^{(0)}(z) + \frac{\alpha_s}{2\pi} P_{q_i q_j}^{(1)}(z) + \dots \\ P_{qg}(z, \alpha_s) &= P_{qg}^{(0)}(z) + \frac{\alpha_s}{2\pi} P_{qg}^{(1)}(z) + \dots \\ P_{gq}(z, \alpha_s) &= P_{gq}^{(0)}(z) + \frac{\alpha_s}{2\pi} P_{gq}^{(1)}(z) + \dots \\ P_{gg}(z, \alpha_s) &= P_{gg}^{(0)}(z) + \frac{\alpha_s}{2\pi} P_{gg}^{(1)}(z) + \dots \end{aligned} \quad (2.64)$$

Once determined at a particular scale, the DGLAP equations can be used to evolve the PDF amplitude to other scales, providing a complete description of proton constituents.

Figure 2.6 shows an example of an NNPDF next-to-next-to-leading order set of PDF calculations [44] for two different values of Q^2 .

Cross sections

The experimentally measured cross section σ of an arbitrary HS process initiated by colliding hadrons A and B with four-momenta P_A and P_B , respectively, to an inclusive final state X can be generally

³ Not to be confused with a *probability distribution function*.

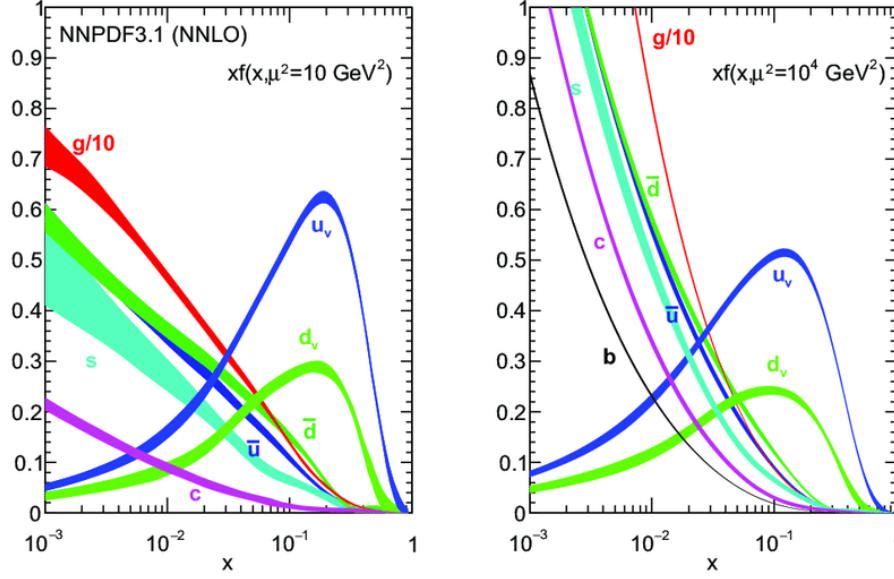


Figure 2.6: Parton distribution functions from the NNPDF collaboration [44]. Shown are PDFs at squared factorisation scales 10 GeV^2 (left) and 10^4 GeV^2 (right). Monte Carlo simulations are used to train a neural network to obtain a parameterisation at low- x . The input samples are then evolved in Q^2 via the DGLAP equations.

expressed in terms of the short-distance parton-parton cross section $\hat{\sigma}$ weighted by PDFs $f_{h/H}$ [45]:

$$\sigma_{AB \rightarrow X} = \sum_{a,b} \int dx_a dx_b f_{a/A}(x_a, \mu_F^2) f_{b/B}(x_b, \mu_F^2) \quad (2.65)$$

$$\times \sum_{m=0}^n (\alpha_s(\mu_R^2))^{(m+k)} \hat{\sigma}_{ab \rightarrow X} \left(x_a P_a, x_b P_b, \frac{Q^2}{\mu_F^2}, \frac{Q^2}{\mu_R^2} \right). \quad (2.66)$$

This is illustrated in Fig. 2.7. Here $\mu_F \sim Q$ is the *factorisation scale* that marks the transition between long- and short-distance interactions, and n is the order at which the cross section is evaluated, *e.g.* $n = 0$ is the leading order calculation, $n = 1$ is next-to-leading order, *etc.* The power of k is a process-dependent contribution, *e.g.* W boson production will contribute at $k = 0$, whereas high- p_T jet production has $k = 2$. Because experimentally one cannot distinguish between different parton types, the leading summation is over all parton flavours a and b in the two colliding hadrons A and B .

The computation of $\hat{\sigma}$ in Eqn. 2.65 can be performed as a perturbation series in the running coupling α_s for $n > 0$; for $n = 0$, the calculation is performed in a straightforward way as in QED. At non-leading orders, partons emitted with low p_T , less than the scale μ_F , are considered part of the hadron structure and are thus absorbed (*i.e. factored out*) into the associated PDF. The ability to split small- and long-distance parts of the cross section results from the *factorisation theorem* [47], which can be proved to all orders in perturbation theory. Factorisation is therefore an extremely useful property of QCD, making it a reliable calculational tool for hadron collision observables.

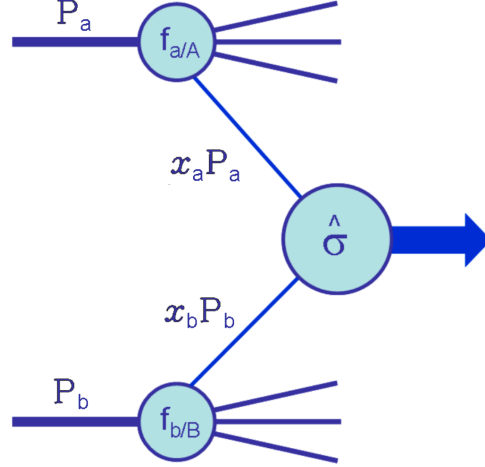


Figure 2.7: Illustration of a generic hadron HS process. The incoming hadrons have four-momenta P_a and P_b , and the partons participating in the HS carry fractions $x_a P_a$ and $x_b P_b$. Soft partons are factored out and absorbed into PDFs $f_{h/H}$. Adapted from [46].

2.3.3 Hadronisation

Upon reaching some cut-off scale, $Q \sim 1$ GeV, showering partons enter the low-momentum transfer, long-distance regime in which confinement begins to take effect and perturbative QCD is no longer applicable. From this point, coloured partons begin to form mesons and baryons by the process of *hadronisation*.

As hadronisation is intrinsically non-perturbative, there currently does not exist an exact or universally accepted mathematical description of the process. Nonetheless, one general approach to hadronisation is the hypothesis of *local parton-hadron duality* [48, 49]: the flow of four-momentum and quantum numbers at the hadron level should follow from the flow of those established at the parton level. Further to this idea is the assumption, based on the observation that perturbation theory works well down to low scales, that $\alpha_s(Q^2)$ can be defined non-perturbatively for any Q ; this is known as *universal low-scale* α_s [50–52].

The aforementioned ideas have been used to guide the physics of hadronisation models which are routinely used by Monte Carlo event generators (described in Sec. 6.4) in hadron-hadron collision simulations.

Independent fragmentation model

In its original scheme [53, 54], partons are assumed to fragment (shower) independently. A fragmenting quark is combined with an antiquark from a quark-antiquark pair created out of the vacuum, producing a meson with energy fraction z . The leftover quark, carrying an energy fraction $(1 - z)$, fragments similarly, thereby creating another, ‘second generation’, meson. Gluons split into quark-antiquark pairs and, with equal probability, one of the two quarks receive all the gluon’s momentum and continues to fragment to produce mesons. This process continues until the remaining energy reaches some cut-off.

While independent fragmentation is the simplest of hadronisation models, it is not used in modern event generators as it suffers from a number of weaknesses:

- Energy (rather than virtuality, *i.e.* virtual squared-mass) dependence can lead to violation of

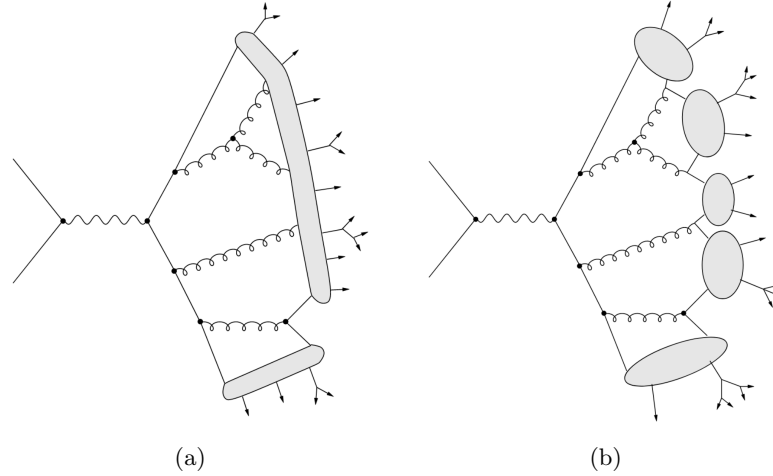


Figure 2.8: Illustrations of the (a) string and (b) cluster hadronisation models. Adapted from [43].

momentum conservation.

- Below the cut-off, there is some residual colour and flavour from the leftover parton in each jet which needs to be neutralised.
- Nearby jets are not merged, but instead remain distinguishable even when they are highly collimated.

String models

In this class of models, the two outgoing quarks from a collision move in opposite directions, losing energy to the colour field as they travel. The “string”, representing the colour flux stretched between the two quarks, breaks up into hadrons through spontaneous quark-antiquark pair production in the string. For gluons that split perturbatively into quark-antiquark pairs during fragmentation, a new string segment is created (Fig. 2.8a). On the other hand, gluons which remain at the end of a shower (*i.e.* when the cut-off is reached) attach directly to the string and produce “kinks”. Each string segment then breaks up as described above, where kinks result in angular distributions of hadrons.

The most widely used model of strings is the so-called Lund model [55], which is implemented in the general-purpose event generator Pythia [56].

Cluster models

Once beyond the perturbative regime of jet development, cluster hadronisation models [57] combine partons into colour-singlet clusters which then decay to form hadrons. The basis of these models is *preconfinement* [58]: the colour structure of a perturbative QCD shower evolution at any intermediate scale Q_0 , where $Q \gg Q_0 \gg \Lambda_{\text{QCD}}$, has colour-singlet clusters with a universal invariant mass distribution that is independent of Q (the starting scale). These colour-singlet clusters are most simply formed by “forcing” all gluons at the end of the shower to split into quark-antiquark pairs (Fig. 2.8b). Neighbouring quarks and antiquarks are then combined into singlet clusters, followed by isotropic decays into pairs

of hadrons whose branching ratios are determined according to the density of states with appropriate quantum numbers [59, 60].

The cluster model, finds use in HERWIG and HERWIG++, with a modified version [61] available in SHERPA [62].

Hadronic jets

Before they decay, hadrons are experimentally observable objects which appear in a detector either in isolation or, more often, in highly-collimated groups called jets. The formation and measurement of jets are outside the scope of this section, and are detailed later in Chap. 5.

Chapter 3

The Large Hadron Collider

No one can destroy The Metal

The Metal will strike you down with a vicious blow

We are the vanquished foes of The Metal

We tried to win, for why? We do not know.

- Tenacious D, *The Metal*

The Large Hadron Collider (LHC) [63–65] is a superconducting particle accelerator and collider at the Conseil Européenne pour la Recherche Nucléaire (European Organisation for Nuclear Research). It was constructed in the same 27 km tunnel that housed the Large Electron-Positron Collider [66, 67], the previous accelerator-collider facility at CERN. The LHC was designed to collide protons at a centre-of-mass energy of 14 TeV 40 million times per second, and heavy ions (lead nuclei) at 5.5 TeV per nucleon pair. The decision on energies was made based on a balance between prospective physics at the TeV scale, the internal diameter needed to equip the existing tunnel with separate rings (unnecessary for oppositely charged particles, as in the case of LEP), and the superconducting magnet technology available at the time [63, 68].

3.1 Machine operation

In addition to a high centre-of-mass energy, another key parameter of a particle collider is *instantaneous luminosity* – the number of collisions per second per unit area. Assuming a Gaussian beam distribution, the instantaneous luminosity can be written as a function of the LHC beam parameters, given as:

$$L = \frac{n_b \cdot f_{\text{rev}} \cdot N_p^2 \cdot \gamma_r}{4 \cdot \pi \cdot \epsilon_n \cdot \beta^*} \cdot F(\theta_c, \sigma_x, \sigma_z), \quad (3.1)$$

where

- n_b : is the number of proton bunches in each ring of the machine. While the maximum number possible is 2808, for nominal Run-2 data-taking conditions there were typically 2544 bunches in each LHC ring.

- f_{rev} : is the 11245.5 Hz per-bunch revolution frequency, as determined by the circumference of the LHC rings and the speed of light;
- N_p : is the *beam intensity* (*i.e.* number of protons per bunch);
- γ_r : is the relativistic gamma (*i.e.* Lorentz) factor for protons;
- ϵ_n : is the normalised transverse beam emittance;
- β^* : is the β function at the collision point, representing the transverse size of the beam; and
- $F(\theta_c, \sigma_x, \sigma_z)$: is a factor that accounts for the luminosity reduction due to beam crossing angle, θ_c , varying transverse bunch sizes at the collision point (the so-called “hourglass” effect), and other geometrical effects.

New physics processes, should they be produced at the TeV scale, are likely to have much smaller cross sections than those typical of the SM (see Fig. 3.1). To observe such rare processes demands high luminosities be delivered by the LHC. Luminosity therefore drives the statistical precision of any measurement, and the ability to observe low cross section processes, as:

$$N_{\text{events}}^{\text{obs}} = \sigma \cdot \epsilon \int dt L, \quad (3.2)$$

where now σ represents the cross section of a given process (given by Nature), ϵ is the efficiency of detecting a given process (determined by experimentalist), and the integral is the *integrated luminosity*.

The high instantaneous luminosity of the LHC does not come without a price: in addition to interesting physics processes, there are a number of (*pile-up*) events occurring in the same (*in-time*) and in adjacent (*out-of-time*) bunch crossings. The number of in-time pile-up events, at design luminosity, is given roughly by:

$$\langle \mu \rangle = \frac{\sigma_{\text{inel}} \cdot L}{f_{\text{rev}} \cdot n_b} \approx \frac{80 \text{ mb} \cdot 10 \text{ nb}^{-1} \text{ s}^{-1}}{11245 \text{ s}^{-1} \cdot 2544} \approx 28 \quad (3.3)$$

where $L = 10^{34} \text{ cm}^{-2} \text{ s}^{-1} = 10 \text{ nb}^{-1} \text{ s}^{-1}$. A summary of the LHC beam parameters and energies, instantaneous luminosities and mean number of interactions per bunch crossing at design operation as well as throughout Run-2 are given in Table 3.1.

3.2 The accelerator chain

The CERN accelerator complex, an overview of which is shown in Fig. 3.2, comprises a number of stages that are required to give protons (and heavy ions) the minimum energy required to stably inject into and circulate the LHC rings. Linac-2¹, the first accelerator in the chain, produces proton beams from a duoplasmatron source and accelerates protons to about $E = 50 \text{ MeV}$. Proton bunches from the linear accelerator are injected into the Proton Synchrotron Booster (PSB), where they are split into four identical PSB rings, boosted to $E = 1.4 \text{ GeV}$, and then recombined into a single bunch.

¹ Linac-2 has been operational for 40 years and as of 12 November 2018 was retired, being succeeded by Linac-4 [72].

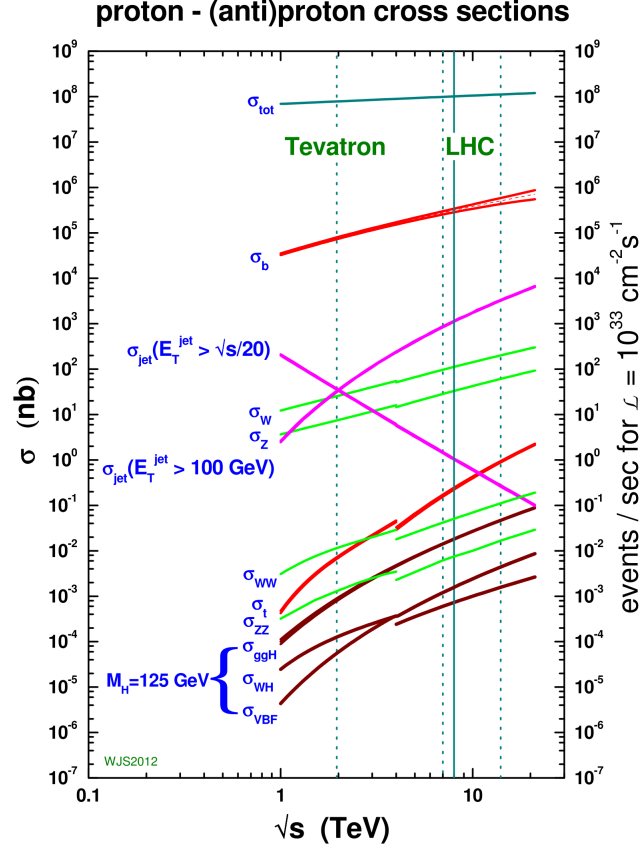


Figure 3.1: Cross sections of selected proton-(anti)proton processes as a function of centre-of-mass energy [69]. The discontinuities around $\sqrt{s} = 4$ TeV is from the transition between proton-anti-proton on the left to proton-proton collisions on the right. The vertical dashed lines indicate centre-of-mass energies run at or attainable by the Tevatron and LHC.

Parameter	Design	2015	2016	2017	2018
Centre-of-mass energy (\sqrt{s}) [GeV]	14000	13000	13000	13000	13000
Number of colliding bunches (n_b)	2808	1000	2208	1866	2556
Bunch charge (N_p) [1e11 charges]	1.5	1.0	1.2	1.2	1.1
Revolution frequency (f_{rev}) [Hz]	11245.5	11245.5	11245.5	11245.5	11245.5
Normalised beam emittance (ϵ_n) [$\mu\text{m rad}$]	3.75	3.47	3.72	2.22	1.99
β^* [m]	0.55	0.80	0.40	0.37	0.30
Peak instantaneous luminosity [$1\text{e}30 \text{ cm}^{-2}\text{s}^{-1}$]	10000	6309.06	13751.86	20571.53	21700.84
Mean interactions per crossing ($\langle\mu\rangle$)	23	13.4	25.1	37.8	36.1
Delivered integrated luminosity [fb^{-1}]	—	4.2	38.5	50.2	63.3

Table 3.1: LHC operating parameters for design conditions and through the Run-2 of data taking. Data retrieved from [70].

Protons are confined longitudinally and laterally into *bunches* using a combination of radio frequency (RF) cavities and focusing quadrupole magnets, respectively. Bunches sit inside RF *buckets* which are

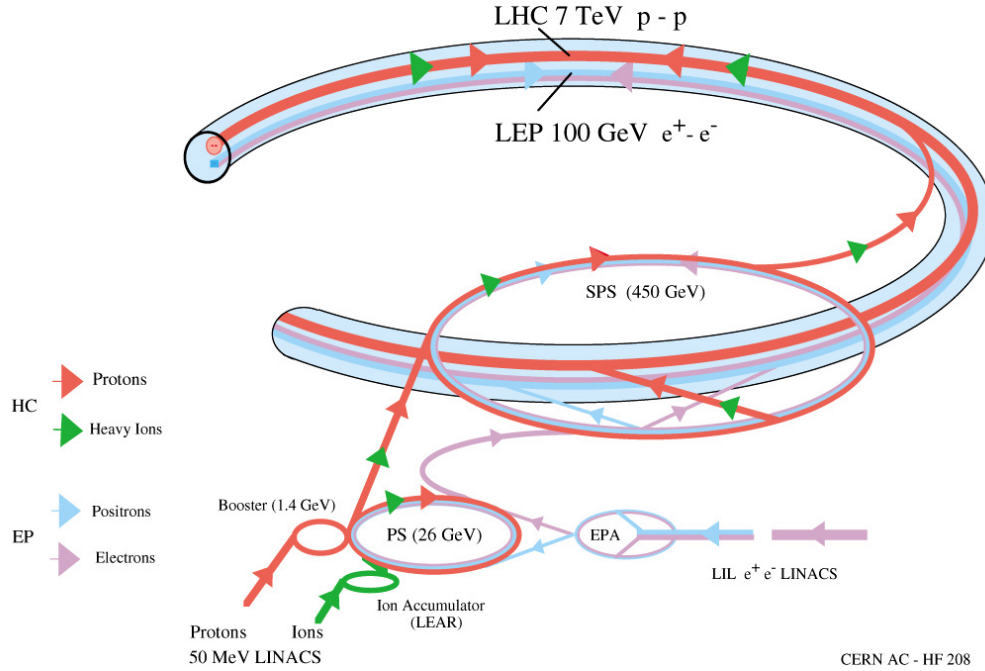


Figure 3.2: The LHC injection complex [71]. The former LEP pre-injectors are also shown at the bottom-right: LEP linear accelerator (LIL) and electron positron accumulator (EPA). Their energies shown for each accelerator represent the per-beam energy at a given stage.

determined by the stable phases of the RF. Beyond the PSB, one bucket is always left empty to allow safe transfer of the bunches into, or out of, each ring. The transfer from one ring to the next is accomplished via “kicker” dipole magnets – magnets that can turn on quickly to deflect bunches out of a ring and into a transfer line. The empty bucket is referred to as an “abort gap”, ensuring that no bunch passes through the the kicker magnets during rise-time. In the absence of an abort gap, at least one bunch would be deflected between ring and transfer line, causing potential damage to the instruments.

At design operation, six PSB bunches of $E = 1.4$ GeV are captured by the Proton Synchrotron (PS). Each bunch is split in three, accelerated to $E = 25$ GeV, and each of those is then split in four. The final “bunch train” contains 72 bunches of $\sim 10^{11}$ protons each and 12 consecutive empty buckets, the latter providing a sufficient gap for the kicker rise-time.

Up to four bunch trains can be injected into the Super Proton Synchrotron (SPS), where they are accelerated to 450 GeV, and then injected into the LHC. To reach design luminosity, $10^{34} \text{ cm}^{-2}\text{s}^{-1}$, this entire process is repeated 24 times, taking about 15 minutes to completely fill each of the LHC rings.

This *multiple splitting scheme* of bunches proved to be very effective. During the first two years of Run-2 (2015–2016), the LHC demonstrated excellent performance at a centre-of-mass energy of 13 TeV, and in 2016 exceeded its design luminosity by 38% using 96-bunch trains with beam intensities $\sim 2 \times 10^{11}$; beam-induced outgassing of one of the kicker magnets limited the intensity from increasing beyond this value [73].

The LHC collisions occur at four different points around its ring, as shown in Fig. 3.3, where seven² experiments are housed. The ring is divided into eight sectors, with Point 1 located at the south-most part. Hadron beams are injected from the SPS between points 1 and 2, and between points 1 and 8, and intersect at points 1, 2, 5 and 8. The ATLAS Experiment (see Chap. 4) is stationed

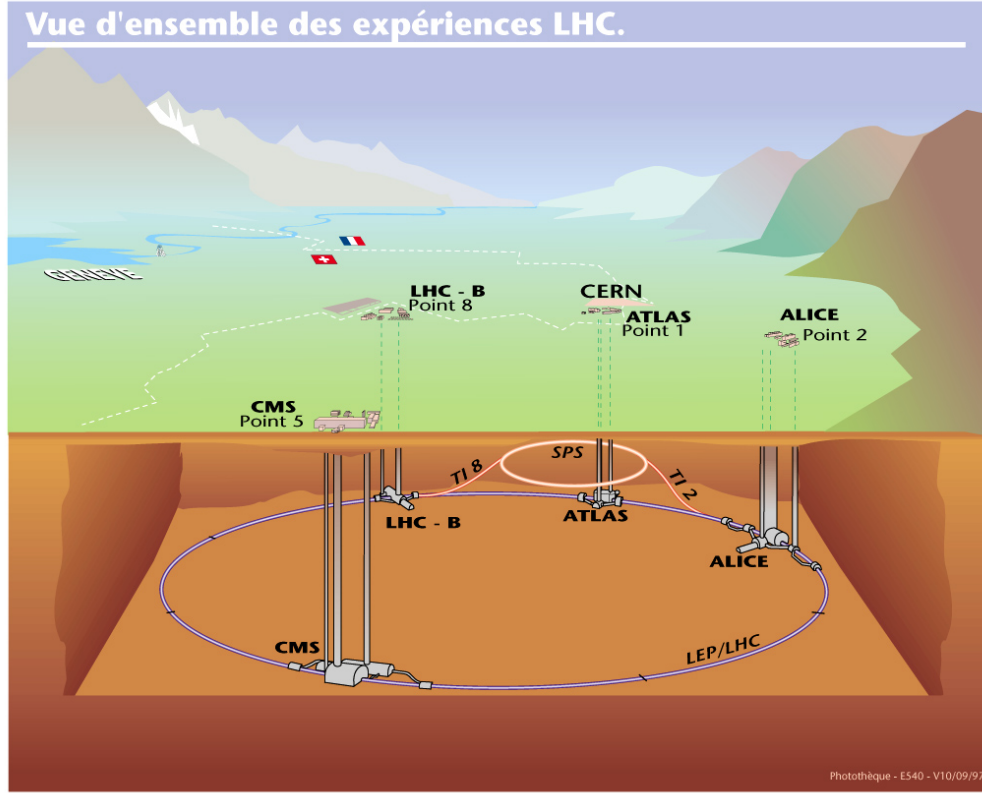


Figure 3.3: The interaction points where experiments at the Large Hadron Collider reside [77]. ATLAS is housed at Point 1, located on the LHC at about one o'clock. Also shown are the other four points, indicated along the ring by small notches between the main points, that divide the ring into eight sectors.

at Point 1, and Point 2 is the home to ALICE [74], a heavy-ion detector designed for the study of strongly-interacting matter. The CMS (Compact Muon Solenoid) detector [75] is located at Point 5, and LHCb [76], a b -quark physics experiment, is located at Point 8.

In June 2017, following record-setting runs with 2554 bunches per beam (96- and 144-bunch trains), a major vacuum problem in a magnet interconnection was found³. Beam-induced heating of the ice that formed as a result caused ice particles to fall into the beam, transforming it into gas (*i.e.* electron clouds) [81]. This led to frequent, unplanned beam dumps that significantly impacted the luminosity. To mitigate the issue, two approaches were taken.

First, a new filling scheme⁴, coined “8b4e”, replaced the standard 25 ns bunch-spacing; instead of a continuous trains of bunches separated by 25 ns, 8b4e consists of “mini-trains” of only 8 filled bunches separated by 25 ns, followed by 4 empty bunches. Compared to the nominal bunch structure, this irregular pattern suppressed the formation of electron clouds. Second, a solenoid magnet was installed around the affected magnet interconnection [83] to reduce the multipactor effect – the exponential increase of electrons caused by secondary emission in resonance with the alternating electric fields of the RF cavity.

With these two measures in place, the original performance of the LHC was recovered, however, the

² Not discussed or shown in Fig. 3.3 are the LHCf [78], TOTEM [79], and MoEDAL [80] experiments.

³ Commonly referred to by the LHC community as the “Gruffalo”.

⁴ For a wonderful description and visual of LHC Run-2 filling schemes, see [82].

8b4e scheme limited the number of bunches until the end of 2017 data taking when the air was finally evacuated. While this was compensated for by increasing beam intensity and lowering emittances, it significantly increased pile-up, ultimately requiring *luminosity leveling* for the two high-luminosity experiments, ATLAS and CMS.

In the last year of Run-2 (2018), a peak instantaneous luminosity $2.17 \times 10^{34} \text{ cm}^{-2}\text{s}^{-1}$ was reached, and a maximum of 88.6 mean interactions per bunch crossing was seen. A remarkable record-setting 912.4 pb^{-1} of data was delivered to ATLAS in a single day, on 22 July 2018. Figure 3.4 shows the luminosity profiles of the three fills – corresponding in this case to three ATLAS runs – responsible for this integrated luminosity, as well as the beam intensity profiles along with beam energy.

Despite the technical hurdles, the LHC demonstrated excellent performance during Run-2, exceeding design specifications and delivering a total of 156 fb^{-1} of pp collision data to ATLAS.

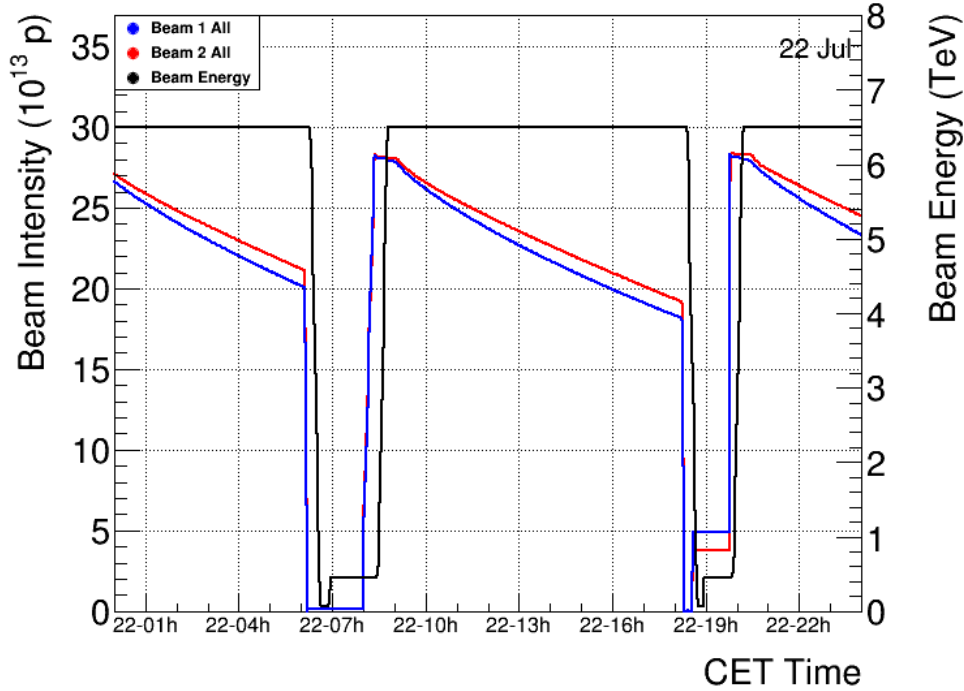
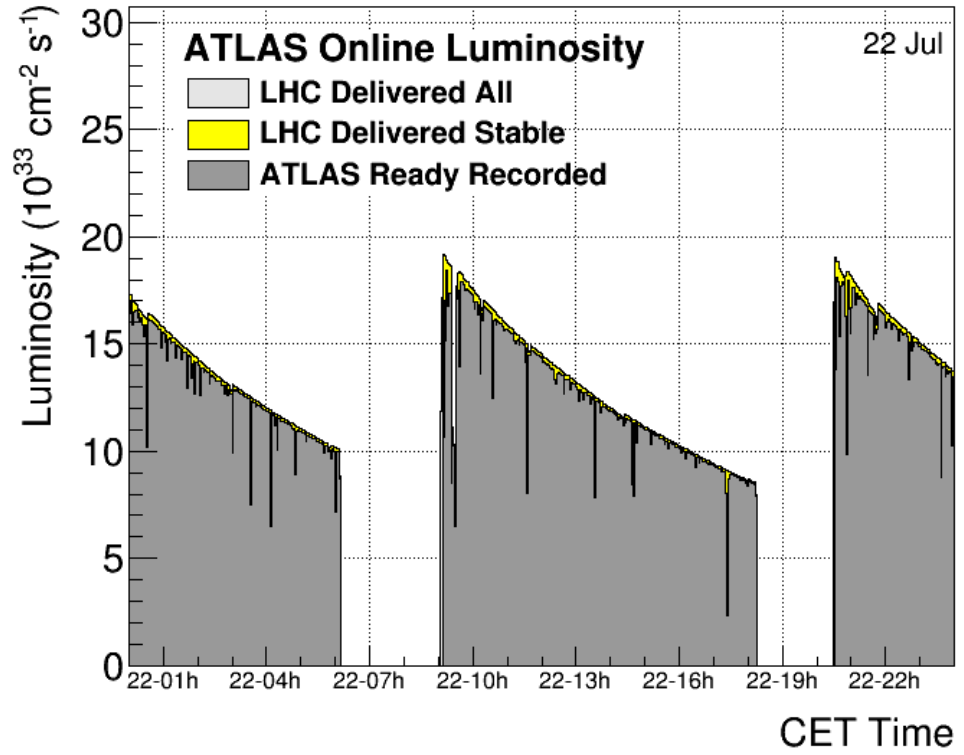


Figure 3.4: Typical (a) luminosity and (b) beam intensity profiles for three LHC fills – 6957, 6960, and 6961 – that took place on 22 July 2018. The corresponding ATLAS runs are 356205, 356250, and 356259. A total of 912.4 pb^{-1} of pp collision data was delivered during these fills/runs. Visible in (b) is the LHC energy ramp from 450 GeV to 6.5 TeV between fills.

Chapter 4

The ATLAS Experiment

What we observe is not nature itself, but nature exposed to our method of questioning.

- Werner Heisenberg

The ATLAS detector [84] was designed to provide high-resolution measurements of LHC proton-proton (pp) and heavy-ion collisions. The main detector volume comprises four primary subsystems – a magnet system, an inner tracking detector, calorimeter, and muon spectrometer. Each subsystem uniquely contributes to measurements that are used to infer type, energy, momentum, *etc.*, of particles produced in collisions. The overall layout of the ATLAS detector is shown in Fig. 4.1.

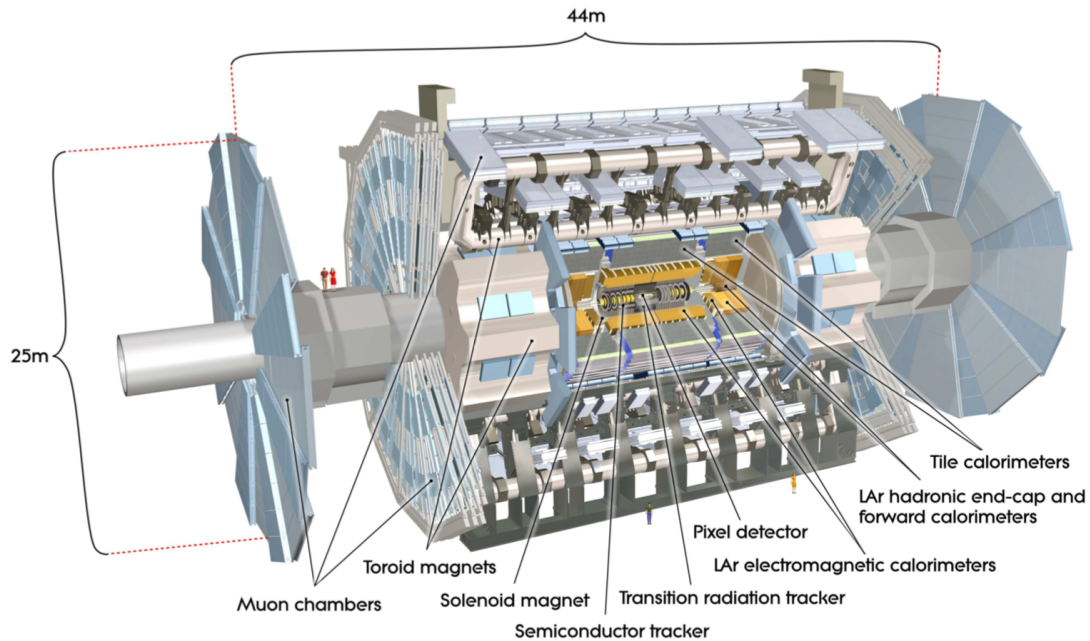


Figure 4.1: Cut-away view of the ATLAS detector [84]; each of the detector subsystems is labelled. The detector dimensions are 25 m in height and 44 m in length, and its overall weight is approximately 7000 tonnes.

Beyond the main detector volume are four smaller companion detectors for coverage in the very forward (*i.e.* a very small angle with respect to the beams, outside the main detector's acceptance) region.

The purpose of these detectors include luminosity measurements and detection of forward protons and neutrons.

Interesting physics signatures (*e.g.* a significant transverse momentum imbalance or high-momentum objects) are programmed into hardware- and software-based trigger systems which precipitate the recording of collision data. Upon acceptance of a triggered event, the complete set of detector (online) measurements are read out and written to disk for further (offline) processing. Finally, the recorded data are used to reconstruct objects – *e.g.* electrons, muons, jets, *etc.* – for use in physics analyses.

This chapter begins with an overview of the physics goals and requirements of the ATLAS detector (Sec. 4.1) that drove the experiment’s design. Details of the primary subsystems – the magnet (Sec. 4.2), tracking (Sec. 4.3), calorimeter (Sec. 4.4), and muon (Sec. 4.5) systems – and the primary luminometer (Sec. 4.6) are then given. Concluding this chapter is a discussion of the trigger and data acquisition system (Sec. 4.7). A general overview of subsystem performance during Run-2 data-taking is given later in Chap. 5.

4.1 Physics and detector requirements

The origin of the ATLAS detector coordinate system is defined by the nominal interaction point. The directions of the proton beams define the (longitudinal) z -axis and the (transverse) x - y plane. The positive x -axis is defined as pointing from the interaction point inward, toward the centre of the LHC ring, and therefore the positive y -axis is defined as pointing upward. The detector is conceptually divided into two sides, denoted side-A and side-C, where the former is defined as the side with positive z . The detector is nominally forward-backward symmetric with respect to the interaction point. The azimuthal angle, ϕ , is measured around the beam (z -)axis and the polar angle, θ , is measured from the beam axis. Most often Lorentz-invariant (along the z -axis) quantities are used to represent the polar angle. For massive objects, rapidity, $y = 1/2 \ln[(E + p_z)/(E - p_z)]$, is preferred; for massless objects (or for $E \gg m$, *i.e.* negligible mass), pseudorapidity, $\eta = -\ln[\tan \theta/2]$, is used. Transverse kinematic quantities – such as transverse momentum, p_T , and missing transverse energy, E_T^{miss} – are measured in the x - y plane. The distance $\Delta R = \sqrt{(\Delta\eta)^2 + (\Delta\phi)^2}$ is the separation in pseudorapidity-azimuthal angle space.

The ATLAS detector was designed to exploit the full physics potential of the LHC. Due to the anticipated experimental conditions, fast and radiation-hard electronics and detector elements were necessities. High-granularity subsystems were therefore designed to provide the resolution necessary for precision measurements of particle kinematics, and to withstand particle fluxes and to reduce the effect of overlapping collisions. Further requirements on the detector design were defined by a set of processes covering as much new phenomena as could be observed at the TeV energy scale. At a design luminosity of $10^{34} \text{ cm}^{-2}\text{s}^{-1}$ and centre-of-mass energy of $\sqrt{s} = 13 \text{ TeV}$, the LHC is able to produce large numbers of QCD and electroweak interactions, permitting precision tests of the underlying theories. For example, the total production cross section of the Higgs boson, as measured by ATLAS at $\sqrt{s} = 13 \text{ TeV}$, is $\sigma \approx 50 \text{ pb}$ (see Fig. 4.2). This means roughly five Higgs bosons are produced by the LHC every ten seconds, giving the opportunity to test its couplings and decay mechanisms.

In general, processes involving physics beyond the Standard Model (BSM) would involve decays of possibly heavy particles to very high p_T leptons and jets, and potentially generate significant E_T^{miss} . For example, some BSM models hypothesise new heavy gauge bosons, W' and Z' , which decay predominantly to two jets, could be produced with masses up to $\sim 7 \text{ TeV}$. The study of their decay modes would therefore

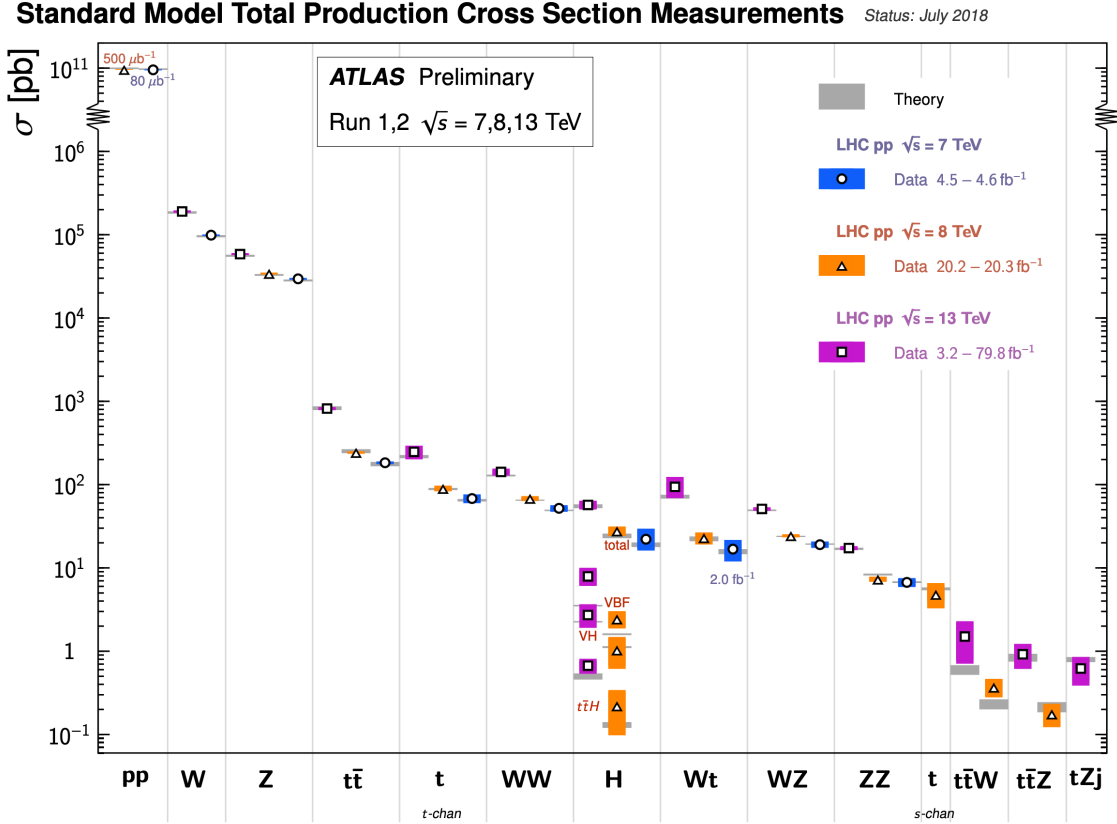


Figure 4.2: Summary of Standard Model total production cross section measurements made by ATLAS in analyses utilising datasets produced at 7, 8, and 13 TeV, compared to the corresponding theoretical expectations [85]. All theoretical expectations were calculated at NLO or higher.

require high-resolution measurements of jet kinematics. When produced in association with a charged lepton, efficient low- p_T lepton triggers are pivotal for rejection of the overwhelming QCD background. In supersymmetric models, decays of squarks and gluinos would also result in large cascades of leptons and jets. Furthermore, if R -parity [86] is conserved, these decay chains would contain a weakly-interacting lightest stable supersymmetric particle (LSP), leading to large E_T^{miss} in the final state.

The expected cross sections of many of the processes mentioned above are small, typically less than ~ 1 pb. Therefore, in addition to the detector requirements mentioned above, large datasets are required for observation. With an inelastic proton-proton (pp) cross section of 80 mb, $\sim 10^9$ pp collisions per second will be produced by the LHC. As a result, each candidate BSM event will be accompanied by tens of generally uninteresting inelastic events, introducing serious experimental challenges to determine the decay products of interest. Moreover, the nature of pp collisions leads to QCD jet production cross sections that dominate over the rare processes mentioned above. To observe the experimental signatures of rare processes' final states thus requires large datasets, and imposes further demands on the detector's capability to correctly identify a wide range of particles.

The general performance benchmarks of the ATLAS detector are summarised in Table 4.1. Note that for muons, the required p_T resolution is given for muons with $p_T = 1$ TeV as an upper bound (the resolution is better at lower p_T).

Detector component	Required resolution	Coverage	
		Measurement	Trigger
Inner tracking	$\sigma_{p_T}/p_T = 0.05\% p_T \oplus 1\%$	$ \eta < 2.5$	—
EM calorimetry	$\sigma_E/E = 10\%/\sqrt{E} \oplus 0.7\%$	$ \eta < 3.2$	$ \eta < 3.2$
Hadronic calorimetry			
barrel and endcap	$\sigma_E/E = 50\%/\sqrt{E} \oplus 3\%$	$ \eta < 3.2$	$ \eta < 3.2$
forward	$\sigma_E/E = 100\%/\sqrt{E} \oplus 10\%$	$3.1 < \eta < 4.9$	$3.1 < \eta < 4.9$
Muon spectrometer	$\sigma_{p_T}/p_T = 10\%$ at $p_T = 1$ TeV	$ \eta < 2.7$	$ \eta < 2.4$

Table 4.1: General performance goals of the ATLAS detector components, as described in [84]. Note that the muon spectrometer is independent of the inner tracker for high- p_T muons.

4.2 Magnet system and magnetic field

The ATLAS magnet system is a hybrid of superconducting magnets, consisting of a central solenoid that surrounds the inner detector volume, and three toroids (one in the barrel and one in each endcap) arranged with an eight-fold azimuthal symmetry around the calorimeters; it was this configuration that drove the design of the rest of the detector. Figures 4.3 and 4.4 show, respectively, the spatial arrangement of the coil windings and the full magnet system enclosed in vacuum vessels.

The bending radius of a charged particle track provides the momentum of said particle,

$$p[\text{GeV}] \sim 0.3 \cdot R[\text{m}] \cdot B[\text{T}]. \quad (4.1)$$

Momentum resolution depends highly on the *sagitta* (*i.e.* the deviation of a charged particle's trajectory from a straight line):

$$s \approx q \cdot B[\text{T}] \cdot L[\text{m}]^2 / 8p \quad (4.2)$$

where q is charge, L is the length of the region through which the particle traverse, and p is the particle's momentum. Thus, it is important to have very large fields and volume.

This section gives details of the properties of the magnets as well as the magnetic field.

4.2.1 Central solenoid magnet

The central solenoid resides at the heart of ATLAS, weighing approximately 5.5 tonnes with a length of 5.3 m and a 2.5 m diameter. It provides a ~ 2 T axial (z) field at the centre of the tracking volume. It operates nominally at 4.5 K, with a current of 7.73 kA.

Two main factors decided the design of the central solenoid: reliability and transparency. Reliability of operation is of utmost importance as the solenoid is installed deep inside the detector; any access for servicing would be almost impossible or at least very time consuming. Moreover, there are no spare solenoids. As the electromagnetic (EM) calorimeter is situated outside the solenoid, the solenoid needed

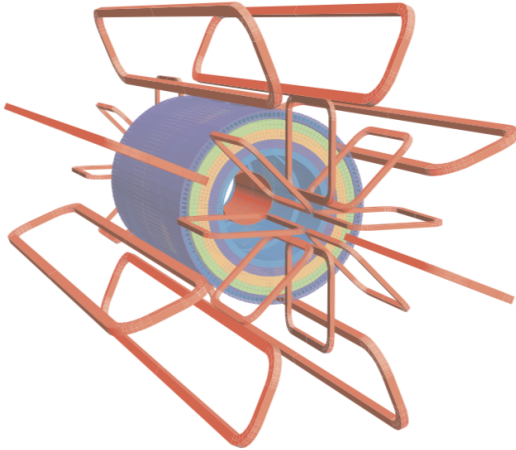


Figure 4.3: Geometry of magnet windings and tile calorimeter steel [84]. The eight barrel toroid coils, with the interleaved end-cap toroids, are visible. Also visible is the solenoid winding (inner orange cylinder), located inside the calorimeter. The tile calorimeter is modelled by four layers with different magnetic properties, plus an outer return yoke.

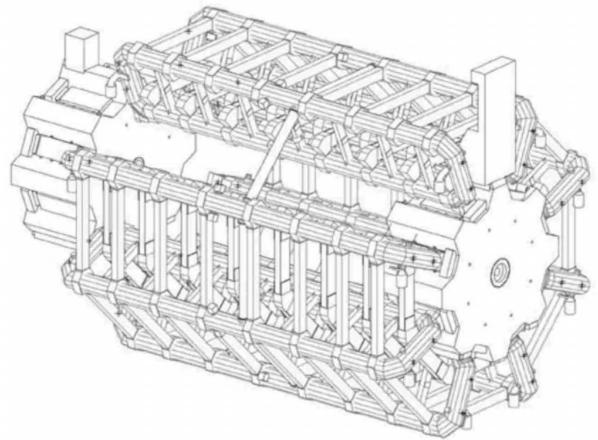


Figure 4.4: Schematic of the magnet system within its cryogenics [87]. Its dimensions are 26 m in length and 20 m in diameter, and has a stored energy of 1.6 GJ. The Central Solenoid is hidden and cannot be seen.

to be as transparent as possible to incident particles in order to achieve the best performance of the calorimeter. With 222 windings per metre, the solenoid contains roughly 9 km of superconducting wire wound around an aluminium support cylinder, contributing only ~ 0.66 radiation lengths [88] to the upstream material.

4.2.2 Toroid magnets

In addition to the central solenoid, the ATLAS magnet system comprises three toroid magnets, one barrel and two endcaps, that generate fields tangential to the beamline. Like the central solenoid, the conductor and coil-winding technologies are based on pure aluminium-stabilised superconducting Nb/Ti/Cu. The three toroids each consist of eight coils individually encased in racetrack-shaped, stainless steel vacuum vessels, and are assembled radially and symmetrically around the beam axis.

The barrel toroid is 25.3 m in length, with inner and outer diameters of 9.4 m and 20.1 m, respectively, with a peak field of 2.5 T. It surrounds the calorimeters and the end-cap toroids, and therefore generates a field that fills both the barrel and end-cap regions. The end-cap toroids are 5 m in length, with respective inner and outer diameters of 1.65 m and 10.7 m, and generate a field of 3.5 T. They are rotated by 22.5° with respect to the barrel toroid (Fig. 4.3) for radial overlap and to optimise the bending power at the interface of the two coil systems.

4.3 Inner detector

The Inner Detector (ID) was designed to be as hermetic as possible about the interaction point (IP), and to provide information for input into pattern recognition algorithms for track-fitting. High resolution momentum measurements as well as precise primary and secondary vertex measurements of charged

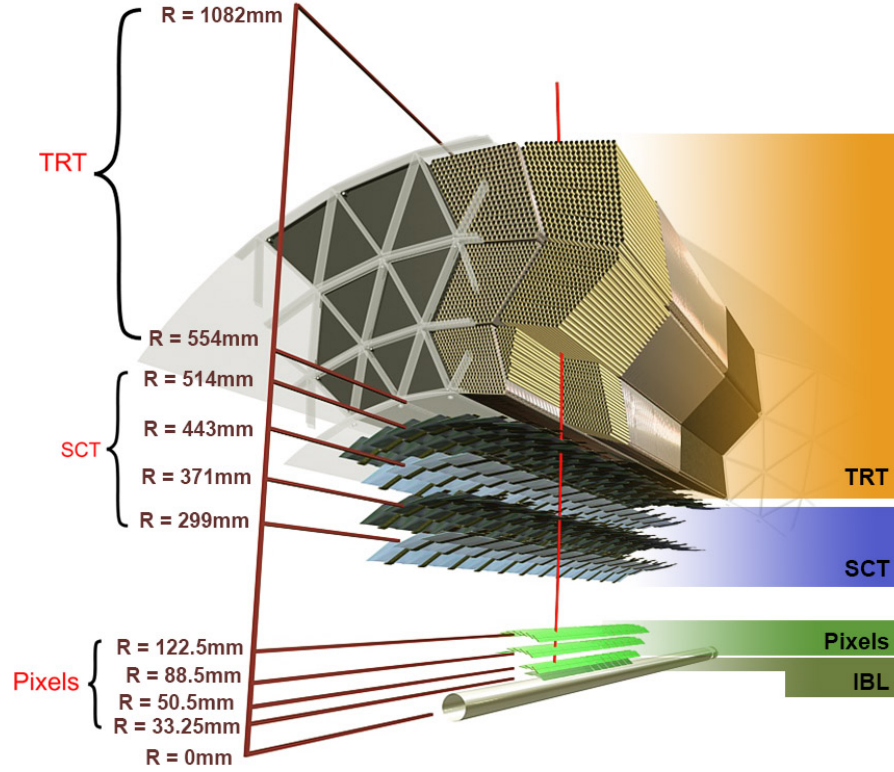


Figure 4.5: A detailed layout of the Inner Detector (ID), including the new Insertable B-Layer (IBL) [89]. The vertical red line represents a charged particle track at $\eta = 0.3$.

particles with $p_T > 0.4$ GeV are provided within the pseudorapidity range $|\eta| < 2.5$ with enhanced electron identification within $|\eta| < 2.0$.

The ID consists of three independent but complementary tracking detectors – a silicon pixel tracker, a silicon strip tracker (SCT), and a transition radiation tracker (TRT). Each tracker consists of a barrel part and two endcap parts with a different number of sensitive detecting layers. They are contained within a cylindrical envelope of length ± 3512 mm and radius 1150 mm that is immersed in the 2 T magnetic field generated by the central solenoid. Figure 4.5 shows a detailed layout of the ID barrel.

As charged particles traverse the active ID elements, they deposit small amounts of energy (*i.e.* “hits”); in most cases 40 hits are associated to a single charged particle. Hits are used as inputs to the reconstruction software to form tracks and determine the p_T of their associated particles.

4.3.1 Pixel detector

The Pixel detector provides the highest resolution tracking of the three ID detectors. It comprises four cylindrical layers in the barrel at radii 33.5, 50.5, 88.5 and 122.5 mm. In the end-caps, it consists of three disks on either side of the interaction point at $|z| = 495, 580$ and 650 mm.

The innermost barrel layer, the *insertable B-layer* (IBL) [90, 91], was installed for Run-2 to provide high-resolution hit information to improve primary vertex and impact parameter information, and extend coverage to $|\eta| = 3.0$. It consists of 14 carbon composite staves, each supporting 20 sensors, 12 planar and 8 3D. The planar sensor is a development of the Pixel detector sensor design with significantly reduced

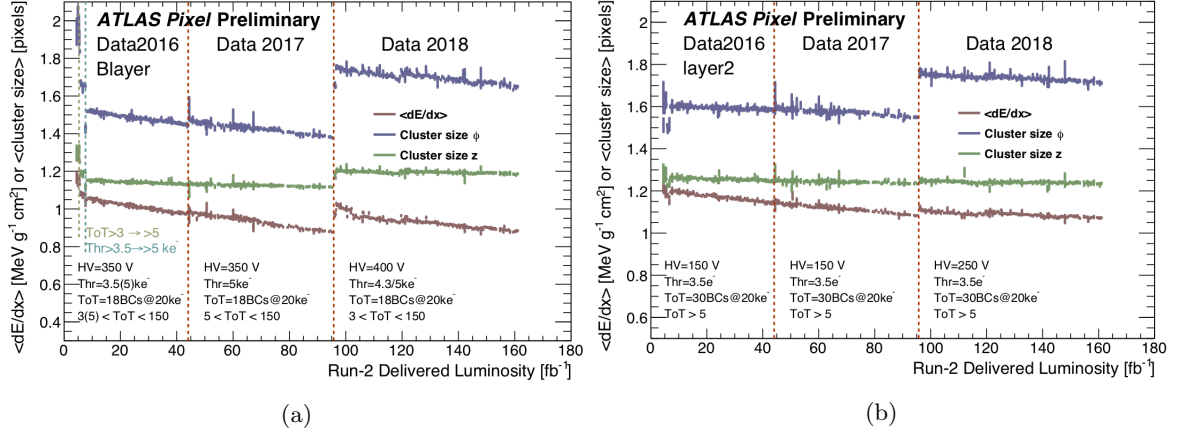


Figure 4.6: The dependence of the average cluster size and the measured dE/dx on the delivered luminosity for the (left) IBL and (right) layer2 of the pixel detector [95]. Each point represents a single run, and only runs recorded in 2016, 2017 and 2018 are shown (the 4.4 fb^{-1} delivered in 2015 is not shown). The gradual decrease of the measured dE/dx is due to the reduced charge collection fraction as a result of radiation damage.

inactive edges to minimise efficiency loss. The 3D sensor [92] is a new technology developed for increased radiation hardness, and its lower operating voltage is advantageous in terms of power consumption after being irradiated.

The IBL pixels are rectangular in shape with a nominal size of $50 \times 250 \mu\text{m}^2$, and thickness that depends on the sensor type: $200 \mu\text{m}$ for planar and $230 \mu\text{m}$ 3D for sensors. There are about 12 million IBL pixels in total, divided among 280 identical readout chips. In the remaining part of the Pixel detector, pixels have a nominal dimension $400 \times 50 \mu\text{m}$, with a thickness of $250 \mu\text{m}$ ($230 \mu\text{m}$) in the barrel (end-caps). Totalling more than 92 million pixels, this detector makes up nearly 90% of the full ATLAS detector readout channels.

The pixels are n^+ -doped semiconductors that are designed to operate at bias voltages between 150 600 V. When a charged particle passes through the bulk, it creates electron-hole pairs which are collected on the surfaces of the silicon; a minimum ionising particle (MIP) will liberate roughly 2×10^4 electrons [93]. To achieve a good signal-to-noise ratio, the analog signal is compared to a threshold, and only the time over threshold, ToT, is recorded. The ToT is the time measured (in clock cycles) that the analog signal induced by charged particles has spent over the threshold. However, even in the case of normally incident particles, several neighbouring pixels could record a signal over threshold. In such cases, consecutive pixel hits (*i.e.* clusters) are treated as a single hit by the reconstruction software. Whereas clusters originating from electronics noise typically have $\text{ToT} \approx 4$, clusters resulting from MIPs can have $\text{ToT} \geq 8$ [94].

Due to its close proximity to the interaction point, the pixel detector lives in an extremely harsh radiation environment. As a result, radiation damage to the silicon causes a gradual decrease in average cluster sizes and energy deposited, dE/dx , throughout the detector's lifetime (see Fig. 4.6), requiring replacement of the detector beyond Run-3 [95].

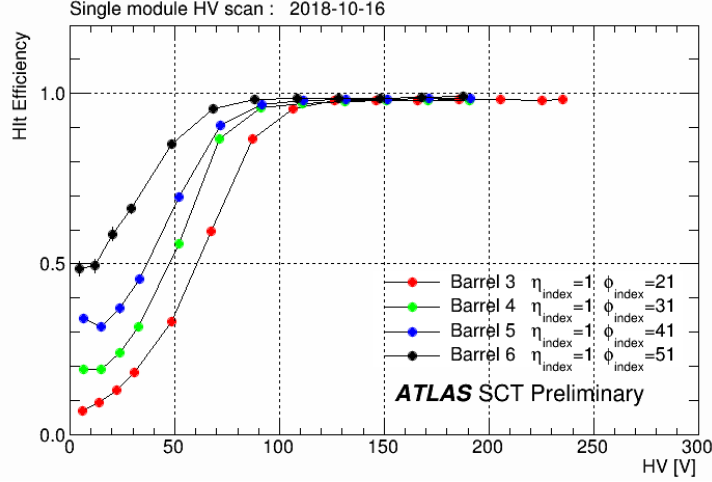


Figure 4.7: Hit efficiencies as a function of HV for four typical modules from the inner-most SCT layer (‘Barrel 3’) to the outer-most layer (‘Barrel 6’) as of October 2018 [98, 99]. Hit efficiency gets lower as HV is lowered. The closer to the beam pipe, the more reduced is the efficiency at low HV region as expected due to radiation damage from the higher particle flux in this region.

4.3.2 Semiconductor Tracker

The SCT is conceptually similar to the pixel detector, except it uses silicon strips $80\ \mu\text{m}$ wide and $12\ \text{cm}$ long. In the barrel, there are 15 912 sensor modules arranged in four radial layers at $R = 299, 371, 443$ and $514\ \text{mm}$, while in the end-caps the SCT comprises nine disks at situated at positions in $848 < |z| < 2720.2\ \text{mm}$ from the interaction point, providing coverage up to $|\eta| = 2.5$. The barrel layers carry a total of 2 112 modules with a rectangular shape of size $6 \times 12\ \text{cm}^2$. There are 988 modules in each end-cap with three different wedge shapes to accommodate the more complex geometry. Each sensor has a thickness of $285\ \mu\text{m}$. To improve spatial resolution, each barrel layer consists of “double-layers” – two sensor modules glued back-to-back at small angles of $40\ \text{mrad}$, measuring $R\text{-}\phi$, with similar layouts in disks 2-6 in the end-caps. The angle between the two layers is optimised for resolving “ghost” ambiguities in cases when several charged particles traverse a single double-layer [96]. These specifications yield a spatial resolution of $17\ \mu\text{m}$ ($R\text{-}\phi$) and $580\ \mu\text{m}(z/R)$ in both the barrel and end-cap regions.

As in the case of the pixel detector, the SCT suffers from degrading effects as a result of the high radiation doses. For good charge collection efficiency over its lifetime, SCT sensors were designed to operate over a range of voltages which depend on sensor position, the integrated luminosity, and length of warm-up periods [97]. Figure 4.7 shows the SCT hit efficiencies were near 99% at a nominal 150 V HV supply following the end of Run-2. This figure also demonstrates, as a result of radiation damage to the layers, the reduced efficiency at low HV for barrel regions closer to the beam pipe.

4.3.3 Transition Radiation Tracker

The TRT is a straw-tube tracker, consisting of $4\ \text{mm}$ diameter polyimide straw tubes made from kapton and reinforced with thin carbon fibres. The inner walls of the straws have a $0.2\ \mu\text{m}$ coating of aluminium. At the center of each tube is a gold-plated tungsten wire of $31\ \mu\text{m}$ diameter. The walls of the straws are held at a constant high negative voltage $\sim -1.5\ \text{kV}$, and the wire at ground potential. Each straw is filled with either argon- or xenon-based gas mixtures, covering up to $|\eta| = 2.0$.

The TRT barrel contains 52 544 straw tubes 1.5 m in length that run parallel to the beam axis. They are arranged into 73 planes, and cover a radius from 0.5 m to 1.1 m and $|\eta| < 1$. Each TRT end-cap comprises 122 800 straws 0.4 m in length arranged radially in wheels. The 160 straw planes in the end-caps provide coverage in the range $0.8 < |z| < 2.7$ and $1 < |\eta| < 2$. Interleaved between barrel (end-cap) straws are polymer fibres (foils), which serves as the transition radiation material.

As a charged particle passes through the TRT, it ionises some of the gas, creating on average 5–6 ionisation clusters per mm of path length. The free electrons in the straws then drift in the strong electric field toward the anode and cascade near the wire, resulting in a detectable signal [100]. Charged particles may produce transition radiation as they traverse a material boundary. The transition radiation can be absorbed by the Xe/Ar atoms in same tubes traversed by, or adjacent to, the incident charged particle. The signal on each wire is amplified, shaped and discriminated against two adjustable thresholds – one low (LT) and one high (HT) threshold.

The LT threshold is used for tracking purposes; electron drift-time measurements, provided by recording the time at which the ionisation signal exceeds the LT, are used to determine the position of tracks. Particle identification, *i.e.* separating electrons from charged pions, is achieved using the fraction of HT hits associated to a track. The probability for a given particle to emit transition radiation depends on the relativistic factor, $\gamma = E/m$, making the emission of transition much more like for an electron than for a pion of the same momentum [101].

Beginning in 2012, increasing numbers of xenon gas leaks were observed. The leaks affected 1/4 of the barrel modules and 1/14 in the end-caps. Due to the high cost of xenon, these modules were filled instead with the much less expensive argon gas. However, argon has a lower transition radiation absorption probability than xenon, leading to significantly varying HT probabilities across the detector. While this problem does not affect tracking properties (which use LT thresholds), discrimination between electrons and pions is affected [102], leading a slightly lower particle identification efficiency.

4.3.4 Beam Conditions Monitor

The LHC beams are susceptible to incidents that can potentially damage detectors. As a preventative measure, ATLAS has employed a detector to monitor beam conditions.

Attached to the pixel detector is the Beam Conditions Monitor (BCM), used for beam background measurements and complementary luminosity measurements to those coming from LUCID (Sec. 4.6). The BCM consists of four small diamond modules (*stations*) on either side of the interaction point, at $|z| = 1\,840$ mm with a mean radial distance of $r = 55$ mm ($|\eta| \approx 4.2$) from the beam axis. Modules are arranged in a cross about the beam axis, separated azimuthally by $\phi = \pi/2$, with two modules in the horizontal and two in the vertical plane. The sensors have an area of 1×1 cm and thickness of 1 mm, and are made of polycrystalline chemical vapour deposited (pCVD) diamond.

They provide very good time resolution – a 2 ns signal rise time and average pulse length of 3 ns – and therefore are able to distinguish between particles originating from the collision point and those arriving along the beam line (*i.e.* beam background) based on time-of-flight and pulse height information provided by its modules. The choice of pCVD diamond as a radiation-hard sensor material ensures the stability and durability of the detector over its lifetime. Moreover, pCVD diamond is highly resistive and thus does not require a reverse-biased p-n junction as silicon does. It is an insulating material and, due to its large energy gap ($E_g \sim 5.5$ eV), has no free carriers to contribute to noise.

An example of a beam incident is the scraping of a beam inside of the beam pipe, that could result

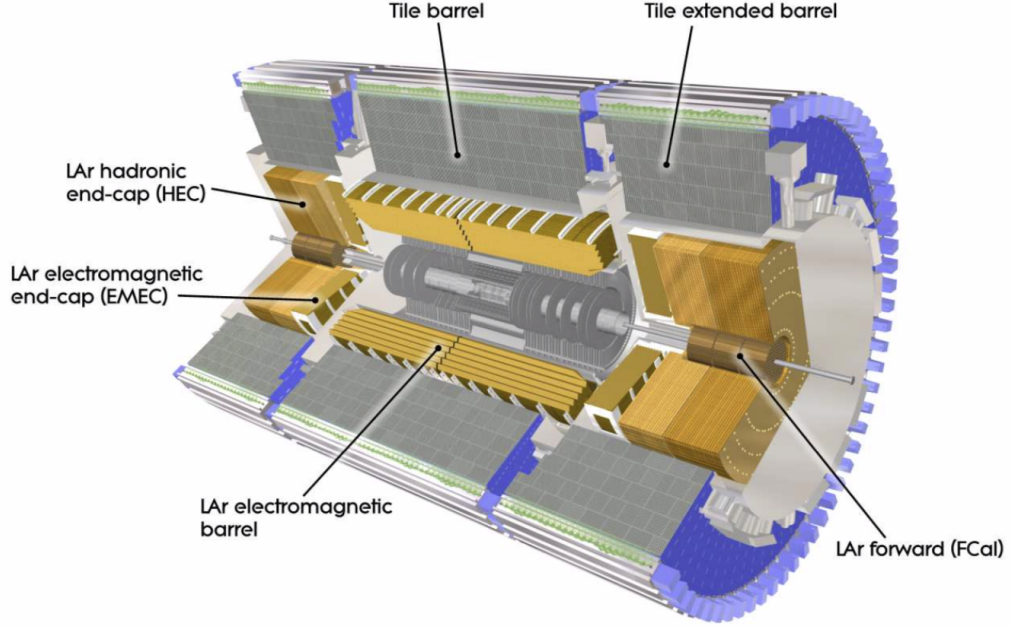


Figure 4.8: A cut-away view of the ATLAS calorimeter system [84].

in a dangerously high flux could flow through the ATLAS detector subsystems. In such a case, the BCM would detect the high flux of particles as not originating from the collision point – based on the difference between their time-of-arrival at the BCM stations – and initiate a “beam dump” signal. Once the signal is sent, the beam is ejected from the LHC ring in $\sim 250 \mu\text{s}$. The BCM is the only ATLAS detector that can signal a beam dump.

4.4 Calorimetry

Surrounding the ID and Central Solenoid is the ATLAS calorimeter system. It comprises several different sampling subdetectors and technologies, designed to cope with the large range of energy depositions, and covers the range $|\eta| < 4.9$ with full ϕ -symmetry. An overall view of the calorimetry is shown in Fig. 4.8. The electromagnetic (EM) barrel calorimeter and end-cap EM and hadronic calorimeters all use liquid argon (LAr) as the active material. Liquid argon was chosen for its radiation-hardness, uniformity and response linearity, and permits the set of end-cap calorimeters to be housed in a single cryostat and use of common readout electronics. Scintillating tiles are used as the active medium in the hadronic barrel calorimeter. The unique feature of this detector is that its tiles are oriented radially with respect to the beam axis (positioned in R - ϕ planes), permitting a hermetic design and self-supporting absorber plates [103, 104].

The measurements made by the calorimeters are used to provide information to the Level-1 trigger system. Therefore, a good understanding of cell-to-cell energy distributions, as well as noise, in the calorimeter are crucial. An important figure of merit for a calorimeter is its energy resolution,

$$\frac{\sigma(E)}{E} = \frac{S}{\sqrt{E}} \oplus \frac{N}{E} \oplus C, \quad (4.3)$$

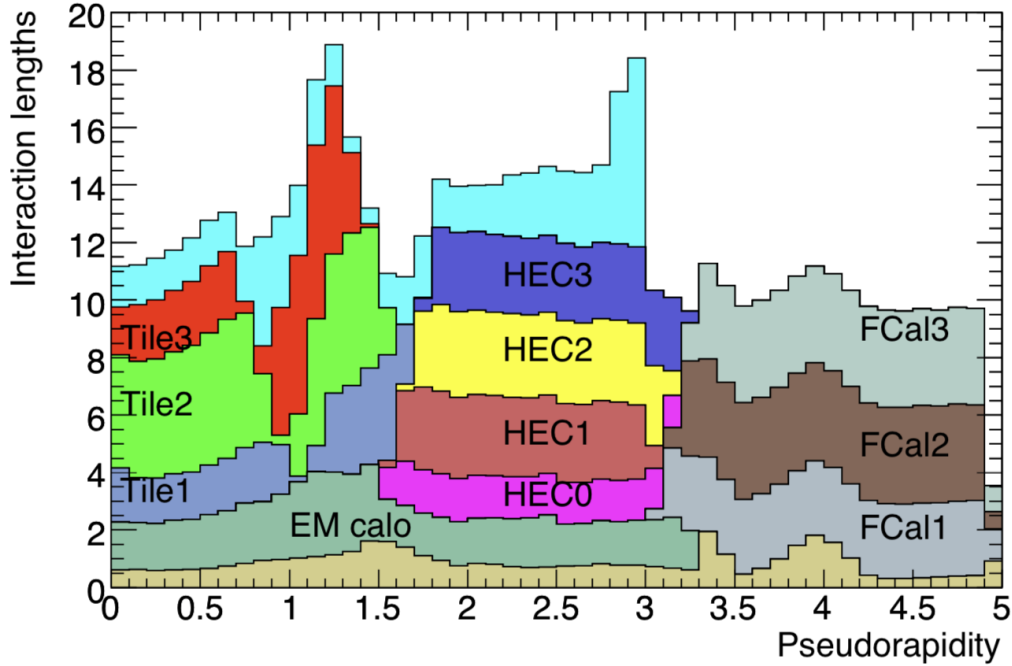


Figure 4.9: The cumulative amount of material, in units of interaction lengths, as a function of $|\eta|$, in front of, and within, the calorimeters [84]. Also shown (cyan) is the total amount of material upstream of the muon spectrometer.

where terms on the right of the equation are summed in quadrature. The first term on the right is related to fluctuations in shower development, and is therefore called the ‘stochastic term’. Second is the ‘noise’ term, corresponding to noise from electronics (and pile-up), which, when a signal is collected in the form of charge, can be minimised with techniques such as signal-shaping and optimal filtering (described later in this section). Last is the ‘constant term’, to which response nonuniformities, arising from *e.g.* geometry or mechanical structure, contribute. An overview of the design energy resolutions of the ATLAS calorimeters was presented earlier in Table 4.1.

The calorimeters were designed to provide good containment of EM and hadronic showers, as well as limit punch-through into the muon system. Roughly 20–40 radiation lengths (X_0) of material in the EM calorimeter is sufficient to contain roughly 95% of shower energy prompted by electrons and photons up to ~ 1 TeV. The some 8–12 interaction lengths (λ) in the hadronic calorimeters contains the remainder of a shower. With a total thickness of $\sim 11\lambda$ at $\eta = 0$, both measurements and simulation have shown punch-through is limited, permitting mostly prompt or decay muons (and neutrinos) to enter the muon spectrometer (see Sec. 4.5). The cumulative amount of material, in interaction lengths, as a function of $|\eta|$, in front of, and within, the calorimeters is shown in Fig. 4.9. The wide η -coverage and shower containment ensure good measurements of E_T^{miss} , a key ingredient for many physics signatures and, in particular, searches for new physics.

4.4.1 Electromagnetic calorimeters

The production of electromagnetic showers at energies ≥ 100 MeV is dominated by two processes: bremsstrahlung, wherein an electron radiates a photon, and pair production, in which a high-energy

photon converts into an e^+e^- pair. Because these processes involving electrons and photons occur via interactions with atomic nuclei, the EM calorimeter absorber layers comprise high-density materials to initiate particle showers. Shower formation ceases when the particles produced fall below a critical energy, E_c , at which point ionisation becomes the dominant process.

Two important characteristics for understanding the development of EM showers in a given material are the *radiation length*, X_0 , and *Molière radius*, R_M . The radiation length describes the main features of electromagnetic showers, *e.g.* lateral and longitudinal extents. It is defined as [105],

$$X_0[\text{g cm}^{-2}] \simeq \frac{716 \text{ g cm}^{-2} A}{Z(Z+1) \ln(287/\sqrt{Z})} \quad (4.4)$$

representing the mean distance over which a high-energy electron loses all but $e^{-1} \approx 0.368$ of its energy via bremsstrahlung. The Molière radius is a characteristic constant of a material that gives the scale of the transverse dimension of an EM shower. It is defined as the radius of a cylinder whose axis coincides with the shower axis and contains, on average, 90% of the shower energy.

$$R_M = m_e c^2 \sqrt{4\pi/\alpha} \frac{X_0}{E_c} \quad (4.5)$$

$$= X_0 \frac{E_s}{E_c}, \quad (4.6)$$

where α is the fine-structure constant and E_s is the multiple-scattering energy, $E_s = 21 \text{ MeV}$ [106].

The ATLAS EM calorimeter has an accordion geometry with alternating layers of lead absorbers and active gaps filled with LAr. The motivation for this geometry is to prevent projective azimuthal dead zones that would otherwise contribute to the noise term of the EM energy resolution. The readout electrodes are located in the gaps and consist of three copper layers insulated by polyimide sheets; the two outer copper layers are held at a high voltage and the middle one is used to read out the signal induced by charges drifting in the LAr via capacitive coupling [107]. Honeycomb-shaped spacers are used to maintain the separation between absorbers and electrodes. Figure 4.10 shows a photograph of a partly-stacked EM barrel module, illustrating the accordion geometry.

Because a particle will have already passed through 1–4 X_0 of upstream material in the ID and solenoid, EM showers may develop well before reaching the calorimeter. In order to measure and help correct for losses that result, a presampler layer of LAr, approximately 11 mm (5 mm) in depth in the barrel (end-cap) and covering up to $|\eta| = 1.8$, is incorporated into the cryostats. Unlike the rest of the calorimetry, the presampler has no absorber, essentially making it a homogeneous detector.

The EM calorimeters are segmented into 2–3 longitudinal layers, depending on $|\eta|$, whose granularity, defined in $\Delta\eta \times \Delta\phi$, varies from layer-to-layer and as a function of $|\eta|$. To provide a high resolution description of the lateral shower profile, and to enhance particle identification, the first layer is highly granular in η . The second layer, where most of a EM shower's energy is deposited, and the third layer, containing only the tail of a shower's energy, provided a coarser segmentation in $\Delta\eta \times \Delta\phi$.

Table 4.2 summarises the layer coverage and granularity of the EM calorimeters, as well the number of readout channels in each region.



Figure 4.10: Photograph of a partly-stacked barrel EM LAr module [84]. Six out of seven outer support rings are also visible. The module and support rings rest on an assembly bench.

Electromagnetic barrel calorimeter

The EM barrel calorimeter (EMB) is made up of two identical half-barrels that are centred around the z -axis with an inner (outer) radius of 2.8 m (4 m) and 3.2 m in length, providing coverage in the region $|\eta| < 1.475$. Each half-barrel is mechanically divided into 16 modules, with a single module providing an angular coverage $\phi = 22.5^\circ$. The EMB and central solenoid share a common vacuum vessel in order to reduce upstream material that would degrade the calorimeter's performance.

In the EMB, the lead absorbers run radially with respect to the beam axis, with the crests of the accordion folds running parallel to the beam axis. The thickness of the lead absorbers changes from 1.53 mm below $|\eta| = 0.8$ to 1.13 mm above to limit the decrease of the sampling fraction as $|\eta|$ increases. The half-barrels each contain 1024 absorbers, interleaved with readout electrodes centred in the LAr gaps. The LAr gaps are about 2.1 mm, corresponding to an electron drift-time of about 450 ns at an operating voltage of 2000 V. For redundancy, each side of an electrode is supplied high-voltage independently; if only one side is powered, only half the signal will be collected. The high-voltage granularity of the EMB and presampler is $\Delta\eta \times \Delta\phi = 0.2 \times 0.2$, corresponding to 32 electrode sectors being powered simultaneously. There are 3424 readout cells/channels per module, including the presampler.

Region	Layer and coverage		Granularity $\Delta\eta \times \Delta\phi$
Barrel	Presampler	$ \eta < 1.52$	0.025×0.1
	Layer 1	$ \eta < 1.40$	$0.025/8 \times 0.1$
	Layer 1	$1.40 < \eta < 1.475$	0.025×0.025
	Layer 2	$ \eta < 1.40$	0.025×0.025
	Layer 2	$1.40 < \eta < 1.475$	0.025×0.025
	Layer 3	$ \eta < 1.35$	0.050×0.025
End-cap	Presampler	$1.5 < \eta < 1.8$	0.025×0.01
	Layer 1	$1.375 < \eta < 1.425$	0.050×0.01
	Layer 1	$1.425 < \eta < 1.5$	0.025×0.01
	Layer 1	$1.5 < \eta < 1.8$	$0.025/8 \times 0.01$
	Layer 1	$1.8 < \eta < 2.0$	$0.025/6 \times 0.01$
	Layer 1	$2.0 < \eta < 2.4$	$0.025/4 \times 0.01$
	Layer 1	$2.4 < \eta < 2.5$	0.025×0.01
	Layer 1	$2.5 < \eta < 3.2$	0.01×0.01
	Layer 2	$1.375 < \eta < 1.425$	0.050×0.025
	Layer 2	$1.425 < \eta < 2.5$	0.025×0.025
	Layer 2	$2.5 < \eta < 3.2$	0.01×0.01
	Layer 3	$1.5 < \eta < 2.5$	0.050×0.025

Table 4.2: Coverage and granularity by layer in the EM calorimeters [84].

Electromagnetic end-cap calorimeter

The electromagnetic end-cap calorimeters (EMECs) are 630 mm thick, one on each side of the EMB, with inner and outer radii of 330 mm and 2098 mm, respectively. They provide coverage in the range $1.375 < |\eta| < 3.2$. Like the EMB, the EMEC uses an accordion-shaped geometry with lead absorbers interleaved with copper electrodes filled with LAr. The lead absorbers run parallel with respect to the beam axis, with the crests of the accordion folds extending radially to the beam axis. The absorber plates are arranged radially, with the accordion waves running axially (see Fig. 4.11).

Each EMEC comprises two coaxial wheels, an inner wheel (IW) and an outer wheel (OW), to ensure good azimuthal response uniformity that would not be attainable with a single accordion structure [108]. The IW sums 4 adjacent electrodes into a readout cell for both samplings, while 12 adjacent electrodes are summed in a front cell and 3 for a middle or back cell in the OW.

Unlike the EMB, the drift gap increases with radius, R . In the IW (OW), the gap varies from 3.1 mm (2.8 mm) at $R = 700$ mm (2000 mm) to 1.8 mm (0.9 mm) at $R = 300$ mm (600 mm). Ideally, a continuously varying high voltage in η would be needed to maintain a constant drift time with increasing gap size. Since such a requirement was not practical to implement, the HV variation is approximated by steps in η that define the 2 (7) HV sectors of the IW (OW). As a result, the high-voltage granularity is 0.2 in ϕ and approximately 0.2 in η ,

4.4.2 Hadronic calorimeters

Hadronic particles shower differently in matter than the EM counterparts due to their strong force interactions; some hadron energy is expended to *e.g.* nuclear breakup and excitation (*i.e.* invisible

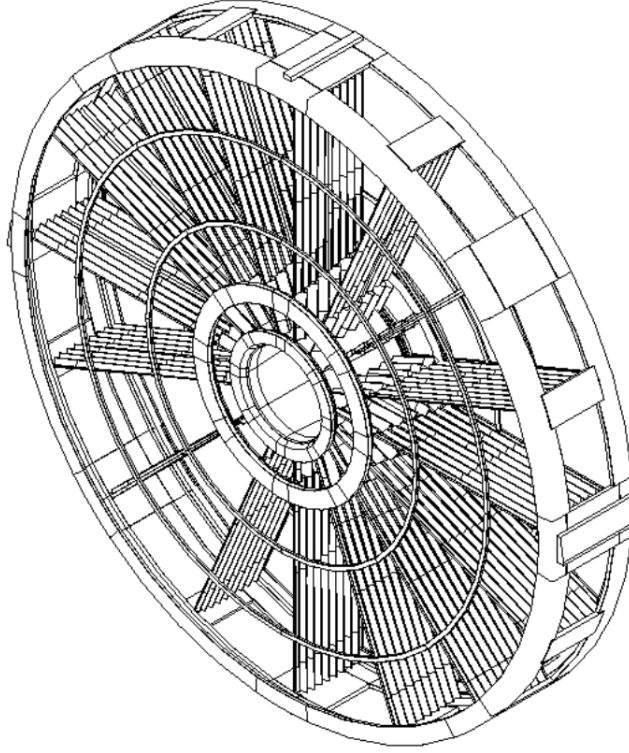


Figure 4.11: A schematic of an EMEC wheel [108]. Only several absorbers are shown to demonstrate their radial arrangement.

energy) rather than to ionisation. The ATLAS calorimetry is non-compensating, meaning a hadron will, on average, deposit a smaller fraction of its energy, in the active material than would an electron or photon. The electromagnetic fraction f_{em} of a hadron's energy deposited in the calorimeters increases with hadron energy according to [109],

$$f_{\text{em}} = 1 - \left(1 - \frac{1}{3}\right)^n, \quad (4.7)$$

where n is the number of generations of nuclear interactions, and f_{em} is therefore an energy-dependent quantity. That is, the non-EM content of the shower decreases as $(1 - 1/3)^n$, and after each collision in the hadronic cascade, $(1 - 1/3)$ of the remaining energy is, on average, available for the subsequent collisions. In the LAr-based hadronic calorimeters, EM and hadronic fractions of the shower energy are measured in the same way as in the EM calorimeters; invisible energy loss is accounted for later in the calibration of hadronic objects (see Sec. 5.3).

Tile calorimeter

Behind the EMB in the region $|\eta| < 1.7$, is the hadronic Tile calorimeter. It is divided along the beam axis into four partitions: two central barrels, approximately 2.6 m in length, covering $|\eta| < 1.0$, and two extended barrels, each 2.6 m in length, with inner and outer radii of 2.28 m and 4.25 m, respectively. Each barrel part consists of 64 modules, or “wedges”, of size $\Delta\phi \sim 0.1$ that are made of steel absorber plates and scintillating plastic tiles.

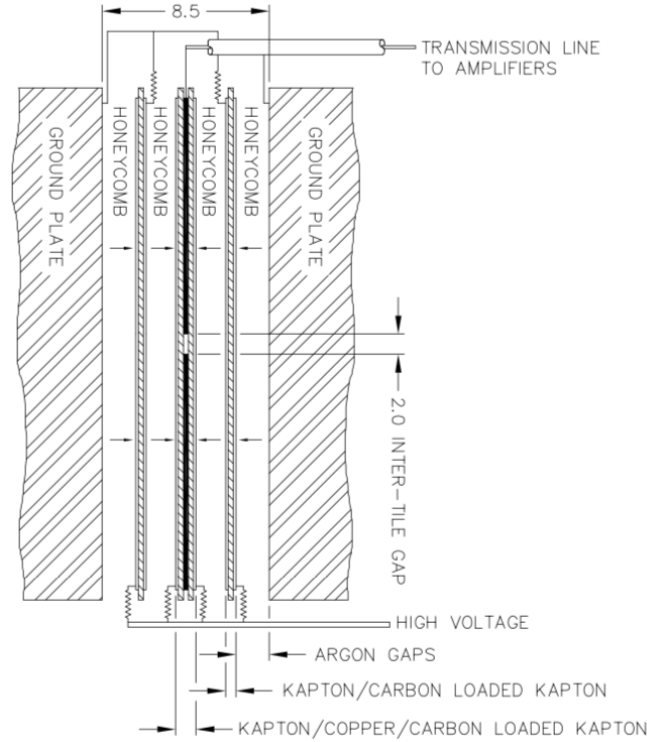


Figure 4.12: Schematic of the arrangement of the HEC readout structure [84]. All dimensions are in mm.

To correct for energy lost in upstream material, the outsides of individual cryostats are instrumented with scintillators, covering $1.0 < |\eta| < 1.2$ and $1.2 < |\eta| < 1.6$. A steel girder around $R \sim 4.25$ m of the Tile calorimeter provides mechanical support as well as a return yoke for the central solenoid magnetic field.

When a charged particle passes through the scintillating tiles, ultraviolet light can be emitted. This light is collected at two edges of each plastic scintillator, and is then transported via wavelength-shifting fibres to photomultiplier tubes which are located at the back of each barrel module. Tiles are finally read out in groups to form three longitudinal sampling layers for further processing.

Hadronic end-cap calorimeter

The hadronic end-cap calorimeters (HECs) use a standard parallel-plate design that uses copper as the absorber material. In each end-cap, a HEC comprises two cylindrical wheels – a front wheel (HEC1) and a rear wheel (HEC2) – each with two longitudinal sections. Each of the four wheels is constructed of 32 identical wedge-shaped modules with an inner radius between 372 mm and 475 mm, and outer radius of 2030 mm. The front wheels are made of 25 copper plates, 24 of which are 25 mm thick and a 12.5 mm front plate. There are 16 copper plates of 50 mm thickness, plus a 25 mm thick front plate, in the rear wheel, leading to a smaller sampling fraction.

The 8.5 mm LAr gaps are divided by three electrodes into four separate 1.8 mm “drift zones” (Fig. 4.12), with a high voltage supplied to each zone individually. The central electrode serves as the readout and defines the lateral segmentation of the calorimeter, and a high voltage is applied to the other two electrodes. The small drift zones reduce problems with space-charge effects at large $|\eta|$, since

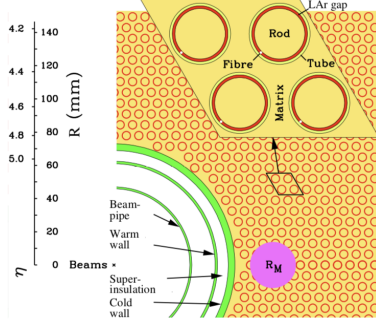


Figure 4.13: Electrode structure of the FCal1, showing the matrix of copper plates, and the copper tubes, rods and LAr gaps comprising the electrodes [84]. The Molière radius, R_M , is represented by the solid disk.

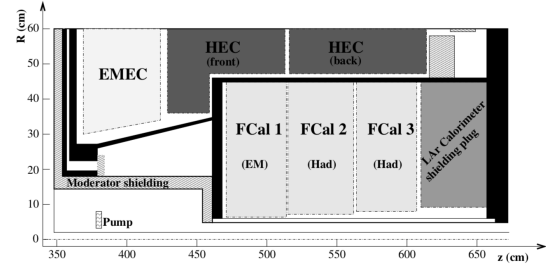


Figure 4.14: A schematic drawing of the placement of three FCal modules in the end-cap cryostat [84]. The black regions indicate parts of the cryostat. The vertical scale is made larger than the horizontal scale for clarity.

the slowly-drifting ions created by incident particles have a short distance to travel before reaching a cathode. The nominal HV of 1800 V results in a typical electron drift time of ~ 430 ns. There are 5 632 readout channels in total, with cell sizes of $\Delta\eta \times \Delta\phi = 0.1 \times 0.1$ in the region $|\eta| < 2.5$ and twice this size for larger $|\eta|$.

Forward calorimeter

Covering the highest $|\eta|$ region, $3.1 < |\eta| < 4.9$, of the main ATLAS volume is the forward calorimeter (FCal). Each FCal comprises three modules – FCal1 (EM), FCal2 and FCal3 (hadronic) – each of 450 mm in depth. For resolution and heat removal optimisation, the first module uses copper absorber material, while the other two modules use tungsten to provide containment and minimise lateral spread of hadronic showers. To reduce shower leakage in the end-cap muon system, a copper alloy shielding plug is mounted at the rear of FCal3.

At a distance of approximately 4.7 m from the interaction point and close proximity to the beamline, the FCal modules are exposed to high particle fluxes. To avoid space-charge effects due to ion build-up while, at the same time, providing a high density, its design requires very small LAr gaps. This requirement is met by a novel rod-in-tube electrode structure, as seen in Fig. 4.13, where the rods run parallel to the beam line. The Molière radius is also illustrated in Fig. 4.13.

There are 12 260 copper rods inserted into holes drilled into a stack of copper plates for the FCal1, and 10 200 and 8 225 tungsten rods inserted similarly into a matrix of tungsten in the FCal2 and FCal3, respectively. Each rod acts as the anode, several of which are summed together at the detector into a readout channels, or “tube group”. Each tube group is then summed with three adjacent groups to form a readout channel. Tube groups that reside at the periphery of the FCal modules remain unsummed and therefore act on their own as a readout channel.

The gap sizes vary in each module (270 μm in FCal1, 370 μm in FCal2, and 500 μm in FCal3), and are filled with LAr. In the FCal1, the triangular current pulse at the electrode has a full drift time of 60 ns. Since the electric field inside the gaps of all FCal modules is the same, FCal2 and FCal3 drift times scale with gap size.

All three FCal modules are housed a common support tube inside the end-cap cryostats. The

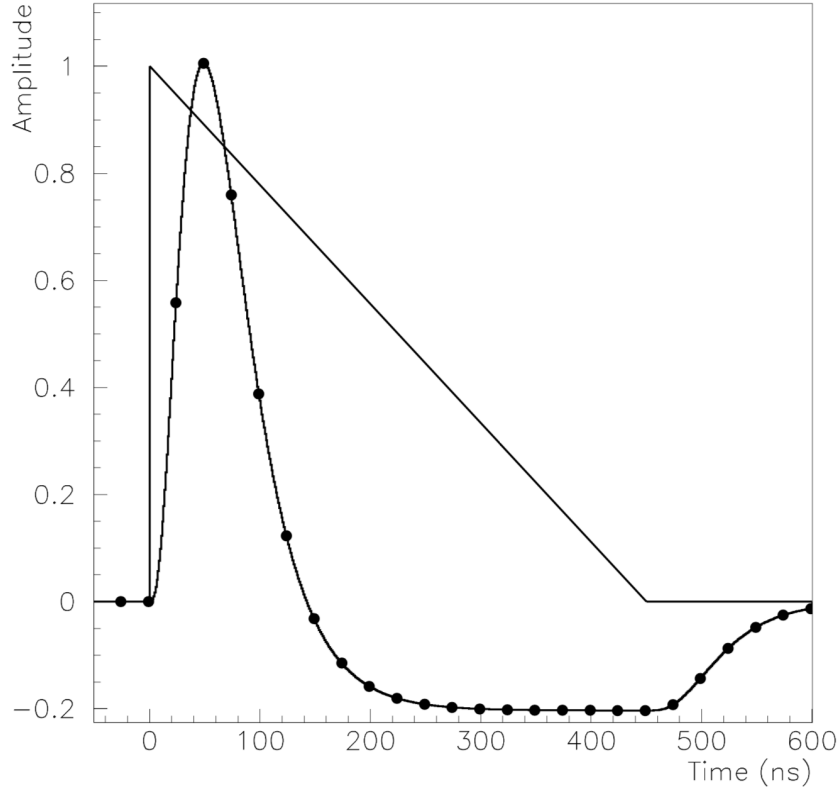


Figure 4.15: Amplitude as a function of time for a triangular pulse of the current in an EMB cell and the FEB output after bi-polar shaping of the pulse. Also shown are the 25 ns sampling points.

placement of an FCal within end-cap is shown in Fig. 4.14.

4.4.3 LAr signal and readout methodology

Charged particles create showers of additional particles as they traverse the calorimeter absorber material. A charged particle produced in the shower passes through the gaps and ionise the LAr, thereby creating electron-ion pairs in the liquid. The electrons and ions then drift under the influence of an electric field applied across the gaps, and are collected on the electrodes. The LAr readout electronics are split into two parts: a front-end, located on the periphery of the detector cryostats, and a back-end, located off-detector in an underground service cavern.

Front-end boards (FEBs), located on the detector cryostats in front-end crates [110], are responsible for reading out and digitising the raw triangular calorimeter signal *pulses*, and transmitting the signal to the back-end electronics. Each FEB has 128 channels, requiring a total of 1524 FEBs for the 182468 calorimeter readout channels. A pulse is amplified on a FEB using three gains – low, medium, and high – and then undergoes a bi-polar shaping. The resulting shaped (or bipolar) pulse maintains the amplitude of the raw signal, but has a zero net area in order to reduce the long tail from the detector response and limit the bandwidth to reduce thermal and pile-up noise. The shaped pulse is sampled every 25 ns, and the measurements are stored until the Level-1 trigger decision is made on the event. The triangular cell current pulse from a EMB cell and the shaped physics pulse with 25 ns samplings are illustrated in Fig. 4.15.

Upon being accepted by the trigger, the optimal gain for the pulse is chosen and four samples – with at least one on the rising edge of the pulse, one near the maximum amplitude and the remaining two mapping out the pulse tail – are passed to an analog-to-digital converter to produce a digitised energy measurement. For special runs, and during calibrations, as many as 32 samples could be read out so that a well-mapped average pulse shape over the full LAr drift period can be obtained.

The back-end electronics are located in the USA15 underground cavern, away from the high-radiation environment of the detector. The FEB transfers the digitised samples to its corresponding back-end readout driver (ROD) that performs the digital signal processing to produce measurements of the energy. Optimal filtering coefficients [111], calculated during calibration runs for each channel, are applied to the digitised signal to optimise the resultant energy and timing resolution. The measured energy is finally recorded, to be used later for object reconstruction and calibration.

4.5 Muon Spectrometer

The ATLAS Muon Spectrometer (MS) includes three large air-core superconducting toroids (discussed earlier in Sec. 4.2), one for each end-cap and one for the barrel, precision tracking chambers and a fast triggering system. The choice of air-core magnets was driven by the requirement to minimise the amount of material traversed by muons after exiting the calorimeters to prevent energy loss, and thus degraded p_T resolution, due to interactions with inactive material. High-precision tracking of muons is based on Monitored Drift Tube (MDT) and Cathode Strip Chamber (CSC) technologies, while Resistive Plate Chambers (RPC) and Thin Gap Chambers (TGC), designed for rapid response, provide the Level-1 trigger in the barrel and end-cap regions of ATLAS, respectively. While the trigger chambers were not designed to provide precision position measurements, they are able to provide information complementary to the precision detectors. For example, the MDTs provide only bending coordinate (η) information for muon track reconstruction, therefore the secondary non-bending (ϕ) coordinate is solely provided by the triggering chambers. The MS provides muon reconstruction in the region $|\eta| < 2.7$ and triggering in $|\eta| < 2.4$. An illustration of the MS is shown in Figure 4.16.

The MS, like the ID, is a charged particle tracking detector. It is located at the outermost region of ATLAS since muons are typically the only particle (with some exceptions, *e.g.* neutrinos) that can exit the calorimeters. The MS chambers provide multiple measurements of a muon track. By collecting a series of space point hits, the trajectory, or “track”, of a muon can be reconstructed. Based on the bending radius of a track through the MS magnetic field (see Sec. 4.2), momentum and charge can also be determined. Furthermore, multiple measurements help to reject fake tracks and improve muon identification in regions with dead channels or local detector inefficiencies.

In the central barrel region, muon detectors are arranged in three concentric cylinders – at $R \approx 5.0$, 7.5 and 10.0 m – about the beam line. There are four instrumented tracking station disks per end-cap that are mounted perpendicular to the beam line, at $z \approx 7.4$, 10.8, 14.0 and 21.5 m.

The reconstruction efficiency, integrated over the detector acceptance, is $\sim 94\%$ [112]. At $\eta = 0$, there is a small gap in the detector for routing service cables. Excluding this region, the efficiency increases to 97%. The transverse momentum resolution of the MS for muons with $5 < p_T < 400$ GeV was determined to be,

$$\frac{\sigma_{p_T}}{p_T} = \frac{0.29 \text{ GeV}}{p_T} \oplus 0.043 \oplus 4.1 \times 10^{-4} \text{ GeV}^{-1} \times p_T. \quad (4.8)$$

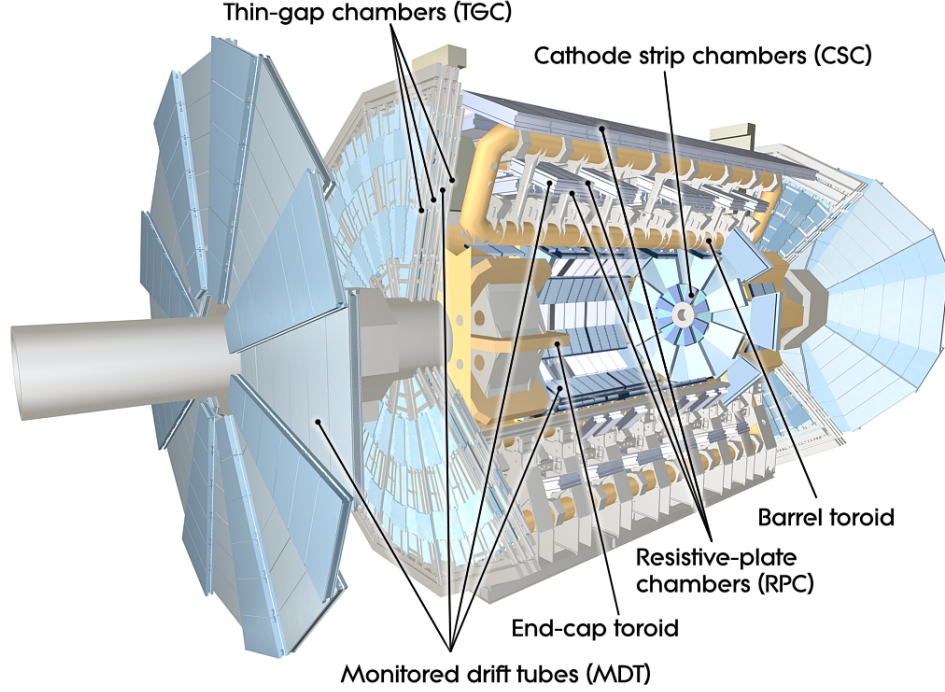


Figure 4.16: The ATLAS Muon Spectrometer with subsystems labeled [84].

During the long shutdown preceding Run-2, the remaining chambers in the transition region between the barrel and end-caps were installed [113].

The remainder of this section provides an overview of the MS subsystems.

4.5.1 Monitored Drift Tubes

The MDT chambers provide high-precision tracking measurements over the most of the region of the MS, $|\eta| < 2.7$. They consist of 3–4 layers of cylindrical aluminium drift tubes with approximately 30 mm outer diameter, 400 μm wall thickness and lengths that vary between 0.9 m and 6.2 m, depending on the position of the chamber. One advantage to the tube concept is that the cylindrical geometry results in a radial electric field, and therefore the measurement accuracy depends only slightly on a muon’s angle of incidence onto a chamber plane. This is an important characteristic since the angle of incidence of infinite momentum tracks onto a chamber plane can reach 45° .

Each drift tube is filled with an Ar/CO₂ gas mixture at 3 bar absolute pressure to provide single-tube position resolution of at least 80 μm at low gas gain used to minimise aging effects. At the centre of each tube is a 50 μm -diameter anode, or “sense”, wire that is positioned within a chamber with an accuracy better than 20 μm for a chamber resolution of 40 μm [114]. The wires operate at a nominal voltage of 3080V. Owing to their physical size, the chambers can suffer from significant deformation due to gravitational sagging or thermal swelling. Therefore, a laser alignment system is built in to the MDTs to help maintain the required position resolution.

There are MDT chambers in all three layers of the MS barrel and the three outer layers of the end-caps. In the inner-most end-cap station, MDTs are replaced with CSCs to cope with the higher particle fluences in these regions. In total, there are 1200 MDT chambers containing about 400 000

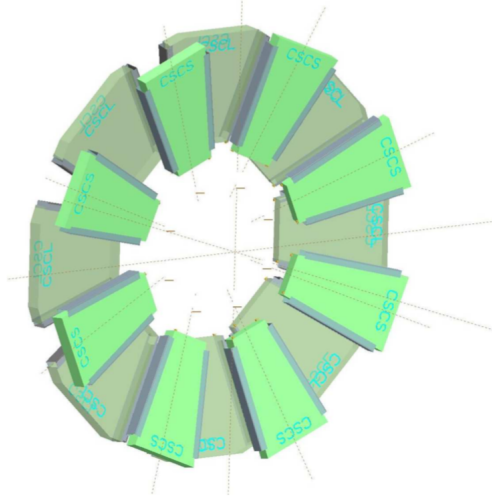


Figure 4.17: Layout of a CSC end-cap, showing the eight small and eight large chambers [84].

tubes covering an active area of 5 000 m².

4.5.2 Cathode Strip Chambers

The CSCs cover the high-rate, inner-most region, $2.0 < |\eta| < 2.7$, of the end-caps. The high fluence in this region results in a high occupancy, therefore MDTs cannot be used due to their limited rate of 150 Hz/cm², whereas the CSCs can withstand a rate up to 1 kHz/cm². They combine high spatial, time and dual-track resolution and low neutron sensitivity.

The CSCs are multiwire proportional chambers with planes consisting of two cathode strips on either side of a set of anode wires that run radially with respect to the beamline. On one side of the set of anode wires, cathode strips are perpendicular to wires (*i.e.* parallel to the beamline) to provide the precision coordinate, and on the other side the cathodes are oriented parallel to the wires for the transverse coordinate. Each end-cap CSC comprises two disks with eight chambers (eight small and eight large), and each chamber has four planes with Ar-CO₂ gas between them. Figure 4.17 shows the layout of a CSC end-cap wheel. Unlike most other ATLAS subdetectors, CSC anode wires are not read out, only the cathode strips are. The two cathodes are segmented, one providing a precision coordinate, in η , with strips perpendicular to the wires, and the other providing transverse coordinate measurements, in ϕ , with parallel strips.

The resolution achieved with this configuration depends on the signal-to-noise ratio and pitch of the readout. With a readout pitch of 5.31 mm and 5.56 mm in the large and small chambers, respectively, in the bending direction, a resolution of 60 μ m per CSC plane is achieved; the resolution of a MDT tube layer is 80 μ m. A coarser cathode segmentation is employed in the non-bending direction, leading to a resolution of 5 mm.

4.5.3 Resistive Plate Chambers

The RPCs are typical avalanche detectors, consisting of a 2 mm gas gap between an anode plate and a cathode plate, with metallic strips for readout on the outside of the plates. Although primarily designed for triggering, the RPCs provide secondary coordinate measurements to supplement the MDT position

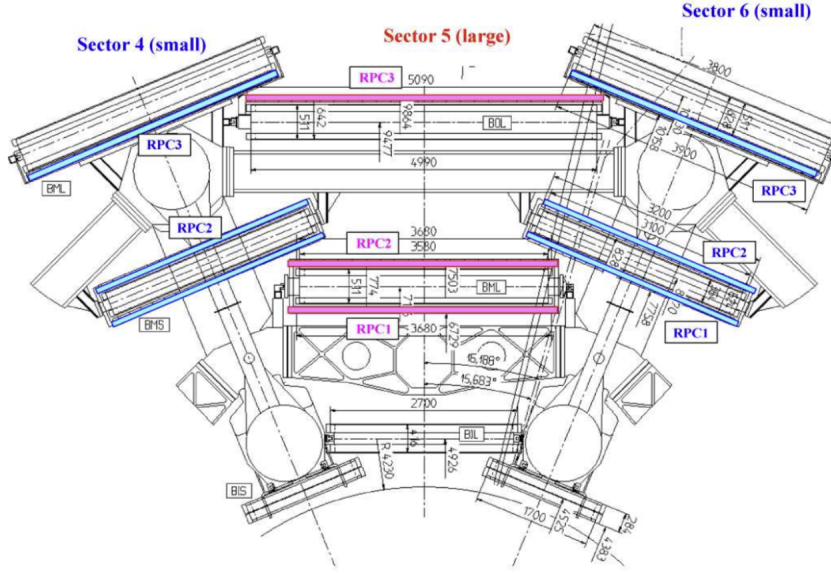


Figure 4.18: Cross-section through the upper part of the barrel with the RPCs coloured [84]. All dimensions are in mm.

information. Two sets of independent readout strips are used to measure the coordinates of a hit – one in the η -direction and the other in the ϕ -direction. A track going through three stations (see Fig. 4.18) gives six measurements in both directions, and helps reject fake tracks from noise hits and provides high-efficiency triggering in the presence of small chamber inefficiencies.

The RPCs were designed for triggering in the central region, $|\eta| < 1.05$, providing information to the Level-1 trigger system. Like the MDTs, the RPCs are arranged in three concentric cylindrical double-layers, providing full azimuthal coverage about the beam line. Figure 4.18 shows how the three RPCs (coloured) are positioned relative to the three MDT chambers. The first two layers at $R = 7820$ and 8365 mm provide trigger information for low- p_T muons. The high- p_T trigger makes use of the third layer, considerably further away at $R = 10229$ mm, muons, combined with the low- p_T trigger information. Overall, the RPCs provided close to 90% in mean efficiency during Run-2 data taking [115].

4.5.4 Thin Gap Chambers

The TGCs provide muon trigger capability and determination of the second, azimuthal (*i.e.* non-bending) coordinate to complement the precision measurements of the MDT that are made in the radial (*i.e.* precision) direction. They are located in the end-caps, with two layers positioned on the inner MS station and seven on the middle station.

Like the CSCs, the TGCs are multiwire proportional chambers with 2.8 mm gaps filled with a mixture of CO_2 and C_5H_{12} . The TGCs are arranged into end-cap disks and provide triggering in the region $1.05 < |\eta| < 2.4$. Wires run through the gaps with 1.4 mm spacings, collecting charge from ions created as the muons traverse the gas. With a high voltage of ~ 2900 V applied around the TGC wires, and the small wire-to-wire distance, very good time resolution is achieved, with signals arriving most often within a time window of 25 ns.

Radial and azimuthal coordinates are read out by combining the cathode wires with separate readout strips coupled to them into groups. To match the readout granularity to the required momentum

resolution, the number of anode wires within a readout group ranges from 6 to 31 as a function of η , corresponding to widths from 10.8–55.8 mm. Both the wire groups and radial strips are staggered between layers to optimise position resolution.

4.6 The LUCID detector

One of the dominant systematic uncertainties in precision physics measurements is related to luminosity. Such measurements therefore require accurate and precise determination of delivered luminosity. Searches for physics beyond the Standard Model also rely on information about the integrated luminosity in order to accurately evaluate backgrounds (*i.e.* the “uninteresting” processes), and determine the sensitivity to signatures of new physics.

Outside of the main volume of the ATLAS detector resides the primary luminosity monitor, LUCID (**L**uminosity **C**herenkov **I**ntegrating **D**etector) [84], that provides bunch-by-bunch luminosity measurements. Although luminosity measurements can be made by several detectors in ATLAS – the BCM, EMEC, FCal and Tile calorimeters, as well as Inner Detector silicon detectors – LUCID is the only one dedicated to measuring the instantaneous luminosity.

The high instantaneous luminosity delivered by the LHC results in multiple pp collisions occurring in bunch crossings, and the mean number of interactions per bunch crossing, $\langle\mu\rangle$, characterises the instantaneous luminosity at any give time. As such, the main purpose of LUCID is to detect inelastic pp scattering in the forward region, based on the principle that μ is proportional to the number of detected scattered particles.

4.6.1 Detector design and algorithms

The LUCID detectors are positioned at $z = \pm 17$ m with respect to the nominal interaction point, each comprising four groups of four photomultiplier tubes (PMTs) located around the beam pipe. The PMTs have quartz-based windows with and four quartz fibre bundles that act as the detecting media (Cherenkov radiators). As a charged particle traverses a PMT window or fibre, Cherenkov light can be produced, which is then read out by the PMT¹ [116]. A PMT is said to have a hit when the number of photoelectrons recorded in an event is larger than a given threshold. Dedicated electronics are used to read out the raw PMT signals, or *hit counts*, as measured by photomultiplier tubes for each of the 2808 nominal LHC colliding bunch pairs. These counts are then integrated over in well-defined time intervals, (*i.e.* *luminosity blocks*, LBs) typically 60 seconds in width, to obtain a measure of the luminosity

A number of luminosity *algorithms*, which combine information from several PMTs in various ways, are used to convert the hit counts to a visible interaction rate per bunch crossing, μ_{vis} . Other detectors that provide complementary measurements also have their own algorithms, *e.g.* track-counting and LAr calorimeters, as discussed below. The LUCID algorithms used in Run-2, as well a short description of each, are shown in Table 4.3. The per-bunch instantaneous luminosity is then obtained via,

$$\mathcal{L}_b = \frac{\mu_{\text{vis}} f_r}{\sigma_{\text{vis}}} \quad (4.9)$$

where $f_r = 11245$ Hz is the proton bunch revolution frequency at the LHC, and the visible cross section, σ_{vis} , encodes the absolute luminosity calibration for a given algorithm. The algorithm-specific σ_{vis}

¹ The Run-2 detector described here is actually called “LUCID2”, but is referred to simply as “LUCID”.

Algorithm	Year(s)	Description
BiHitOR	2015	Required a hit in any of the four PMTs on the A-side of ATLAS. Similar algorithms were available for the C-side, as well as combined A+C-side algorithms, but the C-side suffered significant timing drifts as PMT high-voltage settings were adjusted.
BiHitOR	2016-2017	Counted the average number of hits per bunch crossing summed over four PMTs on both the A- and C-sides.
C12	2018	Due to a large number of PMT failures, a single PMT that showed good stability and gave results similar to the BiHitOR algorithm, was used for baseline luminosity estimates.

Table 4.3: Luminosity algorithms used in Run-2, the year(s) they were employed, and a brief description of their respective PMT configurations.

are determined empirically via dedicated low-luminosity *calibration* runs performed once a year using the van der Meer method [117]. This method involves scanning the LHC beams through one another to determine their horizontal and vertical widths at the interaction point. The rate of interactions is measured as a function of the displacement, and by knowing the number of circulating protons, the absolute luminosity scale can be determined.

4.6.2 Calibration transfer for final luminosity determination

A calibration transfer procedure is used to extrapolate the absolute calibration of the LUCID luminosity measurements made in low- μ data-taking runs to the high-luminosity regimes, typical of normal physics running, where $\mu \approx 50$. The LUCID detector suffers from response non-linearities [118] that must be corrected for. Correction factors are derived from linear fits to the ratio of μ values measured by LUCID and the silicon trackers. The measured values of μ are taken from long physics fills where μ significantly decreases over time, allowing for the stability of the correction factors to be monitored through data taking.

This procedure assumes that the silicon-based track-counting suffers from no significant non-linearity between the low- and high-luminosity regimes. To be sure track-counting is linear between regimes, track-counting luminosity measurements are compared with those from independent detectors, *e.g.* the LAr calorimeters. Figure 4.19 presents such comparisons between the luminosities as determined using either the FCal or EMEC to those using the track-counting algorithm, “TIGHT_TRACKS”, for a single run taken in 2016. The ratio between the LAr- and track-based luminosity measurements are plotted as a function of luminosity block, with each bin containing 50 luminosity blocks. The FCal and EMEC luminosity measurements are determined using a subset of their total number of high voltage (HV) channels that have shown to be stable for most runs. In this study, their individual HV channel-dependent calibration factors – represented in the plot as a single variable, ζ in the figure – are derived by fitting the individual HV channel currents as a function of the track-based luminosity measured in a predetermined baseline run. The baseline run is typically chosen to be a relatively long run with stable conditions. The uniformity of the ratios demonstrates not only that the track-based measurements do not suffer from non-linearities arising from changes in μ , but also highlights the stability of the LAr HV channels – and hence luminosity measurements – throughout a nominal data-taking run.

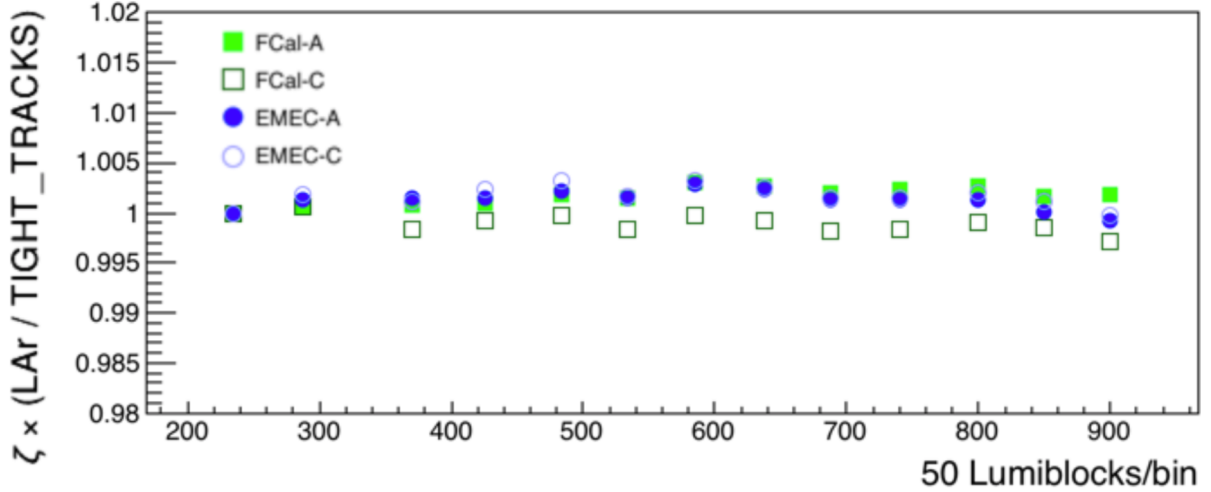


Figure 4.19: Ratios between the luminosity as measured by the LAr calorimeters and track-counting. See the text for details.

The total integrated luminosity delivered by the LHC was 156 fb^{-1} , of which 147 fb^{-1} was recorded by ATLAS. Per-year uncertainties range between 2.0–2.4%, and the uncertainty on the combined Run-2 dataset is $\pm 1.7\%$, dominated by the uncertainty associated with the calibration transfer.

4.7 Trigger and data acquisition

The ATLAS trigger and data acquisition (collectively, TDAQ) system is a combination of hardware- and software-based algorithmic decision-making. It takes a 40 MHz collision rate provided by the LHC and effectively filters the data to output recorded events at a rate of 1 kHz. Considering that the rate of “interesting” events is ~ 10 orders of magnitude smaller than the background rate, and the breadth of the ATLAS physics programme, the TDAQ system is responsible for selecting one of 40000 events delivered by the LHC every millisecond. This presents a monumental challenge for the ATLAS TDAQ system – a rapid and crucial decision must be made for each event. Once an event is rejected, it is forever lost.

The first stage of filtering is provided by the Level-1 (L1) trigger. It is a hardware-based trigger that uses fast electronics and field programmable gate arrays (FPGAs) to make decisions within a $2.5 \mu\text{s}$ time window. The L1 trigger uses coarse granularity input signals from the calorimeters and MS to evaluate threshold and topological criteria to reduce the 40 MHz LHC collision frequency to 100 kHz. It selects events with high- p_T objects as measured in the calorimeters and MS, and those events with large transverse energy imbalances (*i.e.* E_T^{miss}). The L1 defines what are called “regions of interest” (RoI), the $\eta \times \phi \times z$ regions in which any of the L1 trigger thresholds have been surpassed. The RoIs are then passed to the High-Level Trigger.

The second stage of the trigger system, the High-Level Trigger (HLT), uses software-based decision-making that employs reconstructed quantities that are the same or that mimic those used in offline event reconstruction software. It uses the full detector granularity to completely reconstruct events. The HLT comprises some 40000 CPUs in close proximity to the detector itself, so as to reduce the data-transfer latency ($\sim 350 \text{ ms}$), and further reduces the event rate to approximately 1 kHz. These events are then

fully assembled into an event record that is passed on to a data storage system for offline analysis.

The HLT software is an amalgamation of the event filter and HLT used in Run-1 [119]. Trigger signatures are organised into “working groups” based on the different detector elements and physics goals. Each such signature group, *e.g.* jets and E_T^{miss} , e/γ , develops their own trigger software and online calibrations, validates online performance and data quality constraints, provides offline reconstruction algorithms, and further calibrations and validation for data analysis.

Trigger signatures are cataloged by the L1 and HLT selection algorithms that are configured before or during data taking. There are various such “menus”, the most heavily used being the physics menu for proton-proton collision data taking and the corresponding Monte Carlo menu used in simulation. A menu typically includes several different types of triggers and thresholds to select “interesting” events. For example, a single menu may include single and di-electron triggers with various thresholds based on different combinations of p_T , isolation and identification criteria on specific objects.

A full sequence of triggers from L1 and the HLT is called a “chain”. Some triggers in a chain may run “unprescaled”, meaning that any time such an event is accepted by the L1 trigger, it will be passed to the HLT. Others, in particular low- p_T triggers, may be run at relatively high prescales so that only a subset of such events will pass the trigger². While prescales are typically set at the beginning of a run, they can be adjusted on-the-fly during a run. The prescaling approach is necessary due to the limitations on bandwidth and disk space.

At the HLT, events are divided into different “streams”, each containing the output from a number of different trigger chains. A single stream may contain, for example, all events passing an electron or muon trigger. Events may be added to several streams if they meet both L1 and HLT trigger requirements. The number and contents of the set of streams are decided at the beginning of a run. There is typically a “debug” stream that is reserved for events that could not be evaluated in the allotted time for a trigger decision.

A single ATLAS data-taking run can last up to 24 hours, or more. Typically, one long run is taken during a LHC fill and, if necessary, a run is stopped for detector calibrations. Therefore, runs are divided into LBs that are no more than about 60 s each. A LB is the smallest unit of time/data used in ATLAS analyses. Individual LBs can be included or excluded from physics analyses, depending on the data quality and detector behaviour.

An important requirement of the TDAQ system is to ensure all triggers and detectors are synchronised with one another. Most ATLAS subdetectors run on a 40 MHz clock to match that of the LHC, and so the phases of all systems must be adjusted to ensure a given clock cycle in all systems corresponds to the same bunch crossing. Without correct timing, the different subdetectors may associated incorrect bunch crossings and therefore miss an important physics signal. To maintain synchronisation between the LHC clock and detectors, the LHC clock signals are distributed to the ATLAS TDAQ system via optical cables. These signals are in turn distributed to the individual detector electronics systems, at which point a re-synchronisation of the clock frequency is performed to account for possible phase changes that could result in timing differences at the level of a few nanoseconds.

² A prescale of N means the TDAQ system will accept ‘one out of N events.’

Chapter 5

Dataset and object reconstruction

Sometimes it's hard to hold on, so hard to hold on to my dreams

It isn't always what it seems when you're face to face with me.

- Lita Rossana Ford / Ozzy Osborne, *If I Close My Eyes Forever*

The analysis presented in this thesis uses ATLAS proton-proton (pp) data collected during 2015–2018, a period denoted “Run-2”. Crucial to this analysis are reconstructed (analysis-level) objects, including charged leptons (*i.e.* electrons and muons) and jets, whose basic definitions are described in this chapter.

This chapter provides an overview of the Run-2 dataset and data quality requirements, and the methods for reconstructing the relevant objects. As they do not pertain to reconstruction, the concepts of object quality and isolation are introduced later in Chap. 6, in the discussion of the analysis.

The dataset, including a description of data quality requirements in ATLAS, is described in Sec. 5.1. The first step towards the reconstruction of any inner detector (ID) or calorimetric object begins with a clustering algorithm. Clustering algorithms used in ATLAS are discussed in Sec. 5.2. Lastly, Sec. 5.3 details the reconstruction and calibration of objects relevant to the analysis presented herein, namely, electrons, muons, and jets.

5.1 Dataset and data quality

This section discusses the ATLAS Run-2 dataset, as well as the general data quality requirements that must be met in order to be considered usable for physics analyses.

5.1.1 Dataset

During Run-2, the LHC provided pp collisions at $\sqrt{s} = 13$ TeV¹. The LHC performance, in terms of peak instantaneous luminosity, increased throughout Run-2, with peaks ranging from $5 \times 10^{33} \text{ cm}^{-2}\text{s}^{-1}$ to more than $2 \times 10^{34} \text{ cm}^{-2}\text{s}^{-1}$, exceeding its design by more than a factor of two. The ATLAS detector recorded a total of 147 fb^{-1} of integrated luminosity, 139 fb^{-1} of which was determined to be “good for physics” (described in the next subsection), corresponding to an overall data quality efficiency of $\sim 95\%$. A pictorial representation of the LHC delivered, ATLAS recorded, and “good for physics” data accumulated during Run-2 pp collisions is shown in Fig. 5.1.

¹ During Run-1, the LHC only ran at $\sqrt{s} = 7$ and 8 TeV.

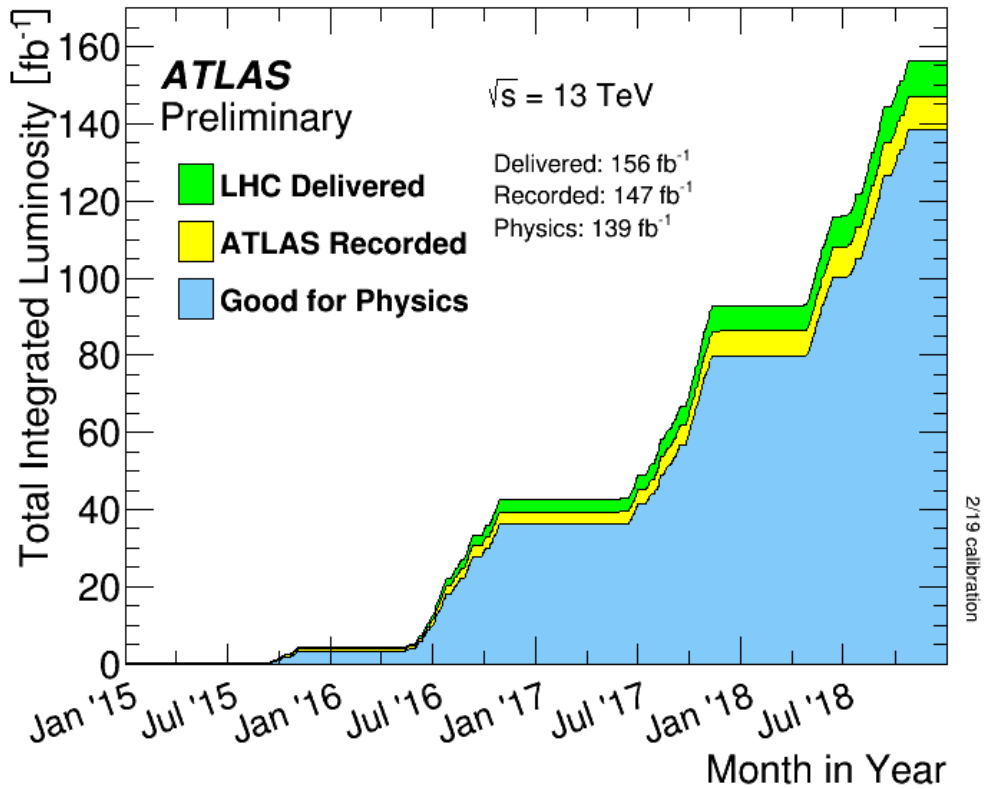


Figure 5.1: Cumulative integrated luminosity versus time delivered to ATLAS (green), recorded by ATLAS (yellow) and certified to be good quality data (blue) during stable beams for pp collisions at $\sqrt{s} = 13 \text{ TeV}$ between 2015–2018 [120].

5.1.2 Data quality

The quality of data recorded by ATLAS is subject to intense scrutiny to ensure detector conditions are well understood and to remove any intolerable detector-related problems – *e.g.* missing or corrupt data, HV trip, *etc.* – from the dataset. Such problems could result in poorly reconstructed objects, causing issues upstream when analysing the data. In most cases, rejected data are accounted for in the data quality efficiency. Exceptions to this include “global” defects – the rejection of data not driven by an ATLAS detector issue. These global defects include data recorded during the ID’s so-called “warm start”², magnet problems, non-standard bunch spacing and very high, or very low, μ conditions. Global defects are used to define the data-taking periods over which data quality efficiencies are calculated, and therefore do not contribute to losses, the main sources of which result from non-nominal solenoid and toroid magnetic fields. Dominant in 2018 were losses incurred at the start of low- μ runs when the detector was configured for low- μ but the LHC was delivering high- μ before luminosity leveling [121]. In 2016–2017, however, such losses were not considered as global defects, and therefore resulted in a lower overall efficiency.

Data quality assessment begins in real-time as the data is being recorded. The goal in this “online” environment is to flag, as quickly as possible, detector failures or reconstruction issues in order to limit

² The time at the beginning of a run during which high voltages ramp up and pre-amplifiers in the pixel detector are turned on.

the amount of unrecoverable data resulting from severe coverage losses, timing shifts and data corruption.

As mentioned briefly in Sec. 4.7, the data are recorded within streams: the *physics* streams (for data analysis), *calibration* streams (for alignment, calibration constant measurements, *etc.*) and the *express* stream (for data quality and monitoring). The express stream contains 2–4% of data, and consists of a mixture of all types of events so as to be representative of all data collected. Any problem found in any of the streams “offline” that could affect data quality are flagged as defective and logged in a dedicated defect database. There are generally two types of defects: *tolerable* and *intolerable*. Data with a tolerable defect is flagged and recorded for book-keeping purposes and can still be used for physics analyses. An intolerable defect results in rejection of the affected interval of validity (*i.e.* the time interval during which data was affected, in units of LBs) and thus cannot be used for analysis. The defect database is then used to produce a list of luminosity blocks and runs that are declared “good for physics”; such a list is called a “Good Runs List” (GRL).

Overall, ATLAS performed very well and with high efficiency in taking good quality data throughout Run-2. Table 5.1 gives a summary of detector uptimes and good data quality efficiencies (in percent) during stable beams in pp collision physics runs at $\sqrt{s} = 13$ TeV between 2015–2018.

Dataset	Inner Detector			Calorimeters		Muon Spectrometer				Magnets		Trigger	
	Pixel	SCT	TRT	LAr	Tile	MDT	CSC	RPC	TGC	CS	Tor	L1	HLT
2015 (@ 25 ns)	93.84	99.77	98.29	99.54	100	100	99.96	100	99.97	100	97.79	99.97	99.76
Good for physics: 88.79% (3.2 fb^{-1})													
2016	98.98	99.89	99.74	99.72	98.71	99.95	99.80	100	99.96	99.15	97.23	98.33	100
Good for physics: 93.07% (32.99 fb^{-1})													
2017	99.97	99.94	100	99.48	99.41	99.90	99.24	99.89	99.89	100	99.17	99.95	99.96
Good for physics: 95.67% (44.39 fb^{-1})													
2018	99.78	99.77	100	99.67	100	99.80	99.72	99.98	99.98	100	99.58	99.99	99.99
Good for physics: 97.46% (58.45 fb^{-1})													

Table 5.1: Luminosity-weighted relative detector uptime and good data quality efficiencies (in percent) during stable beams in pp collision physics runs at $\sqrt{s} = 13$ TeV between August 2015 and October 2018. All numbers correspond to nominal data-taking conditions runs taken during this time.

5.1.3 Pile-up

The LHC is typically recognised in popular culture for its unprecedented centre-of-mass energy, $\sqrt{s} = 13$ TeV, rather than for its unprecedented instantaneous luminosity; together, these two characteristics are what make the LHC a potential “discovery machine”. However, as luminosity increases, so too does the number of pp interactions per bunch crossing. Therefore, in addition to the collision of interest, the “hard-scatter” (HS), numerous other (typically uninteresting) collisions also occur. These additional collisions are collectively referred to as “pile-up”, and present a serious challenge to detector subsystems and physics analyses.

Many ATLAS subsystems have sensitivity, or readout, windows much longer than the 25 ns LHC pp bunch spacing. This means the reconstruction of every physics object is affected by pile-up in some way, *e.g.* additional energy contributions to jets. The evolution of pile-up over the years of Run-2, as recorded by ATLAS, is shown in Fig. 5.2.

In general, there are five distinct sources of pile-up background.

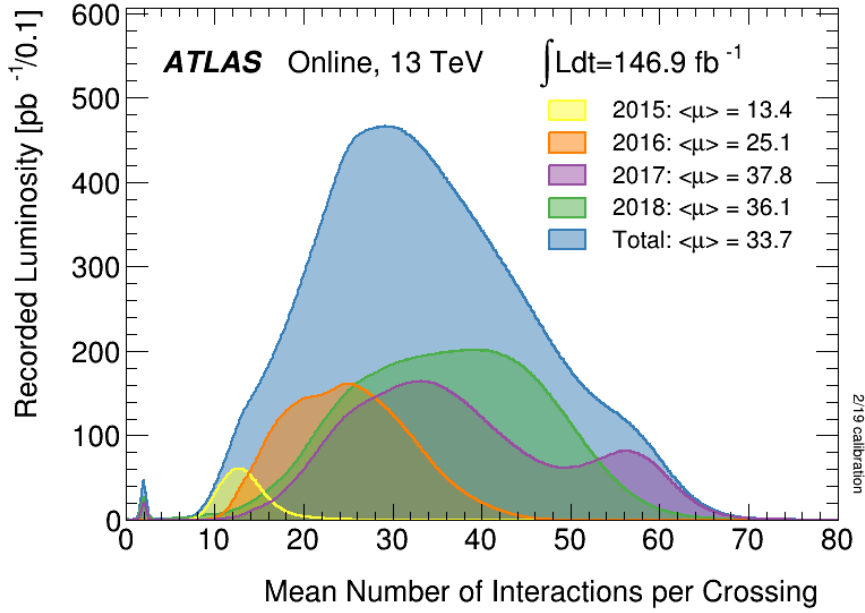


Figure 5.2: Distribution of $\langle\mu\rangle$, the mean number of interactions per bunch crossing, for the 2015–2018 pp collision data at $\sqrt{s} = 13$ TeV [120]. The average is taken over all in-time colliding bunch pairs, and therefore is representative of only in-time pile-up (discussed in the main text). All data was recorded by ATLAS during stable beams.

- *In-time pile-up*: Multiple pp collisions occurring in the same bunch crossing. This source depends on $\langle\mu\rangle$.
- *Out-of-time pile-up*: multiple pp collisions occurring in bunch crossings adjacent to the collision of interest. This source depends on $\langle\mu\rangle$, and can be significant when detector readout, or electronic integration, exceeds 25 ns. In such cases, these collisions affect the signal of the collision of interest.
- *Cavern background*: A gas of “slow” particles (*e.g.* low energy, ~ 1 MeV, neutrons) filling the cavern during a LHC run, contributing mostly to random, or fake, hits in the muon system. This source is proportional to $\langle\mu\rangle$. Cosmic rays also contribute to this background, in which case the rate is constant on average, and can be present even without collisions.
- *Beam halo*: Initiated by protons scraping against an upstream collimator, resulting in showers of predominantly muons nearly parallel to the beam line. As the particles pass through the detector, they can leave background signals in the muon system and, if produced at large angles, can potentially ionise calorimeter cells sufficiently to produce significant signals in them. This source is proportional to the current in the two rotating beams as well as $\langle\mu\rangle$.
- *Beam gas*: Collisions between protons in a bunch with residual gas inside the beam pipe, proportional to the current in the two rotating beams. These backgrounds arise from proton interactions with carbon, oxygen, nitrogen or hydrogen (*i.e.* proton-proton) and are highly asymmetric. Therefore, additional collision vertices are created, however, they are normally well outside the typical 12 cm interaction region and do not contribute largely overall to pile-up.

The most dominant sources of background are in-time and out-of-time pile-up. In the case of in-time pile-up, each HS event is typically accompanied by, on average, ~ 34 other pp collisions. These “soft” collisions produce additional tracks in the ID and showers in the calorimeters, negatively impacting the reconstruction of objects arising from the HS event of interest. As already mentioned, out-of-time pile-up significantly affects detectors that have a response time longer than the time interval between consecutive LHC bunch crossings. For example, the LAr calorimeters have a pulse shape roughly 450 ns long. This long pulse shape is therefore susceptible to deformation due to energy deposits from successive collisions.

5.2 Clustering algorithms

Clustering algorithms are used to define collections of sensitive detector elements (*i.e.* clusters) that serve as inputs to the reconstruction software to build tracks and, ultimately, different species of particles. In the calorimeters, ATLAS uses two principal algorithms to construct calorimeter clusters: a “sliding-window” algorithm and a “topological” algorithm.

In 2017, when the ATLAS migrated from release 20.X to 21.X of Athena [122], the experiment’s software framework, the topological cell clustering approach used for jet reconstruction was introduced also for electrons and photons. This choice was motivated by the use of a common set of tools for isolation-based calculations and to permit a combined tracker-plus-calorimeter particle flow reconstruction algorithm [123].

5.2.1 Sliding-window calorimeter clustering

The sliding-window (SW) algorithm is based on summing LAr calorimeter cells within a fixed-size rectangular window, positioned such that it contains a local maximum of transverse energy, E_T . The SW algorithm proceeds in three steps: building towers, finding a precluster (seed) and filling clusters.

The first step to building clusters is “tower building”. A grid, in η - ϕ space, is defined by $N_\eta \times N_\phi = 200 \times 256$ elements of size $\Delta\eta \times \Delta\phi = 0.025 \times 0.025$ within the acceptance of the inner tracker (*i.e.* $|\eta| < 2.5$). A “tower” is then built by combining the energy of all cells in all longitudinal layers in each element. Next, the $N_\eta^{\text{window}} \times N_\phi^{\text{window}} = 5 \times 5$ windows slide, in steps of $\Delta\eta \times \Delta\phi = 0.025 \times 0.025$, across each element of the tower grid to locate a transverse energy (defined as the summed E_T of the towers contained in the window) local maximum. If the local maximum is above a threshold, $E_T^{\text{thresh}} \approx 3$ GeV, a precluster (or seed) is formed. The position of the seed is dependent on the calorimeter layer, and defined by an energy-weighted average of all cells in each calorimeter layer. Note that the dimensions of the window used to determine the position of a precluster, $N_\eta^{\text{preclus}} \times N_\phi^{\text{preclus}}$, is typically smaller than the sliding window itself in order to be less sensitive to noise.

Finally, an EM cluster is formed from all the cells in a region-dependent window of size $N_\eta^{\text{cluster}} \times N_\phi^{\text{cluster}}$, centred on the precluster. In the EMB, the window size is $N_\eta^{\text{cluster}} \times N_\phi^{\text{cluster}} = 3 \times 7$, larger in ϕ (*i.e.* the bending coordinate of the central solenoid) in order to capture bremsstrahlung radiation and other particles resulting from electron interactions with material upstream of the calorimeter. In the EMEC, the window size is $N_\eta^{\text{cluster}} \times N_\phi^{\text{cluster}} = 5 \times 5$, larger now in η because of the smaller physical cell size.

Although the SW algorithm has been superseded by a dynamical topological clustering approach for object reconstruction, it is still used to define Regions of Interest (RoI) for triggering purposes in the LAr calorimeters.

5.2.2 Topological calorimeter clustering

In contrast to the SW clustering, topological clustering results in three-dimensional clusters with variable numbers of adjacent cells and therefore do not have a fixed size or shape. Topological clusters, or topoclusters for short, are built by grouping together adjacent cells that have significant energy deposits compared to cell noise.

Topocluster formation is an iterative process that starts by constructing proto-clusters from seed cells. The observable of interest is the *cell significance*, calculated as,

$$\zeta^{\text{EM}} = \left| \frac{E^{\text{EM}}}{\sigma_{\text{noise}}^{\text{EM}}} \right| \quad (5.1)$$

where $|E^{\text{EM}}|$ is the absolute cell energy at the EM scale³, and $\sigma_{\text{noise}}^{\text{EM}}$ is the expected noise in the cell.

If a laterally or longitudinally neighbouring cell adjacent to a seed has a cell significance above a medium threshold, $\zeta_{\text{neighbour}}^{\text{EM}}$, it lends itself as a seed for its neighbouring cells. Once the set of candidate cells is exhausted (*i.e.* no cells remain that satisfy $\zeta^{\text{EM}} > \zeta_{\text{neighbour}}^{\text{EM}}$), all cells adjacent to the peripheral cells of the proto-cluster satisfying a low threshold, $\zeta_{\text{cell}}^{\text{EM}}$, are added to form the final topocluster.

Topoclusters of the type “4-2-0” ($\zeta_{\text{seed}}^{\text{EM}} > 4\sigma$, $\zeta_{\text{neighbour}}^{\text{EM}} > 2\sigma$, and $\zeta_{\text{cell}}^{\text{EM}} > 0\sigma$) are used in the standard ATLAS reconstruction of calorimetric objects. It is optimised to efficiently find low-energy clusters without being inundated by noise. The null threshold on $\zeta_{\text{cell}}^{\text{EM}}$ ensures that all cells adjacent to the proto-cluster are included in the final step.

Ideally, a cluster would result from an individual particle, and be sufficiently isolated so as to not overlap with one another. Of course, this is not typical in the LHC environment, and so it is highly probable that two particles be merged into a single cluster. A topocluster can be split following its formation if it contains a set of local maximum cells within it, where each cell has the following properties:

- $E > 500$ MeV;
- an energy greater than that of any adjacent cell; and
- has itself at least four adjacent cells that are part of the same parent cluster.

In the case that a single cluster has multiple such local maxima, it is split such that each resulting cluster has no more than a single local maximum. Therefore, topoclusters with only one or no local maximum are untouched by the splitting algorithm. It has been observed that by excluding calorimeter layers in which no large maxima are expected, such as the presampler, formation of noise-based clusters is suppressed [124].

5.2.3 Adaptation of the 4-2-0 method for electrons

A limitation of the SW algorithm is its inability to evolve in a fashion characteristic of an EM shower since it has fixed dimensions. Moreover, a fixed-size window is unable to capture low-energy photons radiated due to bremsstrahlung interactions in the ID, resulting in energy-deprived EM clusters. Therefore, a modified topological clustering approach [125] was designed to address these two shortcomings of the SW algorithm. It is important to note that the same set of topoclusters are used for jet, electron and photon reconstruction, therefore there is no need for duplication of topoclusters.

³ The cut on absolute energy is used to symmetrise the contribution from clusters formed from electronics noise, which could be negative.

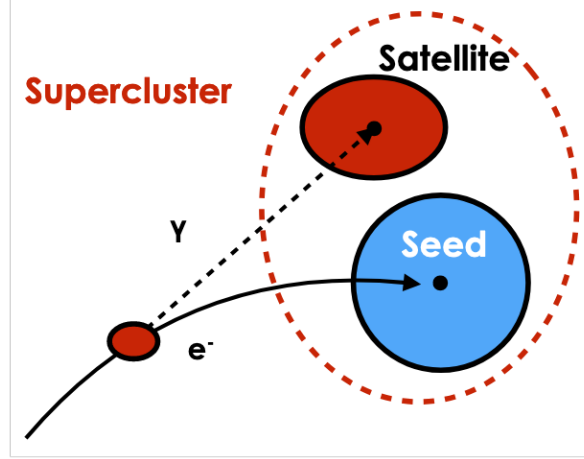


Figure 5.3: Illustration of a supercluster constructed from an electron seed and photon satellite [125].

To pick out EM topoclusters built in the calorimeters, a selection based on the EM fraction,

$$f_{\text{EM}} = \frac{E_{\text{L1}} + E_{\text{L2}} + E_{\text{L3}} + w \cdot (E_{\text{E4}} + E_{\text{PS}})}{E_{\text{cluster}}}, \quad w = \begin{cases} 1, & 1.37 < |\eta| < 1.63 \\ 0, & \text{otherwise} \end{cases} \quad (5.2)$$

where E_{Li} is the cluster energy in layer i of the EM calorimeter, is used. The term $(E_{\text{E4}} + E_{\text{PS}})$ is only considered in the transition region since electrons in this η range tend to deposit non-negligible amounts of energy in the E4 scintillators of the tile calorimeter and presampler. Based on Monte Carlo studies [125], a value of $f_{\text{EM}} > 0.5$ was chosen as a pre-selection requirement as it rejects $\sim 60\%$ of clusters produced by pile-up background while maintaining good efficiency for selecting real electron topoclusters.

5.2.4 Superclusters

The EM topoclusters are used as inputs to define and reconstruct electron (and photon) *superclusters*. A supercluster (SC) comprises an EM topocluster and one or more *satellite clusters*, *i.e.* a nearby secondary cluster expected from a photon shower. The primary motivation for SCs is to recover low-energy bremsstrahlung photons that result from interactions in the ID. Figure 5.3 shows an example of an SC formed by an electron (seed) and a photon (satellite), the latter having been produced in an electron-material interaction in the ID.

The building of SCs begins with the list of those 4-2-0 topoclusters satisfying $f_{\text{EM}} > 0.5$, described above, sorted in order of decreasing p_{T} . For a topocluster to become an electron SC seed, it must have a minimum energy of 1 GeV and be matched to a track with at least 4 silicon hits. Once a SC seed is found, the satellite-finding stage begins. A satellite is required to be within $\Delta\eta \times \Delta\phi = 0.075 \times 0.125$ of a seed barycentre, and have no track associated to it. For a topocluster within $\Delta\eta \times \Delta\phi = 0.125 \times 0.3$ of a seed, it is considered a satellite if it and the seed share the same track. Once all topoclusters have been considered, the next topocluster that was not used as a satellite in the p_{T} -ordered list is checked to determine if it meets the requirements to be a seed. If it does, the SC-building procedure starts again, this time considering only “unused” (*i.e.* not a seed or satellite) topoclusters as potential satellites.

This procedure iterates through the list of p_T -ordered topoclusters until all have been examined. The last step is the process of *cell summation*, where each seed cluster and its associated satellites are combined to form the final list of SCs.

5.3 Object reconstruction and calibration

After an event is accepted by the trigger system and read out, the flow of data roughly proceeds as follows:

1. recorded “raw” data is *promptly* reconstructed at the CERN Data Centre (*i.e.* Tier-0), producing reconstructed objects (*e.g.* electrons, jets, *etc.*);
2. the raw and promptly-reconstructed object data are distributed among the roughly 13 computing centres (*i.e.* Tier-1 sites);
3. at Tier-1 sites, the reconstructed object data are further processed for particle identification, calibration, *etc.*, to create analysis object data.

Beyond this, additional corrections and calibrations, as well as quality and isolation criteria are typically applied to objects at the analysis stage (described later in Sec. 6.5). This section is dedicated to the processes undergone in points 1–3 above.

5.3.1 Tracks

Tracks are vital in the reconstruction and identification of charged particles. There are two track-finding strategies employed in ATLAS – *inside-out* and *outside-in*.

Cluster building

The inside-out pass first builds clusters from hits in the silicon of the precision trackers produced by charged particles. A connected component analysis (CCA) [126] algorithm is used to group these energy deposits in the pixels and strips into clusters. The clusters are then used to create three-dimensional *space-point* measurements (one space-point from the pixel and two, one from each side of a strip layer, from the SCT), representing the point where a charged particle traversed the active material of the trackers.

A single cluster can be created by one or multiple particles, corresponding to *single-particle* clusters and *merged* clusters, respectively. Merged clusters typically result from highly collimated charged particles. These two types of clusters are illustrated in Fig. 5.4. There are also *shared* clusters which are used in multiple reconstructed tracks but are not sufficiently compatible with a merged cluster to be labelled as such by the reconstruction software.

Track seeds

From the clusters, track seeds are formed from sets of three space-points. A pattern-recognition algorithm, using a pion hypothesis to model energy losses from particle interactions with detector material, connects track seeds and additional space-points to build track candidates. In the case that a track seed with $p_T > 1$ GeV does not lead to a full track (*i.e.* at least 7 silicon hits per track candidate),

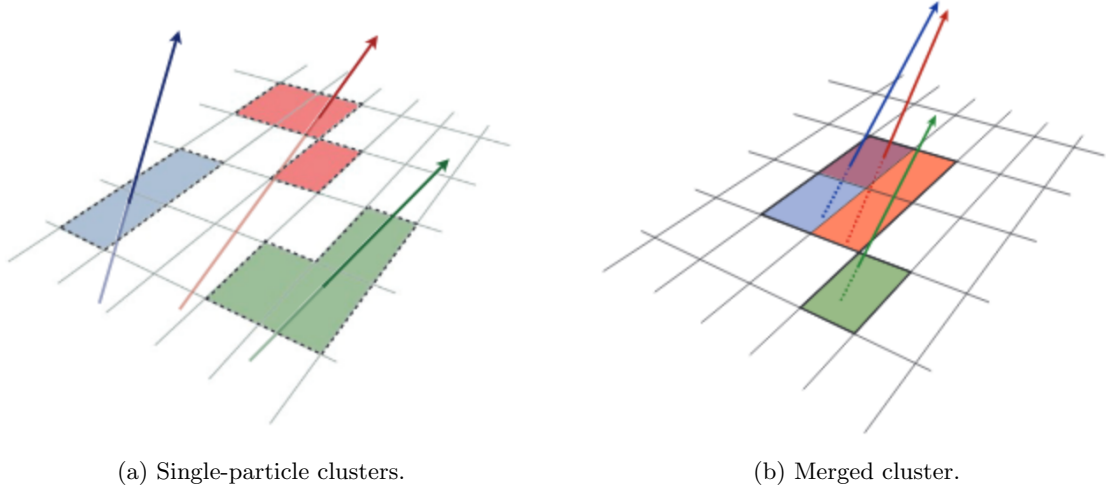


Figure 5.4: Illustration of different (coloured) charged particles traversing pixel clusters, resulting in (a) single-particle clusters and (b) a merged cluster [127].

but is within an EM conical region-of-interest, pattern recognition is run again, this time using an electron hypothesis, allowing for larger energy loss resulting from bremsstrahlung at each particle-material intersection.

Ambiguity treatment

To resolve ambiguities in track cluster/space-point assignments, tracks are processed in order of a *track score* that is based on intrinsic resolutions and cluster multiplicities expected in different tracking detectors, number of holes (*i.e.* a missing hit where one would be expected), goodness of fits, and track momentum. Clusters cannot be shared by more than two track candidates, and a single track candidate can have no more than two shared clusters. Therefore, if a candidate track cluster causes violation of either criterion, it is removed from the candidate and the candidate is scored again.

Lastly, track candidates are required to have the following properties:

- $p_T > 400$ MeV
- $|\eta| < 2.5$
- > 7 pixel+SCT clusters
- at most one shared pixel cluster or two shared SCT clusters
- at most two holes in pixel+SCT clusters
- at most one pixel hole
- $|d_0| < 2.0$ mm
- $|z_0 \sin \theta| < 3.0$ mm

where d_0 is the transverse impact parameter calculated with respect to the beam line, z_0 is the longitudinal difference along the beam line between the point at which d_0 is defined and the primary vertex, and θ

is the track’s polar angle. The track resolution of d_0 (z_0) ranges between 99–25 μm (170–75 μm) for $0.5 < p_T < 10$ GeV in $0.2 < |\eta| < 0.4$. Failure to meet any of these criteria results in the rejection of a track candidate.

Track creation

The last step of the inside-out pass extends tracks seeded in the silicon detectors into the TRT. Track candidates are extrapolated into the TRT where hits compatible with the extrapolation are added to the candidate. A track is said to have a *TRT extension* if the hits added to the track candidate result in a good quality fit, as determined based on the χ^2 of the candidate, and track score, which is calculated using a similar approach to the ambiguity treatment above.

Finally, a fit is performed on each track passing the above ambiguity treatment, as well as those tracks with TRT extensions, before being added to the final track collection. The final tracks are typically subject to additional discrimination in object reconstruction to remove low-quality tracks and to further suppress fake tracks.

The second, outside-in, pass is performed last wherein standalone TRT track segments are reconstructed in regions seeded by the electromagnetic calorimeter. The segments are extrapolated back into the silicon detectors by associating hits not already used for tracks constructed from the inside-out pass. Even segments that are not associated to a silicon hit are added to the final track collection as they can be used for other tasks, *e.g.* for photon conversion reconstruction.

5.3.2 Electrons

Only central, *i.e.* $|\eta| < 2.47$, electrons are used in the analysis presented in this thesis, and so reconstruction of electrons beyond this region (*i.e.* “forward” electrons) is not detailed here; for details on forward electron reconstruction, see [128, 129]. While much of what is presented in this section applies to both electrons and photons, only the specific details pertaining to electrons are described.

In ATLAS parlance, an “electron” is an object consisting of a (super)cluster built in the calorimeter and a reconstructed charged-particle track matched to the cluster. The procedure of reconstructing electrons can be generally divided into four parts: electron track reconstruction, track matching, candidate reconstruction, and electron identification. An illustration of an electron passing through the ATLAS detector is shown in Fig. 5.5.

Reconstructing electron track candidates

To reconstruct electron objects, first EM topoclusters⁴ – the building of which is described in the previous section – are selected for electron candidacy. Clusters are required to meet “loose” requirements on variables used for shower shape discrimination; the hadronic leakage ratio, R_{Had} , defined as the ratio of E_T in the hadronic to the E_T in the EM calorimeters; and the energy distribution ratio in η for the middle layer of the EM calorimeter, R_η , corresponding to the energy ratio in 3×7 cells to that in 7×7 cells centred at the electron cluster position. These initial clusters are used in standard track reconstruction (discussed in the previous subsection) to produce electron track candidates.

⁴ When there is no chance of ambiguity, “EM topoclusters” will be referred to simply as “topoclusters” for the rest of this section.

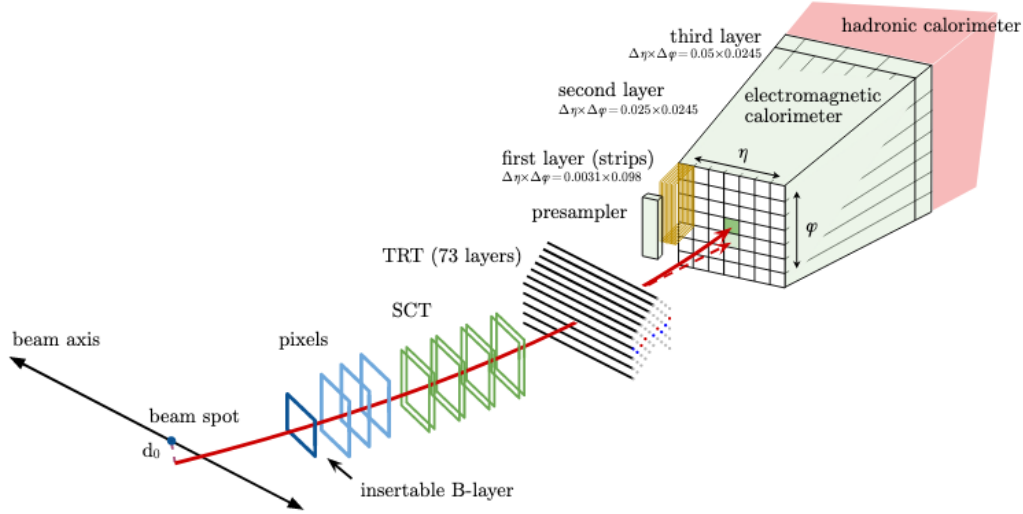


Figure 5.5: An illustration a path an electron could take as it passes through ATLAS [130]. The solid red line represents the electron’s trajectory, traversing the ID and then entering the EM calorimeter. The dashed red line indicates the path of a bremsstrahlung-radiated photon produced through electron-material interaction.

Electron track candidates are fitted using the ATLAS Global χ^2 Track Fitter [131] to account for additional energy losses in cases when the standard track fit fails. Tracks with at least four silicon hits loosely matched⁵ to EM clusters are refitted using a Gaussian Sum Filter [132] to better account for lost energy and improved track parameter estimation.

Track matching and electron candidacy

The loosely-matched, refitted electron track candidates are then subject to further matching, but with stronger requirements in η and ϕ , to EM clusters. If multiple tracks are matched to a single cluster, tracks with pixel hits are favoured, followed by tracks with hits in the SCT but no pixel hits. Tracks that match better in $\Delta R = \sqrt{(\Delta\eta)^2 + (\Delta\phi)^2}$, wherein the track-to-cluster extrapolation is performed, are preferred unless differences are small. In the case of a small ΔR difference, the track with more pixel hits is preferred. Additionally, track momentum is rescaled to the cluster energy to better account for cases when the momentum is significantly affected due to bremsstrahlung radiation.

The combination of an EM cluster and its matched track is considered as an electron candidate if the track has at least four hits in the silicon layers and no associated vertex from a photon conversion. At this point the electron-candidate clusters are used to build superclusters (described in Sec. 5.2). Prior to calibration, the size of each supercluster constituent is reduced to three (five) cells in the η direction in the barrel (end-cap) region, with respect to the constituent’s barycentre. This limitation removes cells which do not contain a significant amount of energy, and as a result keeps the fraction of the shower’s true energy not contained in a cluster (*lateral leakage*) approximately constant as a function of energy.

⁵ Loosely matched imposes requirements on the position of the cluster barycentre and position of the track extrapolated to the second/middle layer of the EM calorimeter

Electron Calibration

Uniformity corrections are applied to data to equalise the response of the EM calorimeter longitudinal layers between data and simulation. These corrections were derived using data collected in 2012, and were validated by reprocessing the 2012 data under Run-2 conditions, *e.g.* using four samples from the bipolar shape (see Sec. 4.4) instead of five to determine the energy deposited in a calorimeter cell. Other corrections, including those accounting for geometrical effects, were also derived from Run-1 data that are validated through reprocessing. Some regions of the LAr calorimeters operate at non-nominal HV due to short circuits occurring in specific LAr gaps. The correction to account for these regions is updated whenever a new short is found that requires a reduced HV.

Next, calibrations are applied to candidate electrons to correct for energy lost in the material upstream of the calorimeter, energy deposited in cells neighbouring the cluster, and energy lost beyond the LAr calorimeter. A single correction is applied to account for all these effects. It is determined using multivariate algorithms trained on single-particle samples, binned in p_T and $|\eta|$, produced by the GEANT4-based simulation of the ATLAS detector [133].

As a last step, correction factors are derived from large samples of simulated $Z \rightarrow ee$ events and applied to reconstructed electrons. The electron energy resolution of the detector is inferior to that of the simulation. Therefore, smearing factors derived from $Z \rightarrow ee$ data events are applied to the simulated electron energies to match the resolution of the physical detector.

Electron identification

Central electrons are identified using a likelihood (LH) method, with inputs from the ID, calorimeter, and quantities combining information from the two subsystems [130].

The same single-particle simulated events used in the calibration procedure are employed in the LH method to provide the signal and background probability density functions (pdfs) of input variables. The signal, L_S , and background, L_B , LH functions are based on the products of n pdfs, $P_{S(B)}$,

$$L_{S(B)}(\mathbf{x}) = \prod_{i=1}^n P_{S(B),i}(x_i), \quad (5.3)$$

where \mathbf{x} is the vector of input variables (*e.g.* longitudinal and lateral shower shapes, track quality, track-cluster matching, and particle identification by the TRT) and $P_{S(B)}(x_i)$ is the value of the signal (background) pdf at x_i ; the signal corresponds to prompt electrons, and the background to jets with prompt electron signatures (*i.e.* “fake” electrons), electrons from photon conversions and electrons produced in hadron decays (*i.e.* non-prompt electrons).

The signal and background LH functions are used to form, for each candidate electron, the discriminant,

$$d_L = \frac{L_S}{L_S + L_B}. \quad (5.4)$$

The discriminant is used to define multiple levels of prompt-electron signal efficiencies and their corresponding levels of background rejection, collectively known as *working points* (WP). Because d_L sharply peaks at unity (zero) for signal (background), a more convenient way to represent the discriminant to

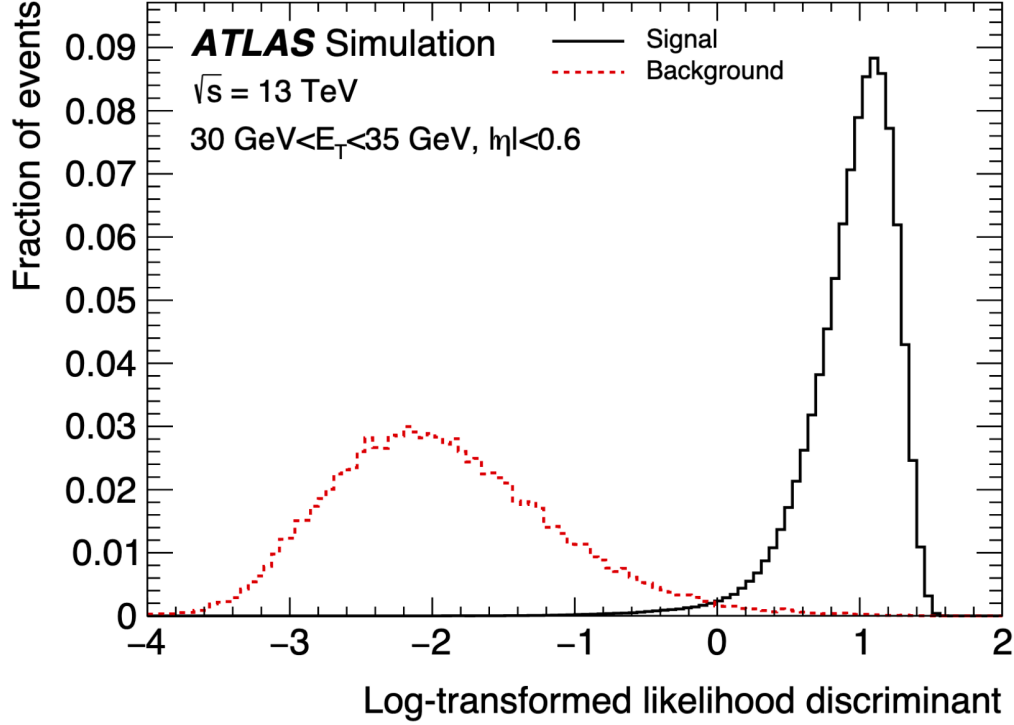


Figure 5.6: The transformed LH-based discriminant, normalised to unit area, for reconstructed electron candidates with good tracks and $30 < E_T < 35$ GeV within $|\eta| < 0.6$ [130]. The black histogram represents prompt electrons in simulated $Z \rightarrow ee$ events, and the red histogram represents the simulated background from fake-enriched events.

define WPs is to transform the LH discriminant in Eq. 5.4,

$$d_L' = -\tau^{-1} \ln(d_L^{-1} - 1), \quad (5.5)$$

with non-zero positive-definite constant τ . Figure 5.6 shows an example of the transformed discriminant for prompt electrons from Z boson decays and for background. Working points are then defined by selecting a value of d_L' above which is considered as signal.

The advantage of the LH method over the selection-based method is that the LH combines the information from all discriminating variables to give a measure of the probability that an electron candidate is a real electron, taking into account correlations more effectively. In contrast, the selection-based method requires a candidate to satisfy each selection criterion separately, often affecting the selection efficiency negatively due to the similarities between the distributions of discriminating variables.

5.3.3 Muons

Position and direction measurements are provided by all ATLAS subdetectors through which a charged particle traverses in order to reconstruct segments of the particle's trajectory. The combination of all such measurements can be used therefore used to identify muons and also reconstruct complete trajectories through the full detector.

Four methods are used in ATLAS to reconstruct different “types” of muons, depending on the

subdetectors used:

- *Standalone/extrapolated*: tracks reconstructed only in the MS, that are extrapolated to the interaction point;
- *Combined*: tracks reconstructed in the MS and matched to those compatible from the ID;
- *Segment-tagged*: reconstructed ID tracks extrapolated to the MS, typically associated to track segments in the MS not included in a full MS track. These muons help to improve the total muon reconstruction efficiency since they usually correspond to low- p_T muons which do not reach the middle and outer MS stations; and
- *Calorimeter-tagged*: reconstructed ID tracks in the region with no MS coverage, $|\eta| < 0.1$. These tracks are matched to calorimeter clusters consistent with those produced by minimum-ionising particles. Even though they have the lowest purity of all four muon types, calorimeter-tagged muons are used to recover acceptance loss in the non-instrumented regions of the MS.

Because combined muons (CB) have the highest purity (accounting for $\sim 96\%$ of all reconstructed muons), they are most often used in physics analyses, including the one presented here. Therefore, this section details only CB-type muons.

Segment reconstruction

Muon reconstruction begins by searching for hit patterns in each of the MS chambers, which are then used to form straight track segments. The search algorithm requires that any reconstructed track segment is loosely compatible with the interaction point. In each MDT chamber and nearby RPC or TGC trigger chamber, hits are searched for that are aligned on a trajectory in the bending plane of the detector. A segment is then formed by performing a linear fit to the hits found in each layer. Segments in the CSC detectors are constructed by combinatorially matching hits in the η - ϕ plane.

Track reconstruction

Complete MS tracks are built from the reconstructed segments in different layers. A segment-seeded combinatorial algorithm uses the segments constructed in the middle layer, since this is where most trigger hits are. The search then continues, using segments from the inner and outer layers as seeds. Seed segments are selected based on the number of hits associated to the segment, the quality of the straight-line fit to the hits that comprise the segment. Segments are matched to one another according to their relative positions and angles. A complete MS track is required to have at least two matched segments, except in the transition region between the barrel and end-cap where a single segment with both η and ϕ information can be considered a track.

It is possible that the same segment is included in multiple reconstructed tracks. Therefore, an overlap removal procedure is used to select the track to which the segment is best assigned. The segment is also allowed to be shared among two tracks should the segment be equally compatible with both. A high efficiency for close-by muons (*i.e.* those sharing a common segment) is achieved by keeping all tracks that are identical in two of the three layers, provided they share no hits in the outermost layer.

The last step performs a global χ^2 fit to the hits associated with each track. Any hit that provides a large contribution to the χ^2 is removed from the track, and the track is refitted. Hits compatible with a

fit that are not initially included in a track can be considered through a hit recovery procedure. In the case that a hit is recovered and added to a track, the track is again refitted.

MS-ID track matching

Standalone tracks are extrapolated back to the interaction point and matched to ID tracks to form single, combined tracks which benefit from the complementary momentum sensitivities in the two tracking detectors; in general, the ID dominates in momentum resolution for $p_T \lesssim 30$ GeV and the MS in the region $p_T \gtrsim 200$ GeV. The compatibility of the MS-ID track match is determined on the basis of a χ^2 test. Lastly, a full MS+ID track fit is performed on the hits comprising the matched MS and ID tracks, resulting in the final CB muon trajectory.

Muon identification

Identification of prompt muons (*e.g.* those not produced by pion or heavy-flavour quark decays) is performed using a selection-based method, unlike electron identification which uses the LH method (see. Sec. 15).

Several variables, as determined from Monte Carlo studies, have been found that offer good discriminating power between prompt muons and those from hadron decays. The variables used for CB muon identification are the charge-to-momentum (q/p) *significance* ratio and ρ' ,

$$q/p \text{ significance} := \left| \frac{(q/p)_{\text{ID}} - (q/p)_{\text{MS}}}{\sqrt{\sigma(q/p)_{\text{ID}}^2 + \sigma(q/p)_{\text{MS}}^2}} \right| \quad (5.6)$$

$$\rho' := \left| \frac{p_T^{\text{ID}} - p_T^{\text{MS}}}{p_T^{\text{CB}}} \right|, \quad (5.7)$$

and the normalised χ^2 of the CB track. Similar to electron identification, working points are defined based on the values of these variables as evaluated on muons, as well as additional requirements on the number of and η regions in which muon hits are recorded.

Muon calibration

Unlike simulated electron energy resolution, simulation of the MS does not provide sufficient detail to adequately describe muon momentum resolution [134]. Therefore, muon correction factors are extracted from data and applied to simulated events to equalise their resolutions and efficiency.

To extract the calibration parameters, both p_T^{ID} and p_T^{MS} are used, and so only CB muons contribute to the procedure. The corrections are defined in η - ϕ regions that are homogeneous in terms of detector technology and performance. Both the ID and MS are divided into 18 η regions, with an additional two-fold division in ϕ for the MS. The ϕ division is to separate the two types of MS sectors: those that include magnet coils and those between two coils. The two sectors employ independent chamber alignment techniques, and cover detector regions with different material distribution. Therefore, each sector will have a different momentum scale and resolution.

The ID and MS correction factors are then extracted from dimuon invariant mass distributions in $J/\psi, Z \rightarrow \mu\mu$ data events, using a binned maximum-LH fit with templates derived from the same type of events produced in simulation. To obtain the corrected momentum of CB muons, $p_T^{\text{Cor,CB}}$, the corrected

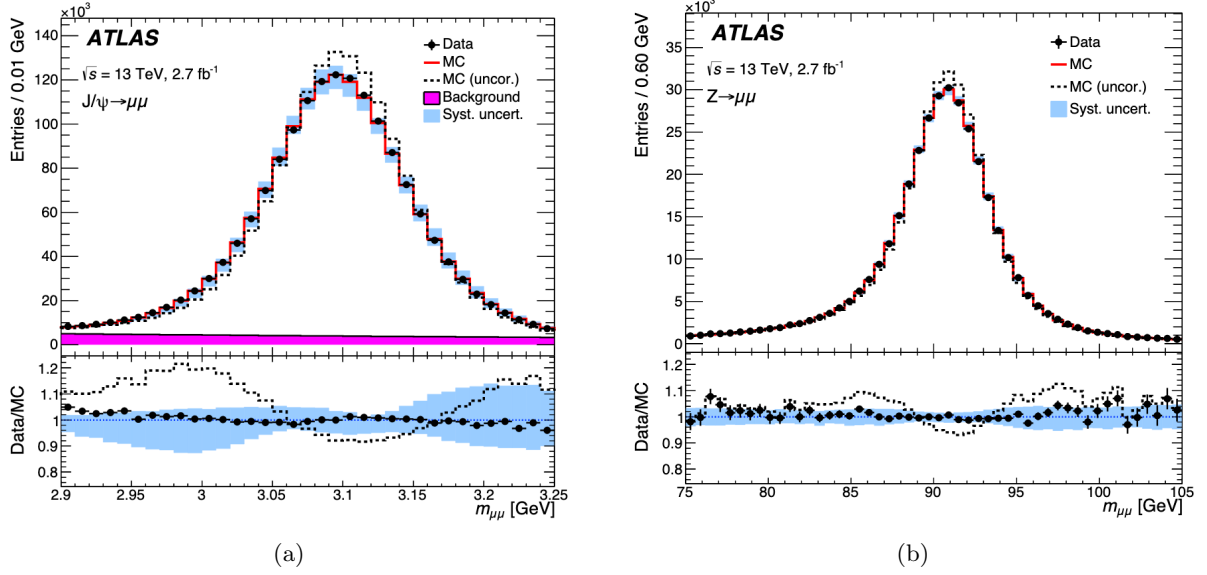


Figure 5.7: Dimuon invariant mass spectrum of (a) $J/\psi \rightarrow \mu\mu$ and (b) $Z \rightarrow \mu\mu$ candidate events reconstructed with CB muons [134]. The upper panel shows the invariant mass distributions as constructed from data and simulation, and the lower panel shows the data to MC ratios.

ID and MS momenta are combined using a weighted average,

$$p_T^{\text{Cor,CB}} = f \cdot p_T^{\text{Cor,ID}} + (1 - f) \cdot p_T^{\text{Cor,MS}}, \quad (5.8)$$

where f , the weighted average, is derived from

$$p_T^{\text{MC,CB}} = f \cdot p_T^{\text{MC,ID}} + (1 - f) \cdot p_T^{\text{MC,MS}} \quad (5.9)$$

which assumes the relative contribution from the ID and MS to the CB momentum measurement is unchanged before and after applying the corrections.

The overall effectiveness of the calibration procedure is demonstrated in Fig. 5.7, which compares the dimuon invariant mass distributions for $J/\psi \rightarrow \mu\mu$ and $Z \rightarrow \mu\mu$ candidate events in data to those in uncorrected and corrected MC events. It is clearly visible that the uncorrected MC tends to be narrower and shifted with respect to data, while after corrections the MC and data lineshapes mostly agree within systematic uncertainties. The small variations beyond the uncertainties at low dimuon invariant mass are due to imperfect energy loss corrections and the description of the magnetic field in muon reconstruction.

5.3.4 Jets

Jets are collimated sprays of colourless particles arising from the fragmentation and subsequent hadronisation of coloured partons (quarks or gluons); an overview of the hadronisation process are given in Sec. 2.3. Figure 5.8 shows an illustration of jet production and how they can be measured.

The dominance of jet production in LHC collisions results also in their being the dominant source of background in many physics analyses. Therefore, significant effort has gone into not only making use

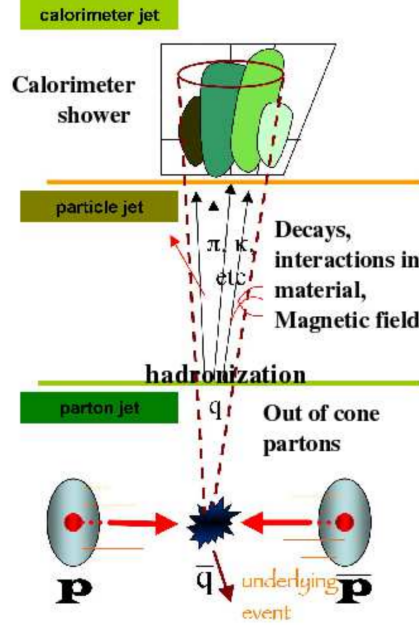


Figure 5.8: Illustration of jet production and how jets are measured [135].

of jets as a tools to understand the underlying physical processes through which they are produced, but also to suppress them in instances when their presence is contaminating.

As in the case of electrons, only jets produced within the acceptance of the ID are used in the analysis of this thesis, and so only the reconstruction of “central” jets is discussed in this section.

Jet algorithms and reconstruction

Jet algorithms are tools used for the classification of constituent particles (or calorimeter cells) into jets. While there is no unique definition for a jet that is independent of the algorithm that constructs it, several characteristics of jet algorithms are motivated [136, 137]:

- *Collinear stability*: the same set of jets in an event should be reconstructed if any constituent is replaced with two having the same momentum, direction and half of the original energy;
- *Infrared stability*: soft radiation between two distinct jets should not cause them to be merged; and
- *Tractability*: the same algorithm needs to be implemented in theoretical calculations and experiment without modification, and should be computationally inexpensive.

It is worth noting that while the most common constituents for jet reconstruction are the 4-2-0 topo-clusters, jet algorithms can also use tracking information – so-called “track jets” [138] – as well as combined information from the inner tracker and calorimeters – referred to as “particle flow” jets [123]. In this section, constituents refer only to the 4-2-0 topo-clusters.

The most commonly used jet algorithms are the sequential k_t , Cambridge/Aachen (C/A) and anti- k_t algorithms. While each is slightly different, they all combine four-momentum of constituents nearby in momentum space.

Each of the algorithms begin by first calculating distance parameters. For each constituent, i , a quantity d_{Bi} , representing the distance between constituent i and the beam axis, is defined according to:

$$d_{Bi} := p_{T_i}^{2p}, \quad (5.10)$$

where p_{T_i} is the momentum transverse to the direction of the beam line of the i 'th constituent. The parameter p governs the relative power of energy to that of geometrical term, $\Delta R^2_{(i,j)}$, discussed below; it is this parameter that distinguishes the k_t , C/A and anti- k_t algorithms.

Then, for every pair of constituents, (i, j) , a quantity $d_{(ij)}$ is defined according to:

$$d_{(i,j)} := \min(p_{T_i}^{2p}, p_{T_j}^{2p}) \times \frac{\Delta R^2_{(i,j)}}{D^2} \quad (5.11)$$

where $\Delta R^2_{(i,j)} = (y_i - y_j)^2 + (\phi_i - \phi_j)^2$ is the opening angle between the two constituents in y - ϕ space. The fundamental parameter of the algorithm, D , scales the $d_{(i,j)}$ with respect to the $d_{Bi,j}$ such that any pair of the final jets, (j_k, j_l) , are separated by at least $\Delta R^2_{(k,l)} = D^2$.

Both d_{Bi} and $d_{(i,j)}$ quantities assume the origin of the hard-scatter vertex (*i.e.* the *primary vertex*, PV) is the center of the detector and therefore their angular coordinates, (y, ϕ) , are defined from the PV to the barycentre of the cluster. Before jet building, the direction of each topo-cluster is adjusted to instead point back to the hard-scatter primary vertex instead, a procedure called *origin correction*⁶.

This correction applies only to cluster momentum, therefore cluster energy remains unchanged.

After the origin correction, the algorithms generally proceed as follows.

The $d_{(i,j)}$ and d_{Bi} distance quantities are computed first from all clusters, and the smallest of these is determined. If the smallest distance parameter is a $d_{(i,j)}$, the four-momenta of the two constituents are summed to form a *proto-jet*, and the constituents are removed from further consideration. The quantities $d_{(i,j)}$ and d_{Bi} are recalculated using the remaining constituents and proto-jets, and the process repeats. Alternatively, if the smallest of quantities is a d_{Bi} , then cluster or proto-jet corresponding to this quantity is considered a jet and is removed completely from the successive iterations of the algorithm, and the next smallest distance parameter is determined. The algorithm continues until all clusters and proto-jets have been classified as jets whose momentum is referred to being at the *constituent scale*.

Jets constructed from this algorithm are theoretically favoured as they do well in including all the p_T from the original partons; that is, the sequential algorithms provide a good mapping between jets and partons.

As mentioned earlier, the three jet algorithms differ only by the value of their parameter p . These values result in distinct properties of jets produced by the algorithms, each with their own features and biases.

- k_t ($p = 1$): Experimentally k_t jets pose challenges as they do not have well-defined areas, and may include constituents that are widely separated in y - ϕ .
- C/A ($p = 0$): Interestingly, these jets have no dependence whatsoever on the p_T of their constituents. Constituents are combined based solely on their proximity to one another, thereby reducing the number of jets containing many soft constituents that are not representative of a hard-scatter parton.

⁶ During Run-1, the origin correction was applied during jet calibration. As of Run-2, it was applied at the cluster-level.

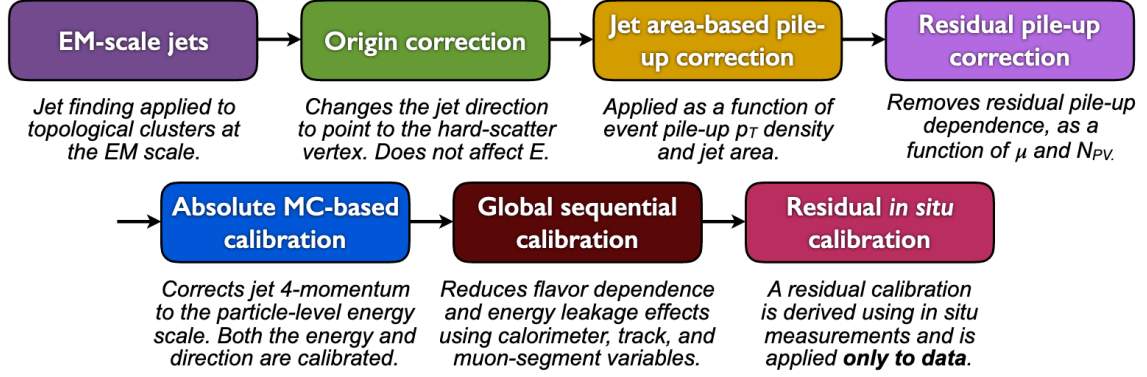


Figure 5.9: Reconstruction and calibration stages for EM-scale jets [139]. Each stage beyond the origin correction is applied to jet four-momentum.

- anti- k_t ($p = -1$): This algorithm maintains infra-red and collinear safety, but constructs jets that tend to be very conical. Typically only high- p_T constituents are combined, and grouping of many low-energy constituents is generally avoided.

In ATLAS, the jets are most often constructed by the anti- k_t algorithm with distance parameter $R = 0.4$. Such “small-radius” (small- R) jets are used exclusively in the analysis presented in Sec. 6.

Once jets are built, they are subject to a *jet energy scale* calibration procedure that takes into account two primary effects: pile-up and invisible energy resulting from hadronic interactions. A final set of *in situ* calibrations are performed last to account for differences that remain between data and MC simulations.

Pile-up subtraction

Electromagnetic topo-clusters are used as inputs to the anti- k_t algorithm (presented above) with radius parameter $R = 0.4$ to reconstruct small- R jets (herein referred to as “EMTopo04” jets). *Truth jets* are obtained from simulated samples of dijet, and Z bosons and photons in association with jets (*i.e.* Z/γ +jets). The EMTopo04 jets are then calibrated such that their energy scale is matched (or “restored”) to those of the simulated truth jets which are reconstructed at the truth-level scale. This process is called the *jet energy scale* (JES) calibration. JES calibration consists of a number of steps, an overview of which is presented in Fig. 5.9.

Topo-clusters used in jet reconstruction are sensitive to overlapping energy deposits from particles which are not part of a given jet. If these additional energy deposits, arising primarily from in-time and out-of-time pile-up, are not accounted for, results in mismeasurements of jet kinematics. To mitigate these undesirable effects, contributions from pile-up are estimated on an event-by-event and jet-by-jet basis. There are two variables used for *pile-up correction*:

- *Jet active area*, A : A large number of simulated *ghost particles* of infinitesimal momentum are added uniformly in solid angle to each event. The active area of each jet is then estimated by the number of associated ghost particles, resulting in an area of $A \simeq \pi R$ for anti- k_t jets [139].
- *Pile-up p_T density*, ρ : Estimated on an event-by-event basis, it is the the median of the ratio between each jet’s p_T and its active area A , corresponding to the average amount of transverse

momentum added to each jet per unit jet-area. The density ρ is calculated using jets reconstructed with the k_t algorithm – due to its tendency to include soft backgrounds (characteristic of pile-up) – that must be within $|\eta| < 2.0$ so that only calorimeter regions with sufficient granularity are considered.

A first pile-up correction, *jet area subtraction*, is performed by taking the difference between each original jet p_T and its corresponding value of ρA . However, since ρ is derived from only central parts of the calorimeter that have lower occupancy, it does not describe well the sensitivity of higher-occupancy cores of high- p_T jets. In particular, these high- p_T jets have a residual dependence on the number of primary vertices, N_{PV} , and the average number of interactions per bunch crossing, $\langle\mu\rangle$. Therefore, a *residual pile-up correction*, parameterised by N_{PV} and $\langle\mu\rangle$ plus two additional parameters, α and β , which depend on jet η and jet algorithm, is applied to the area-subtracted p_T .

The final jet p_T , after both area-based and residual corrections, is given by [139]

$$p_T^{\text{corr}} = p_T^{\text{reco}} - \rho \times A - \alpha(N_{PV} - 1) - \beta \times \mu, \quad (5.12)$$

where p_T^{reco} refers to the momentum of the reconstructed jet at the EM scale before corrections.

Jet energy scale and η calibration

Following the application of pile-up corrections, reconstructed jet four-momentum is corrected to the truth-level jet energy scale. This *absolute* JES calibration is derived from simulated dijet samples; the reconstructed jets and truth-level jets are geometrically matched, and are required to fulfill isolation requirements [139] in order to avoid ambiguities in matching. The average energy response between reconstructed jets and truth-level jets, defined as $E^{\text{reco}}/E^{\text{truth}}$, are compared to derive a correction in E^{reco} from E^{truth} . The average energy response is parameterised as a function of E^{reco} and the jet calibration factor is taken as the inverse of the average energy response.

Jet η reconstruction biases can be caused by transitions between different calorimeter geometries (*e.g.* abrupt changes in granularity) or technology. Such biases can artificially alter reconstructed jet energy between transitions, resulting in mismeasured jet four-momentum. The *η calibration* uses the difference between η^{reco} and η^{truth} , and a correction in E^{reco} from E^{truth} is derived. This calibration only alters jet p_T and η , not the full jet four-momentum.

After both JES and η calibrations are applied, a jet is considered to be calibrated at the “EM+JES” scale.

Global Sequential Calibration

Calorimeter response and therefore jet reconstruction are both sensitive to jet composition and the distribution of energy in a jet. For example, quark-initiated jets typically include hadrons with a large fraction of the overall jet p_T that penetrate deep into the calorimeters, whereas gluon-initiated jets usually comprise many softer constituents that result in lower calorimeter response and wider transverse profile. The *global sequential calibration* (GSC), a multivariate extension to the EM+JES technique, was designed to reduce the dependence of calorimeter response on the type of jet-initiating parton. In practice, any variable x can be used in the GSC, however it is wise to choose those that characterise the longitudinal and lateral profiles.

For each variable, a multiplicative correction factor to the jet energy measurement can be derived by inverting the calibrated jet response as a function of this variable [140]. After a correction is applied, the dependence of the response on the variable corresponding to the correction is removed without affecting the average energy, thereby reducing the spread of jet energy and resulting in improved resolution. This process is sequential in the sense that the correction, C^i , for a given variable, x_i , is applied to jets which have been previously corrected by C^{i-1} for a variable x_{i-1} . That is, the jet p_T after correction x_i is given by:

$$p_T^i = C^i(x_i) p_T^{i-1} = C^i(x_i) C^{i-1}(x_{i-1}) p_T^{i-2} = \dots \quad (5.13)$$

***In situ* calibration**

The last step in jet calibration accounts for differences in jet response between data and simulated samples, the so-called *in situ calibration* methods. Such differences include imperfect detector response and material effects in MC simulation, and inaccuracies in simulating hard-scatter, pile-up and EM and hadronic interactions in the detector, and are quantified by balancing jet p_T against other well-measured reference objects.

The response for each *in situ* calibration is defined in data and MC, and is given by the ratio of reconstructed jet p_T to a reference object p_T ,

$$\frac{\langle p_T^{\text{jet}} / p_T^{\text{ref}} \rangle_{\text{data}}}{\langle p_T^{\text{jet}} / p_T^{\text{ref}} \rangle_{\text{MC}}} \quad (5.14)$$

There are four such methods:

- *η -intercalibration*: Corrects the average response of “forward” jets ($0.8 < |\eta| < 4.5$) to that of well-measured central jets ($|\eta| < 0.8$) using dijet events. The two jets considered are expected to be balanced in p_T , and any imbalance can be attributed to the differing responses in the different calorimeter regions from which the jets are reconstructed.
- *Z +jets and γ +jets balance*: Corrects for differences in the average response of central jets by balancing jet p_T with other well-measured reference objects, *i.e.* charged leptons (e or μ) from a Z boson decay or the energy from a photon. This calibration applies to jets with E up to 950 GeV.
- *multijet balance*: The last stage of the *in situ* calibrations used to extend calibrations of jets with p_T up to 2 TeV. This calibration balances a high- p_T jet against a recoil system comprising three or more jets with p_T sufficiently low so as to be in the range of the already-calibrated Z/γ +jets above.
- *in situ combination*: Data-to-MC ratios derived from the Z/γ +jets and multijet calibrations defined above are combined across overlapping regions in jet p_T to provide pseudo-continuous corrections. The inverse of the combined data-to-MC ratio is taken as the *in situ* correction that is applied to data.

Overall, the combined set of *in situ* corrections provide a consistent calibration at a level of about 4% at 20 GeV to 2% at 2 TeV.

To each of these energy scale calibration methods is an associated uncertainty, discussed in Sec. 6.11, that is included in the limit-setting procedure of Sec. 6.12.

Chapter 6

The dijet+lepton analysis

*Would you run from the struggle?
Or would you stand and fight for what is right to you?*
- Daimachus, *Rise to Power*

The SM of particle physics is by no means complete, and many proposed extensions to the theory exist (*i.e.* BSM theories) that attempt to address its shortcomings (see Sec. 2.2). A single BSM model can predict multiple new particles and final-state topologies. Given the large number of these models, experimentalists searching for new physics need to devise novel experimental techniques to fully cover the enormous parameter space of masses, cross sections, and decay channels of possible new particles if they hope to observe rare processes; signals of new physics may be hidden in unexplored kinematic regimes and final states.

In this chapter, a generic search for new physics is presented. A new particle X of an unknown mass decaying to two partons that hadronise to form jets can appear as a resonance (or “bump”) in an otherwise smoothly-falling dijet invariant mass distribution, m_{jj} . The aim is to remain as model-agnostic as possible, therefore events entering the analysis are subjected to only a limited set of selection criteria so as to not bias the results towards any one model.

Such a programme is not expected to match the sensitivity of a dedicated search targeting a specific model, however it is capable of probing a wide range of possible BSM models. Moreover, in the event that a deviation between data and SM predictions is observed, the analysis can then lend itself to a dedicated follow-up analysis where model-specific selection criteria can be imposed.

6.1 Introduction

Searches for heavy resonances in dijet invariant mass distributions began over 30 years ago, starting in 1988 during the era of the CERN Super Proton-Antiproton Synchrotron (SPS) [141]. The SPS was a proton (p) antiproton (\bar{p}) collider that operated at a centre-of-mass energy of $\sqrt{s} = 0.63$ TeV. In 1988, the Underground Area 1 (UA1) experiment [142] published the first dijet search paper [143] using SPS collision data, with hopes to discover a new particle beyond those predicted by the SM. Data collected by the UA2 detector [144] were used to publish search results in 1993 [145], several years following the end of data-taking. Two-jet decays of the SM W and Z bosons were observed in 1991 [146], but no hints

of BSM resonances were seen¹.

At around the same time in North America, Fermilab’s Tevatron [148, 149] was colliding protons and antiprotons at $\sqrt{s} = 1.8$ TeV and eventually at $\sqrt{s} = 1.96$ TeV. The Collider Detector at Fermilab (CDF) [150, 151] began looking for new physics in the late 1990s [152, 153] by analysing the Tevatron data. About half a decade later, the D0 experiment [154, 155] also contributed to such searches [156] at the Tevatron. In 1995, both the D0 and CDF experiments published results announcing the discovery of the top quark [157–159]. However, despite collecting nearly 100 times more data at over twice the centre-of-mass energy than delivered to the UA experiments, only results consistent with the SM were reported by the Tevatron collaborations [160].

More recently, inclusive searches for strongly-produced heavy resonances in dijet invariant mass distributions have been conducted by ATLAS [161, 162] and CMS [163, 164] at $\sqrt{s} = 13$ TeV that have excluded $1.0 \leq m_X \leq 6.5$ TeV resonances hypothesised in a variety of BSM models. As a result of the new kinematic regime that opened up during Run-2 of the LHC, these studies initially focused on searches at large invariant mass. However, as the integrated luminosity of the dataset increased, and in the absence of any enhancement at high mass, there is a renewed interest in searching in the “bulk” – where statistics are largest – of the dijet invariant mass distribution for possible low-mass enhancements. Low-mass regions are difficult to access in traditional inclusive dijet resonance searches as they typically rely on jets for triggering on events; in ATLAS, the minimum jet trigger threshold of $p_T \approx 400$ GeV is imposed to keep rates at a manageable level for the TDAQ system.

A number of methods have been employed by both ATLAS and CMS to overcome the high- p_T thresholds used in inclusive searches in order to extend searches to lower dijet invariant masses, *e.g.* using trigger-level information [165] and data-scouting [166]. Other techniques involve requiring the presence of an associated object whose p_T trigger threshold is lower than that of jets, such as a photon produced via initial state radiation (ISR) [167] (colloquially, “dijet+ISR”).

The analysis presented here (colloquially referred to as the “dijet+lepton” analysis) complements the dijet+ISR analysis by requiring, in lieu of a photon, an isolated light charged lepton (e or μ)². In contrast to jet triggers, lepton trigger thresholds can be as low as $p_T = 26$ GeV without prescaling. Therefore, exploiting a triggered lepton can provide a handle on low-mass dijet systems without compromising the event rate. Furthermore, the final-state lepton also provides access to processes involving top quarks, and W and Z bosons which inclusive searches are not sensitive to, meaning a wide range of exotic models can in principle be targeted by this analysis.

Many BSM models [168–171] predict new heavy resonances in production modes yielding a final state consisting of at least two jets accompanied by a lepton. At hadron colliders, possible processes include t -channel $q\bar{q}' \rightarrow VX$ and s -channel $q\bar{q}' \rightarrow X' \rightarrow VX$, where $V = W(\rightarrow \ell\nu), Z(\rightarrow \ell\ell)$, and the X, X' can be either scalar or vector particles; the representative Feynman diagrams for these two processes are shown in Fig. 6.1.

Searches for signatures of specific models may benefit from model-specific requirements in event selection: a missing transverse energy (E_T^{miss}) threshold (in the case of leptonic decays of W bosons or top quarks), additional leptons (in the case of associated Z boson production), quark-flavour tagging (*e.g.* of bottom quarks), high jet multiplicities, *etc.* However, the aim of the analysis presented in this thesis is to remain as generic, or model-agnostic, as possible, so such selections are not applied here.

¹ The UA collaborations discovered the W and Z bosons in leptonic decay channels [147] within a three-month span in 1983.

² The CMS experiment currently has no analog to the dijet+lepton final state as presented in this thesis.

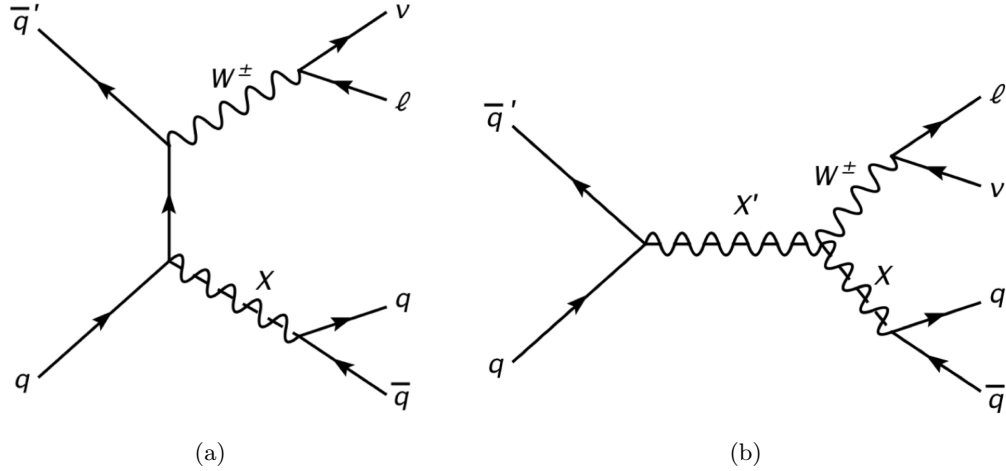


Figure 6.1: Representative Feynman diagrams for a generic resonance X decaying to two partons in association with a leptonically decaying W boson in the (a) t -channel and (b) s -channel. The latter channel includes an additional resonance X' decaying to a W and a X .

The analysis presented in this chapter is based on Ref. [172]. The search for BSM resonances is performed in the dijet invariant mass distribution constructed from dijet events with at least one e or μ , plus additional *performance-based* kinematic and isolation requirements (*i.e.* selection criteria that give high efficiency while promoting genuine, well-reconstructed final-state objects) on the objects of interest. The data are also used to set limits on the production cross sections of Gaussian approximations of signal shapes with different widths and masses; such generic shapes can be used to exclude any BSM model whose shapes are compatible with a Gaussian distribution. To demonstrate the physics reach of this analysis, the data are interpreted in terms of the BSM models discussed earlier in Chap. 2.2 – a technicolor model and a simplified Dark Matter model – and limits are set on their production cross sections, again, without any additional selection criteria imposed. These, in turn, are used to set mass limits on the new particles hypothesised in their respective models.

This chapter is organised as follows. First, the analysis strategy is presented in Sec. 6.2. It gives an overview of decisions – *e.g.* motivations for object definitions and kinematics, how the SM background is to be estimated, *etc.* – that are made prior to observing data (so-called “blinded” analysis step). The dominant Standard Model backgrounds are presented in Sec. 6.3, and the description of Monte Carlo (MC) modelling, and signal and background samples used in the analysis are presented in Sec. 6.4. Section 6.5 details the event preselection – triggers, event quality and cleaning, and object definitions – and Sec. 6.6 defines the signal and control regions. The kinematic distributions for the signal and control regions are presented in Sec. 6.7. In Sec. 6.8, fit hypothesis studies are performed in the control region to determine the suitability for use in the signal region. Additional studies are performed on the fit hypotheses to evaluate signal extraction efficiencies and robustness against statistical fluctuations in Sec. 6.9. The signal region data are finally analysed in the search phase, presented in Sec. 6.10. Section 6.11 provides a discussion of the systematic uncertainties impacting the analysis, and Sec. 6.12 concludes this chapter, presenting cross section limits on generic resonance shapes and selected BSM models set based on the results of the search.

6.2 Analysis strategy

The triggers, object definitions, and event selection used in this analysis are motivated by previous, well-established analyses. For electron and muon selections, this analysis follows closely the ATLAS WW cross section paper [173], which requires high-quality leptons in the final state so as to reduce the contamination from mis-reconstructed objects. Jet selections and the procedure used to describe the dijet invariant mass distribution are guided by previous dijet searches [174, 175]. When setting limits based on the results of the model-agnostic search, Gaussian approximations of signal shapes of various masses and decay widths are used. Systematic uncertainties related to jet reconstruction are incorporated through parameterisations of the respective uncertainties from simulated signal samples.

The outline of the analysis strategy is as follows:

1. Devise a set of a performance-based selections – a compromise between high object purity and efficiency – for candidate objects (*i.e.* jets, electrons and muons).
2. Define a control region (CR) that can be used to:
 - (a) study possible issues or problems in jet reconstruction; and
 - (b) guide the choice of the background estimation method, *e.g.* determine an acceptable range for the m_{jj} spectrum to probe to ensure a smoothly-falling distribution that can be modelled by a known and well-established fit method.
3. Perform initial studies in the CR to determine the background estimation method. Two such methods are considered:
 - (a) a *global fit* method using the family of functions used previously in numerous previous dijet analyses, *e.g.* [146, 161, 176–181], are of the form:

$$f(x|\theta) = \theta_0(1-x)^{\theta_1}x^{\theta_2+\theta_3\ln x+\theta_4\ln^2 x} \quad (6.1)$$

where $x \equiv m_{jj}/\sqrt{s}$, and the θ_i are the fit parameters to be estimated; and

- (b) a *sliding window fit* method, detailed in Sec. 6.8.

A number of statistical tests (described below) are used to gauge the performance of a given method to describe the m_{jj} distribution in the CR. If the results of both methods are statistically compatible, they are then subjected to additional tests to measure their sensitivity to injected signals and statistical fluctuations that could mimic a signal (so-called “robustness tests”). The fit method that performs best on the robustness tests is selected as the nominal fit method. On the other hand, if neither method can adequately describe the CR, the minimum bound on the m_{jj} distribution is increased and this step is repeated. Should both fit methods perform equally well for all criteria, the simplest approach is taken (in this case, the global fit method).

4. Apply the nominal fit method to the m_{jj} distribution of the signal region (SR), and perform the search for the most discrepant region. The p -value (and corresponding z -value) of this region is calculated to measure the level of discrepancy.
5. Set limits on the presence of a generic signal with a shape approximated by Gaussian distribution, and include all systematic uncertainties in the limit-setting procedure.

6. Following the same procedure as in the previous bullet, set limits on production cross sections of two relevant BSM models whose shapes are predicted from MC.

6.2.1 Background estimate performance metrics

A number of metrics are used to evaluate the ability of a given background estimate to describe the observed data. The considered tests characterise the full m_{jj} spectrum with a single numeric value indicating the level of agreement between observation and prediction.

Pearson's χ^2 test

The χ^2 test is applied to evaluate the probability that a set of observed values arose from sampling, at random, the *null hypothesis*³. This test statistic is defined as

$$\chi^2 = \sum_i^N \frac{(d_i - b_i)^2}{b_i}, \quad (6.2)$$

where the d_i and b_i are the data (observed) and background estimate (predicted), respectively, in bin i of their individual histograms, each with N bins. If each fraction in the sum is close to unity, the chosen background estimate can be understood to model the data well. In such a case, the χ^2 statistic should be of order N . This motivates the use of the *reduced* χ^2 , $\frac{\chi^2}{\text{ndf}}$, where $\text{ndf} = N - n - 1$ with n being the number of fit parameters in a given model. The reduced χ^2 therefore has the advantage of making direct comparisons between fit models with different numbers of parameters, as well as different binnings of data.

Equation 6.2 is derived under the assumption that the measured data are normally distributed around the predicted value, and is therefore only a reasonable assumption for bins with event-counts $d_i \gtrsim 20$, *i.e.* when the Poisson distribution approaches a Gaussian. This makes the χ^2 an unreliable statistic in the high-mass tail of the m_{jj} distribution, but valid elsewhere. For large b_i , when the measurements are approximately distributed according to a Gaussian function, the χ^2 test statistic follows a χ^2 distribution for $k = \text{ndf}$ degrees of freedom:

$$f_{\chi^2} \equiv f(\chi^2, k) = \frac{1}{2^{k/2}\Gamma(k/2)} (\chi^2)^{k/2-1} \exp(-\chi^2/2), \quad (6.3)$$

where

$$\Gamma(x) = \int_0^\infty dt \exp(-t) t^{x-1}. \quad (6.4)$$

The probability that, under the null hypothesis, a set of M measurements would yield a χ^2 value greater than or equal to the one obtained is given by:

$$p(\chi^2, M) = \int_{\chi^2}^\infty dz f_{\chi^2}(z, M); \quad (6.5)$$

this probability is referred to as the “ p -value”. A small p -value is indicative of poor agreement between the data and null hypothesis (or poor estimate of the background).

³ In the current context, the null hypothesis is the estimate of the SM background.

Fit residuals

When the Poisson distribution is approximated well by a Gaussian distribution with mean, μ , and variance, σ^2 , equal to b_i (see Eqn. 6.2), the *significance level* (or *z-value*, *i.e.* the deviation from the right of the mean of a Gaussian) can be approximated, in each bin i , by the *residual* [182],

$$s_i = \frac{d_i - b_i}{\Delta b_i}, \quad (6.6)$$

where d_i is the observed event-count, b_i is the value of the fit function after minimising its parameters, and Δb_i is the uncertainty in bin i . In the case of counting experiments, $\Delta b_i = \sqrt{b_i}$; for simplicity, the full set of uncertainties included in the limit-setting procedure are disregarded at this stage.

While a reduced χ^2 of approximately unity is a necessary condition for a good-quality fit, it is not sufficient. A well-behaved regression analysis requires that residuals are normally distributed. Moreover, the RMS of s_i in Eqn. 6.6 should be nearly unity. To evaluate the normality of the residuals, they are first fitted with a Gaussian distribution. It is then determined if the mean and standard deviation of the fit are compatible, within statistical uncertainties, with a theoretical normal distribution. The compatibility of the fit is further evaluated using the Kolmogorov-Smirnov (KS) [183] and Shapirio-Wilk [184] tests.

Kolmogorov-Smirnov normality test

The KS test compares a known theoretical *cumulative distribution function* (in this case, that of the normal distribution), $F_0(x)$, to the *empirical distribution function* (EDF, the distribution of residuals), $F_N(x)$. The EDF for N measurements of an observable can be written as

$$F_N(x) = N^{-1} \sum_{i=1}^N s(x_i), \quad (6.7)$$

where

$$s(x_i) = \begin{cases} 0, & x < x_i \\ 1, & x \geq x_i. \end{cases} \quad (6.8)$$

The test statistic, taken here to be the absolute value of the largest distance between $F_N(x)$ and the cumulative distribution of $F_0(x)$ as measured in a vertical direction, is given by,

$$D_N = \sup_x |F_N(x) - F_0(x)|, \text{ for all } x. \quad (6.9)$$

where \sup_x is the supremum of the set of distances. This statistic is compared to a *critical value*, $D_{N,\alpha}$, that is usually calculated using numerical methods. In this test, a *significance* (or α) *level* of $\alpha = 0.05$ is used in order to reduce the probability of a Type-I error [185]. For all intents and purposes, the critical value used in this analysis is $D_{N>35,\alpha=0.05} = 1.358/\sqrt{N}$ [183]. For $D_N < D_{N,\alpha}$, it can therefore be concluded that the distribution of residuals is in good agreement with a standard normal. In terms of a *p-value* (see Sec. 6.11), a KS probability greater than 0.05 is indicative of compatibility with normality.

Shapiro-Wilk test

A main drawback of the KS test is that it is not overly reliable when parameters are estimated from data [186]. Therefore, a second test for normality comes from Shapiro and Wilk that provides better power over the KS test [187], and thereby reduces the probability of a Type-II error [185]. The statistic is defined as

$$W = \frac{\left(\sum_{i=1}^N a_i x_{(i)}\right)^2}{\sum_{i=1}^N (x_i - \bar{x})^2} \quad (6.10)$$

where $x_{(i)}$ is the i th *order statistic* (*i.e.* the i th smallest value in the sample), and \bar{x} is the sample mean, and the a_i are constants determined from the means, variances, and covariances of the order statistics [188]. Small values of W can be understood as evidence of a departure from normality.

6.3 Standard Model backgrounds

A set of MC-generated samples are used to provide a rough estimate of the dominant SM backgrounds to this analysis, and to give an understanding of the relative contribution of each to the total background. Modelling of the main backgrounds in MC is described in Sec. 6.4, and the details on background suppression are given in Sec. 6.5.

6.3.1 Multijet background

The dominant source of SM background to this analysis is QCD multijet (≥ 2 jets) events. Multijet events can enter the analysis when a jet is misidentified as a lepton (*i.e.* *fake* lepton), or when a lepton is produced in semileptonic decays of heavy-flavour quarks (*i.e.* *non-prompt* lepton). Multijet contributions account for more than 90% of the total background, and therefore drives the choice of fit function.

Modelling of multijet backgrounds is typically performed using data-driven techniques, since MC does not adequately model fake leptons; it is possible the simulation code does not faithfully reproduce the real behaviour of the objects under study, and limited statistics usually result in unreliable estimates of *fake rates* with a sufficiently low uncertainty that can prove to be problematic. Common techniques used in ATLAS for estimating fake rates are the so-called “fake-factor method” [189] and “matrix method” [190]. However, both methods rely not only on having CR that are *orthogonal* to the signal region, but also that the number of fake leptons in each CR is approximately the same number of fakes as the signal region. In this analysis, there are no such CR meeting these criteria. To suppress contamination from fake leptons, the simplest approach is taken: apply stringent selection criteria to object quality, identification, and isolation to ensure genuine, prompt objects.

6.3.2 Top quark background

The second largest source of SM background is top quark pair production. Top quarks predominantly decay to a W boson and a b quark. Relevant to this analysis are $t\bar{t}$ decays where at least one W boson from the top quarks decays leptonically, $W \rightarrow \ell \nu_\ell$, leading to a dijet-plus-lepton final state. Top quark processes constitute roughly 1–10% of the total background.

To reduce $t\bar{t}$ background, a b -jet veto is often used. In the interest of maintaining generality, removing events with b -jets is not wise since many BSM models – including those considered in this analysis – predict heavy resonances that can decay to one or two b quarks. Leptons originating from b quark decays are however suppressed by exploiting the relatively long lifetime of b mesons by imposing requirements on lepton impact parameters to ensure they are prompt, and are not produced at secondary vertices.

6.3.3 W + jets background

The last, and least dominant background considered comes from W +jets events. As in the case of $t\bar{t}$, the W boson in these events decays leptonically and is accompanied by two or more jets. Like top quark processes, the W backgrounds make up between 1–10% of the total background.

In some cases, the W +jet background can be reduced by applying an upper bound on E_T^{miss} . However, like b quarks, the BSM models considered in this analysis can have a significant amount E_T^{miss} , and so imposing such a requirement could greatly reduce sensitivity to these models. Furthermore, W bosons themselves can be produced in association with BSM particles. As such, the W +jets background is an *irreducible* background; that is, its signature is too similar to that of the expected signals that it cannot be completely reduced given the limited selection criteria imposed.

6.4 Monte Carlo simulations and physics modelling

ATLAS relies heavily on MC to study the detector response and model a wide range of physics processes. There are four main components to the ATLAS MC simulation chain: event generation, detector simulation, digitisation, and reconstruction. Athena provides a harmonised reconstruction infrastructure that is used for both simulated and recorded data; for details on object reconstruction relevant to this analysis, see Sec. 5.3.

ATLAS divides MC production into *campaigns* which represent a specific period of data taking. For example, the full Run-2 set of simulated data is contained in the MC16 campaign. Because of the large amount of time required to produce sufficient MC for physics analyses, MC production for a given year of data taking is done in advance of actual data taking. As a result, some assumptions must be made about the LHC performance and detector conditions. To account for different pile-up profiles (see Fig. 5.2) anticipated through the years of running, campaigns are further divided into *subcampaigns*; 2015–2016 data and conditions are represented by MC16a, 2017 by MC16d, and 2018 by MC16e. The numbers of events for each subcampaign are representative of the expected integrated luminosity for a given data-taking year. In the event that conditions change drastically from expectation, only a subcampaign therefore needs to be reproduced, not an entire campaign.

The large ATLAS datasets are stored in Analysis Object Data (AOD) files. These AODs are typically \sim TB in size, and so their use in distributed data analysis is, in most cases, impractical, *e.g.* when many many copies are required for analysers across the globe. Analysis Object Data files are therefore subject to methods referred to as “skimming” and “slimming”; skimming operates at the event level by removing events that *e.g.* do not pass a specific trigger or set of triggers, and slimming operates at the object-level, removing those objects that are not needed for specific analyses (*e.g.* large-radius jets in resolved final states). The output of these procedures is then stored in what are called derived AOD (DAOD) files that are named based on the physics group using them. This analysis uses the STDM4 derivation [191];

events selected by single-lepton triggers are only retained if they contain at least one muon (electron) with $p_T \geq 15$ (20) GeV that passes loose quality requirements and is within $|\eta| < 2.6$.

6.4.1 Event generation

In high-energy pp simulations, a number of processes take place. The first step is event generation. These software generally require as input an initial state (*e.g.* two protons), a collision energy (*e.g.* centre-of-mass energy), and a PDF set. Renormalisation and factorisation scales, μ_R and μ_F , respectively, are often also required, where μ_R is the energy scale at which the generator calculates the strong coupling constant, α_S , and μ_F determines the scale at which the generator samples the PDF set [192].

Parton distribution functions provide a parameterisation of proton structure given by functions of the form, $f(x, Q^2)$ – the probability density to have a particular parton carrying a certain fraction x of its proton’s total momentum at a squared momentum transfer Q^2 . Independent groups produce PDFs experimentally through fixed-target deep-inelastic scattering and collision data; the inherent non-perturbative nature of partons prohibit theoretical calculations of parton densities.

Event generation comprises five distinct parts⁴:

1. *Hard process*: The “interesting” part of the collision wherein the largest momentum transfer between two partons occurs.
2. *Parton shower*: Incoming and outgoing coloured particles radiate gluons which themselves trigger further radiation. This parton shower evolution continues to lower momentum scales until perturbation theory no longer applies and hadronisation models take over.
3. *Hadronisation*: Following the break-down of perturbation theory, hadronisation models are used to describe hadronic states which may or may not be “seen” in the detector.
4. *Underlying event*: In addition to the hard-scatter, additional parton-parton interactions take place, with high probability, that overlie and contaminate the hard-scatter process.
5. *Unstable particle decays*: The decay of heavy, long-lived unstable hadrons.

Event generators are categorised into several classes: *general-purpose*, *matrix-element*, and *specialised*. General-purpose generators are able to fully model high-energy collisions (steps 1-5 above). Matrix element (ME) generators, on the other hand, calculate only the hard-scatter process, and therefore require interfacing to additional software for parton showering and subsequent hadronisation. However, ME generators typically provide more accurate, higher-order calculations, *e.g.* next-to-leading order (NLO) or higher, compared to general-purpose generators. Specialised generators aim to provide a more complete description of specific physics processes, *e.g.* b -jet physics or radiative corrections, over the general-purpose generators. Like ME generators, those of the specialised class require interfacing with a “host” MC generator.

More than thirty event generators are included in Athena [133] to best model the wide range of LHC collision physics [193].

Parton shower and underlying event modelling are quite sensitive even to small changes to event generator input parameters, or filters, *e.g.* a lower threshold on scattered parton p_T . Such parameters can be *tuned* in order to improve agreement between MC and data. Specialised tunes for the MC

⁴ See Sec. 2.3 for further details on these processes.

generators integrated into Athena are determined by various focus groups within ATLAS to improve modelling of a range of data observables [194], as well as for minimum bias events and the underlying event [195]. Authors of MC generators also provide a set of tunes for their software that are derived from various collider data [196–199].

The output of event generation is a collection of final-state particles and their respective four-vectors. This so-called *truth information* is subsequently passed to the next step in the chain: detector simulation.

6.4.2 Simulating the ATLAS detector

The ATLAS simulation framework employs Geant4 [200] as the backbone for transporting simulated-particle four-vectors through the detector. Geant4 provides precise modelling of particle-material interactions through its many physics models – *e.g.* Compton and multiple scattering, bremsstrahlung, ionisation, nuclear interactions, *etc.* – that, in turn, permits precise modelling of the detector and its response to particles with sufficiently long lifetimes (*i.e.* those that reach the detector before decaying).

The geometric detector description of ATLAS is highly-detailed, containing over 7 million distinct volumes comprising about 400 different materials. Particles are transported through the detector and their interactions with the detector material are, in most cases, calculated at every volume boundary. This is a very time-consuming task, and such a level of detail is used primarily for precision physics. Furthermore, because ATLAS computing resources are limited, it is not practical to produce sufficient fully-simulated MC statistics required to match that of data.

The dominant CPU consumer in ATLAS simulations is the calorimeter – where complicated showering occurs and particles are stopped, followed by the production of secondary particle showers – which makes up more than 90% of the total simulation time. To help overcome the statistics barrier, ATLAS has developed fast simulation methods that reduce processing times by about 1-2 orders of magnitude (depending on the process), however at the cost of degradation in precision and accuracy.

The ATLFAST-II (AFII) fast simulation engine [201] achieves fast event-processing in the calorimeters through two principal techniques:

- *Simplified geometry:* Instead of a geometric detector description represented by complex Geant4 volumes, cuboids and cylinders are used as approximations. The detailed material volumes are projected onto infinitely thin 2-dimensional surfaces, and particle-material interactions on these surfaces are determined by applying an effective thickness, measured in radiation/interaction lengths.
- *Parametric detector response:* A large number of Geant4-simulated samples of electrons, photons and charged pions are used as templates to determine energy- and η -dependent parameterisations of shower properties. The parameterisations are then fitted to independent Geant4 events, from which the best fit parameters are extracted.

While AFII does provide good modelling for much of the calorimetry, it does not include the forward calorimeter. Simulation of this detector uses *frozen showers* – a vast library of showers pre-simulated with Geant4. A further limitation to AFII is its inability to model jet substructure well, and so for analyses relying on this, fully Geant4-based simulations are needed⁵.

⁵ For now. Ongoing efforts are being made to improve substructure variable modelling in fast simulation [202].

Slice	Leading jet p_T [GeV]	Number of events (MC16a, MC16d)	Cross section [nb]
JZ0W	0-20	16000000, 15987000	7.8420E+07
JZ1W	20-60	15998000, 15997000	7.8420E+07
JZ2W	60-160	15989500, 15981000	2.4332E+06
JZ3W	160-400	15879500, 15878500	2.6454E+04
JZ4W	400-800	15925500, 15974500	2.5463E+02
JZ5W	800-1300	15993500, 15991500	4.5535E+00
JZ6W	1300-1800	17834000, 17880400	2.5753E-01
JZ7W	1800-2500	15983000, 15116500	1.6215E-02
JZ8W	2500-3200	15999000, 15987000	6.2503E-04
JZ9W	3200-3900	13995500, 14511500	1.9617E-05
JZ10W	3900-4600	13985000, 15988000	1.1962E-06
JZ11W	4600-5300	15948000, 15993000	4.2259E-08
JZ12W	5300+	15815600, 15640000	1.0367E-09

Table 6.1: Multijet Monte Carlo samples used in this analysis used to estimate the multijet contribution to the overall background composition. The generator, PDF, and tune details are given in Sec. 6.4.3.

6.4.3 Background Monte Carlo

As discussed above, MC simulations are relied on for predictions made by the SM, thereby providing a means to compare data against theory. Unfortunately, the available ATLAS MC statistics are insufficient for some analyses, *e.g.* those that involve searches for dijet resonances such as the one presented here. Furthermore, MC16e (representative of 2018 data) multijet samples were not produced by the time of this thesis, so MC16d was naïvely scaled to account for the missing simulated data. While this is not ideal, the data-taking conditions between most of 2017 and 2018 were similar; the instantaneous luminosities reached during most runs were between $1.5 - 1.8 \times 10^{34} \text{ cm}^{-2}\text{s}^{-1}$, and the mean number of interactions per bunch crossing between the two years differed by less than two (see Fig. 5.2). For these reasons, MC is only used in this analysis for a qualitative understanding of relative background contributions to the m_{jj} spectrum, and to perform initial fit hypothesis studies (presented in Sec. 6.8).

All background samples used in this analysis were officially produced with a configuration using a fully Geant4-based simulation by the ATLAS Monte Carlo and Production teams in Athena release 21.0.

Multijet background

The multijet background (Sec. 6.3.1) event sample was simulated with the Pythia v8.186 [203] (Pythia8) general-purpose event generator interfaced to EvtGen v1.2.0 [204] for decay of heavy flavour (B and D) mesons. The NNPDF23 [205] PDF set and the A14 [194] set of tuned parameters were used. Due to the dramatic decrease in cross section with increasing jet p_T , this background MC dataset comprises 13 separate samples (JZ0-12) binned (“sliced”) in leading jet p_T .

Further details of the simulated multijet samples are given in Table 6.1.

Process	Number of events (MC16a, MC16d)	Cross section [nb]
$t\bar{t}$ (inclusive)	119432000, 74486000	7.2935E-01
$W \rightarrow \mu^- \nu$	19101695, 24015767	8.2831E+00
$W \rightarrow e^- \nu$	24916639, 31348039	8.2831E+00
$W \rightarrow \mu^+ \nu$	24997577, 31375307	1.1263E+01
$W \rightarrow e^+ \nu$	20710568, 25836680	1.1300E+01

Table 6.2: The $t\bar{t}$ and W +jets Monte Carlo samples used in this analysis to estimate their contributions to the overall background composition. The generator, PDF, and tune details are given in Sec. 6.4.3.

Top quark pair and W +jets backgrounds

Both $t\bar{t}$ and W +jet events were generated with the NLO ME generator POWHEG-Box v2 [206], interfaced to Pythia8 for parton showering and hadronisation, in conjunction with the CT10 [207] NLO PDF set and AZNLO [208] tune. The generation of $t\bar{t}$ samples includes a model parameter, h_{damp} , set to twice the top quark mass, that controls the matrix element and parton shower matching in POWHEG, effectively regulating the high- p_T radiation. For $t\bar{t}$, a single inclusive sample contains both electron and muon final states, whereas for W +jets the samples are split into electron and muon final states.

Further details of the simulated $t\bar{t}$ and W +jets samples are given in Table 6.2.

6.4.4 Signal modelling and Monte Carlo

Different MC simulation flavours – full Geant4 or ATLFast-II – are used for the signal shape modelling. The overall shape differences between full and fast simulated signal samples is general small, on the order of several percent. Because this analysis does not make use of forward objects or substructure, the choice to use one flavour of simulation or the other was determined purely by the available computing resources, and therefore the timescale in which the samples were needed.

Generic resonance modelling

For the generic search, Gaussian approximations of signal shapes were produced with various peak positions (*i.e.* masses) and widths. This method benefits from a high frequency of mass points, since there is no requirement for official ATLAS MC production.

Gaussian distributions with means $250 \leq m_G \leq 6000$ GeV in steps of 250 GeV were produced for four different intrinsic widths: $\sigma_G/m_G = \{0.05, 0.10, 0.15\}$ and a width defined by the simulated mass resolution, which varies from 7% at low m_{jj} to 3% at the largest masses considered.

Technicolor signal Monte Carlo

The partonic interactions of the technicolor model for the $\rho_{TC} \rightarrow \pi_{TC} W$ process were generated using Pythia6 with the CT10 NLO PDF set. Pythia6 was chosen for the hard-scatter process because the model was readily available in this release, but was not implemented in Pythia8. Final-state partons were showered with Pythia8.

The cross section for this process was maximised by performing a mass scan of the π_{TC} for fixed $m_{\rho_{TC}}$, shown in Fig. 6.2, leading to $\Delta m = m_{\rho_{TC}} - m_{\pi_{TC}} = 1/2 m_{\rho_{TC}}$. The branching ratio of the π_{TC} to

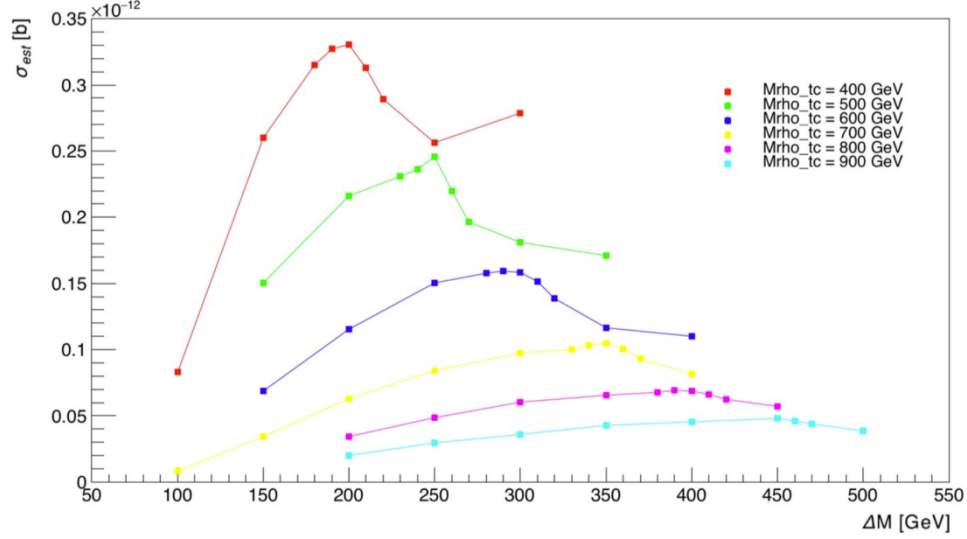


Figure 6.2: Mass scan of π_{TC} for six fixed $m_{\rho_{TC}}$. Shown is the estimated cross section for the $\rho_{TC} \rightarrow \rightarrow \pi_{TC} W$ process as a function of the difference between ρ_{TC} and π_{TC} . The largest cross section for this process is obtained for $\Delta m = m_{\rho_{TC}} - m_{\pi_{TC}} = 1/2 m_{\rho_{TC}}$.

two quarks was assumed to be 100% in order to give best generation efficiency. Because the longitudinal polarisation vector of the W boson contains terms of order the energy regime being probed, transversely-polarised W boson modes are highly suppressed at high energy. Therefore, only longitudinal W_L are considered. Detector modelling for the technicolor model was performed using the full Geant4-based simulation of the ATLAS detector.

Simplified Dark Matter Z' signal Monte Carlo

Signal samples for the Simplified Dark Matter model with a spin-1 Z' decaying to dijets were generated with MadGraph5 and showered with Pythia8, using the NNPDF2.3 NLO PDF set and A14 set of tune parameters. They were generated requiring final states with one or two leptons, and a Z' decaying to two jets. The one lepton final state involves an intermediate W boson, while the two lepton final state involves an intermediate Z boson.

Following recommendations from the LHC-DMWG [171], two sets of benchmark couplings are studied in this thesis for an axial-vector mediator:

- Leptophobic couplings A1 : $g_q = 0.25$, $g_\ell = 0$, $g_{DM} = 1$
- Leptophilic couplings A2 : $g_q = 0.1$, $g_\ell = 0.1$, $g_{DM} = 1$

The Z' decay width is set to its minimum value, given by the sum of the following partial widths:

$$\Gamma_{\text{axial-vector}}^{\chi\bar{\chi}} = \frac{g_{\text{DM}}^2 M_{\text{med}}}{12\pi} (1 - 4z_{\text{DM}})^{3/2} \quad (6.11)$$

$$\Gamma_{\text{axial-vector}}^{q\bar{q}} = \frac{g_q^2 M_{\text{med}}}{4\pi} (1 - 4z_q)^{3/2} \quad (6.12)$$

$$\Gamma_{\text{axial-vector}}^{\ell\bar{\ell}} = \frac{g_\ell^2 M_{\text{med}}}{12\pi} (1 - 4z_\ell)^{3/2} \quad (6.13)$$

$$\Gamma_{\text{axial-vector}}^{\nu\bar{\nu}} = \frac{g_\ell^2}{24\pi} M_{\text{med}} \quad (6.14)$$

where $z_i = m_i^2/M_{\text{med}}^2$, and partial widths for which $z_i > 1/4$ vanish.

In order to limit the signal MC dataset size, samples were generated for eight Z' mass points using only A1 (*i.e.* leptophobic) couplings. The A2 couplings were shown to give very similar signal shapes, and are related to A1 couplings via a simple rescaling of the the A2 cross section to that of the A1. Due to time constraints, ATLFast-II was used for modelling of the ATLAS detector.

6.5 Event selection

One of the most critical pieces of any analysis is its event selection. In some cases, the dominant backgrounds can be shaped and/or reduced, and sensitivity to potential signals can be improved through judicious use of selection criteria.

The dijet+lepton analysis is a generic search for heavy new resonances that decay exclusively to two jets (*dijets*), in events with an associated lepton. Deviations of the data from SM predictions are looked for in the dijet invariant mass, m_{jj} , distribution – the discriminating distribution. In the interest of remaining as model-agnostic as possible, no signal-optimised selections are imposed; the aim is to achieve a good balance between object quality and selection efficiency.

In addition to the SR, a data-driven CR is constructed using an event selection orthogonal to the SR. The CR serves to ensure there are no unexpected features in the discriminating distribution. Such discrepancies might arise *e.g.* from mis-reconstructed jets and mimic signal-like fluctuations in the m_{jj} distribution. It is therefore imperative to consider these effects, and understand their origin if they appear.

6.5.1 Triggering events

The trigger is a crucial first step in selecting events to be used for analysis. Triggers control which collision events are recorded, and are adopted based on final-state topologies of an analysis. Other considerations include trigger rates and efficiency, which ultimately determine the level of statistics one could expect given a set of triggers.

The data used in this analysis were collected using the single lepton triggers with the lowest p_T thresholds, that are unrescaled, available during LHC running between 2015-2018. Triggers were selected as per the recommendations by the ATLAS Muon [209] and Egamma [210] Trigger Signature Groups. A benefit to using unrescaled triggers is that every triggered event that is accepted by the high-level trigger (HLT) is recorded. This is in contrast to low- p_T jet triggers which are highly rescaled due to the abundance of jet production at the LHC.

Object	High-Level Trigger	Year(s) operational	Int.L.[fb ⁻¹]
Muons			
	HLT_mu24_iloose	2016	2.290
	HLT_mu24_ivarloose	2016	2.290
	HLT_mu24_ivarmedium	2016-2018	2.285
	HLT_mu24_imedium	2015-2016	11.473
	HLT_mu26_ivarmedium	2016-2018	135.726
	HLT_mu26_imedium	2015-2017	21.631
	HLT_mu40	2015-2016	8.945
	HLT_mu50	2015-2018	102.738
Electrons			
	HLT_e26_lhtight_nod0_ivarloose	2016-2018	135.728
	HLT_e60_imedium	2015-2016	36.215
	HLT_e60_lhmedium_nod0	2015-2018	135.728

Table 6.3: Single-lepton triggers used in this analysis, years they were enabled, and the total recorded integrated luminosity using events triggered by each.

In general, the ATLAS trigger naming conventions are such that they are self-descriptive. Muon triggers follow the naming `HLT_muNN[_isoInfo]`, where `NN` specifies the nominal p_T threshold of the trigger, and `isoInfo` is an optional isolation requirement⁶. For example, `HLT_mu24_iloose` is the HLT trigger for muons with $p_T > 24$ GeV and loose isolation, and `HLT_mu40` is the HLT trigger for muons with $p_T > 40$ GeV and has no isolation requirement. For electrons, the naming convention is `HLT_eNN_idInfo[_lhInfo][_isoInfo]`, where `NN` specifies the nominal transverse energy, E_T , threshold, `idInfo` is the identification requirement, `lhInfo` is an optional requirement that enters into the electron identification likelihood calculation (discussed in Sec. 5.3), and `isoInfo` is an optional isolation requirement. An example of an electron trigger used in this analysis is `HLT_e26_lhtight_nod0_ivarloose`, which has an E_T threshold of 26 GeV, tight likelihood identification without transverse impact parameter, d_0 , information, and a variable (*i.e.* energy-dependent) isolation requirement.

The full set of single-lepton triggers employed in this analysis are tabulated in Table 6.3. Triggers with $p_T < 30$ GeV thresholds have some isolation and identification requirements to maintain a manageable rate without the need for prescaling. To recover possible efficiency losses at high momenta, additional electron and muon triggers with no isolation or identification requirements are included with thresholds $p_T \geq 40$ GeV. For each trigger, the integrated luminosity quoted was taken from the ATLAS Luminosity Calculator⁷, and accounts for LAr noise bursts and the Level-1 trigger “live fraction” – efficiency corrections for triggered events that are vetoed for *e.g.* data acquisition deadtime or HLT backpressure (*i.e.* when a trigger accept rate is intentionally temporarily reduced or halted). The years that a given trigger was operational was retrieved from the ATLAS Conditions Metadata Portal [211].

Events are considered for preselection if they pass an inclusive-OR of all triggers, since trigger configuration was time-dependent during 2015-2018 (Run-2) data taking. For example, as shown in Fig. 6.3,

⁶ Isolation is described later in this section.

⁷ The ATLAS “lumi-calc” tool can be found at: <https://atlas-lumicalc.cern.ch>.

vertex (PV). A PV is required to have at least three associated tracks, each with $p_T > 400$ MeV. The PV with the highest sum of squared p_T assigned to it is labelled as PV_0 , and assumed to be the source of the hard-scatter process of interest.

Event cleaning

After being accepted by at least one of the triggers listed in Table 6.3, and prior to entering the preselection, an event is required to pass the following basic quality requirements:

- be part of a run included in an appropriate Good Runs List (GRL), as discussed in Sec. 5.1;
- pass standard event cleaning requirements:
 - *LAr error veto*: removal of events with noise bursts in the LAr calorimeters or which have corrupt data;
 - *Tile error veto*: removal of events in which Tile calorimeter errors are present;
 - *SCT corrupt veto*: removal of corrupt SCT events due to single-event upsets;
 - *Incomplete events*: in case a detector goes into a “busy” mode, due to *e.g.* timing desynchronisation, the detector’s trigger, timing and control system needs to be restarted, leading to missing information from an event; and
- have a PV_0 .

While most calorimeter noise is removed by the LAr event veto above, some electronics noise remains. Moreover, the LAr veto is not overly effective at removing noise from beam-induced backgrounds. As such, jets undergo an additional set of “cleaning” criteria that are based on a number of quantities that have shown to provide good discrimination between fake and genuine jets [216].

$Q_{\text{cell}}^{\text{LAr}}$: Quadratic difference between the measured and expected pulse shape in a LAr cell. A large value of this variable is indicative of noise rather than a real energy deposit.

$\langle Q \rangle$: Average jet quality represented as the energy-weighted average of $Q_{\text{cell}}^{\text{LAr}}$ for calorimeter cells comprising the total jet energy.

f_{HEC} : Fraction of a jet’s energy deposited in the HEC with respect to the jet’s total energy.

f_{EM} : Fraction of a jet’s energy deposited in the EM calorimeter with respect to the jet’s total energy.

f_{max} : Maximum energy fraction deposited in a single calorimeter layer.

f_Q^{HEC} : Fraction of energy in the HEC cells for which the signal shape quality is poor.

f_Q^{LAr} : Fraction of energy in the EM calorimeters cells for which the signal shape quality is poor.

t_{jet} : The energy-squared weighted average of the time at which a jet deposits its energy in the calorimeter cells.

f_{ch} : Jet charged fraction, defined as the ratio of the scalar sum of p_T of the tracks originating from the primary vertex associated to the jet divided by the jet p_T .

Fake jets can be reconstructed from spurious calorimeter signals originating from sporadic noise bursts or coherent noise in the detectors. In the HEC, sporadic noise bursts appear as localised energy deposits in only a few cells that comprise most of a fake jet's energy, and are identified by large values of f_{HEC} , $f_{\text{Q}}^{\text{HEC}}$, and $\langle Q \rangle$. Such cases can result in negative energies, E_{neg} , appearing in neighbouring cells due to the capacitive coupling between channels. The EM calorimeters can experience coherent noise which results in high-energy fake jets. Such fake jets are characterised by large values of f_{EM} , $f_{\text{Q}}^{\text{LAr}}$, and $\langle Q \rangle$.

Cosmic rays and beam-induced backgrounds, collectively referred to as *non-collision backgrounds*, result in energy deposits from real objects, but do not originate from a pp collision. To reduce the impact from such objects, t_{jet} and f_{ch} are useful variables. Jets produced in the hard-scatter are expected to be reconstructed with $t_{\text{jet}} \approx 0$. Because a real jet would also normally have associated tracks and deposit its energy in the innermost layers of the calorimeter, the combination of f_{ch} and f_{EM} can provide good discriminating power against jets from other sources [217].

Jets are further categorised based on the locations in the calorimeter that their energy was deposited. *Ugly* jets are those which leave significant amounts of energy in the barrel and end-cap transition regions, or are reconstructed in regions of the calorimeters that have masked (*i.e.* faulty) cells. In either case, ugly jets have poorly reconstructed energies. Therefore, these jets are only accepted if they satisfy $f_{\text{max}} > 0.8$.

All jet cleaning criteria employed in this analysis, and recommended by the ATLAS Jet/ETmiss group, are summarised in Table 6.5. The selections tabulated are referred to as *BadLoose*, a working point designed to provide an efficiency of selecting jets in pp collisions above 99.5 (99.9)% for jets with $p_{\text{T}} > 20(100)$ GeV [216]. If a jet satisfies any of the three classifications, it is discarded and is not considered in the event preselection.

Classification	BadLoose criteria
Sporadic noise bursts (HEC)	$(f_{\text{HEC}} > 0.5 \ \&\& \ f_{\text{Q}}^{\text{HEC}} > 0.5 \ \&\& \ \langle Q \rangle > 0.8)$ $ \ E_{\text{neg}} > 60 \text{ GeV}$
Coherent noise (EM)	$f_{\text{EM}} > 0.95 \ \&\& \ f_{\text{Q}}^{\text{LAr}} > 0.8 \ \&\& \ \langle Q \rangle > 0.8 \ \&\& \ \eta < 2.8$
Non-collision backgrounds	$(f_{\text{EM}} < 0.05 \ \&\& \ f_{\text{ch}} < 0.05 \ \&\& \ \eta < 2)$ $ \ (f_{\text{EM}} < 0.05 \ \&\& \ \eta \geq 2)$ $ \ (f_{\text{max}} > 0.99 \ \&\& \ \eta < 2)$

Table 6.5: BadLoose jet cleaning criteria used for the rejection of bad jets.

Event preselection

An event *preselection* is used to first prune the extensive dataset, and is applied to all events passing the event cleaning requirements.

At the preselection stage, events are required to meet a set of relaxed thresholds, compared to the final event selection where more stringent requirements are applied. The event preselection imposes requirements on minimum p_{T} and other kinematical thresholds, and object quality and isolation working points (defined by dedicated groups in the collaboration) that are described in this section. Having a

loose set of events permits studies useful for defining the final event selection and determining the final selection efficiency.

Muons

Muon candidates are reconstructed using tracking information from both the Muon Spectrometer (MS) and Inner Detector (ID), as described in Sec. 5.3. To be considered for the final event selection, muons are required to have $p_T > 20$ GeV and be within the MS trigger acceptance of the MS. Muon candidates must also meet identification requirements, which take into account the number of combined hits in the ID and MS, as well as the q/p significance. For event preselection, the *Loose* identification working point (WP) [134] is used, which is designed to maximise reconstruction efficiency while also providing good-quality muon tracks.

Muon candidates are further required to have their associated ID tracks meet a d_0 significance requirement, $|d_0/\sigma(d_0)| < 3$, and have the longitudinal impact parameter satisfy $|z_0 \times \sin\theta| < 0.5$ mm, to limit contamination from non-prompt muons arising from heavy-flavour and τ lepton decays.

Lastly, muons must meet the *FCLoose* isolation WP criteria which impose track- and calorimeter-based isolation requirements. For muon tracks reconstructed in the ID (as is the case for CB muons), the isolation requirement is constructed as the ratio between the sum of p_T of tracks within a cone of $\Delta R = 0.3$ and the muon's p_T :

$$\frac{p_T^{\text{varcone30}}}{p_T^\mu} < 0.15. \quad (6.15)$$

The muon calorimeter isolation requirement is similar, but with the numerator being instead the sum of the E_T from all topo-clusters within a cone of $\Delta R = 0.2$,

$$\frac{E_T^{\text{cone20}}}{p_T^\mu} < 0.3. \quad (6.16)$$

The energy of the muon itself, as well as the estimated contributions from pile-up are subtracted from this cone.

Electrons

Electrons entering the preselection are reconstructed using the dynamical, topological cell-clustering approach as described in Sec. 5.3.2. They are required to have $E_T > 20$ GeV and be within $|\eta| < 2.47$. Electrons in the “transition region”, $1.37 < |\eta| < 1.52$, between the electromagnetic barrel and end-cap calorimeters are rejected due to the lower resolution and reconstruction efficiency in this region.

Electron triggers used in this analysis that have thresholds $p_T < 30$ GeV impose an identification requirement, whereas those with higher p_T thresholds do not. Therefore, in order to achieve a level of consistency among the different triggers, the *LooseLH* identification WP [130], a combination of E_T - and $|\eta|$ -dependent requirements, is applied.

Electron candidates must satisfy $|d_0/\sigma(d_0)| < 5$ and $|z_0 \times \sin\theta| < 0.5$ mm impact parameter requirements for the suppression of heavy-flavour decays, as well as tracking and calorimeter isolation requirements. The impact parameter requirements also largely reduce leptonic τ decays as τ leptons travel, on average, roughly $80\mu\text{m}$ before decaying into lighter leptons and neutrinos. The *FCLoose*

isolation WP requires,

$$\frac{p_T^{\text{varcone20}}}{p_T^e} < 0.15, \quad (6.17)$$

$$\frac{E_T^{\text{cone20}}}{p_T^e} < 0.2. \quad (6.18)$$

Jets

Jets used in this analysis are constructed with the anti- k_t algorithm using a radius parameter $R = 0.4$, as implemented in the FastJet software package [218]. The complete jet reconstruction and calibration process is detailed in Sec. 5.3. All reconstructed jets are subject to loose preselection criteria to limit the contamination from non-genuine jets – resulting from energy deposits caused by instrumental effects, cosmic ray showers or other non-collision backgrounds – from entering the final selection.

Jet candidates are required to have $p_T > 20$ GeV and to be within $|\eta| < 2.4$ so as to be covered by the acceptance of the ID before showering in the calorimeters. To suppress jets resulting from pile-up, a jet vertex-tagging (JVT) technique [219] is used. The JVT is built out of two variables, JVF^{corr} and $R_{p_T}^0$, that provide information used to separate hard-scatter jets from those originating from pile-up interactions. The quantity JVF^{corr} [220] is defined for each jet as:

$$\text{JVF}^{\text{corr}} = \frac{\sum p_T^{\text{track}}(\text{PV}_0)}{\sum p_T^{\text{track}}(\text{PV}_0) + \frac{\sum_{i \geq 1} \sum p_T^{\text{track}}(\text{PV}_i)}{k \cdot n_{\text{track}}^{\text{PU}}}}, \quad (6.19)$$

where PV_i , $i \geq 1$, represents the reconstructed event vertices sorted by decreasing $\sum p_T^2$, and $\sum p_T^{\text{track}}(\text{PV}_0)$ is the scalar p_T sum of tracks associated to PV_0 . The term $\sum_{i \geq 1} \sum p_T^{\text{track}}(\text{PV}_i) \equiv p_T^{\text{PU}}$ denotes the scalar p_T sum of tracks associated to jets originating from pile-up interaction i . To correct for the linear increase of p_T^{PU} with the total number of pile-up tracks per event, $n_{\text{track}}^{\text{PU}}$, p_T^{PU} is divided by $k \cdot n_{\text{track}}^{\text{PU}}$. The scaling factor k is approximated by the slope of $\langle p_T^{\text{PU}} \rangle$ plotted as a function of $n_{\text{track}}^{\text{PU}}$, resulting in $k = 0.01$.

The observable $R_{p_T}^0$ is used to test the compatibility between the p_T of a jet's charged components and its fully calibrated p_T with respect to PV_0 :

$$R_{p_T}^0 = \frac{\sum p_T^{\text{track}}(\text{PV}_0)}{p_T^{\text{jet}}}. \quad (6.20)$$

Because the numerator does not account for neutral particles within a jet, the mean value of this quantity is 0.5.

The JVT discriminant is constructed from a two-dimensional likelihood of JVF^{corr} and $R_{p_T}^0$ based on a k-nearest neighbour classifier [221]. To achieve a signal-jet efficiency better than 95%, a threshold of $\text{JVT} > 0.59$ is imposed on jets with $p_T < 60$ GeV, corresponding to a roughly 4% pile-up fake rate.

Overlap removal

The last step of event preselection is to apply an *overlap removal* (OR) procedure. Overlap removal is used to remove ambiguities, in case different objects are reconstructed from the same set of tracks or calorimeter energy deposits, by multiple algorithms, thereby addressing potential duplication and isolation of two separate but close-by objects. The design of the OR algorithm is analysis-dependent in

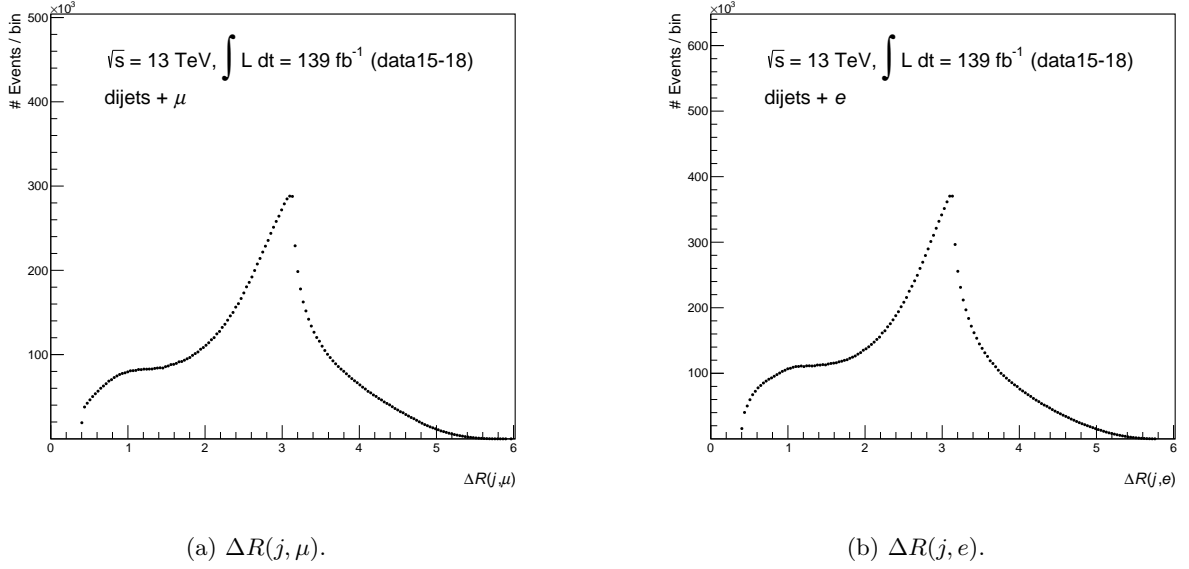


Figure 6.5: Distributions of (a) jet-muon and (b) jet-electron ΔR separation following the final event selection. The absence of events with $\Delta R(j, \ell) < 0.4$ demonstrates the correct implementation of the overlap removal algorithm.

that its performance depends on the definitions of objects involved.

The OR is applied as a sequence of steps, summarised below [222].

1. **Muon-jet OR:** remove the jet in favour of the muon within a cone of $\Delta R(\mu, j) < 0.2$ if the jet has less than three associated tracks; if the jet has three or more tracks, discard the muon.
2. **Electron-jet OR:** remove the jet in favour of the electron within a cone of $\Delta R(e, j) < 0.2$; remove the electron in favour of the jet within $0.2 < \Delta R(e, j) < 0.4$.
3. **Muon-electron OR:** remove the electron if it shares the same track as the muon and the two objects are within $\Delta R(\mu, e) < 0.2$; remove the muon if *calo-tagged*, *i.e.* identified using ID and calorimeter information alone, and shares the same track as the electron within $\Delta R(\mu, e) < 0.2$.
4. **Electron-electron OR:** remove the electron with lower p_T if the two electrons share the same ID track and are within a cone of $\Delta R(e, e) < 0.2$.

Only the surviving events with final-state objects passing the OR algorithm are considered further in the SR or CR event selections.

To validate the overlap removal procedure, it is useful to examine the distributions of the distance parameters $\Delta R(j, \ell)$. Figure 6.5 shows the distributions for jet-muon and jet-electron separation in terms of the differences in (ϕ, η) phase-space between the respective objects. The sharp peak seen at $\Delta R(j, \ell) = \pi$ indicates jets and leptons are typically back to back in R . It can be seen that no events within the overlap regions are accepted into the SR, confirming a correct implementation of the algorithm.

6.6 Final selection and definitions of analysis regions

Following the preselection, events are lastly evaluated for candidacy to enter the SR or the CR. The CR is designed to be orthogonal (in terms of events) to the SR so that initial studies can be performed in an unblinded region before unblinding the SR. Whereas the preselection described above requires only a loose set of selection criteria, more stringent requirements are imposed in the final event selection to *e.g.* limit the contribution from fake objects.

6.6.1 Signal leptons

The final selection imposed on leptons results in what are referred to as “signal” leptons. This selection follows from previous studies performed in final states with a single lepton and jets [223].

Beyond preselection, leptons are required to have $p_T > 60$ GeV as well as satisfy more stringent isolation and identification criteria. Both electrons and muons are required to pass the *FCTight* isolation WP, to suppress contributions from non-prompt leptons arising from heavy-flavour decays. This WP has an efficiency of 99% (87%) for muons (electrons) with $p_T > 60$ GeV. To further suppress pollution of fake electrons to the SR, electrons must satisfy the *TightLH* quality definition. Muons are required to pass only the *Medium* identification criteria since they are less susceptible to being faked by a jet following overlap removal applied in the preselection step. Because of the wide range of thresholds on the triggers used, these requirements ensure a consistent definition among all leptons of the same flavour.

6.6.2 Signal jets and determining the minimum m_{jj}

A primary objective of this analysis is to construct the widest possible range of dijet invariant masses, and it is therefore desirable to begin the search at low m_{jj} . For jets passing the preselection, the highest- (*i.e.* leading) and second-to-highest- p_T (*i.e.* subleading) jets in each event are taken as the signal jets, used to construct the m_{jj} distribution.

Several factors are considered when deciding on the minimum value of m_{jj} : lepton-jet p_T correlations, selection efficiencies, and binning.

Transverse momentum balance

Figure 6.6, which shows distributions of the leading jet p_T as a function of the minimum lepton p_T threshold, demonstrates the strong correlation between the lepton that triggered the event and the leading jet: as the lepton minimum p_T increases, the peak in the leading jet p_T distribution increases to roughly match that of the lepton. Based on this observation, and because of the strong correlation between leading jet p_T and m_{jj} , an absolute minimum m_{jj} threshold is set to 120 GeV, *i.e.* twice the minimum lepton (or equivalently, leading jet) p_T .

Analysis-level selection efficiencies

Although dedicated studies have shown the single-lepton triggers used in this analysis have high efficiencies (see Sec. 6.5), those studies do not include requirements on jets. Inefficiencies can arise due to specific selections following a trigger that may distort the m_{jj} distribution in such a way as to produce BSM signal-like features, and would result in additional systematic uncertainties. To avoid possible issues

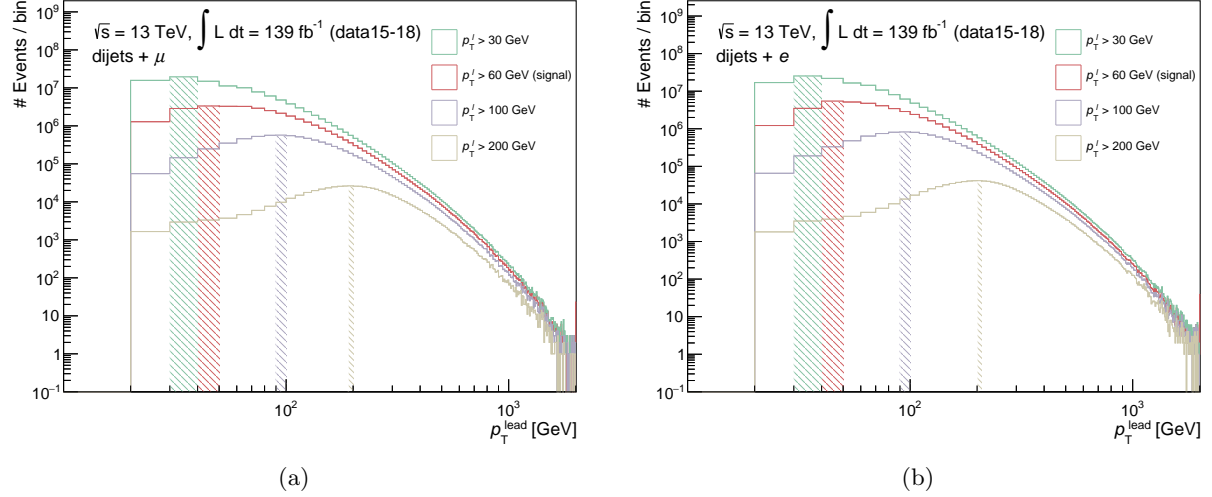


Figure 6.6: Transverse momentum of leading jets as a function of (a) muon and (b) electron transverse momentum. Peak bins in the distribution are hatched to guide the eye. All preselection and signal lepton requirements are applied to the events.

related to selection inefficiencies, it is advantageous to determine a lower bound for m_{jj} at which point the efficiency begins to plateau.

The selection efficiency is studied as a function of the p_T of the leading jet, p_T^{lead} , due to the strong correlation it has with m_{jj} . Thus, the goal is to determine the minimum value of p_T^{lead} at which the selection efficiency with respect to its distribution plateaus. It is assumed that the efficiency with respect to the m_{jj} distribution reaches a plateau at roughly twice this value of p_T^{lead} , and hence the minimum m_{jj} can be established.

The *bootstrap* method [224] is used to calculate the selection efficiencies. In this method, it is assumed that a lower p_T threshold trigger, L , has a known efficiency; for the case at hand, the lower threshold triggers are assumed to be $\approx 100\%$ efficient. This low-threshold trigger is compared to the highest-threshold trigger, T , and a relative trigger efficiency is calculated as

$$\epsilon(T) = \epsilon(T|L) \cdot \epsilon(L), \quad (6.21)$$

where $\epsilon(T|L)$ is the conditional probability that T is triggered given that L has been triggered. Equation 6.21 can be reinterpreted in a more useful form by employing Bayes' theorem, expressing the efficiency in terms of the number of events triggered by T and L ⁸,

$$\epsilon(T) = \frac{N(T \cap L)}{N(L)} \quad (6.22)$$

with $N(T \cap L)$ being a joint probability, *i.e.* that both T and L trigger the same event, and $N(L)$ is the number of events triggered by L regardless of whether or not T was triggered. The uncertainty on the

⁸ Although $\{T\} \subset \{L\}$, it is possible for an L trigger to miss an event that a T trigger fired on, *e.g.* an L trigger was accidentally disabled for a number of lumiblocks. Therefore the numerator in Eqn. 6.22 cannot simply be reduced to $N(T)$.

M u o n t r i g g e r s				
Period	L trigger	$\int \mathcal{L} dt$ [fb $^{-1}$]	T trigger	$\int \mathcal{L} dt$ [fb $^{-1}$]
2015	HLT_mu24_imeium	3.220	HLT_mu50	3.220
2016-2018	HLT_mu26_ivarmedium	135.726	HLT_mu50	102.738
E l e c t r o n t r i g g e r s				
Period	L trigger	$\int \mathcal{L} dt$ [fb $^{-1}$]	T trigger	$\int \mathcal{L} dt$ [fb $^{-1}$]
2015	HLT_e60_medium	3.220	HLT_e60_lhmedium_nod0	0.0897740
2016-2018	HLT_e26_lhtight_nod0_ivarloose	135.728	HLT_e60_lhmedium_nod0	135.728

Table 6.6: Triggers used in calculating selection efficiency.

efficiency is

$$\Delta\epsilon = \sqrt{\frac{\epsilon(1-\epsilon)}{N(L)}}. \quad (6.23)$$

Efficiencies are calculated independently for data recorded in 2015 and 2016-2018 since different L and T triggers were operational in these two run periods. The L and T triggers used to calculate the efficiencies for each run period are given in Table 6.6. They were selected such that an L trigger has a larger or equal associated integrated luminosity for a given period than the corresponding T trigger. All events entering the calculation are required to pass preselection, and have at least one signal lepton. From the results in the study presented earlier, and the correlation between leading jet p_T and m_{jj} , a minimum m_{jj} threshold of 120 GeV is also imposed.

Figure 6.7 compares the leading jet p_T distributions for the different muon and electron L and T triggers given in Table 6.6, with the selection efficiencies shown in the bottom panel. A slight drop in selection efficiency of less than 2% can be seen in the 2015 electron channel in the range $180 < p_T < 650$ GeV, followed by fluctuations of the same order in the range $650 < p_T < 1000$ GeV. This inefficiency is likely due to misconfiguration of the HLT_e60_lhmedium_nod0 trigger, or it being disabled during a number of luminosity blocks during runs in 2015. However, this inefficiency is representative of only a small fraction of the full dataset, and so has a negligible impact on the overall efficiency. Overall, a better than 98% efficiency is reached beginning at $p_T^{\text{lead}} \approx 100$ GeV, therefore establishing the minimum value for m_{jj} of roughly 200 GeV.

Jet mass resolution and binning

The binning of the m_{jj} distribution used in this analysis follows from Ref. [225], which was inherited from the ATLAS inclusive dijet search [226]. Because a large number of studies would need to be repeated for a new binning scheme, the binning remains unaltered. Therefore, in choosing a minimum value of m_{jj} , the binning of the distribution needs to be considered. Bin widths are chosen such that they are representative of the jet mass resolution of the detector at a given bin (see Sec. 6.8). Because a bin edge does not land exactly on 200 GeV, the choice for the minimum m_{jj} is 216 GeV.

6.6.3 Signal region definition

Based on the studies presented earlier in this section, the dijet+lepton SR is defined by events meeting the following criteria:

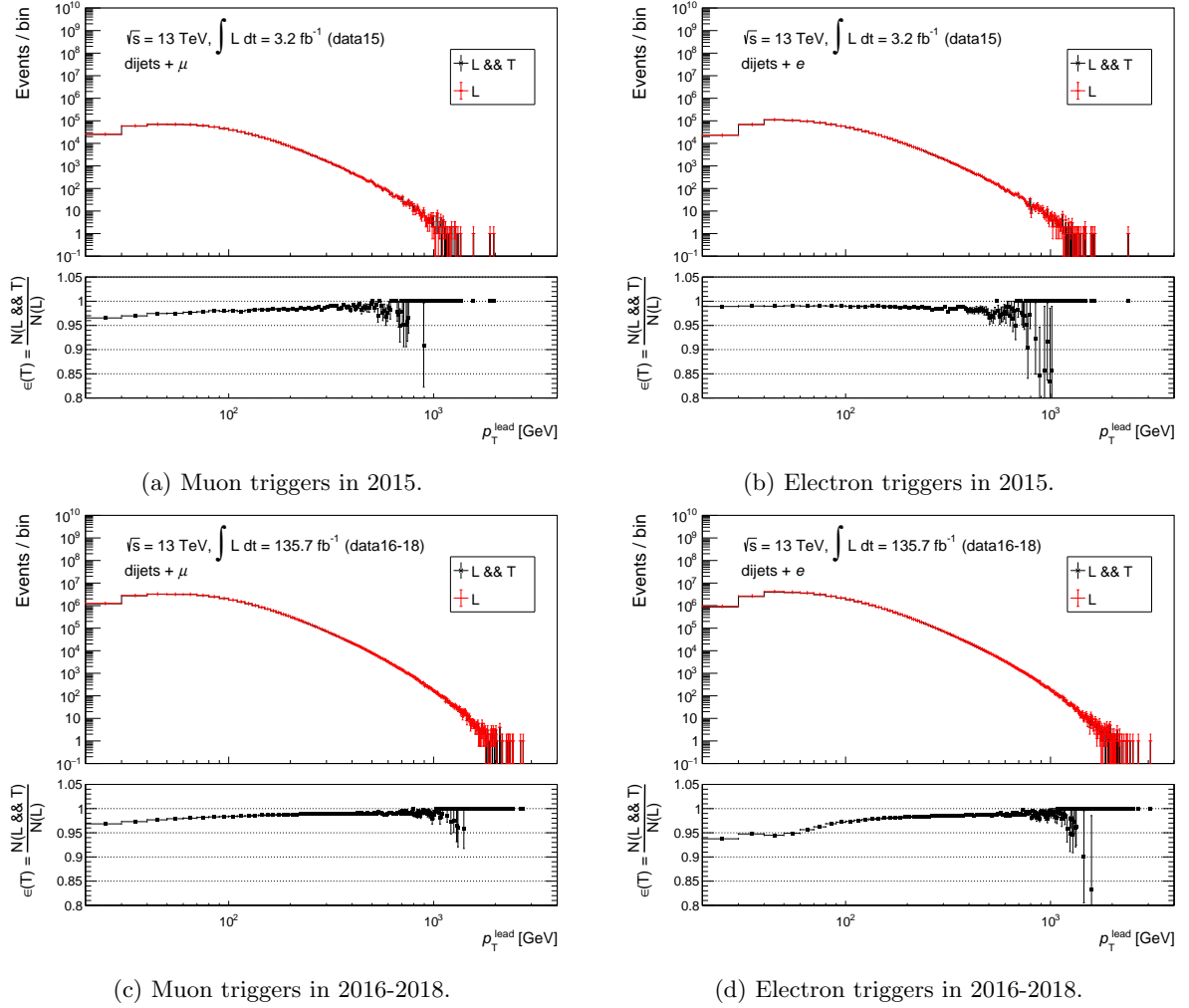


Figure 6.7: Selection efficiency as a function of leading jet p_T for events passing the lepton triggers in Table 6.6 and satisfying the preselection requirements. A minimum threshold $m_{jj} > 120$ GeV on the two leading jets is also imposed.

- contain at least one signal lepton;
- contain at least two signal jets with $p_T > 20$ GeV; and
- the invariant mass of the leading and subleading jets (*i.e.* the dijet system) must be $m_{jj} > 216$ GeV.

A complete summary of the final SR selection is tabulated in Table 6.7.

6.6.4 Control region definition

Typically, blinded analyses use CRs to perform initial studies on analysis choices, *e.g.* choosing a suitable background hypothesis (*i.e.* the fit function). In defining a CR, an attempt is made to ensure its shape is similar to that of the SR and that it is signal-free to yield a reliable estimate of the background. Depending on the study being performed, CRs can be constructed from data or MC.

A complication in this analysis is that no CR exists sharing exactly the same physics and kinematics as the SR. Moreover, no reliable comparison can be drawn between data and MC due to the limited

Object	Variable/Parameter	Threshold
Muons		
	Algorithm	Combined
	p_T	$> 60 \text{ GeV}$
	$ \eta $	< 2.4
	Quality	<i>Medium</i>
	Isolation	<i>FCTight</i>
	$ d_0/\sigma(d_0) $	< 3.0
	$ z_0 \times \sin \theta $	$< 0.5 \text{ mm}$
Electrons		
	p_T	$> 60 \text{ GeV}$
	$ \eta $	< 2.47 , excluding $1.37 < \eta < 1.52$
	Quality	<i>TightLH</i>
	Isolation	<i>FCTight</i>
	$ d_0/\sigma(d_0) $	< 5.0
	$ z_0 \times \sin \theta $	$< 0.5 \text{ mm}$
Jets		
	Algorithm	anti- k_t
	R	0.4
	p_T	$> 20 \text{ GeV}$
	$ \eta $	< 2.4
	JVT	> 0.59 (for $p_T < 60 \text{ GeV}$)
	m_{jj}	$\geq 216 \text{ GeV}$

Table 6.7: Signal region event selection.

statistics of the multijet background MC samples after applying the final-state lepton requirement. This requirement largely reduces the number of multijet signal events, and introduces spikes in the multijet m_{jj} distribution that result in a non-smooth spectrum. Furthermore, because multijet MC events do not typically contain real final-state leptons, they will very likely enter the SR as a result of a fake, or non-prompt, lepton being triggered on, and it is known that fake objects are not modelled well by MC. Therefore, a MC-based m_{jj} distribution of the SR will be dominated by a mismodelled background.

The approach taken in this analysis is to define a data-driven CR that, while not being an ideal representation of the SR, can be used to study the impact of jet reconstruction issues and fakes. For example, jets with similar p_T that are mis-reconstructed could result in the migration of events preferentially in a few bins that can be misinterpreted as a signal. In other cases, jets could be misidentified as electrons (or vice versa), leading to a SR contaminated by events that do not contain real leptons, resulting again in possible false-positive signals. A m_{jj} spectrum not comprised of genuine dijet events may also be difficult to describe with a QCD-motivated functional form. Finally, having a data-driven CR dominated by multijet events can potentially be used to evaluate the suitability of the proposed fit hypothesis to describe the SM background.

A “loose lepton” control region (LL-CR) is constructed from data events. The primary goals of this CR are as follows:

- to confirm that jet mis-reconstruction does not create spurious, or unexpected, “bumps” in the m_{jj} distribution;
- biases do not arise, which may be misintepreted as a signal, due to analysis selection; and

- provide an orthogonal set of events to the SR with potential to serve as a guide for the fitting strategy.

The LL-CR is populated with events similar to the SR, with the exception that the signal lepton must satisfy only loose quality requirements and fail the more stringent criteria imposed by tighter working points; this selection ensures an orthogonal set of events with respect to the SR. Due to the loose quality criteria, the LL-CR will contain a significant number of fake events, therefore enhancing the contribution from multijet events.

6.7 Signal and control region kinematics

This section presents the kinematics of the SR and LL-CR. Initial background estimates are also performed on the LL-CR.

6.7.1 Signal region kinematics

All SR distributions are constructed following the event selection given in Table 6.7. Figures 6.8 and 6.9 show the muon and electron cutflow distributions, respectively, for 2015-2018 data. Also shown in the figures are the multiplicity, p_T , and η distributions of triggered muons and electrons, corresponding to the events entering the SR.

The number of triggered electrons is observed to be roughly 30% greater than that of triggered muons. This difference can in part be accounted for by the higher electron trigger efficiency, $\epsilon(|\eta| < 2.47) > 95\%$, than that of muons, $\epsilon(|\eta| < 1.05) \approx 70\%$, $\epsilon(1.05 < |\eta| < 2.4) \approx 88\%$. Despite the more stringent selection requirements imposed on electrons, it is also probable that a non-negligible fraction of such events are triggered by misidentified electrons, especially at higher energies and $|\eta|$.

Figure 6.10 shows the distributions of jet cutflow, multiplicity, and leading and subleading jet p_T in the combined muon-plus-electron channel. No unexpected features are observed in distributions related to jets, however some interesting kinematic effects can be seen. First, the leading jet p_T distribution begins to monotonically decrease below about 100 GeV. The energy-mass relation tells that

$$m_{jj} = \sqrt{(E_1 + E_2)^2 - |\mathbf{p}_1 + \mathbf{p}_2|^2} \quad (6.24)$$

$$= \sqrt{m_1^2 + m_2^2 + 2(E_1 E_2 - \mathbf{p}_1 \cdot \mathbf{p}_2)} \quad (6.25)$$

$$\approx \sqrt{2p_{T1}p_{T2}[\cosh(\eta_1 - \eta_2) - \cos(\phi_1 - \phi_2)]}, \quad (6.26)$$

where the last line holds for massless particles or when $E \gg m_1, m_2$. Therefore, the two jets must be back-to-back in cases where the leading jet has low p_T in order to meet the minimum m_{jj} threshold.

6.7.2 Loose-lepton control region

In addition to checking for biases, another utility of the LL-CR is that it can be used for initial studies of the background description *ansatz*. To get a sense of the compatibility between this region and the SR, their kinematic distributions are compared. If the LL-CR and SR distributions have similar statistics and shapes, the former can provide insight into the family of functional forms for a description of the background that can be applied to the latter.

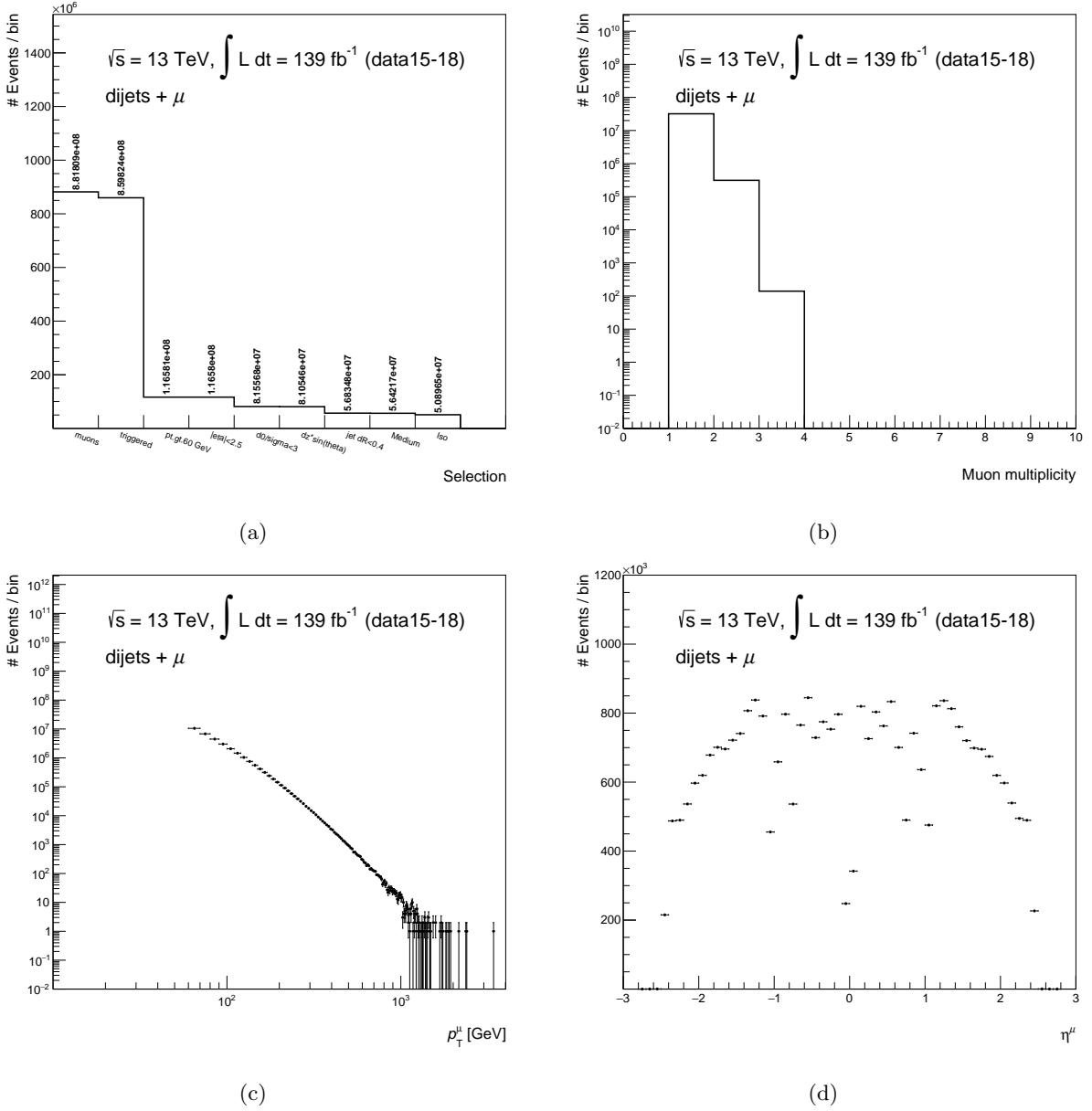
Figure 6.8: Muon (a) cutflow, (b) multiplicity, (c) p_T , and (d) η distributions of the SR.

Figure 6.11 compares leading and subleading jet p_T and η distributions in the SR and LL-CR regions in the top panel, and in the bottom is the ratio of the SR to LL-CR. In all figures, the LL-CR is normalised to the number of events in the SR. The kinematic differences between the SR and LL-CR are quantified by the reduced χ^2 over the full p_T and η ranges considered. Whereas both regions contain jets evenly distributed in η , significant discrepancies can be seen between the two regions for both the leading and subleading jet distributions, corresponding to $\chi^2/\text{ndf} \approx 45$ and $\chi^2/\text{ndf} > 200$, respectively. However, when considering events only for jet $p_T > 60$ GeV, where most of the statistics are, $\chi^2/\text{ndf} \sim 1$. Therefore, while not an ideal representation of the SR, the LL-CR can still be useful for determining the fit hypothesis to be used for the SR.

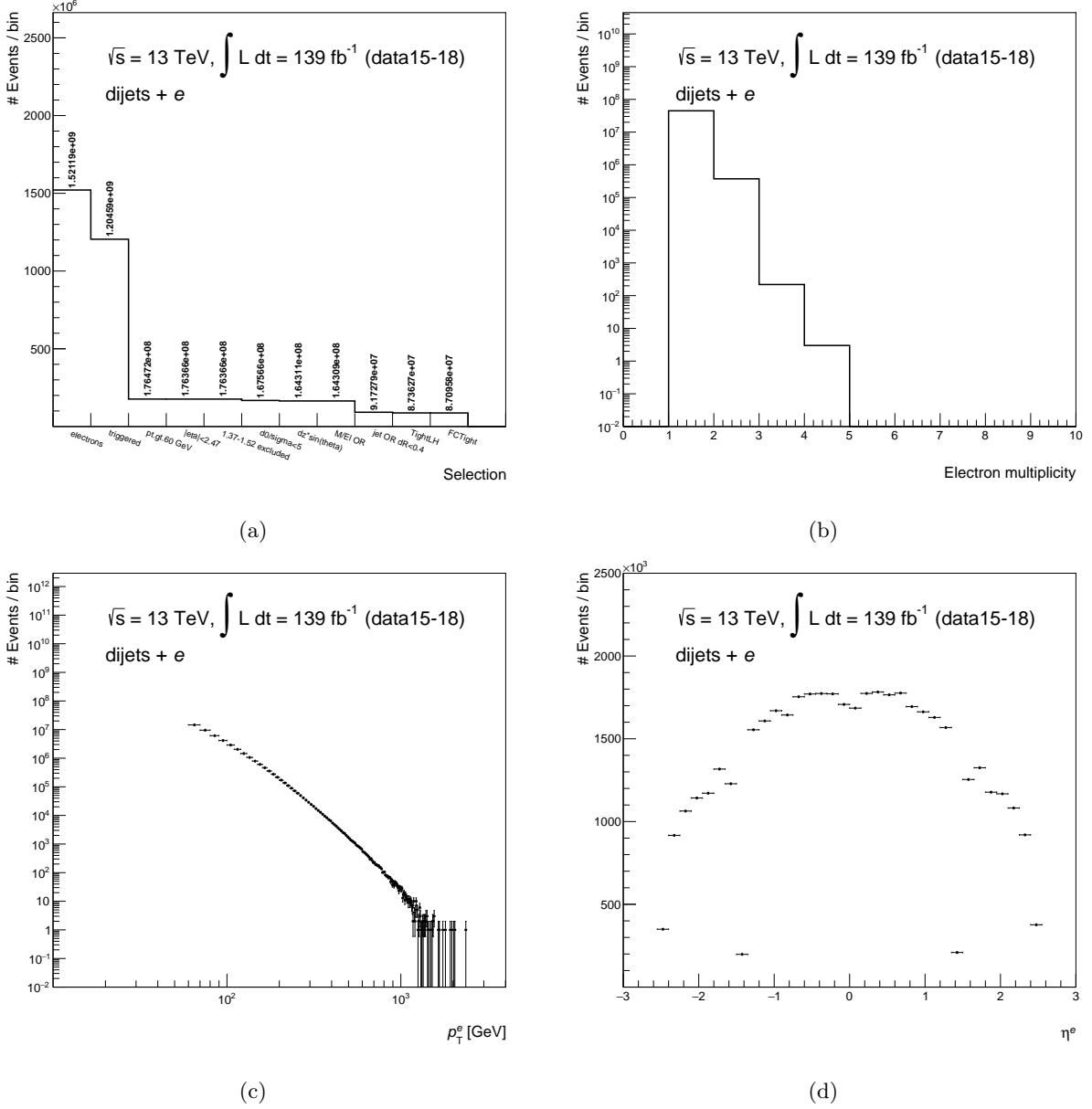


Figure 6.9: Electron (a) cutflow, (b) multiplicity, (c) p_T , and (d) η distributions following the final event selection.

6.8 Describing the SM background

Two fitting strategies are compared in this analysis to determine which best describes the dijet invariant mass distribution. The first is a “global fit” method, wherein a single fit is performed to model the full m_{jj} range considered. This hypothesis is based on a set of functional forms, first presented in Sec. 6.2, that have previously shown to give reliable estimates of the backgrounds largely comprised of multijet events. The second method provides additional flexibility by fitting small “windows” – comprised of a set number of bins – of the m_{jj} spectrum. These overlapping window fits are then combined to describe the full spectrum. This method is usually resorted to in the event that the global fit strategy fails to

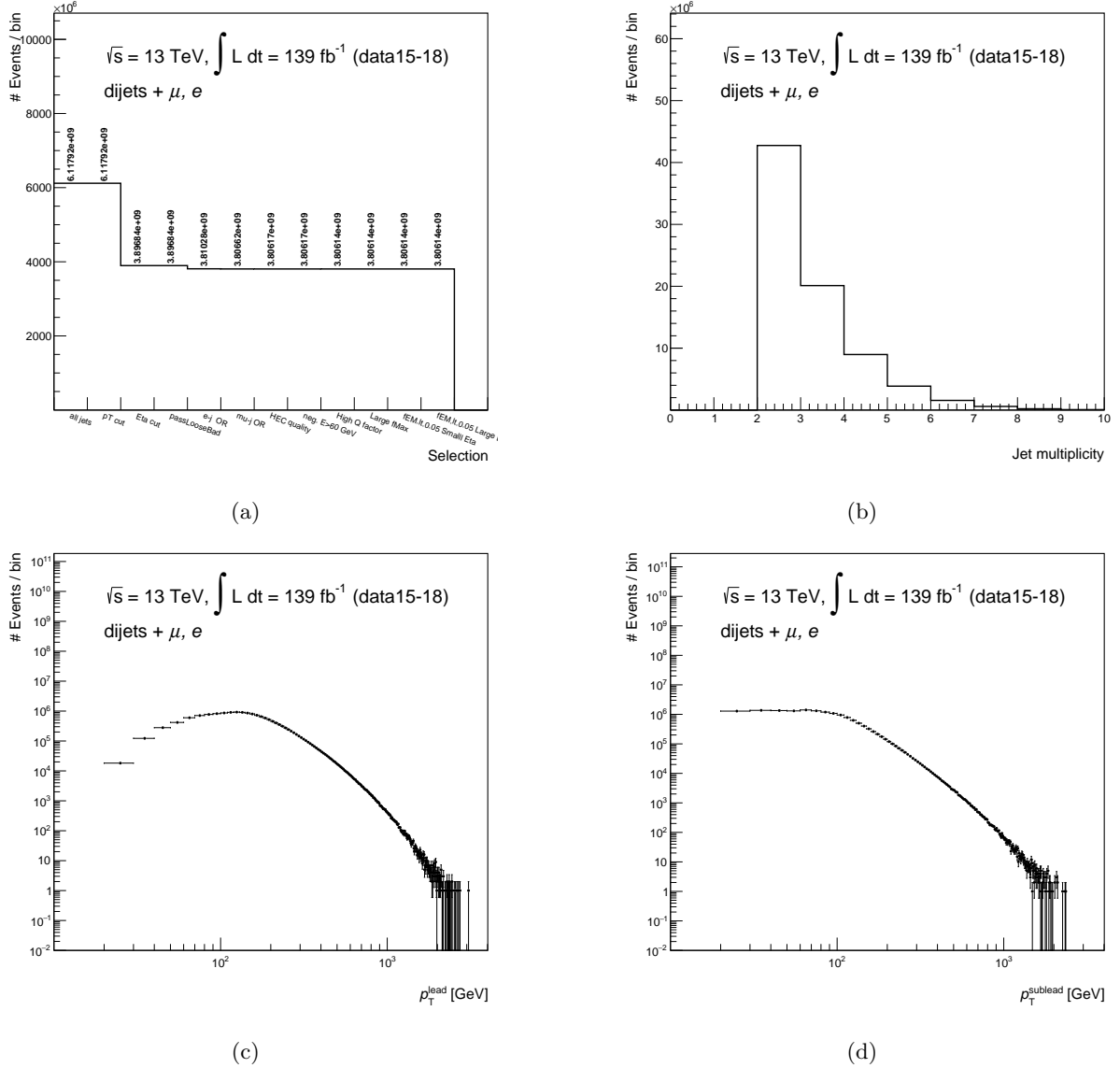


Figure 6.10: Jet cutflow, multiplicity, and p_T . Distributions (b)-(d) show only jets passing the SR selection criteria.

give an adequate description of the background.

To determine the quality of a given background estimate, the χ^2 test statistic is used, as well as the distribution of residuals (see Sec. 6.2). If the global fit and sliding window methods show similar compatibility, they are subject to additional tests of robustness (discussed in the next section).

6.8.1 Background hypothesis I: dijet function

Relative to the expected signals being sought out, SM backgrounds have very large cross sections. If there exists a smooth functional form that is capable of describing the overall shape of the m_{jj} spectrum, large statistics become advantageous; the overall background shape can be determined with high precision – independent of having knowledge of the detector response – by a fit of a parameterised function to the

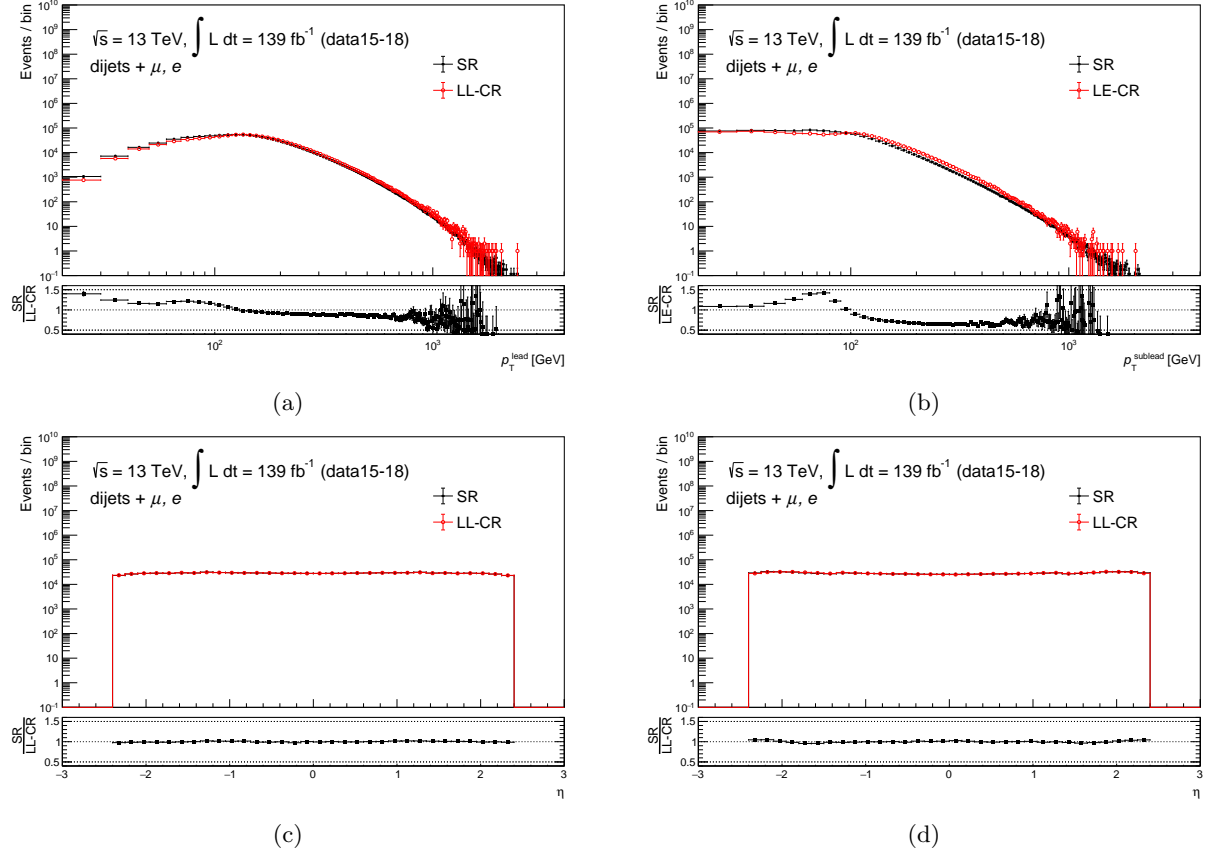


Figure 6.11: Comparisons between the SR and LL-CR for (a) leading jet p_T , (b) subleading jet p_T , (c) leading jet η , and (d) subleading jet η .

data, permitting small, localised excesses to be identified. The challenge to the global fit approach is the determination of an appropriate analytic parameterisation.

Previous dijet analyses have used a global fit method, wherein a single, few-parameter analytic function is used to describe the full range of a m_{jj} spectrum. While the background to be modelled consists mostly of QCD events, a complex mixture of parton distribution functions (PDFs), parton showering, and the effects of detector response and kinematic selections also plays a role in the underlying m_{jj} distribution. Fortunately, previous dijet analyses have been able to rely on a suite of functional forms that have so far worked well for this task – the family of so-called “dijet functions”.

The dijet functions take the form,

$$f_{3p} \equiv f(x|\theta) = \theta_0(1-x)^{\theta_1}x^{\theta_2} \quad (6.1)$$

where $x \equiv m_{jj}/\sqrt{s}$, and the θ_i are the parameters to be estimated. Starting roughly 20 years ago, searches applied the dijet function to increasingly larger datasets and wider ranges in m_{jj} , and Eq. 6.1 evolved.

With increasing integrated luminosity, statistical uncertainties are reduced, and finer features of the QCD-dominated spectrum become more apparent, leading to deviations between the measured spectrum and a relatively simple functional form. Past dijet analyses – *e.g.* [146, 161, 180, 181], as well as the

preliminary results from this analysis [225] based on an 80 fb^{-1} dataset – have shown that as dataset statistics increase in size, additional parameters are required to model m_{jj} distributions sufficiently well. This statement is based on the fact that several of the dijet functions’ parameters are most influenced by the large statistics at lower m_{jj} . As such, a number of functional forms are initially compared, the complete list of which are given in Eq. 6.27.

$$f_{4p} \equiv f(x|\theta) = \theta_0(1-x)^{\theta_1} x^{\theta_2+\theta_3 \ln x}, \quad (6.27a)$$

$$f_{5p} \equiv f(x|\theta) = \theta_0(1-x)^{\theta_1} x^{\theta_2+\theta_3 \ln x+\theta_4 \ln^2 x}, \quad (6.27b)$$

$$f_{5p}^{\text{alt}} \equiv f(x|\theta) = \theta_0(1-x)^{\theta_1} x^{\theta_2+\theta_3 \ln x+\theta_4/\sqrt{x}} \quad (6.27c)$$

Although seemingly *ad hoc*, there is a level of physics motivation behind the dijet functions [227]; the x^θ term is representative of the leading-order QCD matrix element, while the $(1-x)^\theta$ term is a common parameterisation for the behaviour of parton distribution functions that vanishes as x approaches unity.

This analysis considers a wider m_{jj} range comprised of larger statistics than previous searches; there is no *a priori* reason to expect a simple analytic function to remain suitable to describe the dataset. It needs to be shown whether the increased precision at which this analysis probes the m_{jj} distribution will resolve small differences between the analytic parameterisation and the true complexity of the underlying distribution.

6.8.2 Background hypothesis II: sliding window fit

Traditionally, resonance searches in dijet channels are conducted by looking for a localised excess above a smooth background. The smooth background is described by a global fit of the entire mass spectrum with *ad hoc* functional forms, *e.g.* the dijet functions described above. However, these functions are, of course, only approximations to the true underlying m_{jj} distributions. With increasing statistics their approximate nature becomes apparent, and obtaining a background model from these functions becomes increasingly more challenging, especially when the data span several orders of magnitude.

A method employed in the ATLAS dijet [162] and Trigger-Level [165] analyses, that were based on the 2015-2016 dataset of 36 fb^{-1} , is a sliding window fitting procedure (SWiFT) [228]. This method uses one of the *ad hoc* functional forms (f_{3p} , f_{4p} , f_{5p}) that “slides” across the m_{jj} spectrum, performing overlapping fits on a set number of localised bins (*i.e.* windows). A window is defined by some fixed number of bins around its center, which is positioned at bin boundaries. The algorithm is configured with a maximum value of m_{jj} , m_{jj}^{max} , beyond which a single fit is applied to the remaining bins not included in the slide. The SWiFT background is then extracted by fitting the combination of all overlapping windows using an analytic function.

The advantage of this method over the global fit is that it permits the analysis to move away from the situation in which the low-mass range of m_{jj} drives the optimisation of the fit parameters. This is because the smaller fit windows in the low-mass region are unaffected by those in the high-mass region. On the other hand, the SWiFT method is more complicated to correctly implement than a global fit. First of all, unlike the functional forms, it has several tunable parameters. For example, a window width (*i.e.* number of bins) needs to be defined and optimised manually by the user. Second, m_{jj}^{max} needs to be chosen in an optimal way, requiring significant study. Therefore, unless a significant improvement is found using the SWiFT method over the parameterised functions, the simpler method will be used for the search phase.

6.8.3 Resolution-based binning of the dijet invariant mass spectrum

A suitable choice of binning in the m_{jj} spectrum is important to the search phase of this analysis if the approach to describe the SM background is to use a smoothly-falling function. That is, the binned spectrum needs to preserve the smoothly-falling nature of the QCD background, and therefore the choice of binning should not introduce false bumps or kinks. It is also advantageous to have narrow bins to provide more inputs for the fit function, thus improving fit quality. However, the experimental resolution ultimately dictates the binning. The bin width for a given mass should be wide enough such that effects from bin-to-bin event migration due to resolution are limited. As such, a binning is used in this analysis respecting these constraints is derived starting from the dijet mass resolution of trigger jets, as employed in the ATLAS high-mass dijet search [179].

The result of the binning algorithm leads to an estimated m_{jj} resolution that varies between 0.07 at low m_{jj} to 0.03 at the highest values in the range considered, giving the following lower bin edges for the m_{jj} spectrum constructed in this analysis:

$$\begin{aligned} \text{Binning} = \{ & 216, 229, 243, 257, 272, 287, 303, 319, 335, 352, \\ & 369, 387, 405, 424, 443, 462, 482, 502, 523, 544, 566, 588, 611, 634, 657, 681, 705, 730, \\ & 755, 781, 807, 834, 861, 889, 917, 946, 976, 1006, 1037, 1068, 1100, 1133, 1166, 1200, \\ & 1234, 1269, 1305, 1341, 1378, 1416, 1454, 1493, 1533, 1573, 1614, 1656, 1698, 1741, 1785, \\ & 1830, 1875, 1921, 1968, 2016, 2065, 2114, 2164, 2215, 2267, 2320, 2374, 2429, 2485, 2542, \\ & 2600, 2659, 2719, 2780, 2842, 2905, 2969, 3034, 3100, 3167, 3235, 3305, 3376, 3448, 3521, \\ & 3596, 3672, 3749, 3827, 3907, 3988, 4070, 4154, 4239, 4326, 4414, 4504, 4595, 4688, 4782, \\ & 4878, 4975, 5074, 5175, 5277, 5381, 5487, 5595, 5705, 5817, 5931, 6047, 6165, 6285, 6407, \\ & 6531, 6658, 6787, 6918, 7052, 7188, 7326, 7467, 7610, 7756, 7904, 8055, 8208, 8364, 8523, \\ & 8685, 8850, 9019, 9191, 9366, 9544, 9726, 9911, 10100, 10292, 10488, 10688, 10892, 11100, \\ & 11312, 11528, 11748, 11972, 12200, 12432, 12669, 12910, 13156\} \text{ GeV.} \end{aligned}$$

The minimum value of $m_{jj} = 216$ GeV is used in all studies that follow.

6.8.4 Background modelling using Monte Carlo

Modelling the signal region in Monte Carlo

Complete knowledge of the m_{jj} distribution cannot be determined from data alone, since it is not possible to estimate the relative contributions from individual backgrounds. Therefore, MC simulations are used to gain some understanding of the m_{jj} spectrum.

The number of simulated events should ideally be comparable to, or larger than, the number of data events. However, because the simulated dataset size is insufficient compared to data, one therefore cannot draw rigid conclusions regarding the performance of the fit method when applied to data. Nevertheless, simulations are not random; they are based on SM predictions of the shape of the m_{jj} distribution that comprise SM events. Within statistical uncertainties, the simulated set of events entering the SR m_{jj} distribution is expected to form a relatively smooth, continuous shape.

If a background estimate method models the shape of the MC distribution well, it becomes a candidate

for estimating the distribution constructed from data. Otherwise, a poor description of the simulated distribution would be a strong indication that the background hypothesis is not suitable to model the SR.

The backgrounds used to construct the MC-based SR, detailed in Sec. 6.4, are multijet, $t\bar{t}$, and W +jet samples. Whereas $t\bar{t}$ and W +jet are inclusive samples, the multijet samples are generated in p_T “slices” (see Table 6.1).

All multijet slices are generated with roughly the same number of events, and each has an associated weight $w_i, i \in [0, 12]$ to give the expected physical shape to the combined set of slices. To normalise to the desired integrated luminosity, each slice is given its own weight, calculated approximately as,

$$w_s = \frac{\mathcal{L}_{\text{int}} \cdot \sigma \cdot \varepsilon_{\text{filter}}}{N_{\text{events}}}, \quad (6.28)$$

where \mathcal{L} is the integrated luminosity, σ and $\varepsilon_{\text{filter}}$ are the slice-dependent cross section and filter efficiency, respectively, and N_{events} is the number of events in the slice.

Figure 6.12 shows the results of likelihood fits using f_{4p} and f_{5p} applied to the SR constructed from MC events. Based on the χ^2/ndf test statistic alone, it is evident that both fit functions fail to adequately describe the distribution. The final-state lepton requirement results in large spikes in the multijet component of the MC-based background as a result of significant reduction in the already limited statistics. For the given statistical uncertainty in MC, there is no way to determine the best fit hypothesis of the two considered. However, the convergent fits to the MC m_{jj} spectrum demonstrate the dijet functions can be expected to adapt to the high-mass tail, the region which is typically difficult to model due to it having limited statistics.

Because SWIFT tends to be overly accommodating to bin-to-bin fluctuations, the spikes would cause drastic pulls of its fit. Therefore, SWIFT is used only for data in which the m_{jj} spectrum is smooth.

6.8.5 Modelling the LL-CR

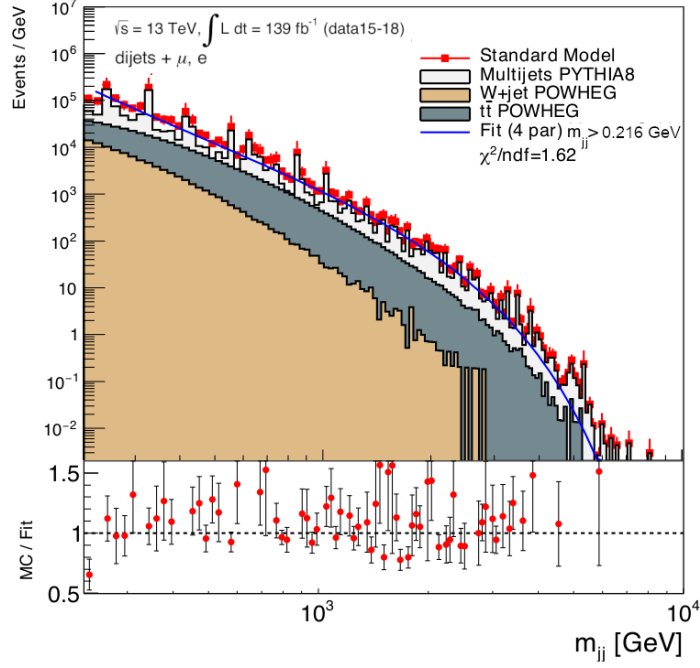
Determination of the most suitable fit hypothesis for the data-based SR is not possible using MC simulations alone. Therefore, before observing the SR in data, the LL-CR is used for additional studies of the fit hypotheses. For the LL-CR global fit, f_{4p} and f_{5p} , as well as the SWIFT method, are tested.

To represent the fit quality of each of the functions, the agreement between data and the fit hypothesis is expressed in terms of the bin-by-bin significance, calculated via the fit residuals as,

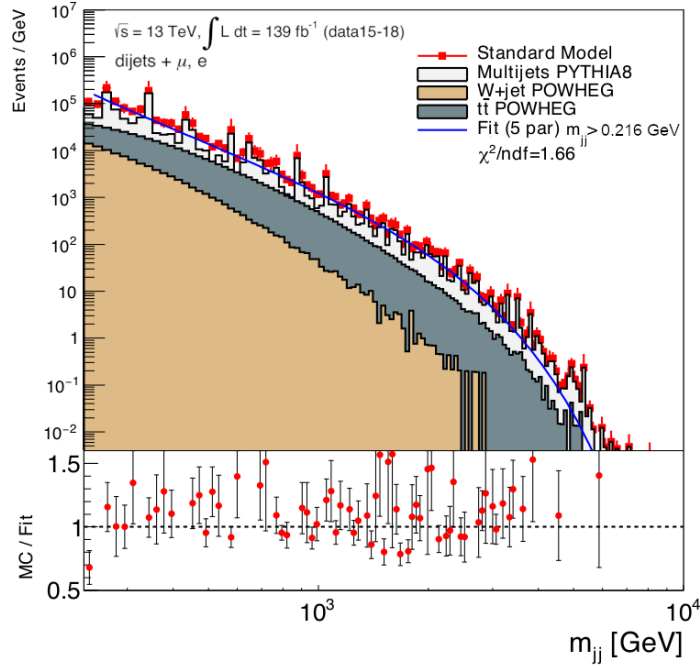
$$S_i = \frac{D_i - F_i}{\Delta D_i} \quad (6.29)$$

where D_i is the content of bin i of the data distribution, F_i is the value of the function after minimisation, and ΔD_i is the uncertainty on the bin, $\sqrt{D_i}$. Note that this definition of S_i does not include uncertainties associated with the fit hypothesis itself; background estimate uncertainties are discussed later, in Sec. 6.11, and are included in the limit-setting procedure as nuisance parameters.

Figures 6.13 and 6.14 (a) show the f_{4p} , and f_{5p} fits to the LL-CR, with the bin-by-bin significances shown in the lower panels. In the same figures, plot (b) shows the distributions of the residuals which are expected to follow a normal distribution in the case of a good quality fit. To test for normality, the Shapiro-Wilk test is used, complemented by the Kolmogorov-Smirnov (KS) test which gives the probability that two samples come from the sample distribution. The Shapiro-Wilk test gives values

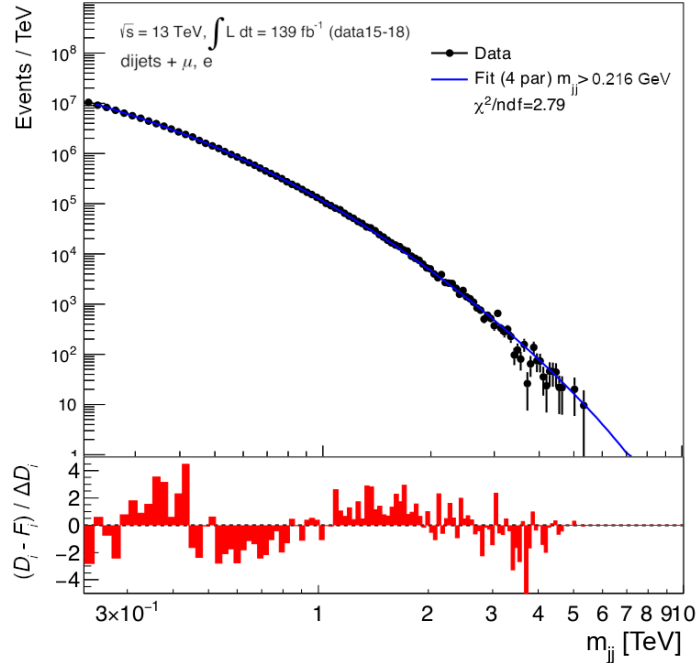


(a)

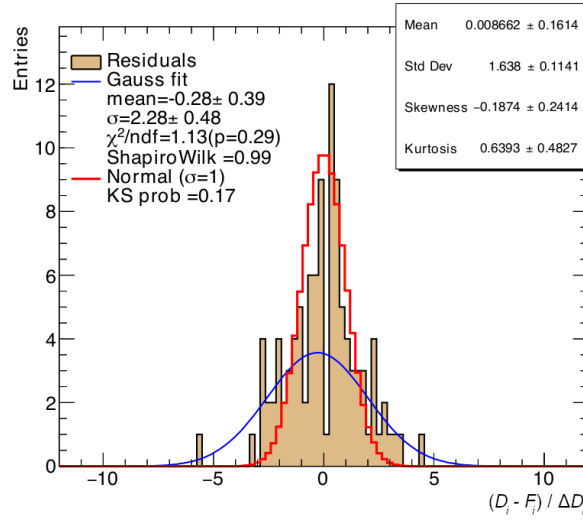


(b)

Figure 6.12: Distributions of the SR constructed from MC simulations, fitted with the (a) f_{4p} and (b) f_{5p} functions. In the lower panels, the ratios between MC and the corresponding fit are shown. The red line specifies the sum of all SM contributions to the m_{jj} distributions. The large spikes originate from multijet JZ0-JZ12 slices due to the significant reduction of statistics after requiring a final-state lepton.



(a)

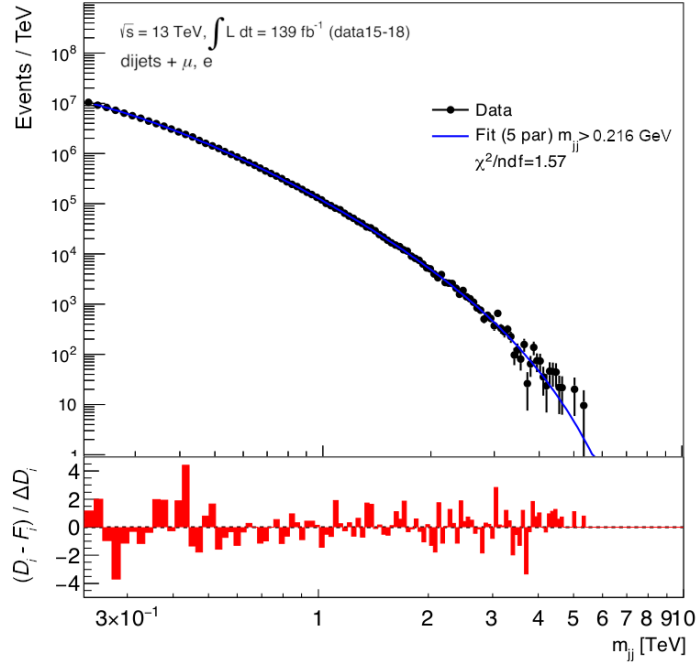


(b)

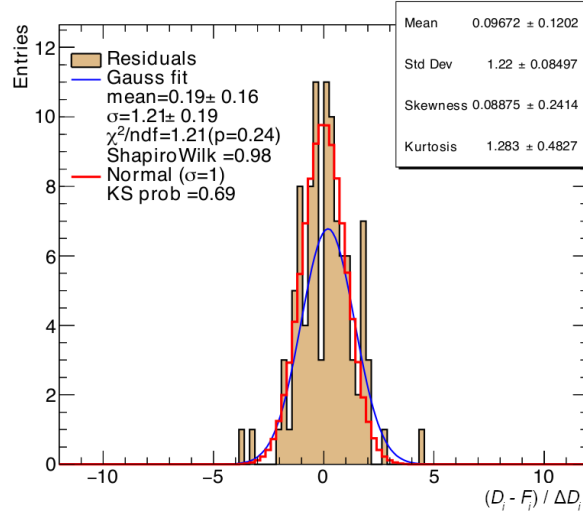
Figure 6.13: Distributions of (a) the f_{4p} fit to the LL-CR, with the bin-by-bin significances in the lower panel, and (b) the distribution of residuals from the fit.

close to one for good quality fits, while for the KS test a value greater than 0.05 is sufficient. A χ^2/ndf goodness-of-fit is also evaluated on the residuals with respect to a normal distribution. All test statistics are evaluated with respect to a normal distribution with mean $\mu = 0$ and standard deviation $\sigma = 1$.

The studies in the LL-CR using the global fit approach indicate f_{5p} outperforms f_{4p} . In particular, f_{4p} gives a $\chi^2/\text{ndf} > 2$; with a $\chi^2 = 304.11$ and $\text{ndf} = 109$, the resulting p -value is less than 0.0001, indicative of a poor fit. The sinisoidal shape of f_{4p} residuals in Fig. 6.13a is reflected by the KS probability, $p = 0.17$. This is due to the fact that although the residuals follow approximately a normal



(a)

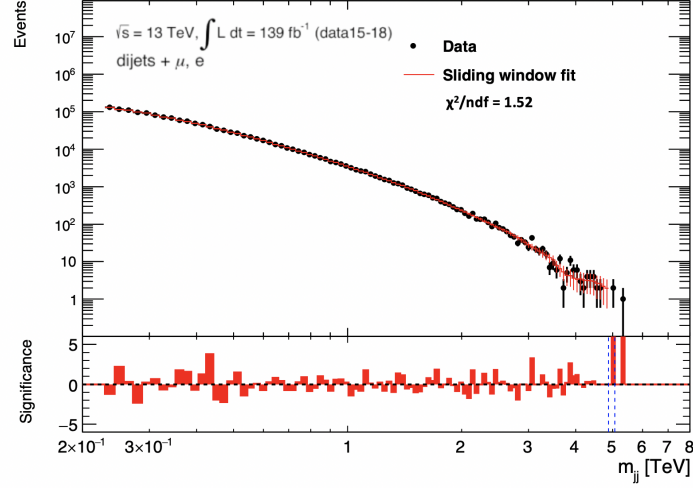


(b)

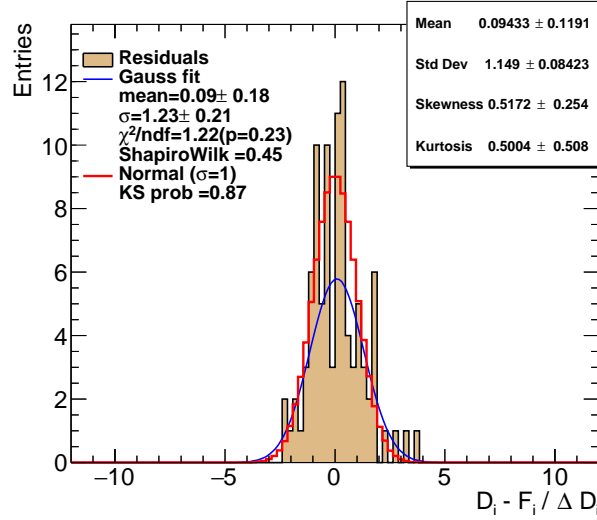
Figure 6.14: Distributions of (a) the f_{5p} fit to the LL-CR, with the bin-by-bin significances in the lower panel, and (b) the distribution of residuals from the fit.

distribution (demonstrated by the Shapiro-Wilk test), the standard deviation of the residuals is $\sigma > 1$ (addressed by the KS test). On the other hand, f_{5p} yields a $\chi^2 = 171.13$ and a p -value of roughly 0.0001, however does not show any sinusoidal behaviour of its residuals, and all test statistics of the residuals are in good agreement with a normal distribution.

In the second approach used to describe the LL-CR, SWIFT is configured with f_{5p} that is used to fit windows which vary in the number of bins they contain; as per Ref. [228], the windows should be at least three times the width of the widest signal considered. It can be seen in Fig. 6.15 that the SWIFT method



(a) LL-CR fit using SWiFT.



(b) SWiFT residuals.

Figure 6.15: Distributions of (a) the SWiFT method to describe to the LL-CR, with the bin-by-bin significances in the lower panel, and (b) the distribution of residuals from the fit.

description of the LL-CR is compatible with that of f_{5p} (Fig. 6.14) with $\chi^2 = 165.68$, $\text{ndf} = 109$, $p\text{-value} = 0.0004$, and residuals statistically consistent between the two fits. The KS probability in the SWiFT case is slightly greater than that of f_{5p} , however a firm conclusion cannot be drawn based on this statistic alone.

6.9 Robustness of the background estimates

In addition to the statistical tests performed above to evaluate the suitability of a given fitting procedure to describe the SM background, it is useful to also investigate the robustness of each estimate in terms of *spurious signals* and sensitivity to *injected signals*. In the case that more than one fit hypothesis are shown to describe the SM background equally well, these tests can determine more rigorously which

estimate should be used in the search phase.

All tests in this section are performed on pseudodata generated from the f_{5p} hypothesis, with fit parameters determined from the LL-CR (Sec. 6.8). The number of pseudodata events is scaled to match that in the SR.

6.9.1 Signal injection test

Signal injection tests are used to study and estimate the signal extraction efficiency. If a given background fit procedure is overly accommodating to features akin to a signal, it will lead to a poor signal sensitivity.

The questions that the signal injection tests aim to address are:

1. How sensitive is the fit hypothesis to the presence of signals introduced in pseudodata?
2. What is the signal extraction efficiency?
3. Given that two background hypotheses apparently describe data equally well, which one should be used in the search phase?

To answer these questions, the following procedure is used:

- Step 1:** Create a set of random histograms using the f_{5p} fit to the LL-CR, scaled to the expected number of events in the SR.
- Step 2:** Calculate the number of events, N_{events} , for each bin of the background distribution over which a Gaussian of a given mass and width will be added. Using $N_{\text{inj}} = 5 \times \sqrt{N_{\text{events}}}$ to approximate 5σ signal strengths, create Gaussian histograms with N_{inj} events for masses between $250 \leq m_{jj} \leq 6000$ GeV at widths $\sigma_G/m_G = \{5, 10, 15\}\%$, and add them to the background templates constructed in Step 1.
- Step 3:** Fit the Gaussian-plus-background histogram constructed in Step 2 with the background-only hypothesis and a signal-plus-background hypothesis.
- Step 4:** For the background-only hypothesis, count the number of events above the background within $\pm 1.5\sigma$ of the peak position; wider widths are more susceptible to statistical fluctuations for small signal amplitudes considered. For the signal-plus-background hypothesis, the number of extracted events is given by the integral of the Gaussian component of the fit.
- Step 5:** Calculate the efficiency, $\epsilon = N_{\text{obs}}/N_{\text{inj}}$, the ratio of the number of observed events to the number of injected events.

Background-only hypothesis

Figure 6.16 shows the efficiency, $\epsilon = N_{\text{obs}}/N_{\text{inj}}$, for the extraction of Gaussian-shaped signals with masses of $\{250, 500, 1000, \dots, 6000\}$ GeV and widths $\sigma_G/m_G = \{5, 10, 15\}\%$, as well as RMS uncertainties, determined by f_{5p} and the SWIFT-based hypotheses. The number of signal events is counted as those above the fitted background estimate within 1.5σ about the Gaussian peak. Note that for a Gaussian of width $\sigma_G/m_G = 15\%$ the study begins at $m_{jj} = 500$ GeV since a fraction of the signal would be lost at the lowest mass point considered. The distributions were produced from 100 sets of pseudodata

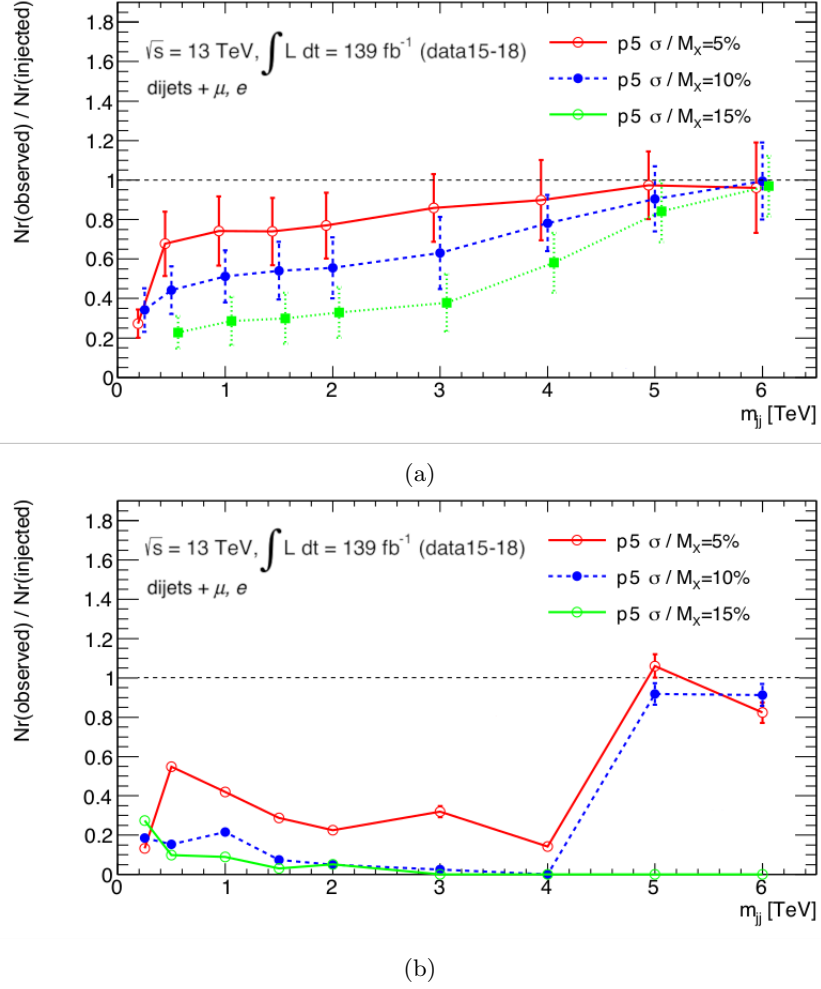


Figure 6.16: Search sensitivity, $N_{\text{obs}}/N_{\text{inj}}$, to Gaussian signal shapes of several widths as a function of signal mass using (a) f_{5p} and (b) SWiFT as the background-only hypotheses. The uncertainties on the data points correspond to the RMS values on the ratios.

constructed from the f_{5p} fit to the LL-CR with Poisson fluctuations applied to each bin. It can be seen that the sensitivity to signals of mass $m_X = 250$ GeV with widths between 5% and 15% is quite low, approximately 30%. For $m_{jj} > 250$ GeV, the narrow 5% width signal sensitivity increases to roughly 70% as its peak becomes more prominent above the background, as opposed to the 10% width signal sensitivity that increases to about 50%, due to a less pronounced peak. For the largest signal width, $\sigma_G/m_G = 15\%$, considered, only modest increases in sensitivity are seen until $m_{jj} \approx 3.5$ TeV, at which point the sensitivity matches that of the narrower widths at lower mass.

In contrast to the f_{5p} hypothesis, it can be seen that SWiFT is overly accommodating to injected signals, with mostly negligible efficiencies for $m_{jj} < 4$ TeV; there is no possibility to recover any signal for a Gaussian with a 15% width. Therefore, SWiFT is not considered further, and the nominal background estimate will come from the f_{5p} .

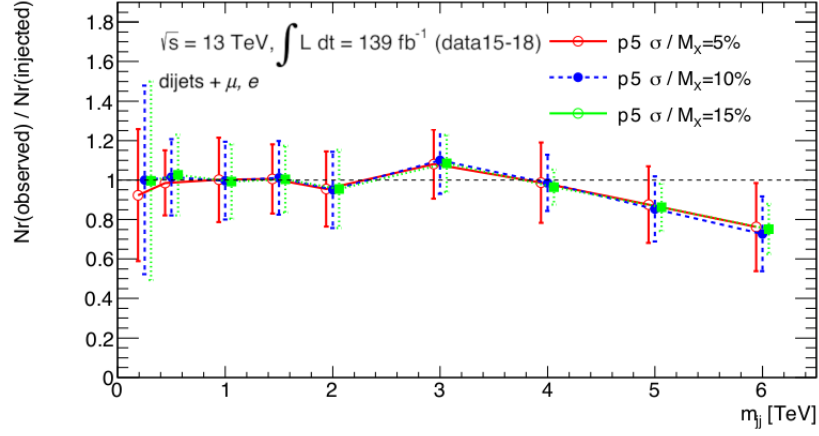


Figure 6.17: Signal extraction efficiency of injected Gaussian signals as determined using the f_{5p} -plus-Gaussian hypothesis in the LL-CR. The details of the plot are found in the text.

Signal-plus-background hypothesis

Another estimate for the sensitivity to injected signals is to use a signal-plus-background hypothesis, in which it is assumed *a priori* that a signal is present in the data. The aim here is to determine the strength, or signal *extraction efficiency* using a Gaussian (signal) component in the fit to test the search procedure in the presence of a signal.

The efficiency to reconstruct injected signals using the f_{5p} -plus-Gaussian hypothesis is shown in Fig. 6.17. As in the background-only study, efficiency calculations were made using 100 sets of pseudodata injected with Gaussian signals with 5σ signal strengths. To facilitate the convergence of the 8-parameter fit, the peak positions and widths of the injected Gaussians are fixed. The number of extracted events is calculated as the integral of the Gaussian component of the fit. Points shown correspond to the average values of the ratio $N_{\text{obs}}/N_{\text{inj}}$ among the 100 sets of pseudodata, and the uncertainties correspond to the RMS of the ratio. As expected, the efficiency is much higher when a signal component is included in the fit, as opposed to the case of the background-only fit. This indicates that the search methodology is able to successfully identify the injected signal at the correct mass.

6.9.2 Spurious signal test

In order to gauge how sensitive the choice of the background estimate is to statistical fluctuations that could fake a signal, a *spurious signal* test is performed. A spurious signal is defined as a significant, localised excess or deficit in a distribution due to differences between the shape in data and that of the estimate. If the background estimate exhibits such behaviour, the window in which the spurious signal appears must either be excluded, or the estimate abandoned altogether. In the case that the background estimate is observed to be sensitive to spurious effects, a systematic uncertainty must be assigned to cover the fit bias. On the other hand, if no statistically significant spurious signal is found, no additional uncertainty need be introduced.

A function “passes” this test if, in the mass range of interest:

1. it does not produce a mean number of spurious signal events exhibiting systematic deviations from zero; and

2. the RMS of the number of spurious signal events does not exceed a certain fraction of the expected statistical uncertainty of the background.

For model-agnostic searches such as this, where no assumption on the signal production cross section is made, this fraction is typically set to 50% of the expected background statistical uncertainty.

In order to test for the presence of a spurious signal in the m_{jj} distribution, 100 templates are created from pseudodata produced from the LL-CR. The initial f_{5p} parameters, θ_i , are taken from the fit to the LL-CR (see Sec. 6.8.4) for this test. A combined f_{5p} -plus-Gaussian fit is applied to all templates beginning at $m_{jj} = 250$ GeV, and is scanned across the distributions in 500 GeV increments. During this mass scan, the peak position and width of the Gaussian component are fixed for a given signal mass point and expected width, while the amplitude of the Gaussian is left as an unconstrained free parameter. A spurious signal is characterised by the amplitude, A , of the Gaussian, and uncertainty, δA , determined by the fit. The value of A is converted into a cross section by dividing it by the integrated luminosity of the dataset considered, taking into account bin width and normalisation.

For each of the 100 pseudodata templates, the Gaussian amplitude $A_i, i \in \{1, \dots, 100\}$, is determined. Then the RMS, $A_{\text{rms}} = \sqrt{1/100 \sum A_i^2}$, is calculated. A strong indicator of no spurious signal is, within statistical uncertainties, $\langle A \rangle \approx 0$.

The number of extracted events using the Gaussian component of the f_{5p} -plus-Gaussian fit for arbitrary fixed widths of 10% and 15% were calculated, and all amplitudes are statistically consistent with zero. Figure 6.18 shows the more flexible case, when all parameters of the f_{5p} -plus-Gaussian fit are unconstrained and free to float. Although the observed spread is larger than when the fit is completely constrained, the observed Gaussian amplitudes are nonetheless statistically consistent with zero. Therefore, either when the fit is fully constrained or unconstrained, no spurious signal is detected, thus confirming the robustness of the choice of fit hypothesis.

6.10 Search phase

The search phase is where the results of previous studies are applied to the SR, and it is established whether or not an excess in data exists. In this section, the search strategy is defined, and studies performed earlier in the LL-CR are repeated to evaluate the fit procedure as applied to the SR.

6.10.1 Search strategy

The main statistical test employed in this analysis to establish the presence or absence of a signal in the m_{jj} distribution is based on the BUMPHUNTER algorithm [185, 229]. The algorithm operates on the binned m_{jj} spectrum, comparing the background estimate with the data in mass intervals of varying contiguous bin multiplicities.

In its present implementation, the BUMPHUNTER algorithm starts with a *signal window*, comprising two bins, that is scanned across the full m_{jj} distribution. The window increases in size by adding one additional bin following every scan until all possible bin ranges, up to half the mass range spanned by the data, have been tested. At each point in the scan, the significance is computed as the difference between the data and the background. The most significant departure of the data from the smooth background estimate (*i.e.* the *bump*) is defined by the set of bins that have the smallest probability of arising from a background fluctuation.

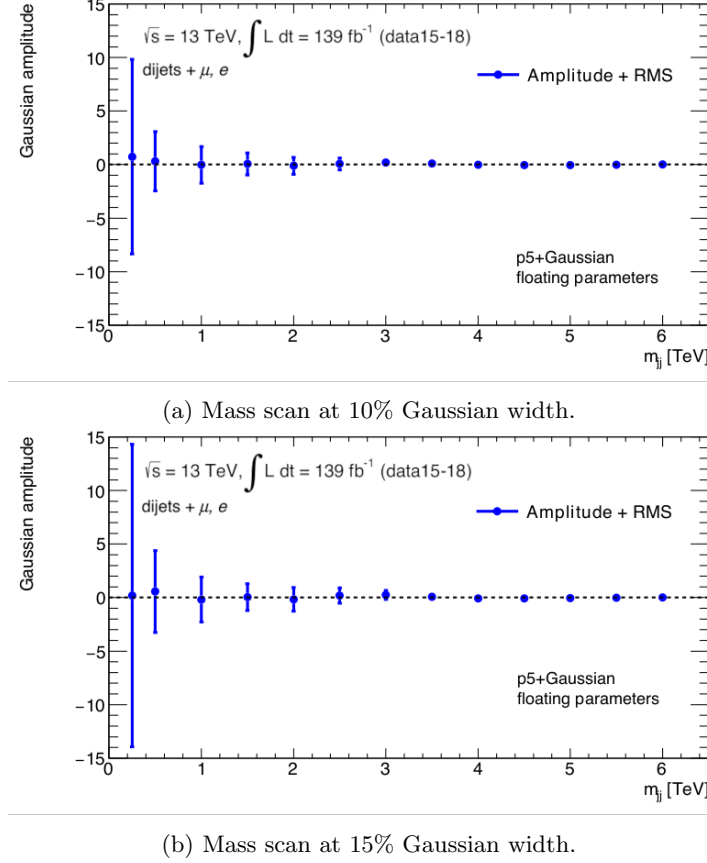


Figure 6.18: The average values of the Gaussian amplitudes calculated from the f_{5p} -plus-Gaussian fits applied to 100 random templates constructed from the LL-CR. The parameters of the f_{5p} component are allowed to float. The vertical error bars represent the RMS of the amplitudes.

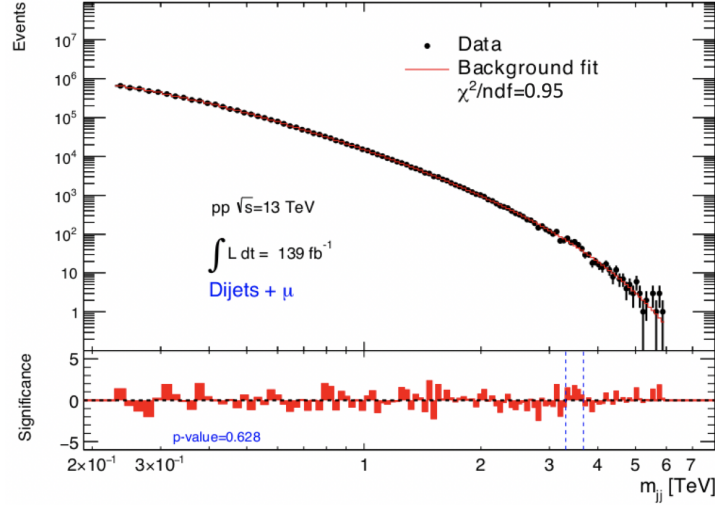
The BUMPHUNTER algorithm takes into account the so-called “look-elsewhere effect” [230, 231]. This is achieved by performing a series of pseudo-experiments – drawn from the background estimate – in order to determine the probability that random fluctuations in the background-only hypothesis would create an excess, at least as significant as the most significant one observed, anywhere in the spectrum.

Lastly, to make practical use of this algorithm, it must be ensured that any new physics signal will not bias the background estimate. If the most significant excess has a local χ^2 p -value smaller than 0.01, another background fit is performed with this region removed. No such exclusion was necessary in this analysis.

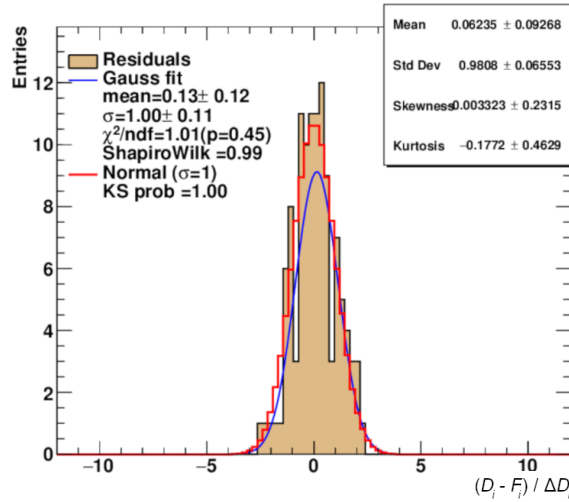
6.10.2 Describing the SR using f_{5p}

A first study to describe the SR is performed using a likelihood (LH) fit to the muon and electron channels’ dijet invariant mass spectra using f_{5p} in the range $216 < m_{jj} < 6300$ GeV.

The results of the fit applied separately in the muon and electron channels are presented, respectively, in Figs. 6.19, and 6.20, along with the corresponding distributions of residuals. The quality of the fit is given in terms of the χ^2/ndf and corresponding p -value. In the lower panel of the figures is the BUMPHUNTER significance, as well as the reported global p -value of the most significant deviation. The f_{5p} hypothesis describes the data well, and no significant deviation is observed in the independent



(a)



(b)

Figure 6.19: Distributions of (a) the dijet invariant mass spectrum for $m_{jj} > 216$ comprising muon events with the f_{5p} LH fit applied. The lower panel shows the results from the BUMP HUNTER algorithm, along with the reported global p -value. In (b) the residuals of the fit are shown.

channels.

6.10.3 Robustness tests of f_{5p} in the SR

Figure 6.21 shows the comparison between the SR and LL-CR m_{jj} spectra. The LL-CR is scaled to the number of events in the SR. A slow decrease in the ratio SR/LL-CR is observed beginning at $m_{jj} \approx 300$ GeV, with a difference at the level of about 20% beyond $m_{jj} > 2$ TeV. In view of this difference in shape between the SR and LL-CR, it is important to assess the signal reconstruction efficiency in the SR and its susceptibility to spurious signal.

The following tests are conducted using pseudodata generated from a f_{5p} fit to the SR, and follow the same procedure performed in Sec. 6.9 in the LL-CR.

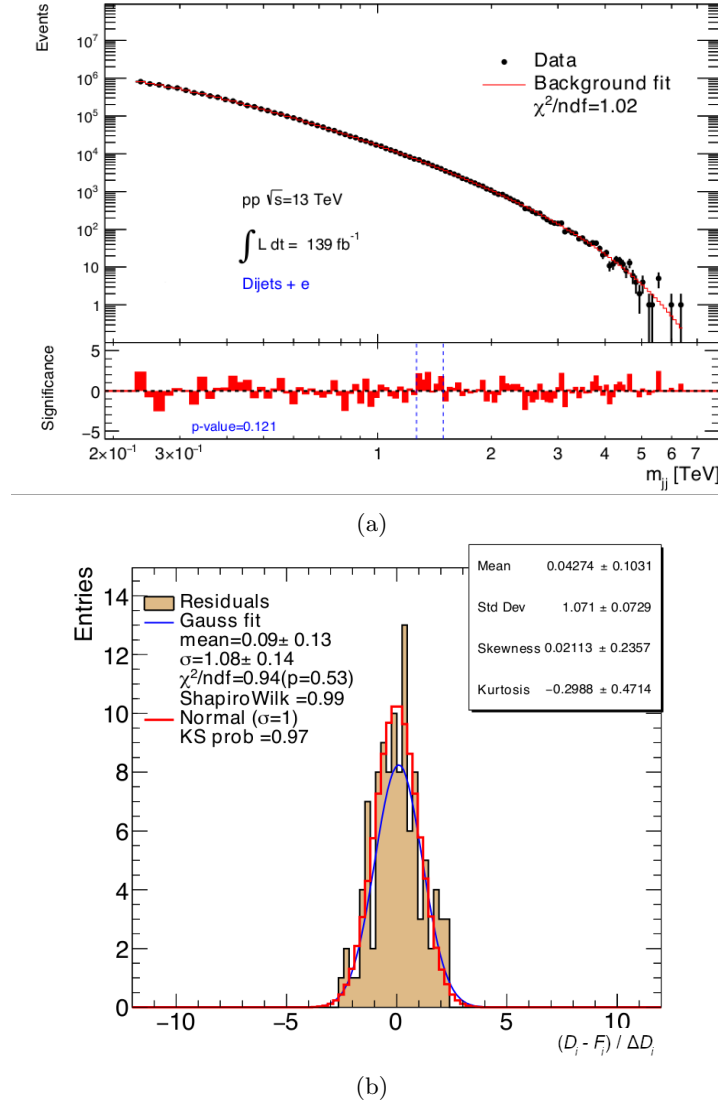


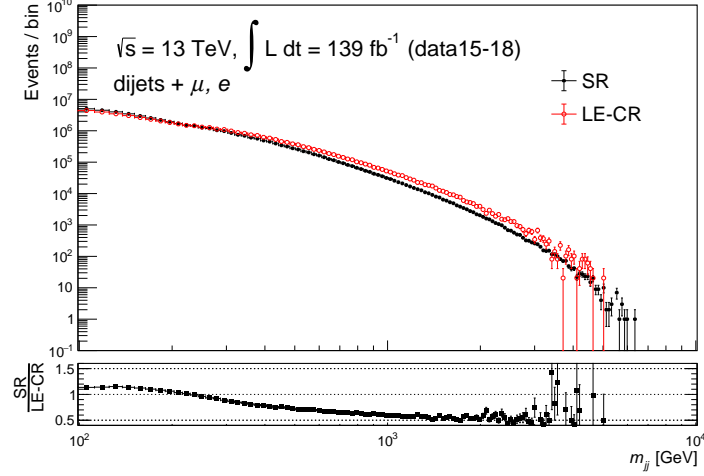
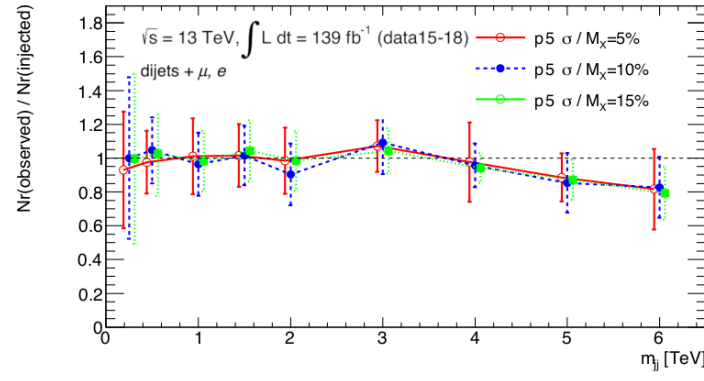
Figure 6.20: Distributions of (a) the dijet invariant mass spectrum for $m_{jj} > 216$ comprising electron events with the f_{5p} LH fit applied. The lower panel shows the results from the BUMPHUNTER algorithm, along with the reported global p -value. In (b) the residuals of the fit are shown.

SR signal injection test

Figure 6.22 shows the signal extraction efficiency using the f_{5p} -plus-Gaussian fit. The efficiency in the SR is similar to that in the LL-CR, with slight improvements of 2-3% for wider signal widths of 10% and 15% and at high $m_{jj} > 4$ TeV. Although small, the improvements yield efficiencies statistically compatible with 100%.

SR spurious signal test

The distributions for the number of extracted events using the Gaussian component of the f_{5p} -plus-Gaussian fit for fixed widths of 10% and 15% are presented in Fig. 6.23. All parameters of the f_{5p} component of the fit are unconstrained and free to float. As in the LL-CR, all amplitudes are statistically

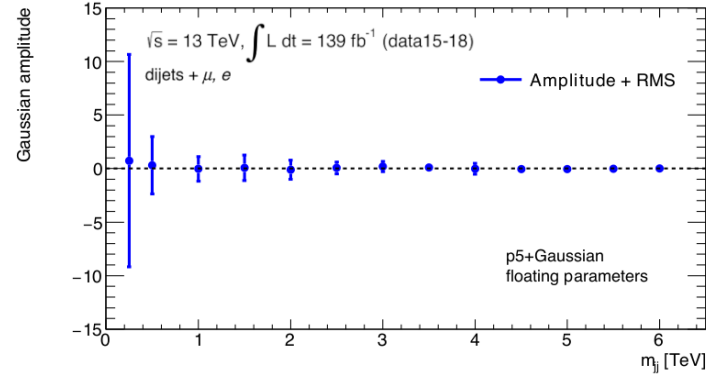
Figure 6.21: Comparison between the SR and LL-CR m_{jj} distributions.Figure 6.22: Signal extraction efficiency of injected Gaussian signals as determined using the f_{5p} -plus-Gaussian hypothesis in the SR. The details of the plot are found in the text.

consistent with zero. It is therefore concluded no detrimental spurious signal exists, thereby confirming the robustness of the f_{5p} fit to the SR.

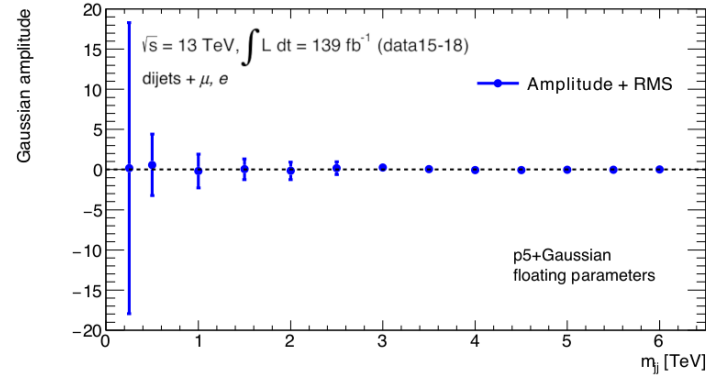
6.10.4 Results

As done earlier in the individual electron and muon channels, a LH fit based on the f_{5p} hypothesis is used to describe the combined dijet+lepton m_{jj} spectrum in the range $216 < m_{jj} < 6300$ GeV.

The result of the LH fit is presented in Fig. 6.24, along with the distribution of residuals. The quality of the fit is again given in terms of the reduced χ^2 statistic. Based on the this statistic alone, the fit hypothesis describe the SR data well, with $\chi^2 = 100.28$, $\text{ndf} = 109$, and $p\text{-value} = 0.71$. In the lower panel of the figures is the bin-by-bin BUMP HUNTER significance, as well as the reported global p -value.

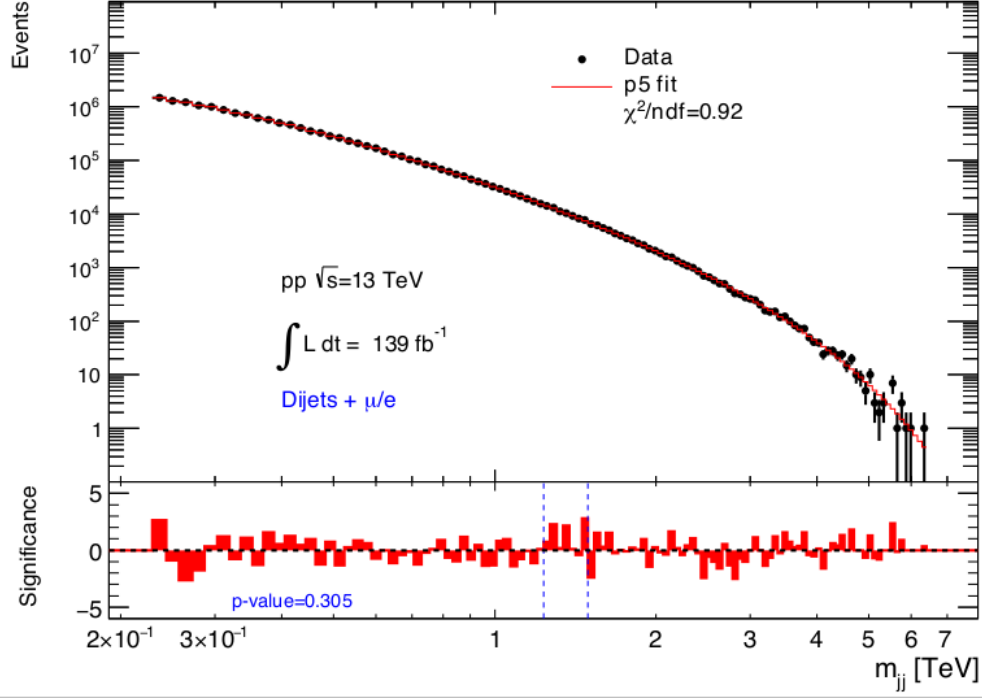


(a) Mass scan at 10% Gaussian width.

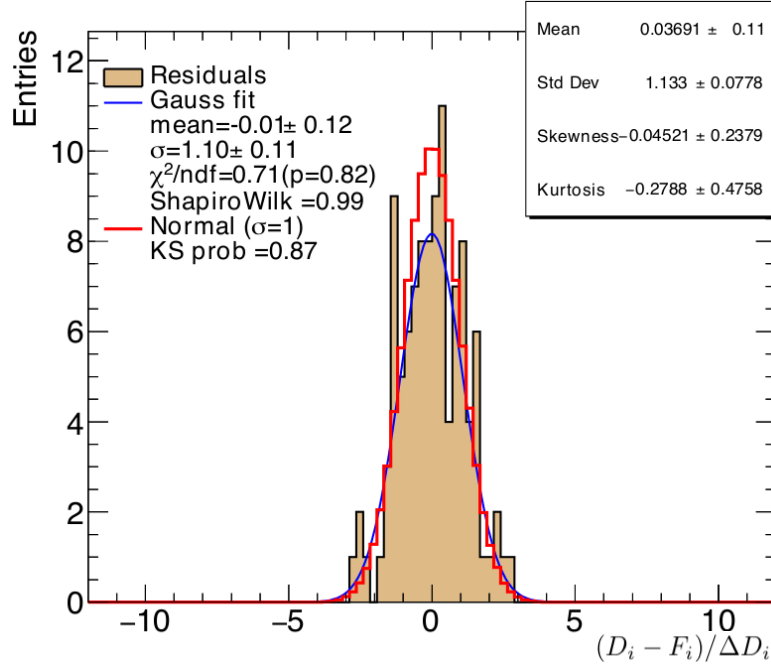


(b) Mass scan at 15% Gaussian width.

Figure 6.23: The average values of the Gaussian amplitudes calculated from the f_{5p} -plus-Gaussian fits applied to 100 random templates constructed from the f_{5p} background-only hypothesis. The parameters of the f_{5p} component are allowed to float in the fit. The vertical error bars represent the RMS of the amplitudes.



(a)



(b)

Figure 6.24: Distribution of (a) the dijet invariant mass distribution constructed from events with at least one isolated lepton (μ or e) with $p_T > 60$ GeV using 139 fb^{-1} of pp data collected by the ATLAS experiment during Run-2, between the years 2015-2018. The upper panel shows the data together with the background-only fit hypothesis (solid red line), corresponding to $\chi^2/\text{ndf} = 0.92$, with $\chi^2 = 100.28$ and $\text{ndf} = 109$, in the considered mass range, $216 < m_{jj} < 6300$ GeV. In the lower panel, the bin-by-bin significances of the data-fit differences [185] as calculated by the BUMPHUNTER algorithm. The vertical dashed (blue) lines indicate the most discrepant m_{jj} interval. Taking into account the look-elsewhere effect, this most significant deviation corresponds to $p\text{-value} = 0.305$. In (b) the residuals of the fit are shown to be consistent with a normal distribution.

As indicated in the lower panel by the dashed (blue) vertical lines, the largest deviation is a 7-bin excess in the interval $1.23 \leq m_{jj} \leq 1.49$ TeV. Considering only statistical uncertainties, this deviation corresponds to a global p -value of 0.305, according to the BUMPHUNTER statistic, which takes into account the look-elsewhere effect. When transformed into a significance in terms of an equivalent number of standard deviations (the so-called “ Z ”-value), the p -value corresponds to 0.5σ . Based on the channel-specific distributions Figs. 6.19 (dijets+muon) and 6.20 (dijets+electron), the largest deviation is attributed to the electron channel.

Figure 6.25 shows a so-called “tomography” plot of the windows tested by the BUMPHUNTER algorithm, indicated by the horizontal lines of different widths and location that span x -axis, and the y -axis which gives the value of the BUMPHUNTER test statistic obtained for a given window. Figure 6.26 compares the BUMPHUNTER statistic obtained for each pseudo-experiment (blue) to that observed in real data (red arrow). The probability of obtaining a deviation at least as significant as the reported excess is determined by the number of events below the arrow.

It is concluded that no significant excess, indicative of new physics beyond the SM, is observed in the dijet invariant mass distribution as constructed in this analysis using the full Run-2 ATLAS pp dataset.

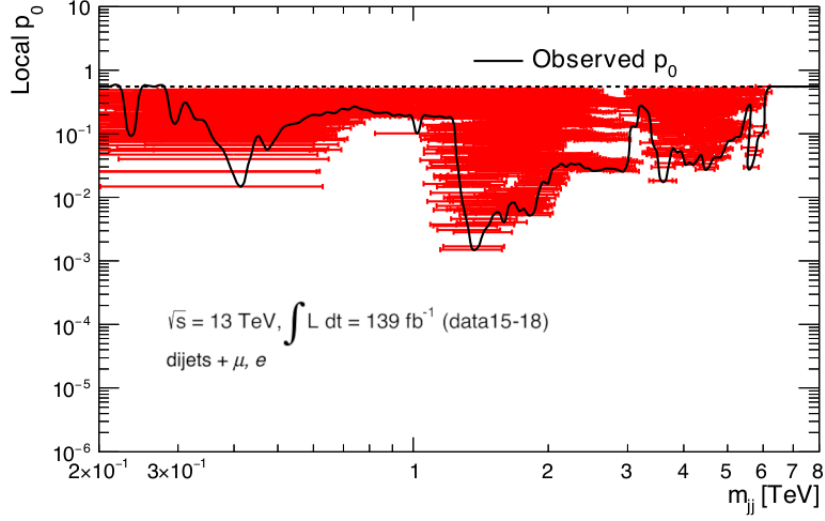


Figure 6.25: The accompanying “tomography” plot to Fig. 6.24, indicating the Poisson probability associated with each possible set of bins in the dijet invariant mass distribution. The BUMPHUNTER algorithm searches in every consecutive set of bins for the most discrepant region, and calculates the p -value associated with the observed excess or deficit, assuming Poisson statistics in the combined set of bins. Each horizontal (red) line spans a set of bins under consideration and the vertical location indicates the calculated local p -value associated with the observed data in that set of bins. The most discrepant intervals are indicated by the locations where the smooth black curve intersects with a red horizontal line.

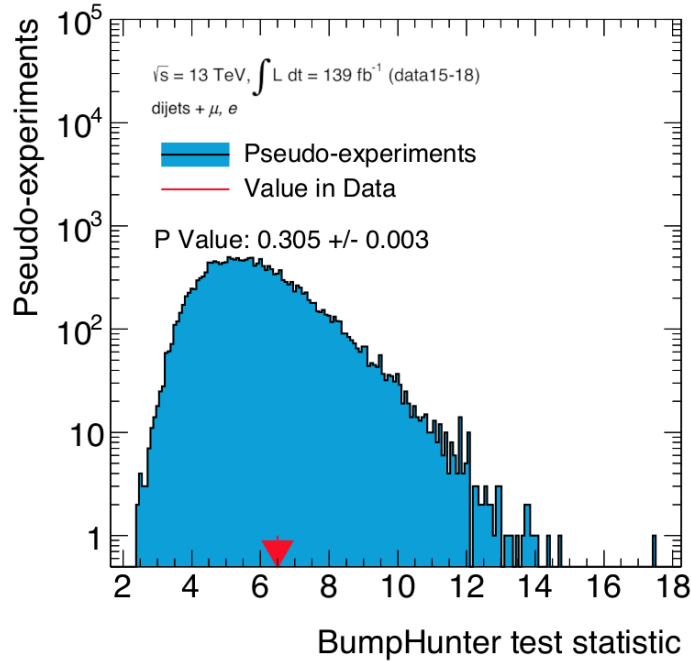


Figure 6.26: Comparison between the observed BUMPHUNTER test statistic and the test statistics resulting from the pseudoexperiments. The blue histogram represents the values from pseudo-experiments, and the red arrow indicates the measured value in data. The p -value of the measurement is defined to be the fraction of pseudo-experiments resulting in a more extreme BUMPHUNTER test statistic than was observed in data.

6.11 Systematic uncertainties

This section details the full set of uncertainties pertaining to the background estimate and signal considered in this analysis. All uncertainties discussed are included as nuisance parameters in the limit-setting procedure, described in Sec. 6.12.

Systematic uncertainties are split into two categories: those relevant to the background estimate, and those relevant to the signal. There are two types of systematic uncertainties associated with the background estimation method:

- The choice of the background-only hypothesis, since the specific form chosen is somewhat arbitrary, and other parameterisations not tested could be equally as suitable to describe the background.
- The statistical uncertainty related to the quality of the fit result that depends on the statistical precision of the data, and therefore affects the precision of the fit function parameters.

Uncertainties associated with jets, leptons, triggers, luminosity, and parton distribution function (PDF) are considered for signal.

The details of each set of uncertainties are provided below. A summary of all systematics is presented at the end of this section, in Table 6.8.

6.11.1 Background estimate uncertainties

Function choice

As discussed in Sec. 6.8, the function with the best χ^2 value and residuals most consistent with a normal distribution is taken as the “nominal” background-only hypothesis, f_{5p} . An alternative function, f_{5p}^{alt} , was found to give a fit quality compatible with the nominal f_{5p} . This alternative function was employed also in the preliminary results of this analysis [225], and takes a similar form to the nominal function of Eqn. 6.27b,

$$f_{5p}^{\text{alt}} \equiv f(x|\theta) = \theta_0(1-x)^{\theta_1}x^{\theta_2+\theta_3 \ln x+\theta_4/\sqrt{x}}, \quad (6.27c)$$

where the replacement $\ln^2 x \rightarrow 1/\sqrt{x}$ is made with respect to f_{5p} .

In light of having two functions that provide statistically compatible estimates of the background, there is no *a priori* reason to prefer one over the other. Moreover, many other functions not considered in this analysis may also exist that are compatible with the ones chosen. Therefore, a systematic is assigned to account for the choice of one function over another.

The function choice uncertainty is determined by the relative difference between the nominal and the alternate functions that is calculated in each bin. A collection of pseudodata are generated from the nominal background estimate, and from each both a nominal and alternative background is derived. To define the $\pm 1\sigma$ function choice uncertainty, bin-by-bin differences between the nominal and alternate background estimates, $\Delta b_i(f_{5p}, f_{5p}^{\text{alt}})$, are calculated and scaled to the root mean square of the difference. The uncertainty is then represented by a Gaussian prior on a parameter $\theta_{\text{FC}} \in [0, +1\sigma]$, where $\theta_{\text{FC}} = 0$ corresponds to the nominal function, $\theta_{\text{FC}} = +1\sigma$ to the alternative, and values in between correspond to a linearly-scaled intermediate function, $f_{5p}(1 + \theta_{\text{FC}} \frac{f_{5p}^{\text{alt}} - f_{5p}}{f_{5p}})$. Limits calculated using this parameterisation can therefore accurately represent a variety of reasonable background estimates. The restricted range on

θ_{FC} prevents the background prediction from moving outside the range of the two functions considered, which could correspond to a function with a poor background estimate.

Fit parameters

The second uncertainty is that associated to the quality of the nominal function fit itself. Under ideal circumstances, this uncertainty would be represented as a confidence band on the function, determined by the covariance matrix of the fitted parameters. However, if the function parameters are strongly correlated, or when the likelihood function has a badly-behaved maximum (*e.g.* multiple maxima exist), it may not be possible to accurately compute the covariance matrix [232]. This problematic behaviour is realised in this analysis for fits that include a signal template normalisation parameter that is small and has a hard physical cut-off at zero. As a result, a different method is necessary to estimate the error band.

The confidence interval on a function is meant to represent the $\pm 1\sigma$ region within which the fit would fall in the large-number limit of repeated trials. Therefore, given a sufficiently large set of pseudo-experiments and fitting each, the confidence interval can be determined.

On the order of 10,000 pseudo-experiments are generated from the nominal background hypothesis, post-fit to data, with Poisson fluctuations applied to each bin. Each experiment is fitted using the same initial conditions as the observed data. The uncertainty on the fit in each bin is defined to be the RMS of the function value in that bin.

The two uncertainties associated with the background estimate are shown in Fig. 6.27. The yellow band indicates the $\pm 1\sigma$ statistical uncertainties on the nominal f_{5p} (blue line). The largest deviation of f_{5p}^{alt} (red line) from f_{5p} , corresponding to the function choice uncertainty, is seen for $m_{jj} \gtrsim 4$ TeV, where the fit choice uncertainty reaches 50% of the $\pm 1\sigma$ statistical variation of f_{5p} , and becomes the dominant uncertainty for $m_{jj} \geq 5$ TeV. In the region $m_{jj} < 3$ TeV, the function choice uncertainty is negligible compared to the $\pm 1\sigma$ statistical variation, while for $m_{jj} > 5$ TeV the function choice uncertainty dominates. It is therefore expected that the systematic uncertainty associated with the background estimate will yield weaker limits in the high-mass region of the m_{jj} distribution.

A systematic uncertainty can also be applied from spurious signal tests, as described in Sec. 6.9. Such an uncertainty is complementary to the function choice uncertainty. The upper bound on the RMS of the Gaussian amplitudes is used as an estimate for the number of possible spurious signal events. When converted to a cross section, the contribution from such effects is found to be less than 0.1%, and is thus neglected.

6.11.2 Jet energy scale and resolution

The remaining systematic uncertainties are applied only to new physics signal shapes.

Associated with the jet calibration procedure, discussed in Sec. 5.3, are the jet energy scale (JES) and jet energy resolution (JER) uncertainties. These uncertainties are generally derived in specific regions of jet p_T and η , and are then split into about 130 JES components and 117 JER components, which can be used in limit-setting as nuisance parameters (NP).

The addition of more than 200 degrees of freedom to the limit setting would be computationally intensive, and in some cases the majority of these NPs would have no effect on the limits. In the case that an analysis is insensitive to jet-jet correlations arising from changes to the JES and JER (typically

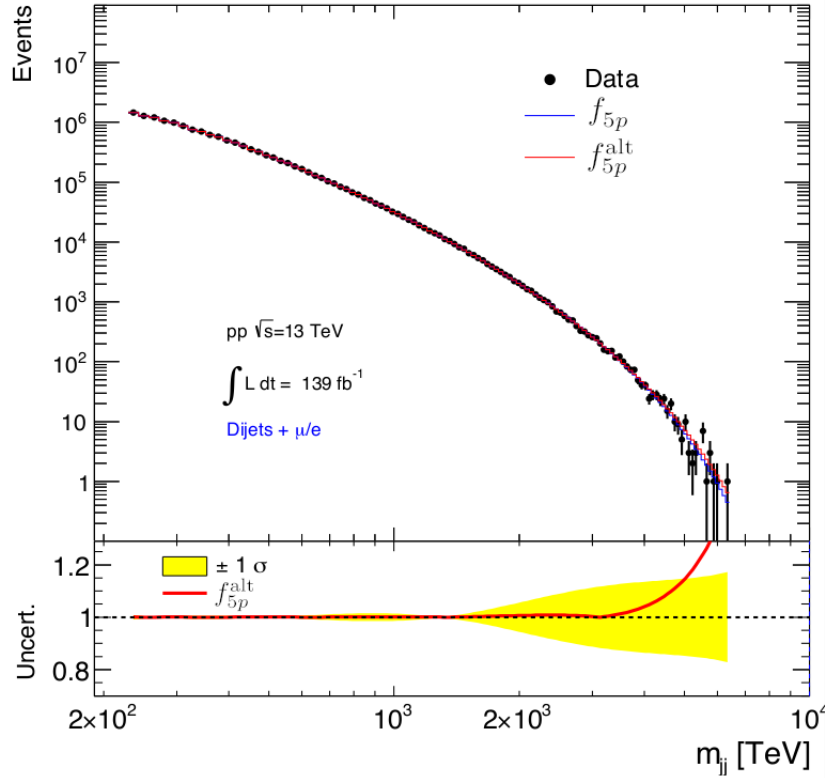


Figure 6.27: Comparison between the f_{5p} (Eqn. 6.27b) and f_{5p}^{alt} hypotheses (Eqn 6.27c) fits to data. In the lower panel, the yellow area indicates the $\pm 1\sigma$ statistical uncertainties on f_{5p} , and the red curve shows the function choice uncertainty.

the case when the uncertainties are negligible with respect to others), a so-called “strongly-reduced” NP scenario can be used. To construct a strongly-reduced scenario, the full covariance matrix containing each uncertainty is first constructed and diagonalised. The N largest uncertainty components are taken as individual NPs, and the remaining M are split into “groups” which are summed in quadrature for an additional set of NPs. The formed groups are not physically motivated, but are constructed in such a way to minimise the correlation loss in different regions of (p_T, η) phase space, and are otherwise completely arbitrary with respect to the NPs they contain. As a result, while the individual NPs naming convention is somewhat self-explanatory, *e.g.* `EtaInterCalib_NClos...1{up,down}`, the set of grouped NPs are simply denoted as `GroupedNP_m...1{up,down}`, where ‘m’ is the group number and ‘1{up,down}’ denotes a 1σ up or down variation, respectively, of the NP.

The most dramatic reduction scenarios consist of six (or seven⁹) JES and eight JER uncertainties. There are three such reduction scenarios, each having a different arbitrary combination of the individual JES and JER parameters. In each scenario, the jet-jet correlations are varied in a way that probes an analysis’s sensitivity to the correlations. While the total JES uncertainty is held constant in each of the scenarios, the correlations can change significantly, therefore the resulting JES uncertainty observed by an analysis may differ by a large amount. In order to ensure this analysis is unaffected by JES and JER uncertainties, each of the three scenarios is evaluated to determine if the observed on the limits are

⁹ Fully Geant4-based simulated signal samples have six, and ATLFast-II has seven; the extra uncertainty in the latter case is associated with MC non-closure [139].

impacted.

Jet energy scale

The JES uncertainties are generally derived in specific regions of jet p_T and η before being split into the roughly 130 components. As mentioned earlier, this analysis uses a reduced set of only six uncertainties. Three of the six JES uncertainties come from the η -intercalibration, which account for physics mismodelling, and detector and statistical uncertainties. The other three are arbitrary combinations of uncertainties arising from:

- *in situ* Z/γ +jet and multijet balance calibrations, mostly relevant for jets with $p_T < 1$ TeV and $1 < p_T < 2$ TeV, respectively;
- *in situ* calibrations, for jets with $p_T > 2$ TeV;
- pile-up, which affects low- p_T jets, typically with $p_T < 40$ GeV;
- jet flavour response and simulated jet composition;
- punch-through, which depends on the number of muon segments upstream of high- p_T jets reconstructed from topoclusters in the hadronic calorimeter; and
- MC non-closure, relevant only for fast simulation samples, that accounts for the differences between data and MC modelling.

Overall, the uncertainty on EM+JES-calibrated, $R = 0.4$ jets within $|\eta| < 2.4$ is at a level of 4% at 20 GeV, 1% at 200 GeV, and 3% at 2 TeV, and is fairly constant in η [139].

With respect to signal models, these uncertainties shift the signal peaks, but do not affect signal acceptance. As a result, signal peak positions are shifted to higher or lower m_{jj} due to the migration of events between bins. This effect is accounted for in the limit-setting procedure by using MC signal templates for $\pm 1\sigma$ in each of the uncertainties, allowing for each to be marginalised independently. Figure 6.28 shows the effect from JES uncertainties on a Z' signal with a mass of 2 TeV. It is worth noting that the η -intercalibration NP shown (as well as the other two) has no effect on the signal. This is expected because, as mentioned in Sec. 5, the η -intercalibration applies only to forward jets, which are outside the fiducial region definition of this analysis.

Jet energy resolution

A JER uncertainty, $\sigma(E)$, arises when the detector resolution is not correctly simulated in MC. The reduced eight-NP JER scenario accounts for uncertainties related to JES, pile-up and electronic noise, *in situ* calibration methods (see Sec. 5) and their non-closure (which account for data and MC discrepancies when using different methods), as well as differences between nominal data and MC simulations.

Random cones – sums of cluster energies in randomly-distributed cones of $R = 0.4$ in zero-bias data – are used to determine the contribution from pile-up to energy resolution noise term. The difference between two such cones is expected to be proportional to pile-up noise. Electronics noise is determined from dedicated calibration runs, for which the average number of interactions per bunch crossing, $\langle\mu\rangle$, is zero. The full noise term is constructed by adding, in quadrature, the contributions from random cones and electronics noise. For nominal data and MC simulation comparisons, the aim is to match

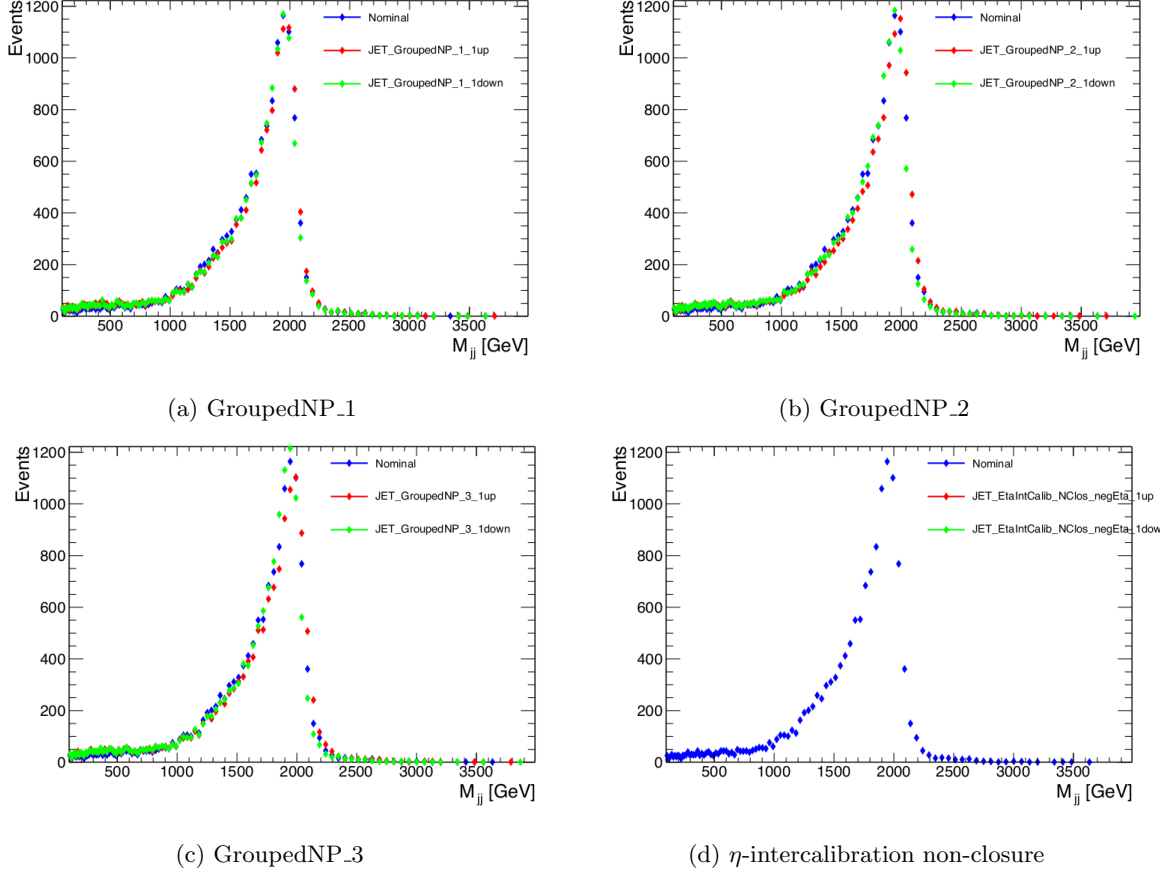


Figure 6.28: Effects of four of the JES systematics on a Z' signal of mass 2 TeV. The remaining two not shown are associated with η -intercalibration and therefore have no impact on the signal shape.

JER in data with that in MC; if the data-driven JER is larger than MC, the MC is smeared to match that in data; if the MC-based JER is larger than data, nothing is done as it is not desirable to degrade resolution in data.

Like the JES, the JER is calculated by varying signal templates by $\pm 1\sigma$ for each set of uncertainties. In contrast to JES, the effect of the JER does not alter the peak position, but instead slightly increases the width of the peak.

6.11.3 Lepton uncertainties

Lepton uncertainties include energy scale and resolution, and identification. For these uncertainties, a simplified correlation scheme is used, reducing the 69 scale and 9 resolution uncertainties to 2 scale and 1 resolution uncertainty.

Lepton objects are not used in this analysis directly for measurements on the final discriminant, however both lepton energy scale and resolution can impact signal acceptance, due to the requirement $p_T > 60$ GeV on leptons. While the limits do not depend on the number of MC signal events, as they are normalised to the theoretical cross sections, a small shift in the signal mass peak is not excluded as a result of the correlation between lepton and jet p_T .

Overall, the lepton-related uncertainties have a negligible effect on the limits, but nonetheless are

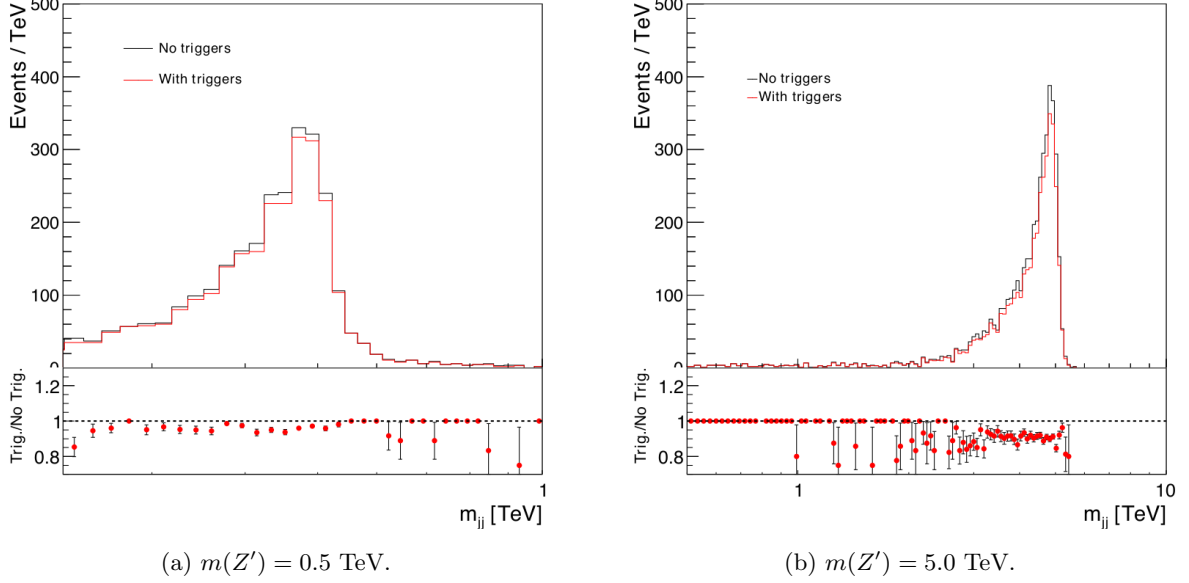


Figure 6.29: Example of trigger effects on the m_{jj} shapes for two Z' signal mass points.

included as NPs in limit calculations.

6.11.4 Systematic uncertainties from triggers

Systematic effects that arise due to the choice of triggers could impact the signal shapes, and therefore also the limits. In order to determine if ATLAS MC can correctly reproduce trigger effects on signal shapes, the trigger requirement is removed in these studies.

Figure 6.29 shows the m_{jj} distributions for two Z' signal mass points. It can be seen that aside from the normalisation, the overall signal shape is essentially unaltered. As an additional check, the calculation of limits with and without the requirement of a trigger is performed, and no impact on the limits were observed. Therefore, even in the worst-case scenario, *i.e.* with trigger requirements removed, a negligible (if any) effect on the limits stems from the triggers.

As discussed in Sec. 6.6, the trigger selection efficiencies also need to be considered in calculating limits. A 1% flat uncertainty is included to take such uncertainties into account.

6.11.5 Luminosity uncertainty

The uncertainty on the integrated luminosity is derived, following a methodology similar to that detailed in [233], from calibrations of the luminosity scale using x - y beam-separation scans.

The combined 2015-2018 integrated luminosity uncertainty is 1.7%. It is treated as a single normalisation uncertainty applied to the signal templates.

6.11.6 Scale uncertainties

The calculated dijet cross section depends on the renormalisation and factorisation scales, μ_R and μ_F , respectively. A value for each of these scales must be therefore set during the generation of signal MC events, and the choices of scales will affect the cross sections to some degree.

Additional sets of signal MC samples were generated by varying independently μ_R and μ_F by factors of 0.5 and 2.0. In both cases, the resulting templates and cross sections were compared to the nominal scales. The resulting variation in signal acceptance and shape was found to be roughly 0.3% – negligible compared to the statistical variations of the observed limits. Therefore, no scale uncertainty is applied in the limit setting.

6.11.7 PDF uncertainty

Parton distribution function uncertainties can affect the acceptance and shape of a given signal. The standard procedure used to estimate the magnitude of this effect involves generating signal events with several different PDF sets using the `SysCalc` tool [234]. The differences between the sets of events are calculated at each mass point considered, and the largest difference at each point is assigned to an uncertainty.

Although changes in signal shape are not uncommon, and in some cases are larger than those related to acceptance, shape uncertainties are difficult to define since the reason for the underlying differences between pdf sets cannot be clearly identified. Furthermore, the signal shape could be largely distorted by the limit-setting procedure if a marginalised best-fit of the associated NP forces the signal to be more background-like. Additional complications arise for theorists who wish to reinterpret results when the signal shape is permitted to vary in the limit setting. As such, it is not standard practice in ATLAS to include uncertainties related to shape-changing effects, and following from previous studies [235], this analysis adopts a 1% flat PDF systematic uncertainty.

6.11.8 Gaussian signal shape uncertainties

The uncertainties on the background estimate are unchanged between generic and model-dependent limits. Furthermore, the acceptance uncertainties due to lepton energy scale and resolution, and luminosity can all be applied to Gaussian-shaped signals in exactly the same way as presented previously. On the other hand, when setting limits on cross sections of generic Gaussian-shaped signals, instead of benchmark models generated with MC, the JES and JER uncertainties are not well-defined. Moreover, many more Gaussian mass points exist where MC signal does not. Therefore, a different approach is needed to include jet-related uncertainties on Gaussian masses and shapes.

Systematics related to jet reconstruction of generic signals are determined by first analysing the effect of such uncertainties on Z' signal model MC. Because MC signal shapes are mostly unchanged between the three subcampaigns, MC16a, MC16d, and MC16e, the MC16d sample was selected, without bias, to derive the systematics.

Changes in m_{jj} of signal models due to JES and JER uncertainties are calculated at different Z' masses and widths, and are parameterised using second-degree polynomial functions. The polynomials are then used to shift the peak of, and widen, the Gaussian distributions according to each systematic variation, for every mass point considered. This method allows for an analytic extrapolation of systematic variations to mass points that do not exist in MC, as illustrated by two examples, one for JES and another for JER, shown in Fig. 6.30. The data points are calculated by fitting the input signal shape with a Gaussian distribution within 2 RMS about the signal peak position.

The result after applying the method to Gaussian-shaped signals with widths of 5% and 10% is shown in Fig. 6.31; the shifts in peak position and widening of the original Gaussians (in red) are evident.

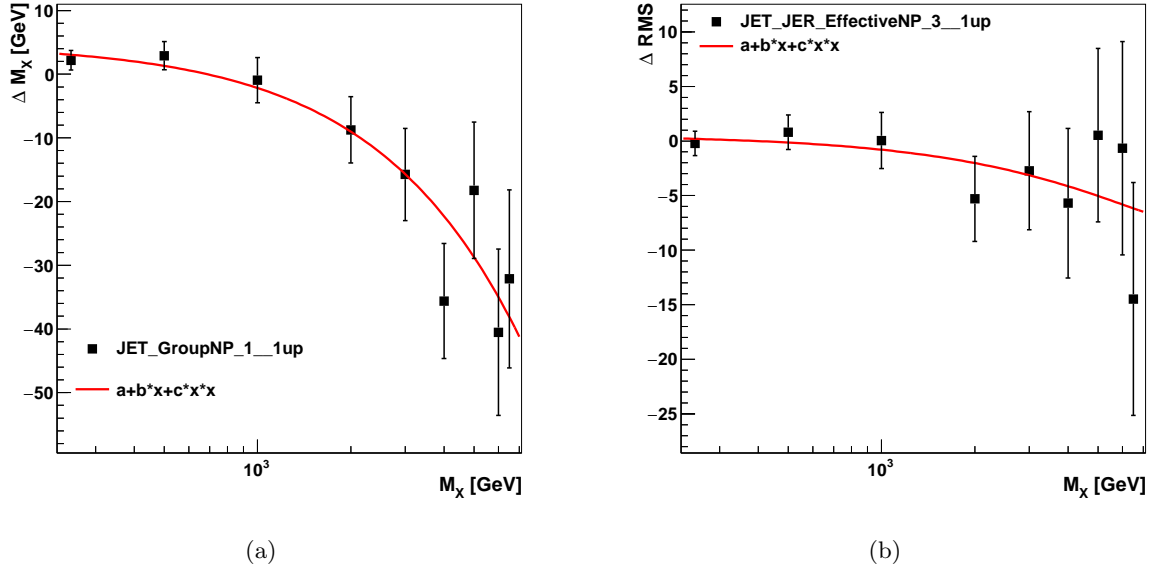


Figure 6.30: Example parameterisations of a single (left) JES and (right) JER uncertainty. The data points correspond to MC simulation, and the solid red line show the second-order polynomial fit to the data points. More details are given in the main text.

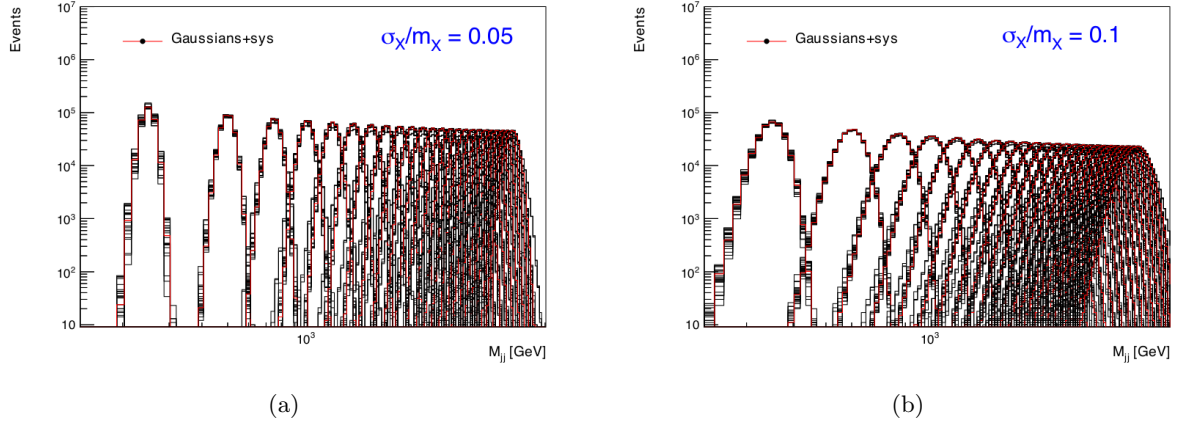


Figure 6.31: Generic Gaussian signal shapes of various masses and widths (a) 5% and (b) 10% without (black) and with (red) parameterised JES and JER systematics applied.

6.11.9 Summary of uncertainties

A summary of all uncertainties considered in this analysis is presented in Table 6.8.

6.12 Limit setting

At the end of Sec. 6.10, it was determined that there is no statistically significant evidence for new physics in the dijet invariant mass spectrum considered. The observed data are used to set limits on the possible number of events arising from BSM physics in resonant dijet decay processes. This section

Systematic	250 GeV	1000 GeV	3000 GeV	6000 GeV
Fit function choice*	0.5%-50% of background, depending on m_{jj}			
Fit statistics*	0.5%-20% of background, depending on m_{jj}			
JES_GroupNP_1	1%	0.8%	0.4%	0.3%
JES_GroupNP_2	0.2%	0.4%	0.6%	0.9%
JES_GroupNP_3	0.2%	0.3%	0.3%	1.4%
JES_NonClosure (3 shifts)	0.1%	0.1%	0.1%	0.2%
JER (8 shifts)	0.1%	0.1%	0.1%	0.1%
Lepton energy scale	< 0.05%	< 0.05%	< 0.05%	< 0.05%
Lepton energy resolution	< 0.05%	< 0.05%	< 0.05%	< 0.05%
Trigger	1.0%			
Luminosity	1.7% for 2015-2018 integrated luminosity			
PDF	1.0% for MC signal models, none for generic limits			

Table 6.8: Summary of all systematics used for limit calculations at several different mass hypotheses. Uncertainties marked (*) apply only to the background estimation; all other uncertainties pertain only to signal. JES and JER uncertainties represent the absolute values of shifts at the given masses.

provides an brief overview of Bayesian statistics, and then describes the method used to set limits.

6.12.1 Statistical background

Baye's theorem

The crux of the method used for setting limits in this analysis is *Bayes' theorem* [236]. Bayes theorem relates a conditional probability $P(A|B)$, the probability of event A given event B already occurred, of two outcomes via prior knowledge of the probability of each outcome, $P(A)$ and $P(B)$. Mathematically, the theorem is written as,

$$P(A|B) = \frac{P(B|A)}{P(B)} P(A), \quad (6.30)$$

where $P(A)$ is the *prior probability* – the probability of event A before evidence – and $P(A|B)$ is the *posterior probability* – the probability of event A after evidence. The factor that relates the prior and the posterior is called the *likelihood ratio*.

At this point, it is instructive to first define several basic statistical terms and specify their notation [224, 237] which are used later.

Bayesian probability A subjective measure of the likelihood that an event will occur. Loosely speaking, *prior* probability is an analyser's intrinsic degree of belief in a given hypothesis, $\pi(H)$, whereas a *posterior* probability represents the degree of belief given some additional knowledge based on previous outcomes. As such, the posterior is a conditional probability, $P(H|A)$, with A representing some previous outcome.

Probability distribution function For an ensemble of measurements of a discrete variable x , a function $f(x)$ can be constructed to predict possible outcomes of future measurements. The function $f(x)$ is itself a probability, necessarily normalised over the full space of possible outcomes, Ω , such that $\sum_{\Omega} f(x) = 1$.

Probability density function (pdf) If x is a continuous variable, $f(x)$ has units $[x]^{-1}$, and so the probability of an outcome in some interval $[x, x + dx]$ is $f(x)dx$. As in the discrete case, this is necessarily normalised over the full space of possible outcomes, Ω , such that $\int_{\Omega} f(x)dx = 1$.

Likelihood When a measurement is made, the conditional probability of obtaining a result x given the values of model parameters θ , $P(x|\theta)$, can be expressed as a likelihood, $\mathcal{L}(\theta|x)$. That is, given a result x , $\mathcal{L}(\theta|x)$ gives the probability that the θ would lead to x , which, in turn, gives insight into the plausibility that a particular set of θ is the true one. Note that the likelihood is not a true probability distribution since the integral of it over all parameter values is not necessarily unity. The likelihood should be interpreted as a function of the parameter values for fixed data.

With these definitions in hand, Bayes' theorem of Eq. 6.30 can be equivalently expressed in terms of likelihoods:

$$P(H|x) = \frac{\mathcal{L}(H|x)\pi(H)}{\int \mathcal{L}(H'|x)\pi(H')dH'} \quad (6.31)$$

where the primes are used on H in the denominator to distinguish the range of all hypotheses being integrated over from the actual hypothesis being tested. Note that the denominator represents the prior probability, $\pi(x)$, of the dataset and is essentially a normalisation factor.

Constructing the posterior

In real-world experiments, the hypothesis H is typically not a single parameter, but actually depends on a potentially large number of unknown parameters. In searches for new physics, most such parameters typically correspond to uncertainties which affect the comparison between observed data and a given model, and only one parameter is of interest, *e.g.* signal strength. It is therefore of utility to express Eq. 6.31 in terms of the *parameter of interest*, μ , and the other, *nuisance parameters* θ :

$$P(\mu, \theta|x) = \frac{\mathcal{L}(\mu, \theta|x)\pi(\mu, \theta)}{\int \mathcal{L}(\mu', \theta'|x)\pi(\mu', \theta')d\mu'd\theta'} \quad (6.32)$$

In the present case, the prior probability of producing a given number of signal events is assumed to be independent of the nuisance parameters. Because the analyser is only concerned with the μ , the nuisance parameters θ can be marginalised out to obtain the posterior probability density,

$$\begin{aligned} P(\mu|x) &= \int P(\mu, \theta|x)d\theta \\ &= \frac{1}{C} \int \mathcal{L}(\mu, \theta|x)\pi(\mu, \theta)d\theta \end{aligned} \quad (6.33)$$

with $1/C$ a constant normalisation factor equal to the denominator in Eq. 6.31. Equation 6.33 gives, regardless of the nuisance parameters, the probability of μ given the data x .

Equation 6.33 can be used to provide a definite limit, to a specific level of probability, on the signal strength which may be present in the data. For example, the value of the signal strength parameter that falls beyond the region containing 95% of the (normalised) integrated pdf, *i.e.* the 95% quantile, represents the amount of signal said to be excluded with 95% probability.

Just as the prior probability of producing some number of signal events is independent of the nuisance parameters, *e.g.* luminosity, jet energy resolution, there is no prior relationship between systematic

uncertainties, *e.g.* the uncertainty on luminosity does not depend on the jet energy resolution uncertainty. Thus, in this analysis all nuisance priors can be added independently to the posterior and marginalised out:

$$P(\mu|x) = \frac{1}{C} \int \mathcal{L}(\mu, \theta|x) \pi(\mu, \theta) \prod_i \pi(\theta_i) d\theta_i. \quad (6.34)$$

All terms in Eq. 6.34 are determined by the model and experimental conditions with the exception of the signal strength prior, $\pi(\mu)$.

Choice of prior

Like many other dijet resonance searches [164–166, 179], this analysis adopts a uniform prior for $\pi(\mu) = 1$, which is flat for all permitted values of μ , meaning any cross section is equally likely. The uniform prior yields precisely the same upper limits as the frequentist CL_s method [238, 239], and also makes reinterpretation of the results easier due to its simplicity.

6.12.2 Credible intervals and upper limits

A credible interval, in the Bayesian framework, is defined as the region wherein the true value of a parameter is expected to be with some probability. This region can be determined by finding the interval $[\mu_{\text{lo}}, \mu_{\text{up}}]$ about μ which contains a fraction $1 - \alpha$ of the posterior probability $p(\mu|x)$ [25]:

$$1 - \alpha = \int_{\mu_{\text{lo}}}^{\mu_{\text{up}}} p(\mu|x) d\mu \quad (6.35)$$

There are several ways to choose the bounds of integration, μ_{lo} and μ_{up} [224]; since here upper limits are placed on production cross sections, the natural choice is to employ the *upper limit* scheme.

For a value of $\alpha = 0.95$ (*i.e.* the 95th quantile), the *confidence limit* on the number of signal events present in the observed data is determined by integrating the posterior pdf from in the interval $[\mu_{\text{lo}} = 0, \mu_{\text{up}}]$, where μ_{up} is the *credibility level*, the point at which 95% of the integral is contained. That is, it can be stated that the true value of the signal present in the observed data is less than μ_{up} with 95% probability.

In addition to *observed* upper limits, it is also important to know the *expected* upper limits. For a given background-only (or *null*) hypothesis, the expected upper limit gives a measure of how much the observed upper limit is affected by statistical fluctuations, and what the median of the spread of possible outcomes is. The expected limits also provide a way to interpret the observed limits in terms of standard deviations from the null hypothesis. The standard method for determining expected limits in ATLAS is to use the Frequentist approach; a large number of pseudo-experiments are generated¹⁰ based on the nominal template defined by the best fit values of the nuisance parameters which give the maximum likelihood, having fixed $\mu = 0$. The 95th quantile is calculated from each pseudo-experiment, and the resulting distribution of quantiles determines the 1σ and 2σ uncertainty bands.

6.12.3 Efficiency calculations

The limits to be presented can be formulated in terms of detector-level variables, thereby removing the dependence of the limits on detector acceptance and efficiency. All such factors are expected to be

¹⁰ Jargonists would say pseudo-experiments are *thrown*.

smaller than unity.

There are two types of corrections that need to be taken into account when converting the detector-level limits to the “truth”, or particle-level, limits; (1) signal reconstruction efficiency that can be determined using the signal-injection tests (these are close to 100% across the m_{jj} range considered); and (2) the efficiency related to jet and lepton reconstruction.

Taking into account the trigger efficiency of $\epsilon_{\text{trig}} = 0.88$, the measured limits and the MC cross sections are expected to be weaker by $\sim 12\%$ if they are corrected for trigger effects. The $\pm 1\sigma$ bands on the limit plots account for about $\pm 25\%$ of the central values of the expected limits, and become significantly larger uncertainty at large m_{jj} . The effects from the trigger efficiency are well within these $\pm 1\sigma$ bands, *i.e.* trigger-related uncertainties are typically smaller than the statistical variations of the observed limits around the expected ones.

In order to correct the detector-level results to the truth-level for future reinterpretation, the total efficiency should be evaluated by including the lepton reconstruction, identification and isolation efficiencies, in addition to the trigger efficiency. The reconstruction and identification efficiencies are at present not available to analyses that have adopted the latest recommendations from ATLAS Combined Performance Groups. For 2015-2016 data, the efficiencies are close to 78% (95%) for *tight* electrons [130] (*medium* muons [134]) with $p_T > 60$ GeV and *Gradient* isolation. The weighted average of these efficiencies is 84%. Therefore, the total lepton reconstruction efficiency, including the trigger efficiency of 88% discussed above, is about 74% for 2015-2016 data. It must be noted that this is a rough estimate based on deprecated working points, however it is a conservative estimate since it is expected that the efficiencies of the new working points will be improved.

To assist theorists in the reinterpretation of the results presented herein, the efficiency and acceptance corrections from signal MC are given in Tables 6.9 and 6.10 for the models considered in this analysis. Only statistical uncertainties are considered; the complete set of systematic uncertainties are included in the limits presented in the next section. The columns of these tables are defined as:

- M : nominal masses of the resonances (in GeV);
- N_{gen} : the number of events generated (before any cuts);
- σ : the cross section of the MC process (in pb);
- $N_{\text{acc}}^{\text{lep}}$: the number of truth-level events after requiring at least one signal lepton;
- $N_{\text{acc}}^{\text{full}}$: the total number truth-level events after requiring at least two signal jets with $m_{jj} > 216$ GeV;
- A : the acceptance, *i.e.* the number of the truth-level events, after all SR selection requirements, divided by N_{gen} ;
- N_{rec} : the number of events after event reconstruction, including trigger efficiencies, and SR selection requirements;
- σ^{vis} : the visible cross section, taking into account acceptance and efficiency;
- ϵ : the final reconstruction efficiency of the signal events, *i.e.* $N_{\text{rec}}/N_{\text{acc}}^{\text{full}}$.

M [GeV]	N_{gen}	σ [pb]	$N_{\text{acc}}^{\text{lep}}$	$N_{\text{acc}}^{\text{full}}$	A	N_{rec}	σ^{vis} [pb]	ϵ
250	10000	6.470E-01	5639	3385	0.339 ± 0.007	2027	1.312E-01	0.599 ± 0.017
300	10000	3.350E-01	6189	4676	0.468 ± 0.008	3207	1.075E-01	0.686 ± 0.016
350	10000	1.880E-01	6867	5758	0.576 ± 0.010	3899	7.331E-02	0.677 ± 0.014
400	10000	1.150E-01	7470	5781	0.578 ± 0.010	3992	4.591E-02	0.691 ± 0.014
450	10000	7.370E-02	7772	6090	0.609 ± 0.010	4344	3.202E-02	0.713 ± 0.014
500	10000	4.880E-02	8020	6415	0.641 ± 0.010	4670	2.279E-02	0.728 ± 0.014
1000	10000	2.130E-03	9168	8564	0.856 ± 0.013	6476	1.380E-03	0.756 ± 0.012
1500	10000	1.970E-04	9447	9160	0.916 ± 0.013	7002	1.379E-04	0.764 ± 0.012
2000	10000	2.150E-05	9616	9478	0.948 ± 0.014	7172	1.542E-05	0.757 ± 0.012
2500	10000	2.460E-06	9688	9599	0.960 ± 0.014	6485	1.595E-06	0.676 ± 0.011
3000	10000	2.570E-07	9719	9635	0.964 ± 0.014	7288	1.873E-07	0.756 ± 0.012
4000	10000	6.430E-08	9697	9658	0.966 ± 0.014	7191	4.624E-08	0.745 ± 0.012
5000	10000	3.830E-08	9692	9659	0.966 ± 0.014	7045	2.698E-08	0.729 ± 0.011
6000	10000	3.720E-09	9279	9234	0.923 ± 0.013	6207	2.309E-09	0.672 ± 0.011

Table 6.9: Numbers of ρ_T signal events generated, passed the acceptance cuts, fully reconstructed, and the visible cross sections. The final efficiency is given in the last column. Only statistically uncertainties on the acceptance and efficiencies are considered.

M [GeV]	N_{gen}	σ [pb]	$N_{\text{acc}}^{\text{lep}}$	$N_{\text{acc}}^{\text{full}}$	A	N_{rec}	σ^{vis} [pb]	ϵ
250	20000	1.465E+00	7015	3939	0.197 ± 0.003	2690	1.970E-01	0.683 ± 0.017
500	20000	3.220E-01	8688	7390	0.369 ± 0.005	5136	8.269E-02	0.695 ± 0.013
1000	20000	4.412E-02	10058	9434	0.472 ± 0.006	6646	1.466E-02	0.705 ± 0.011
2000	20000	2.695E-03	11382	11262	0.563 ± 0.007	7483	1.008E-03	0.664 ± 0.010
3000	20000	2.498E-04	11889	11691	0.585 ± 0.007	7695	9.611E-05	0.658 ± 0.010
4000	20000	2.469E-05	11742	11526	0.576 ± 0.007	7542	9.311E-06	0.654 ± 0.010
5000	20000	3.250E-06	11455	11116	0.556 ± 0.007	7272	1.182E-06	0.654 ± 0.010
6000	20000	1.720E-06	11054	10537	0.527 ± 0.006	7137	6.138E-07	0.677 ± 0.010

Table 6.10: Numbers of Z' signal events generated, passed the acceptance cuts, fully reconstructed, and the visible cross sections. The final efficiency is given in the last column. Only statistically uncertainties on the acceptance and efficiencies are considered.

6.12.4 Results

In the absence of any statistically significant deviations of the data from the background-only hypothesis, the Bayesian method [178] as detailed in Sec. 6.12, is used to set 95% credibility level upper limits on cross sections for new physics processes that involve a hypothesised heavy particle decaying exclusively to two jets in events with an isolated lepton.

Limits on Gaussian resonance shapes

One of the simplest generic resonance shapes is that of a Gaussian distribution. Regardless of their simplicity, limits on Gaussian-shaped signals can benefit the theorist community as they can be used for reinterpretation in the context of other models.

It is assumed that events from a Gaussian-like signal that pass the final selection (defined in Sec. 6.6) would form a normal distribution with mean equal to the peak position (*i.e.* mass) and width determined by σ_G/m_G plus contributions from detector effects. Several intrinsic widths are used in this analysis, 5%, 10%, 15%, and one determined by the experimental dijet resolution at each mass considered (generally less than 5% in width). The Gaussian histograms are used as inputs to the limit-setting software –

a combination of the Bayesian Analysis Toolkit [240] and code developed by the analysis team – and the limit-setting procedure gives the maximum number events that could be present in the data at a 95% credibility level for a given signal width and mass. This value, divided by the dataset integrated luminosity, provides a measure of the upper limit on cross section (σ) times acceptance (A) times efficiency (ϵ) times branching ratio (BR) for the signal at that mass.

Figure 6.32 shows the 95% credibility level observed upper limits on $\sigma \times A \times \epsilon \times BR$ on any model predicting a new resonance that is compatible with a Gaussian form. The limit for the Gaussian with $\sigma_G/m_G = 15\%$ begins at $m_{jj} = 500$ GeV since some of the signal would be lost for this width at the minimum m_{jj} of 250 GeV. The expected upper limits and $\pm 1\sigma$ and $\pm 2\sigma$ uncertainty bands shown in the figure are shown for the Gaussian signal with a width equal to the detector resolution. The resulting exclusions range from 40 fb to 0.03 fb in the mass range 0.25–6.0 TeV. As expected, the limits become weaker for broader signal widths for which Gaussian contributions span more bins in the m_{jj} distribution. Signal efficiency ϵ is limited by the lepton triggers, taken to be 86%. However, the efficiency correction to account for this is typically less than the variations of the observed limits around the expected ones.

Limits on BSM models

As a demonstration of the physics reach of this analysis, 95% credibility level upper limits are placed on $\sigma \times B$ for two BSM benchmark models, technicolor and a simplified DM model (described in Sec. 2.2); acceptances and efficiencies for the two models can be found in Table 6.9 and Table 6.10, respectively. The model-dependent limits are calculated using the simulated and reconstructed signal shapes in the exact same limit-setting procedure as for the generic limits. It is important to note that no optimisations of the event selection were performed to enhance the sensitivity to either of these models.

The ρ_{TC} signal model limits are shown in Fig. 6.33, where a ρ_{TC} decays into a π_{TC} and W boson, with $m_{\rho_{TC}} = 2m_{\pi_{TC}}$. A logarithmic x -axis is used for better presentation of the theoretical prediction curve (dashed red). These results exclude production cross sections greater than 0.1 pb for a π_{TC} technimeson particle with a mass in the range of about 280–350 GeV.

The limits on the production of a spin-1 Z' in the context of a simplified dark matter model are presented in Fig. 6.34. The Z' is assumed to have leptophobic couplings, $g_q = 0.25$, $g_\ell = 0$, and with $g_{DM} = 1$. The data exclude production of the Z' in this model with such couplings for masses $m_{Z'} < 1.2$ TeV.

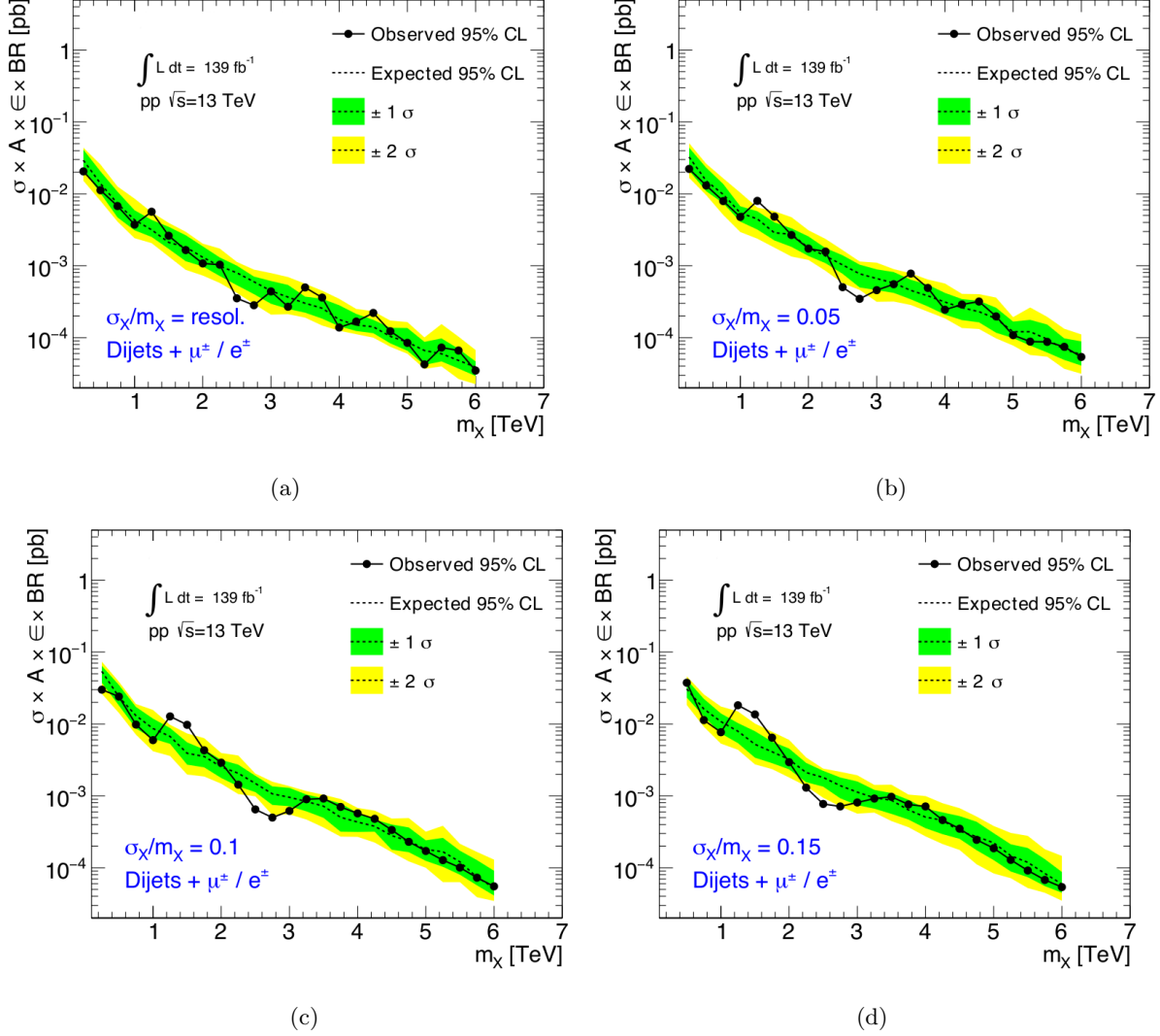


Figure 6.32: Observed (solid black line) and expected (dashed black line) 95% credibility level upper limits on the cross section (σ) times acceptance (A) times efficiency times branching ratio (BR) for Gaussian signal shapes of widths (a) determined by the detector resolution, (b) 5%, (c), 10%, and (d) 15%. over a range of masses between $250 < m_G < 6000$ GeV. The expected upper limit and $\pm 1\sigma$ and $\pm 2\sigma$ uncertainty bands are also shown.

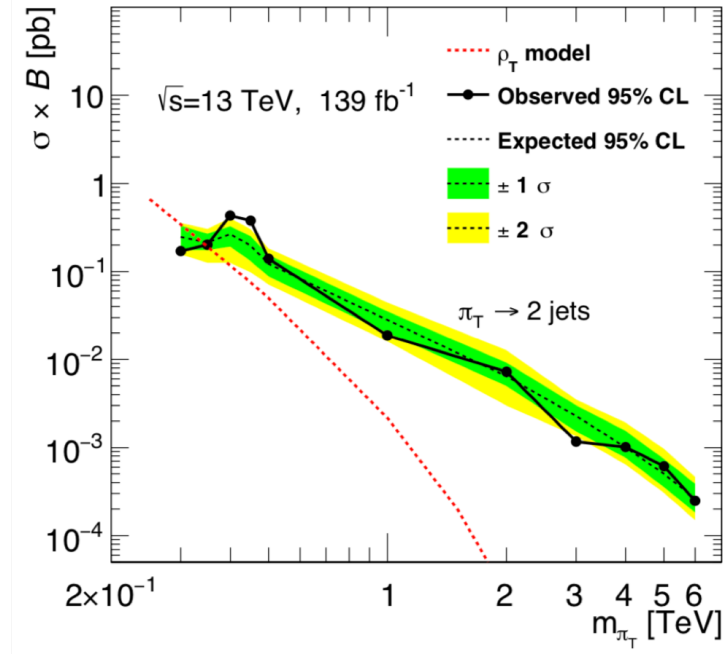


Figure 6.33: Observed (solid black line) and expected (dashed black line) 95% credibility level upper limits on the cross section (σ) times branching ratio (B) on π_{TC} production in the context of the ρ_{TC} signal model. The efficiencies and acceptances for each mass point shown are given in Table 6.9.

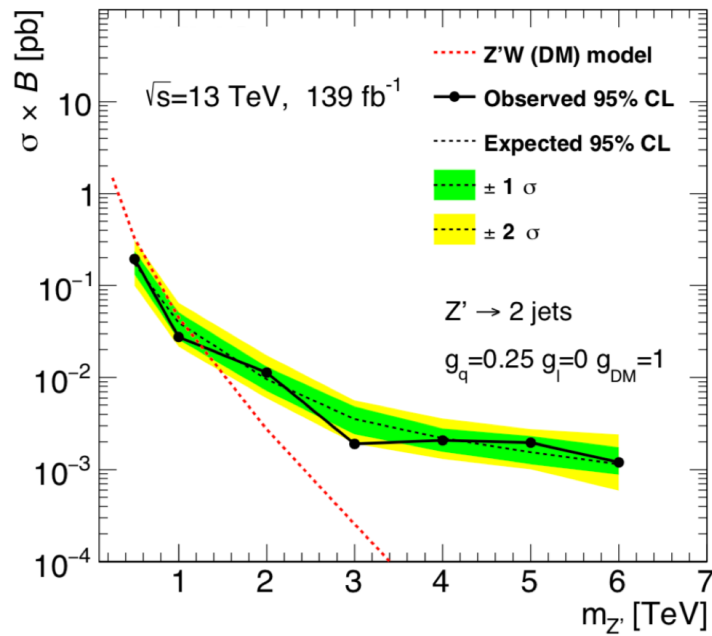


Figure 6.34: Observed (solid black line) and expected (dashed black line) 95% credibility level upper limits on the cross section (σ) times branching ratio (B) on Z' production in the context of a simplified Dark Matter signal model. The efficiencies and acceptances for each mass point shown are given in Table 6.10.

Chapter 7

Conclusion

Moving forward.

Memories left behind.

A new life, a new journey.

I've built anew.

For mankind...for my kind.

- Between the Buried and Me, *Augment of Rebirth*

A search for new resonances in dijet invariant masses distributions in events with associated leptons using an integrated luminosity of 139 fb^{-1} of proton–proton collisions at a centre-of-mass energy of $\sqrt{s} = 13 \text{ TeV}$ recorded by the ATLAS detector was presented.

In the considered dijet invariant mass range of 0.22–6.3 TeV, the most significant deviation with respect to a data-derived estimate of the Standard Model prediction is found at $m_{jj} = 1.3 \text{ TeV}$ with a global p -value of 0.3. This result takes systematic uncertainties and the look elsewhere effect into account. The data are thus consistent with the background-only hypothesis.

In the absence of signals indicating the presence of new physics, this analysis sets 95% credibility-level upper limits on $\sigma \times A \times \epsilon \times B$ for new processes that can produce a Gaussian contribution to the dijet mass distribution in events with isolated leptons with $p_T > 60 \text{ GeV}$. The limits are calculated for a Gaussian width ranging from that determined by the detector resolution to 15% of the resonance mass. The obtained limits range from 40 fb to 0.03 fb for resonance masses between 0.25 and 6 TeV. These results exclude generic BSM models predicting resonances that decay to form two jets in events with associated leptons with cross-sections larger than the reported limits.

Without using selection cuts optimized to specific final states, these results exclude a π_{TC} technimeson in the ρ_{TC} model considered at around 280–350 GeV. In the context of a simplified Dark Matter model, the data also exclude a spin-1 Z' with leptophobic couplings ($g_q = 0.25$, $g_l = 0$ and $g_{DM} = 1$) at masses below 1.2 TeV.

No new physics has been observed in this analysis.

7.1 The future

Proton-proton collisions will resume in 2021, following Long Shutdown 2 of the LHC. This next period of data-taking, denoted Run-3, will be used for commissioning after a wealth of detector upgrades, and the training of the LHC superconducting magnets will begin to allow for the machine to collide protons at its design centre-of-mass energy of $\sqrt{s} = 14$ TeV. It is expected that the Run-3 dataset will be roughly the same size as that produced in Run-2, resulting in a combined Run-2 and Run-3 dataset of roughly 300 fb^{-1} . Rather than push for only modest improvements in existing analyses, ATLAS plans to focus on performance studies, analyses that are statistically limited, and support publications employing new methods.

A significant amount of effort has already been put into a machine learning (ML) based approach to the dijet+lepton analysis, and notable support has been shown by physics convenors to aim for a follow-up Run-2 paper using such an approach. There are two motivations for using ML in this analysis.

7.1.1 Machine learning for signal identification

First is the discrimination power and automation of ML algorithms. Initial studies of signal-optimised selections performed in the context of the dijet+lepton analysis have shown only marginal improvements in signal-to-background separation. Furthermore, the small team of analysers makes the study of “influential” variables that can be used to discern signal events from background difficult as the process is time-consuming.

An interesting new way to train such algorithms is to use a dimensionless *rapidity mass matrix* (RMM) [241, 242]. A RMM encapsulates kinematical information of final-state objects in each event that are relevant to a given analysis, and is represented as an “image” that can be used in popular supervised ML algorithms, *e.g.* neural networks or boosted decision trees, to discriminate between signal and background events.

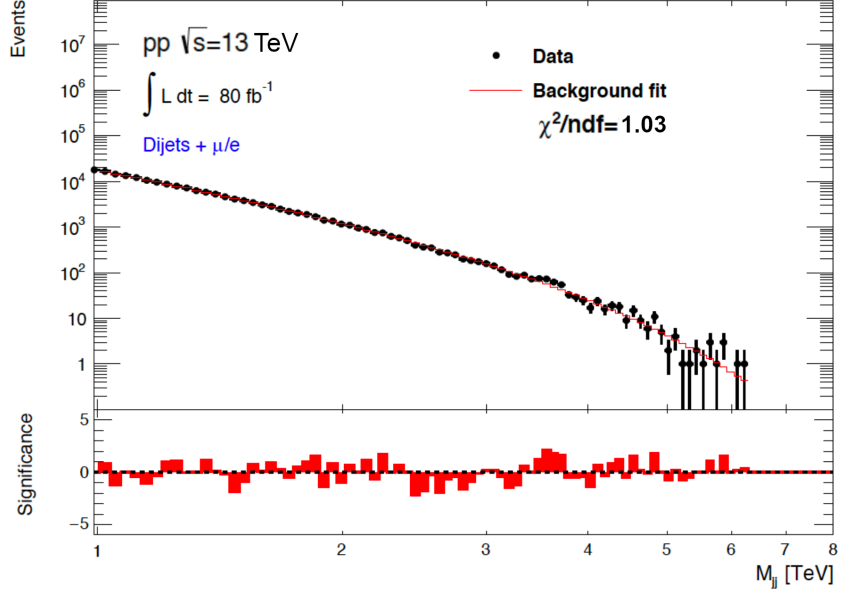
7.1.2 Machine learning for fitting smooth backgrounds

The second motivation for using ML is in the interest of probing even lower dijet invariant masses. One limiting factor in the current dijet+lepton analysis is the inability of the *ad hoc* parameterised functions to describe a wide range of invariant masses with statistics that vary as a function of mass by orders of magnitude. A potentially suitable candidate that has been investigated to replace the parametric background estimate is Gaussian processes (GPs).

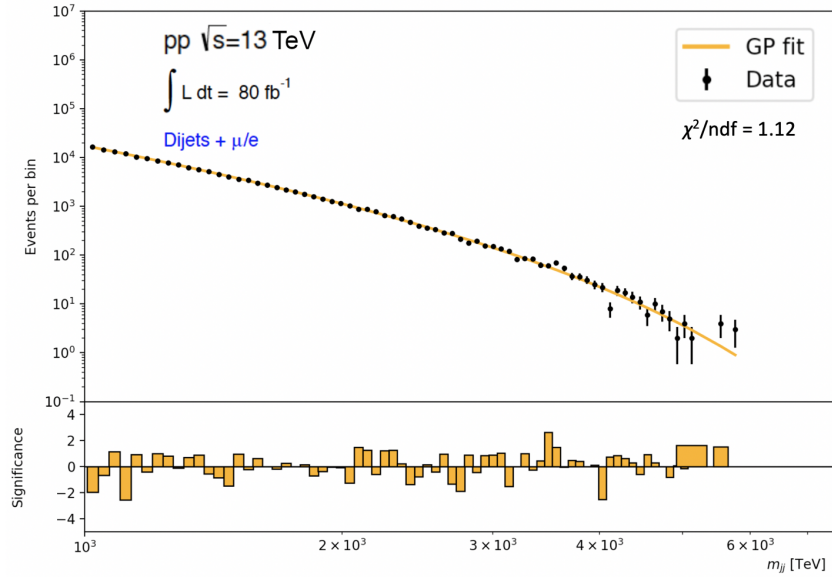
Gaussian processes provide a generalisation of the dijet functions and, more importantly, are not restricted to this particular family of functions or a specific number of parameters, θ_i . They have recently been shown to be much more flexible and robust in modelling large datasets and fitting smooth background distributions [243]. By appropriately choosing the function (covariance kernel) that encodes the relationship between different data points $f(x)$, GPs can provide a description of a broader class of functions and make use of additional information (*e.g.* experimental and theoretical uncertainties, calibration measurements, *etc.*) in a natural way that can aid in modeling complex distributions. Research on the use of GPs in high energy physics is still in its infancy, having only been used in a small number of published works [244, 245].

It should be noted that previous and other current studies of GP formalism applied to background modeling target relatively narrow mass ranges (≤ 1 TeV), whereas the preliminary work in the context

of the dijet+lepton analysis has been to describe a much wider range ($0.22 < m_{jj} < 6.5 \leq \text{TeV}$) with significantly larger statistics. As a result, more complicated covariance and mean functions are required – implying additional degrees of freedom (i.e. hyperparameters) – to model the data. Because the hyperparameters are extremely sensitive to small changes, and because GPs are inherently highly parallelisable, graphical processing units are exceptionally desirable for hyperparameter scans. That said, even with the limited available processing power available from CPUs, GPs can model well a limited range of the dijet invariant mass distribution considered in this analysis. Figure 7.1 shows the fits, along with their χ^2 , to data using the nominal f_{5p} in the current analysis and that of GPs.



(a)



(b)

Figure 7.1: Dijet invariant mass spectrum for $m_{jj} > 1$ TeV fitted with (a) the nominal f_{5p} function with $\chi^2 = 69.01$ and p -value = 0.41, and (b) a GP with $\chi^2 = 75.04$ and p -value = 0.23, each having $\text{ndf} = 67$.

Appendix A

Contributions to the ATLAS Experiment

During the five years of being a member of the ATLAS experiment, I have devoted a significant amount of my time to numerous projects. Provided here is a brief overview of my contributions.

Calorimeter operations

I was fortunate to have spent nearly two years stationed at CERN, during which time my priority was to work in the LAr Operations team. In the first few weeks I worked as a shifter, where I was responsible for monitoring the behaviour of the LAr and Tile calorimeters. As a shifter, I monitored and reported on the daily quality of calorimeter data-taking. Because my interests lie in software, I was quickly absorbed into the LAr Online Software group. My expertise in software development quickly landed me the role as a lead developer in the “trigger tower noise killer” application, the aim of which is to find and disable cells with intrinsically high levels of noise. After several months of being a “Software On-Call”, I started as LAr Run Coordinator for the 2016 heavy-ion runs, responsible for the overall system of LAr calorimeters. My role as Run Coordinator continued through 2017 during proton-proton data taking.

LAr calorimeter relative luminosity measurements

Also while stationed at CERN, I was responsible for providing relative luminosity measurements as determined by the LAr calorimeters [246]. This role entailed writing the software to convert measured currents in the LAr calorimeters to luminosity measurements. Most of the code was inherited from previous generations who had worked on this; I discovered a “bug” that, after being addressed, reduced the LAr-based luminosity measurement by as much as 2%.

Simulation

My career in ATLAS began in simulation. As an undergraduate student at Brock University, I reached out to one Peter Krieger in hopes I would attend University of Toronto as a graduate student. Fortunately

enough, given my background in computer science and motivation as an undergraduate, I was presented with the task to work on the “Mini-FCal” – one of several proposals to address potential issues involving the forward calorimetry in the HL-LHC environment. This work included implementing the proposed detector in ATLAS’s software framework to gauge the impact its associated services had on the existing FCal. Although the upgrade proposal was turned down, I gained an incredible amount of experience with Geant4 and how ATLAS used its framework.

I have worked on the new FastCaloSim software [202], and have been a convenor in the Fast Simulation group for over two years. In my post-doctoral studies I will continue working in this area of software, and also develop heterogeneous computing workflows to utilise cutting-edge technologies for high-energy physics.

acm

I am a co-developer of an official ATLAS Software Group (ASG) software that replaced the previous Run-1 software suite, providing a set of high-level commands to work within the newly-adopted `git` and `cmake` tools. I continue to support `acm` as it is used by a large number of the members in the collaboration for software development.

Physics analysis

Upon arriving at CERN, and due to other factors, there was no obvious analysis team that I should have contributed most of my time to. In my early years as a PhD student, I was primarily involved with operations and simulation work. The first analysis I joined was based on searches for heavy diboson resonances in the $\ell\nu jj$ final state [247]. My contributions included the development and maintenance of the analysis software, and cutflow implementation and various validations thereof. Later I was asked to be the “statistical contact person” for a combination paper [248] that included twelve separate diboson final states. Eventually I decided it would be in my best interest to work on something new in which I would have a more significant role.

This would mark the start of my time working on the dijet+lepton analysis, which constitutes the heart of this thesis. Since this was a “hot off the press” analysis, there were many ways in which I could contribute. I stuck with this analysis for two years because it exposed me the process by which an analysis matures from a thought to a publication. After a year of involvement and following our first preliminary results¹ based on 80 fb⁻¹ of Run-2 data [225], I was asked to be (in ATLAS parlance) an “analysis contact”. As contact person, I have been involved with all major analysis decisions, responsible for organising group meetings, handled communications with convenors and editorial board, co-authored the support note and helped draft the publication, and assisted younger students. I am also the maintainer of the analysis software, and developed the framework for the analysis’s preservation (*i.e.* Docker images and RECAST [249]). I performed the trigger and selection efficiency studies, and developed the infrastructure to use Gaussian processes (GPs) for background modelling that will be pursued in the next iteration of the dijet+lepton analysis. The full Run-2 analysis paper, on which this thesis is based, is currently in preparation and will soon be in circulation to the collaboration.

¹ I am proud to note that the dijet+lepton analysis was one of only a handful of ATLAS analyses selected to release early Run-2 public results.

Bibliography

- [1] Murray Gell-Mann et al. “Amelioration of Divergence Difficulties in the Theory of Weak Interactions”. In: *Phys. Rev.* 179 (5 1969), pp. 1518–1527. DOI: [10.1103/PhysRev.179.1518](https://doi.org/10.1103/PhysRev.179.1518). URL: <https://link.aps.org/doi/10.1103/PhysRev.179.1518> (cit. on p. 3).
- [2] C. N. Yang and R. L. Mills. “Conservation of Isotopic Spin and Isotopic Gauge Invariance”. In: *Phys. Rev.* 96 (1 1954), pp. 191–195. DOI: [10.1103/PhysRev.96.191](https://doi.org/10.1103/PhysRev.96.191). URL: <https://link.aps.org/doi/10.1103/PhysRev.96.191> (cit. on p. 6).
- [3] C. Quigg. *Gauge Theories of the Strong, Weak, and Electromagnetic Interactions: Second Edition*. Princeton University Press, 2013. ISBN: 9781400848225. URL: <https://books.google.ca/books?id=Lt6thfc1gAgC> (cit. on pp. 8, 9).
- [4] Peter W. Higgs. “Broken Symmetries and the Masses of Gauge Bosons”. In: *Phys. Rev. Lett.* 13 (1964), pp. 508–509. DOI: [10.1103/PhysRevLett.13.508](https://doi.org/10.1103/PhysRevLett.13.508) (cit. on p. 8).
- [5] Peter W. Higgs. “Spontaneous Symmetry Breakdown without Massless Bosons”. In: *Phys. Rev.* 145 (1966), pp. 1156–1163. DOI: [10.1103/PhysRev.145.1156](https://doi.org/10.1103/PhysRev.145.1156) (cit. on p. 8).
- [6] F. Englert and R. Brout. “Broken Symmetry and the Mass of Gauge Vector Mesons”. In: *Phys. Rev. Lett.* 13 (1964), pp. 321–323. DOI: [10.1103/PhysRevLett.13.321](https://doi.org/10.1103/PhysRevLett.13.321) (cit. on p. 8).
- [7] G. S. Guralnik, C. R. Hagen, and T. W. B. Kibble. “Broken symmetries and the Goldstone theorem”. In: *Adv. Part. Phys.* 2 (1968), pp. 567–708 (cit. on p. 8).
- [8] T. W. B. Kibble. “Symmetry Breaking in Non-Abelian Gauge Theories”. In: *Phys. Rev.* 155 (5 1967), pp. 1554–1561. DOI: [10.1103/PhysRev.155.1554](https://doi.org/10.1103/PhysRev.155.1554). URL: <https://link.aps.org/doi/10.1103/PhysRev.155.1554> (cit. on p. 8).
- [9] J. Goldstone. “Field Theories with Superconductor Solutions”. In: *Nuovo Cim.* 19 (1961), pp. 154–164. DOI: [10.1007/BF02812722](https://doi.org/10.1007/BF02812722) (cit. on pp. 8, 10).
- [10] Yoichiro Nambu. “Axial Vector Current Conservation in Weak Interactions”. In: *Phys. Rev. Lett.* 4 (7 1960), pp. 380–382. DOI: [10.1103/PhysRevLett.4.380](https://doi.org/10.1103/PhysRevLett.4.380). URL: <https://link.aps.org/doi/10.1103/PhysRevLett.4.380> (cit. on p. 10).
- [11] Y. Nambu and G. Jona-Lasinio. “Dynamical Model of Elementary Particles Based on an Analogy with Superconductivity. I”. In: *Phys. Rev.* 122 (1 1961), pp. 345–358. DOI: [10.1103/PhysRev.122.345](https://doi.org/10.1103/PhysRev.122.345). URL: <https://link.aps.org/doi/10.1103/PhysRev.122.345> (cit. on p. 10).
- [12] Jeffrey Goldstone, Abdus Salam, and Steven Weinberg. “Broken Symmetries”. In: *Phys. Rev.* 127 (3 1962), pp. 965–970. DOI: [10.1103/PhysRev.127.965](https://doi.org/10.1103/PhysRev.127.965). URL: <https://link.aps.org/doi/10.1103/PhysRev.127.965> (cit. on p. 10).

- [13] A. Pich. “The Standard model of electroweak interactions”. In: *2004 European School of High-Energy Physics, Sant Feliu de Guixols, Spain, 30 May - 12 June 2004*. 2005, pp. 1–48. arXiv: [hep-ph/0502010](https://arxiv.org/abs/hep-ph/0502010) [hep-ph]. URL: <http://doc.cern.ch/yellowrep/2006/2006-003/p1.pdf> (cit. on pp. 10, 11).
- [14] Abdelhak Djouadi. “The Anatomy of electro-weak symmetry breaking. I: The Higgs boson in the standard model”. In: *Phys. Rept.* 457 (2008), pp. 1–216. DOI: [10.1016/j.physrep.2007.10.004](https://doi.org/10.1016/j.physrep.2007.10.004). arXiv: [hep-ph/0503172](https://arxiv.org/abs/hep-ph/0503172) [hep-ph] (cit. on p. 12).
- [15] Georges Aad et al. “Observation of a new particle in the search for the Standard Model Higgs boson with the ATLAS detector at the LHC”. In: *Phys. Lett.* B716 (2012), pp. 1–29. DOI: [10.1016/j.physletb.2012.08.020](https://doi.org/10.1016/j.physletb.2012.08.020). arXiv: [1207.7214](https://arxiv.org/abs/1207.7214) [hep-ex] (cit. on p. 12).
- [16] Serguei Chatrchyan et al. “Observation of a new boson at a mass of 125 GeV with the CMS experiment at the LHC”. In: *Phys. Lett.* B716 (2012), pp. 30–61. DOI: [10.1016/j.physletb.2012.08.021](https://doi.org/10.1016/j.physletb.2012.08.021). arXiv: [1207.7235](https://arxiv.org/abs/1207.7235) [hep-ex] (cit. on p. 12).
- [17] Giuseppe Degrandi et al. “Higgs mass and vacuum stability in the Standard Model at NNLO”. In: *Journal of High Energy Physics* 2012.8 (2012), p. 98. ISSN: 1029-8479. DOI: [10.1007/JHEP08\(2012\)098](https://doi.org/10.1007/JHEP08(2012)098). URL: [https://doi.org/10.1007/JHEP08\(2012\)098](https://doi.org/10.1007/JHEP08(2012)098) (cit. on p. 12).
- [18] John Ellis. “Outstanding questions: Physics beyond the Standard Model”. In: *Phil. Trans. Roy. Soc. Lond.* A370 (2012), pp. 818–830. DOI: [10.1098/rsta.2011.0452](https://doi.org/10.1098/rsta.2011.0452) (cit. on p. 12).
- [19] M. Gell-Mann. “A schematic model of baryons and mesons”. In: *Physics Letters* 8.3 (1964), pp. 214–215. ISSN: 0031-9163. DOI: [https://doi.org/10.1016/S0031-9163\(64\)92001-3](https://doi.org/10.1016/S0031-9163(64)92001-3). URL: <http://www.sciencedirect.com/science/article/pii/S0031916364920013> (cit. on p. 12).
- [20] Henry W. Kendall and W. K. H. Panofsky. “THE STRUCTURE OF THE PROTON AND THE NEUTRON”. In: *Sci. Am.* 224N6 (1971). [Sci. Am.224,61(1971)], pp. 61–77 (cit. on p. 12).
- [21] O. W. Greenberg. “Spin and Unitary-Spin Independence in a Paraquark Model of Baryons and Mesons”. In: *Phys. Rev. Lett.* 13 (20 1964), pp. 598–602. DOI: [10.1103/PhysRevLett.13.598](https://doi.org/10.1103/PhysRevLett.13.598). URL: <https://link.aps.org/doi/10.1103/PhysRevLett.13.598> (cit. on p. 13).
- [22] J. J. Aubert et al. “Experimental Observation of a Heavy Particle J ”. In: *Phys. Rev. Lett.* 33 (23 1974), pp. 1404–1406. DOI: [10.1103/PhysRevLett.33.1404](https://doi.org/10.1103/PhysRevLett.33.1404). URL: <https://link.aps.org/doi/10.1103/PhysRevLett.33.1404> (cit. on p. 13).
- [23] J. E. Augustin et al. “Discovery of a Narrow Resonance in e^+e^- Annihilation”. In: *Phys. Rev. Lett.* 33 (23 1974), pp. 1406–1408. DOI: [10.1103/PhysRevLett.33.1406](https://doi.org/10.1103/PhysRevLett.33.1406). URL: <https://link.aps.org/doi/10.1103/PhysRevLett.33.1406> (cit. on p. 13).
- [24] R. Brandelik et al. “Evidence for Planar Events in e^+e^- Annihilation at High-Energies”. In: *Phys. Lett.* 86B (1979), pp. 243–249. DOI: [10.1016/0370-2693\(79\)90830-X](https://doi.org/10.1016/0370-2693(79)90830-X) (cit. on p. 13).
- [25] M. Tanabashi et al. “Review of Particle Physics”. In: *Phys. Rev. D* 98 (3 2018), p. 030001. DOI: [10.1103/PhysRevD.98.030001](https://doi.org/10.1103/PhysRevD.98.030001). URL: <https://link.aps.org/doi/10.1103/PhysRevD.98.030001> (cit. on pp. 14, 15, 139).
- [26] V. C. Rubin and W. K. Ford Jr. “Rotation of the Andromeda Nebula from a Spectroscopic Survey of Emission Regions”. In: *Astrophysical Journal* 159 (Feb. 1970), p. 379. DOI: [10.1086/150317](https://doi.org/10.1086/150317) (cit. on p. 15).

- [27] Maxim Markevitch et al. “Direct constraints on the dark matter self-interaction cross-section from the merging galaxy cluster 1E0657-56”. In: *Astrophys. J.* 606 (2004), pp. 819–824. DOI: [10.1086/383178](https://doi.org/10.1086/383178). arXiv: [astro-ph/0309303](https://arxiv.org/abs/astro-ph/0309303) [[astro-ph](#)] (cit. on p. 15).
- [28] Gianfranco Bertone, Dan Hooper, and Joseph Silk. “Particle dark matter: Evidence, candidates and constraints”. In: *Phys. Rept.* 405 (2005), pp. 279–390. DOI: [10.1016/j.physrep.2004.08.031](https://doi.org/10.1016/j.physrep.2004.08.031). arXiv: [hep-ph/0404175](https://arxiv.org/abs/hep-ph/0404175) [[hep-ph](#)] (cit. on p. 16).
- [29] Y. Akrami et al. “Planck 2018 results. I. Overview and the cosmological legacy of Planck”. In: (2018). arXiv: [1807.06205](https://arxiv.org/abs/1807.06205) [[astro-ph.CO](#)] (cit. on p. 16).
- [30] N. Aghanim et al. “Planck 2018 results. VI. Cosmological parameters”. In: (2018). arXiv: [1807.06209](https://arxiv.org/abs/1807.06209) [[astro-ph.CO](#)] (cit. on p. 16).
- [31] Pieter van Dokkum et al. “A galaxy lacking dark matter”. In: *Nature* 555 (Mar. 2018), 629 EP –. URL: <https://doi.org/10.1038/nature25767> (cit. on p. 16).
- [32] Shany Danieli et al. “Still Missing Dark Matter: KCWI High-resolution Stellar Kinematics of NGC1052-DF2”. In: *The Astrophysical Journal* 874.2 (2019), p. L12. DOI: [10.3847/2041-8213/ab0e8c](https://doi.org/10.3847/2041-8213/ab0e8c). URL: <https://doi.org/10.3847/2F2041-8213%2Fab0e8c> (cit. on p. 16).
- [33] Pieter van Dokkum et al. “A Second Galaxy Missing Dark Matter in the NGC 1052 Group”. In: *The Astrophysical Journal* 874.1 (2019), p. L5. DOI: [10.3847/2041-8213/ab0d92](https://doi.org/10.3847/2041-8213/ab0d92). URL: <https://doi.org/10.3847/2F2041-8213%2Fab0d92> (cit. on p. 16).
- [34] Enrico Morgante. “Simplified Dark Matter Models”. In: *Adv. High Energy Phys.* 2018 (2018), p. 5012043. DOI: [10.1155/2018/5012043](https://doi.org/10.1155/2018/5012043). arXiv: [1804.01245](https://arxiv.org/abs/1804.01245) [[hep-ph](#)] (cit. on pp. 16, 17).
- [35] Kenneth Lane and Lukas Pritchett. “The light composite Higgs boson in strong extended technicolor”. In: *JHEP* 06 (2017), p. 140. DOI: [10.1007/JHEP06\(2017\)140](https://doi.org/10.1007/JHEP06(2017)140). arXiv: [1604.07085](https://arxiv.org/abs/1604.07085) [[hep-ph](#)] (cit. on p. 16).
- [36] Andreas Albert et al. “Recommendations of the LHC Dark Matter Working Group: Comparing LHC searches for heavy mediators of dark matter production in visible and invisible decay channels”. In: (2017). arXiv: [1703.05703](https://arxiv.org/abs/1703.05703) [[hep-ex](#)] (cit. on p. 18).
- [37] Frank Siegert. “Monte-Carlo event generation for the LHC”. PhD thesis. Durham U., 2010 (cit. on p. 19).
- [38] J. D. Bjorken. “Asymptotic Sum Rules at Infinite Momentum”. In: *Phys. Rev.* 179 (5 1969), pp. 1547–1553. DOI: [10.1103/PhysRev.179.1547](https://doi.org/10.1103/PhysRev.179.1547). URL: <https://link.aps.org/doi/10.1103/PhysRev.179.1547> (cit. on p. 20).
- [39] V. N. Gribov and L. N. Lipatov. “Deep inelastic e p scattering in perturbation theory”. In: *Sov. J. Nucl. Phys.* 15 (1972). [*Yad. Fiz.*15,781(1972)], pp. 438–450 (cit. on p. 20).
- [40] L. N. Lipatov. “The parton model and perturbation theory”. In: *Sov. J. Nucl. Phys.* 20 (1975). [*Yad. Fiz.*20,181(1974)], pp. 94–102 (cit. on p. 20).
- [41] G. Altarelli and G. Parisi. “Asymptotic freedom in parton language”. In: *Nuclear Physics B* 126.2 (1977), pp. 298–318. ISSN: 0550-3213. DOI: [https://doi.org/10.1016/0550-3213\(77\)90384-4](https://doi.org/10.1016/0550-3213(77)90384-4). URL: <http://www.sciencedirect.com/science/article/pii/0550321377903844> (cit. on p. 20).

- [42] Yuri L. Dokshitzer. “Calculation of the Structure Functions for Deep Inelastic Scattering and $e+e-$ Annihilation by Perturbation Theory in Quantum Chromodynamics.” In: *Sov. Phys. JETP* 46 (1977). [Zh. Eksp. Teor. Fiz.73,1216(1977)], pp. 641–653 (cit. on p. 20).
- [43] R. K. Ellis, W. J. Stirling, and B. R. Webber. *QCD and Collider Physics*. Cambridge Monographs on Particle Physics, Nuclear Physics and Cosmology. Cambridge University Press, 1996. DOI: [10.1017/CB09780511628788](https://doi.org/10.1017/CB09780511628788) (cit. on pp. 20, 23).
- [44] Luigi Del Debbio. “Parton distributions in the LHC era”. In: *EPJ Web of Conferences* 175 (Jan. 2018), p. 01006. DOI: [10.1051/epjconf/201817501006](https://doi.org/10.1051/epjconf/201817501006) (cit. on pp. 20, 21).
- [45] Sidney D Drell and Tung-Mow Yan. “Partons and their applications at high energies”. In: *Annals of Physics* 66.2 (1971), pp. 578 –623. ISSN: 0003-4916. DOI: [https://doi.org/10.1016/0003-4916\(71\)90071-6](https://doi.org/10.1016/0003-4916(71)90071-6). URL: <http://www.sciencedirect.com/science/article/pii/0003491671900716> (cit. on p. 21).
- [46] John M. Campbell, J. W. Huston, and W. J. Stirling. “Hard Interactions of Quarks and Gluons: A Primer for LHC Physics”. In: *Rept. Prog. Phys.* 70 (2007), p. 89. DOI: [10.1088/0034-4885/70/1/R02](https://doi.org/10.1088/0034-4885/70/1/R02). arXiv: [hep-ph/0611148](https://arxiv.org/abs/hep-ph/0611148) [hep-ph] (cit. on p. 22).
- [47] J C Collins and D E Soper. “The Theorems of Perturbative QCD”. In: *Annual Review of Nuclear and Particle Science* 37.1 (1987), pp. 383–409. DOI: [10.1146/annurev.ns.37.120187.002123](https://doi.org/10.1146/annurev.ns.37.120187.002123). eprint: <https://doi.org/10.1146/annurev.ns.37.120187.002123>. URL: <https://doi.org/10.1146/annurev.ns.37.120187.002123> (cit. on p. 21).
- [48] Ya. I. Azimov et al. “Similarity of parton and hadron spectra in QCD jets”. In: *Zeitschrift für Physik C Particles and Fields* 27.1 (1985), pp. 65–72. ISSN: 1431-5858. DOI: [10.1007/BF01642482](https://doi.org/10.1007/BF01642482). URL: <https://doi.org/10.1007/BF01642482> (cit. on p. 22).
- [49] Ya.I. Azimov et al. “The string effect and QCD coherence”. In: *Physics Letters B* 165.1 (1985), pp. 147 –150. ISSN: 0370-2693. DOI: [https://doi.org/10.1016/0370-2693\(85\)90709-9](https://doi.org/10.1016/0370-2693(85)90709-9). URL: <http://www.sciencedirect.com/science/article/pii/0370269385907099> (cit. on p. 22).
- [50] Yuri L. Dokshitzer and B. R. Webber. “Calculation of power corrections to hadronic event shapes”. In: *Phys. Lett.* B352 (1995), pp. 451–455. DOI: [10.1016/0370-2693\(95\)00548-Y](https://doi.org/10.1016/0370-2693(95)00548-Y). arXiv: [hep-ph/9504219](https://arxiv.org/abs/hep-ph/9504219) [hep-ph] (cit. on p. 22).
- [51] Yuri L. Dokshitzer, Valery A. Khoze, and S. I. Troian. “Specific features of heavy quark production. LPHD approach to heavy particle spectra”. In: *Phys. Rev.* D53 (1996), pp. 89–119. DOI: [10.1103/PhysRevD.53.89](https://doi.org/10.1103/PhysRevD.53.89). arXiv: [hep-ph/9506425](https://arxiv.org/abs/hep-ph/9506425) [hep-ph] (cit. on p. 22).
- [52] Yuri L. Dokshitzer, G. Marchesini, and B. R. Webber. “Dispersive approach to power behaved contributions in QCD hard processes”. In: *Nucl. Phys.* B469 (1996), pp. 93–142. DOI: [10.1016/0550-3213\(96\)00155-1](https://doi.org/10.1016/0550-3213(96)00155-1). arXiv: [hep-ph/9512336](https://arxiv.org/abs/hep-ph/9512336) [hep-ph] (cit. on p. 22).
- [53] R. D. Field and R. P. Feynman. “Quark elastic scattering as a source of high-transverse-momentum mesons”. In: *Phys. Rev. D* 15 (9 1977), pp. 2590–2616. DOI: [10.1103/PhysRevD.15.2590](https://doi.org/10.1103/PhysRevD.15.2590). URL: <https://link.aps.org/doi/10.1103/PhysRevD.15.2590> (cit. on p. 22).
- [54] R. D. Field and R. P. Feynman. “A Parametrization of the Properties of Quark Jets”. In: *Nucl. Phys.* B136 (1978), p. 1. DOI: [10.1016/0550-3213\(78\)90015-9](https://doi.org/10.1016/0550-3213(78)90015-9) (cit. on p. 22).
- [55] Bo Andersson et al. “Parton Fragmentation and String Dynamics”. In: *Phys. Rept.* 97 (1983), pp. 31–145. DOI: [10.1016/0370-1573\(83\)90080-7](https://doi.org/10.1016/0370-1573(83)90080-7) (cit. on p. 23).

- [56] Torbjörn Sjöstrand et al. “An Introduction to PYTHIA 8.2”. In: *Comput. Phys. Commun.* 191 (2015), pp. 159–177. DOI: [10.1016/j.cpc.2015.01.024](https://doi.org/10.1016/j.cpc.2015.01.024). arXiv: [1410.3012 \[hep-ph\]](https://arxiv.org/abs/1410.3012) (cit. on p. 23).
- [57] G. Marchesini and B. R. Webber. “Simulation of QCD Jets Including Soft Gluon Interference”. In: *Nucl. Phys.* B238 (1984), pp. 1–29. DOI: [10.1016/0550-3213\(84\)90463-2](https://doi.org/10.1016/0550-3213(84)90463-2) (cit. on p. 23).
- [58] D. Amati and G. Veneziano. “Preconfinement as a Property of Perturbative QCD”. In: *Phys. Lett.* 83B (1979), pp. 87–92. DOI: [10.1016/0370-2693\(79\)90896-7](https://doi.org/10.1016/0370-2693(79)90896-7) (cit. on p. 23).
- [59] Richard D. Field and Stephen Wolfram. “A QCD Model for e+ e- Annihilation”. In: *Nucl. Phys.* B213 (1983), pp. 65–84. DOI: [10.1016/0550-3213\(83\)90175-X](https://doi.org/10.1016/0550-3213(83)90175-X) (cit. on p. 24).
- [60] B. R. Webber. “A QCD Model for Jet Fragmentation Including Soft Gluon Interference”. In: *Nucl. Phys.* B238 (1984), pp. 492–528. DOI: [10.1016/0550-3213\(84\)90333-X](https://doi.org/10.1016/0550-3213(84)90333-X) (cit. on p. 24).
- [61] Jan-Christopher Winter, Frank Krauss, and Gerhard Soff. “A Modified cluster hadronization model”. In: *Eur. Phys. J.* C36 (2004), pp. 381–395. DOI: [10.1140/epjc/s2004-01960-8](https://doi.org/10.1140/epjc/s2004-01960-8). arXiv: [hep-ph/0311085 \[hep-ph\]](https://arxiv.org/abs/hep-ph/0311085) (cit. on p. 24).
- [62] Enrico Bothmann et al. “Event Generation with SHERPA 2.2”. In: (2019). arXiv: [1905.09127 \[hep-ph\]](https://arxiv.org/abs/1905.09127) (cit. on p. 24).
- [63] Oliver S. Bruning et al. “LHC Design Report Vol.1: The LHC Main Ring”. In: (2004) (cit. on p. 25).
- [64] O. Buning et al. “LHC Design Report. 2. The LHC infrastructure and general services”. In: (2004) (cit. on p. 25).
- [65] M. Benedikt et al. “LHC Design Report. 3. The LHC injector chain”. In: (2004) (cit. on p. 25).
- [66] *LEP design report*. Copies shelved as reports in LEP, PS and SPS libraries. Geneva: CERN, 1984. URL: <https://cds.cern.ch/record/102083> (cit. on p. 25).
- [67] R W Assmann, M Lamont, and S Myers. “A Brief History of the LEP Collider”. In: *Nucl. Phys. B, Proc. Suppl.* 109.CERN-SL-2002-009-OP (2002), 17–31. 15 p. URL: <https://cds.cern.ch/record/549223> (cit. on p. 25).
- [68] CERN. “The future of CERN”. In: (1987). Presented at CERN Annual report 1986, pp.36-39. URL: <https://cds.cern.ch/record/1950870> (cit. on p. 25).
- [69] J. Stirling. *proton-(anti)proton cross sections*. 2012. URL: <http://www.hep.ph.ic.ac.uk/~wstirling/plots/plots.html> (visited on 04/17/2019) (cit. on p. 27).
- [70] CERN. *Accelerator Performance and Statistics*. 2019. URL: acc-stats.web.cern.ch/acc-stats (visited on 04/18/2019) (cit. on p. 27).
- [71] Jean-Luc Caron. “The LHC injection complex.. L’ensemble d’injection du LHC.” AC Collection. Legacy of AC. Pictures from 1992 to 2002. 1993. URL: <https://cds.cern.ch/record/841568> (cit. on p. 28).
- [72] L Arnaudon et al. *Linac4 Technical Design Report*. Tech. rep. CERN-AB-2006-084. CARE-Note-2006-022-HIPPI. revised version submitted on 2006-12-14 09:00:40. Geneva: CERN, 2006. URL: <https://cds.cern.ch/record/1004186> (cit. on p. 26).

- [73] M J Barnes et al. “MKI performance during 2016 and plans for EYETS”. In: (2017), 175–180. 6 p. URL: <https://cds.cern.ch/record/2293529> (cit. on p. 28).
- [74] K. Aamodt et al. “The ALICE experiment at the CERN LHC”. In: *JINST* 3 (2008), S08002. DOI: [10.1088/1748-0221/3/08/S08002](https://doi.org/10.1088/1748-0221/3/08/S08002) (cit. on p. 29).
- [75] S. Chatrchyan et al. “The CMS Experiment at the CERN LHC”. In: *JINST* 3 (2008), S08004. DOI: [10.1088/1748-0221/3/08/S08004](https://doi.org/10.1088/1748-0221/3/08/S08004) (cit. on p. 29).
- [76] A. Augusto Alves Jr. et al. “The LHCb Detector at the LHC”. In: *JINST* 3 (2008), S08005. DOI: [10.1088/1748-0221/3/08/S08005](https://doi.org/10.1088/1748-0221/3/08/S08005) (cit. on p. 29).
- [77] Jean-Luc Caron. “Overall view of LHC experiments.. Vue d’ensemble des experiences du LHC.” AC Collection. Legacy of AC. Pictures from 1992 to 2002. 1998. URL: <https://cds.cern.ch/record/841555> (cit. on p. 29).
- [78] O. Adriani et al. “The LHCf detector at the CERN Large Hadron Collider”. In: *JINST* 3 (2008), S08006. DOI: [10.1088/1748-0221/3/08/S08006](https://doi.org/10.1088/1748-0221/3/08/S08006) (cit. on p. 29).
- [79] G. Anelli et al. “The TOTEM experiment at the CERN Large Hadron Collider”. In: *JINST* 3 (2008), S08007. DOI: [10.1088/1748-0221/3/08/S08007](https://doi.org/10.1088/1748-0221/3/08/S08007) (cit. on p. 29).
- [80] James Pinfold et al. “Technical Design Report of the MoEDAL Experiment”. In: (2009) (cit. on p. 29).
- [81] L. Mether. *16L2: Operation, observations and physics aspects*. Presented at The 8th LHC Operations Evian Workshop. 2017. URL: <https://indico.cern.ch/event/663598/contributions/2782390/> (visited on 04/19/2019) (cit. on p. 29).
- [82] LHC Programme Coordination. *Filling Schemes*. 2019. URL: https://lpc.web.cern.ch/cgi-bin/filling_schemes.py (visited on 04/19/2019) (cit. on p. 29).
- [83] G. Adruini and G. Milanese. *Resistive solenoid in the 16L2 interconnect*. Presented at the 319th LHC Machine Com-mittee (LMC). 2017. URL: https://espace.cern.ch/lhc-machine-committee/Minutes/1/lmc_319.pdf (visited on 04/19/2019) (cit. on p. 29).
- [84] ATLAS Collaboration. “The ATLAS Experiment at the CERN Large Hadron Collider”. In: *JINST* 3 (2008), S08003. DOI: [10.1088/1748-0221/3/08/S08003](https://doi.org/10.1088/1748-0221/3/08/S08003) (cit. on pp. 32, 35, 36, 41, 42, 44, 45, 47, 48, 51–54).
- [85] ATLAS Collaboration. *Standard Model Total Production Cross Section Measurements*. 2018. URL: <https://atlas.web.cern.ch/Atlas/GROUPS/PHYSICS/CombinedSummaryPlots/SM/> (visited on 03/25/2019) (cit. on p. 34).
- [86] Rabindra N. Mohapatra. “Supersymmetry and R-parity: an Overview”. In: *Phys. Scripta* 90 (2015), p. 088004. DOI: [10.1088/0031-8949/90/8/088004](https://doi.org/10.1088/0031-8949/90/8/088004). arXiv: [1503.06478](https://arxiv.org/abs/1503.06478) [hep-ph] (cit. on p. 34).
- [87] Paola Miele and Herman H.J ten Kate. “The superconducting magnet system for the ATLAS detector at CERN”. In: *Fusion Engineering and Design* 58-59 (2001), pp. 195–203. ISSN: 0920-3796. DOI: [https://doi.org/10.1016/S0920-3796\(01\)00432-X](https://doi.org/10.1016/S0920-3796(01)00432-X). URL: <http://www.sciencedirect.com/science/article/pii/S092037960100432X> (cit. on p. 36).

- [88] Akira Yamamoto et al. “Design and development of the ATLAS central solenoid magnet”. In: *Applied Superconductivity, IEEE Transactions on* 9 (July 1999), pp. 852–855. DOI: [10.1109/77.783430](https://doi.org/10.1109/77.783430) (cit. on p. 36).
- [89] Karolos Potamianos. *The upgraded Pixel detector and the commissioning of the Inner Detector tracking of the ATLAS experiment for Run-2 at the Large Hadron Collider*. Tech. rep. ATL-PHYS-PROC-2016-104. 15 pages, EPS-HEP 2015 Proceedings. Geneva: CERN, 2016. URL: <http://cds.cern.ch/record/2209070> (cit. on p. 37).
- [90] M Capeans et al. *ATLAS Insertable B-Layer Technical Design Report*. Tech. rep. CERN-LHCC-2010-013. ATLAS-TDR-19. 2010. URL: <https://cds.cern.ch/record/1291633> (cit. on p. 37).
- [91] B. Abbott et al. “Production and Integration of the ATLAS Insertable B-Layer”. In: *JINST* 13.05 (2018), T05008. DOI: [10.1088/1748-0221/13/05/T05008](https://doi.org/10.1088/1748-0221/13/05/T05008). arXiv: [1803.00844](https://arxiv.org/abs/1803.00844) [[physics.ins-det](#)] (cit. on p. 37).
- [92] S.I. Parker, C.J. Kenney, and J. Segal. “3D — A proposed new architecture for solid-state radiation detectors”. In: *Nuclear Instruments and Methods in Physics Research Section A: Accelerators, Spectrometers, Detectors and Associated Equipment* 395.3 (1997). Proceedings of the Third International Workshop on Semiconductor Pixel Detectors for Particles and X-rays, pp. 328–343. ISSN: 0168-9002. DOI: [https://doi.org/10.1016/S0168-9002\(97\)00694-3](https://doi.org/10.1016/S0168-9002(97)00694-3). URL: <http://www.sciencedirect.com/science/article/pii/S0168900297006943> (cit. on p. 38).
- [93] Daniela Bortoletto. “How and why silicon sensors are becoming more and more intelligent?” In: *JINST* 10.08 (2015), p. C08016. DOI: [10.1088/1748-0221/10/08/C08016](https://doi.org/10.1088/1748-0221/10/08/C08016). arXiv: [1506.05168](https://arxiv.org/abs/1506.05168) [[physics.ins-det](#)] (cit. on p. 38).
- [94] Maria Elena Stramaglia. *Calibration Analysis Software for the ATLAS Pixel Detector*. Tech. rep. ATL-INDET-PROC-2015-003. Geneva: CERN, 2015. DOI: [10.1016/j.nima.2015.11.120](https://doi.org/10.1016/j.nima.2015.11.120). URL: <https://cds.cern.ch/record/2027805> (cit. on p. 38).
- [95] ATLAS Collaboration. *Public Pixel Tracker Plots for Collision Data*. 2018. URL: <https://twiki.cern.ch/twiki/bin/view/AtlasPublic/PixelPublicResults> (visited on 04/02/2019) (cit. on p. 38).
- [96] “ATLAS inner detector: Technical design report. Vol. 1”. In: (1997) (cit. on p. 39).
- [97] *ATLAS inner detector: Technical Design Report, 1*. Technical Design Report ATLAS. Geneva: CERN, 1997. URL: <https://cds.cern.ch/record/331063> (cit. on p. 39).
- [98] The ATLAS collaboration. “Operation and performance of the ATLAS semiconductor tracker”. In: *Journal of Instrumentation* 9.08 (2014), P08009–P08009. DOI: [10.1088/1748-0221/9/08/p08009](https://doi.org/10.1088/1748-0221/9/08/p08009). URL: <https://doi.org/10.1088/1748-0221/9/08/p08009> (cit. on p. 39).
- [99] ATLAS Collaboration. *SCT radiation damage plots, prepared for Radiation damage workshop*. 2019. URL: <https://atlas.web.cern.ch/Atlas/GROUPS/PHYSICS/PLOTS/SCT-2019-001/> (visited on 02/11/2019) (cit. on p. 39).
- [100] Morad Aaboud et al. “Performance of the ATLAS Transition Radiation Tracker in Run 1 of the LHC: tracker properties”. In: *JINST* 12.05 (2017), P05002. DOI: [10.1088/1748-0221/12/05/P05002](https://doi.org/10.1088/1748-0221/12/05/P05002). arXiv: [1702.06473](https://arxiv.org/abs/1702.06473) [[hep-ex](#)] (cit. on p. 40).

- [101] A. Andronic and J.P. Wessels. “Transition radiation detectors”. In: *Nuclear Instruments and Methods in Physics Research Section A: Accelerators, Spectrometers, Detectors and Associated Equipment* 666 (2012). Advanced Instrumentation, pp. 130 –147. ISSN: 0168-9002. DOI: <https://doi.org/10.1016/j.nima.2011.09.041>. URL: <http://www.sciencedirect.com/science/article/pii/S0168900211018134> (cit. on p. 40).
- [102] Bartosz Mindur. “ATLAS Transition Radiation Tracker (TRT): Straw tubes for tracking and particle identification at the Large Hadron Collider”. In: *Nuclear Instruments and Methods in Physics Research Section A: Accelerators, Spectrometers, Detectors and Associated Equipment* 845 (2017). Proceedings of the Vienna Conference on Instrumentation 2016, pp. 257 –261. ISSN: 0168-9002. DOI: <https://doi.org/10.1016/j.nima.2016.04.026>. URL: <http://www.sciencedirect.com/science/article/pii/S0168900216301905> (cit. on p. 40).
- [103] J. Abdallah et al. Tech. rep. (cit. on p. 41).
- [104] O Gildemeister, F Nessi-Tedaldi, and Marzio Nessi. *An economic concept for a barrel hadron calorimeter with iron scintillation sampling and WLS-fiber readout*. Tech. rep. ATL-CAL-91-006. ATL-AC-PN-6. Geneva: CERN, 1991. URL: <https://cds.cern.ch/record/685618> (cit. on p. 41).
- [105] Christian W. Fabjan and Fabiola Gianotti. “Calorimetry for particle physics”. In: *Rev. Mod. Phys.* 75 (4 2003), pp. 1243–1286. DOI: [10.1103/RevModPhys.75.1243](https://doi.org/10.1103/RevModPhys.75.1243). URL: <https://link.aps.org/doi/10.1103/RevModPhys.75.1243> (cit. on p. 43).
- [106] Bruno Rossi and Kenneth Greisen. “Cosmic-Ray Theory”. In: *Rev. Mod. Phys.* 13 (4 1941), pp. 240–309. DOI: [10.1103/RevModPhys.13.240](https://doi.org/10.1103/RevModPhys.13.240). URL: <https://link.aps.org/doi/10.1103/RevModPhys.13.240> (cit. on p. 43).
- [107] B. Aubert et al. “Development and construction of large size signal electrodes for the ATLAS electromagnetic calorimeter”. In: *Nuclear Instruments and Methods in Physics Research Section A: Accelerators, Spectrometers, Detectors and Associated Equipment* 539.3 (2005), pp. 558 – 594. ISSN: 0168-9002. DOI: <https://doi.org/10.1016/j.nima.2004.11.005>. URL: <http://www.sciencedirect.com/science/article/pii/S0168900204023563> (cit. on p. 43).
- [108] M. Aleksa et al. “Construction, assembly and tests of the ATLAS electromagnetic end-cap calorimeters”. In: *JINST* 3 (2008), P06002. DOI: [10.1088/1748-0221/3/06/P06002](https://doi.org/10.1088/1748-0221/3/06/P06002) (cit. on pp. 45, 46).
- [109] R. Wigmans. “Calorimetry: Energy measurement in particle physics”. In: *Int. Ser. Monogr. Phys.* 107 (2000), pp. 1–726 (cit. on p. 46).
- [110] N.J. Buchanan et al. In: 3.09 (2008), P09003–P09003. DOI: [10.1088/1748-0221/3/09/P09003](https://doi.org/10.1088/1748-0221/3/09/P09003). URL: <https://doi.org/10.1088/1748-0221/3/09/P09003> (cit. on p. 49).
- [111] W.E. Cleland and E.G. Stern. “Signal processing considerations for liquid ionization calorimeters in a high rate environment”. In: *Nuclear Instruments and Methods in Physics Research Section A: Accelerators, Spectrometers, Detectors and Associated Equipment* 338.2 (1994), pp. 467 –497. ISSN: 0168-9002. DOI: [https://doi.org/10.1016/0168-9002\(94\)91332-3](https://doi.org/10.1016/0168-9002(94)91332-3). URL: <http://www.sciencedirect.com/science/article/pii/S0168900294913323> (cit. on p. 50).

- [112] G. Aad et al. “Commissioning of the ATLAS Muon Spectrometer with Cosmic Rays”. In: *Eur. Phys. J. C* 70 (2010), pp. 875–916. DOI: [10.1140/epjc/s10052-010-1415-2](https://doi.org/10.1140/epjc/s10052-010-1415-2). arXiv: [1006.4384](https://arxiv.org/abs/1006.4384) [[physics.ins-det](#)] (cit. on p. 50).
- [113] “ATLAS muon spectrometer: Technical design report”. In: (1997) (cit. on p. 51).
- [114] F. Bauer et al. “Construction and Test of MDT Chambers for the ATLAS Muon Spectrometer”. In: *Nucl. Instrum. Meth. A* 461 (2001), pp. 17–20. DOI: [10.1016/S0168-9002\(00\)01156-6](https://doi.org/10.1016/S0168-9002(00)01156-6). arXiv: [1604.02000](https://arxiv.org/abs/1604.02000) [[physics.ins-det](#)] (cit. on p. 51).
- [115] ATLAS Collaboration. *RPC performance plots based on 2018 dataset*. 2018. URL: <https://atlas.web.cern.ch/Atlas/GROUPS/PHYSICS/PLOTS/MUON-2018-09/index.html> (visited on 04/08/2019) (cit. on p. 53).
- [116] Oleksandr Viazlo. “ATLAS LUCID detector upgrade for LHC Run 2”. In: *PoS EPS-HEP2015* (2015), p. 275. DOI: [10.22323/1.234.0275](https://doi.org/10.22323/1.234.0275) (cit. on p. 54).
- [117] S van der Meer. *Calibration of the effective beam height in the ISR*. Tech. rep. CERN-ISR-PO-68-31. ISR-PO-68-31. Geneva: CERN, 1968. URL: <https://cds.cern.ch/record/296752> (cit. on p. 55).
- [118] Morad Aaboud et al. “Luminosity determination in pp collisions at $\sqrt{s} = 8$ TeV using the ATLAS detector at the LHC”. In: *Eur. Phys. J. C* 76.12 (2016), p. 653. DOI: [10.1140/epjc/s10052-016-4466-1](https://doi.org/10.1140/epjc/s10052-016-4466-1). arXiv: [1608.03953](https://arxiv.org/abs/1608.03953) [[hep-ex](#)] (cit. on p. 55).
- [119] “The ATLAS Data Acquisition and High Level Trigger system”. In: *Journal of Instrumentation* 11.06 (2016), P06008–P06008. DOI: [10.1088/1748-0221/11/06/p06008](https://doi.org/10.1088/1748-0221/11/06/p06008). URL: <https://doi.org/10.1088/2F1748-0221%2F11%2F06%2Fp06008> (cit. on p. 57).
- [120] ATLAS Collaboration. *Luminosity Public Results Run-2*. 2019. URL: https://twiki.cern.ch/twiki/bin/view/AtlasPublic/LuminosityPublicResultsRun2#Publications_and_Conference_Resu (visited on 04/09/2019) (cit. on pp. 59, 61).
- [121] B. Muratori and T. Pieloni. “Luminosity levelling techniques for the LHC”. In: *Proceedings, ICFA Mini-Workshop on Beam-Beam Effects in Hadron Colliders (BB2013): CERN, Geneva, Switzerland, March 18-22 2013*. 2014, pp. 177–181. DOI: [10.5170/CERN-2014-004.177](https://doi.org/10.5170/CERN-2014-004.177). arXiv: [1410.5646](https://arxiv.org/abs/1410.5646) [[physics.acc-ph](#)] (cit. on p. 59).
- [122] G. Duckeck et al. “ATLAS computing: Technical design report”. In: (2005) (cit. on p. 62).
- [123] Morad Aaboud et al. “Jet reconstruction and performance using particle flow with the ATLAS Detector”. In: *Eur. Phys. J. C* 77.7 (2017), p. 466. DOI: [10.1140/epjc/s10052-017-5031-2](https://doi.org/10.1140/epjc/s10052-017-5031-2). arXiv: [1703.10485](https://arxiv.org/abs/1703.10485) [[hep-ex](#)] (cit. on pp. 62, 74).
- [124] W Lampl et al. *Calorimeter Clustering Algorithms: Description and Performance*. Tech. rep. ATL-LARG-PUB-2008-002. ATL-COM-LARG-2008-003. Geneva: CERN, 2008. URL: <https://cds.cern.ch/record/1099735> (cit. on p. 63).
- [125] *Electron and photon reconstruction and performance in ATLAS using a dynamical, topological cell clustering-based approach*. Tech. rep. ATL-PHYS-PUB-2017-022. Geneva: CERN, 2017. URL: <https://cds.cern.ch/record/2298955> (cit. on pp. 63, 64).

- [126] Azriel Rosenfeld and John L. Pfaltz. “Sequential Operations in Digital Picture Processing”. In: *J. ACM* 13.4 (Oct. 1966), pp. 471–494. ISSN: 0004-5411. DOI: [10.1145/321356.321357](https://doi.org/10.1145/321356.321357). URL: <http://doi.acm.org/10.1145/321356.321357> (cit. on p. 65).
- [127] M. Aaboud et al. “Performance of the ATLAS Track Reconstruction Algorithms in Dense Environments in LHC Run 2”. In: *Eur. Phys. J. C* 77.10 (2017), p. 673. DOI: [10.1140/epjc/s10052-017-5225-7](https://doi.org/10.1140/epjc/s10052-017-5225-7). arXiv: [1704.07983](https://arxiv.org/abs/1704.07983) [[hep-ex](#)] (cit. on p. 66).
- [128] Georges Aad et al. “Electron performance measurements with the ATLAS detector using the 2010 LHC proton-proton collision data”. In: *Eur. Phys. J. C* 72 (2012), p. 1909. DOI: [10.1140/epjc/s10052-012-1909-1](https://doi.org/10.1140/epjc/s10052-012-1909-1). arXiv: [1110.3174](https://arxiv.org/abs/1110.3174) [[hep-ex](#)] (cit. on p. 67).
- [129] ATLAS Collaboration. “Electron reconstruction and identification efficiency measurements with the ATLAS detector using the 2011 LHC proton-proton collision data”. In: *Eur. Phys. J. C* 74.7 (2014), p. 2941. DOI: [10.1140/epjc/s10052-014-2941-0](https://doi.org/10.1140/epjc/s10052-014-2941-0). arXiv: [1404.2240](https://arxiv.org/abs/1404.2240) [[hep-ex](#)] (cit. on p. 67).
- [130] Morad Aaboud et al. “Electron reconstruction and identification in the ATLAS experiment using the 2015 and 2016 LHC proton-proton collision data at $\sqrt{s} = 13$ TeV”. In: *Submitted to: Eur. Phys. J.* (2019). arXiv: [1902.04655](https://arxiv.org/abs/1902.04655) [[physics.ins-det](#)] (cit. on pp. 68–70, 97, 140).
- [131] T G Cornelissen et al. “The global χ^2 track fitter in ATLAS”. In: *Journal of Physics: Conference Series* 119.3 (2008), p. 032013. DOI: [10.1088/1742-6596/119/3/032013](https://doi.org/10.1088/1742-6596/119/3/032013). URL: <https://doi.org/10.1088/1742-6596/119/3/032013> (cit. on p. 68).
- [132] *Improved electron reconstruction in ATLAS using the Gaussian Sum Filter-based model for bremsstrahlung*. Tech. rep. ATLAS-CONF-2012-047. Geneva: CERN, 2012. URL: <https://cds.cern.ch/record/1449796> (cit. on p. 68).
- [133] G. Aad et al. “The ATLAS Simulation Infrastructure. The ATLAS Simulation Infrastructure”. In: *Eur. Phys. J. C* 70. arXiv:1005.4568. CERN-PH-EP-2010-044 (2010). Submitted to *Eur. Phys. J. C*, 823–874. 53 p. URL: <https://cds.cern.ch/record/1267853> (cit. on pp. 69, 87).
- [134] Georges Aad et al. “Muon reconstruction performance of the ATLAS detector in proton-proton collision data at $\sqrt{s} = 13$ TeV”. In: *Eur. Phys. J. C* 76.5 (2016), p. 292. DOI: [10.1140/epjc/s10052-016-4120-y](https://doi.org/10.1140/epjc/s10052-016-4120-y). arXiv: [1603.05598](https://arxiv.org/abs/1603.05598) [[hep-ex](#)] (cit. on pp. 72, 73, 97, 140).
- [135] S. D. Ellis et al. “Jets in hadron-hadron collisions”. In: *Prog. Part. Nucl. Phys.* 60 (2008), pp. 484–551. DOI: [10.1016/j.pnpnp.2007.12.002](https://doi.org/10.1016/j.pnpnp.2007.12.002). arXiv: [0712.2447](https://arxiv.org/abs/0712.2447) [[hep-ph](#)] (cit. on p. 74).
- [136] J E Huth et al. “Toward a standardization of jet definitions”. In: *FERMILAB-CONF-90-249-E* (1990), 7 p. URL: <https://cds.cern.ch/record/217490> (cit. on p. 74).
- [137] S. V. Chekanov. “Jet algorithms: A Minireview”. In: *Hadron collider physics. Proceedings, 14th Topical Conference, HCP 2002, Karlsruhe, Germany, September 29-October 4, 2002*. 2002, pp. 478–486. arXiv: [hep-ph/0211298](https://arxiv.org/abs/hep-ph/0211298) [[hep-ph](#)] (cit. on p. 74).
- [138] Georges Aad et al. “Jet energy measurement and its systematic uncertainty in proton-proton collisions at $\sqrt{s} = 7$ TeV with the ATLAS detector”. In: *Eur. Phys. J. C* 75 (2015), p. 17. DOI: [10.1140/epjc/s10052-014-3190-y](https://doi.org/10.1140/epjc/s10052-014-3190-y). arXiv: [1406.0076](https://arxiv.org/abs/1406.0076) [[hep-ex](#)] (cit. on p. 74).

- [139] M. Aaboud et al. “Jet energy scale measurements and their systematic uncertainties in proton-proton collisions at $\sqrt{s} = 13$ TeV with the ATLAS detector”. In: *Phys. Rev. D* 96.7 (2017), p. 072002. DOI: [10.1103/PhysRevD.96.072002](https://doi.org/10.1103/PhysRevD.96.072002). arXiv: [1703.09665 \[hep-ex\]](https://arxiv.org/abs/1703.09665) (cit. on pp. 76, 77, 131, 132).
- [140] Georges Aad et al. “Jet energy measurement with the ATLAS detector in proton-proton collisions at $\sqrt{s} = 7$ TeV”. In: *Eur. Phys. J. C* 73.3 (2013), p. 2304. DOI: [10.1140/epjc/s10052-013-2304-2](https://doi.org/10.1140/epjc/s10052-013-2304-2). arXiv: [1112.6426 \[hep-ex\]](https://arxiv.org/abs/1112.6426) (cit. on p. 78).
- [141] J. D. Dowell. “The CERN proton-antiproton collider and the discovery of the W and Z particles”. In: *Science Progress (1933-)* 69.274 (1984), pp. 257–289. ISSN: 00368504, 20477163. URL: <http://www.jstor.org/stable/43420602> (cit. on p. 79).
- [142] Alan Astbury et al. *A 4π solid angle detector for the SPS used as a proton-antiproton collider at a centre of mass energy of 540 GeV*. Tech. rep. CERN-SPSC-78-6. CERN-SPSC-78-06. SPSC-P-92. Geneva: CERN, 1978. URL: <https://cds.cern.ch/record/319371> (cit. on p. 79).
- [143] “Two-jet mass distributions at the CERN proton-antiproton collider”. In: *Physics Letters B* 209.1 (1988), pp. 127–134. ISSN: 0370-2693. DOI: [https://doi.org/10.1016/0370-2693\(88\)91843-6](https://doi.org/10.1016/0370-2693(88)91843-6). URL: <http://www.sciencedirect.com/science/article/pii/0370269388918436> (cit. on p. 79).
- [144] Maris A. Abolins et al. “A Proposal to study high energy anti-proton proton interactions at the Fermilab collider with a 4 pi high resolution electromagnetic / hadronic calorimeter”. In: (1982) (cit. on p. 79).
- [145] J. Alitti et al. “A Search for new intermediate vector mesons and excited quarks decaying to two jets at the CERN $\bar{p}p$ collider”. In: *Nucl. Phys. B* 400 (1993), pp. 3–24. DOI: [10.1016/0550-3213\(93\)90395-6](https://doi.org/10.1016/0550-3213(93)90395-6) (cit. on p. 79).
- [146] UA2 Collaboration. “A measurement of two-jet decays of the W and Z bosons at the CERN $p\bar{p}$ collider”. In: *Zeitschrift fur Physik C Particles and Fields* 49.1 (1991), pp. 17–28. ISSN: 1431-5858. DOI: [10.1007/BF01570793](https://doi.org/10.1007/BF01570793) (cit. on pp. 79, 82, 109).
- [147] P. M. Watkins. “DISCOVERY OF THE W AND Z BOSONS”. In: *Contemp. Phys.* 27 (1986), pp. 291–324. DOI: [10.1080/00107518608211015](https://doi.org/10.1080/00107518608211015) (cit. on p. 80).
- [148] Vladimir Shiltsev et al. “Tevatron electron lenses: Design and operation”. In: *Phys. Rev. ST Accel. Beams* 11 (10 2008), p. 103501. DOI: [10.1103/PhysRevSTAB.11.103501](https://doi.org/10.1103/PhysRevSTAB.11.103501). URL: <https://link.aps.org/doi/10.1103/PhysRevSTAB.11.103501> (cit. on p. 80).
- [149] Stephen Holmes, Ronald S Moore, and Vladimir Shiltsev. “Overview of the Tevatron collider complex: goals, operations and performance”. In: *Journal of Instrumentation* 6.08 (2011), T08001–T08001. DOI: [10.1088/1748-0221/6/08/t08001](https://doi.org/10.1088/1748-0221/6/08/t08001). URL: <https://doi.org/10.1088%2F1748-0221%2F6%2F08%2Ft08001> (cit. on p. 80).
- [150] R. Blair et al. “The CDF-II detector: Technical design report”. In: (1996) (cit. on p. 80).
- [151] F. Abe et al. “The CDF detector: an overview”. In: *Nuclear Instruments and Methods in Physics Research Section A: Accelerators, Spectrometers, Detectors and Associated Equipment* 271.3 (1988), pp. 387–403. ISSN: 0168-9002. DOI: [https://doi.org/10.1016/0168-9002\(88\)90298-7](https://doi.org/10.1016/0168-9002(88)90298-7). URL: <http://www.sciencedirect.com/science/article/pii/0168900288902987> (cit. on p. 80).

- [152] F. Abe et al. “Search for New Particles Decaying to Dijets in $p\bar{p}$ Collisions at $\sqrt{s} = 1.8$ TeV”. In: *Phys. Rev. Lett.* 74 (18 1995), pp. 3538–3543. DOI: [10.1103/PhysRevLett.74.3538](https://doi.org/10.1103/PhysRevLett.74.3538). URL: <https://link.aps.org/doi/10.1103/PhysRevLett.74.3538> (cit. on p. 80).
- [153] F. Abe et al. “Search for new particles decaying to dijets at CDF”. In: *Phys. Rev. D* 55 (9 1997), R5263–R5268. DOI: [10.1103/PhysRevD.55.R5263](https://doi.org/10.1103/PhysRevD.55.R5263). URL: <https://link.aps.org/doi/10.1103/PhysRevD.55.R5263> (cit. on p. 80).
- [154] D. Cutts et al. “Proposal to Study a Large Liquid Argon-Uranium Absorber Calorimeter”. In: (1986). DOI: [10.2172/991770](https://doi.org/10.2172/991770) (cit. on p. 80).
- [155] B. Gomez et al. “E823 (D0 upgrade): Magnetic tracking”. In: (1993) (cit. on p. 80).
- [156] V. M. Abazov et al. “Search for new particles in the two jet decay channel with the D0 detector”. In: *Phys. Rev. D* 69 (2004), p. 111101. DOI: [10.1103/PhysRevD.69.111101](https://doi.org/10.1103/PhysRevD.69.111101). arXiv: [hep-ex/0308033](https://arxiv.org/abs/hep-ex/0308033) [[hep-ex](#)] (cit. on p. 80).
- [157] S. Abachi et al. “Observation of the top quark”. In: *Phys. Rev. Lett.* 74 (1995), pp. 2632–2637. DOI: [10.1103/PhysRevLett.74.2632](https://doi.org/10.1103/PhysRevLett.74.2632). arXiv: [hep-ex/9503003](https://arxiv.org/abs/hep-ex/9503003) [[hep-ex](#)] (cit. on p. 80).
- [158] F. Abe et al. “Observation of top quark production in $\bar{p}p$ collisions”. In: *Phys. Rev. Lett.* 74 (1995), pp. 2626–2631. DOI: [10.1103/PhysRevLett.74.2626](https://doi.org/10.1103/PhysRevLett.74.2626). arXiv: [hep-ex/9503002](https://arxiv.org/abs/hep-ex/9503002) [[hep-ex](#)] (cit. on p. 80).
- [159] Yvonne Peters. “Tevatron Legacy”. In: *Nuovo Cim.* C035N3 (2012), pp. 181–186. DOI: [10.1393/ncc/i2012-11243-4](https://doi.org/10.1393/ncc/i2012-11243-4). arXiv: [1202.6196](https://arxiv.org/abs/1202.6196) [[hep-ex](#)] (cit. on p. 80).
- [160] T. Aaltonen et al. “Search for new particles decaying into dijets in proton-antiproton collisions at $\sqrt{s} = 1.96$ TeV”. In: *Phys. Rev. D* 79 (11 2009), p. 112002. DOI: [10.1103/PhysRevD.79.112002](https://doi.org/10.1103/PhysRevD.79.112002). URL: <https://link.aps.org/doi/10.1103/PhysRevD.79.112002> (cit. on p. 80).
- [161] Georges Aad et al. “Search for new phenomena in dijet mass and angular distributions from pp collisions at $\sqrt{s} = 13$ TeV with the ATLAS detector”. In: *Phys. Lett.* B754 (2016), pp. 302–322. DOI: [10.1016/j.physletb.2016.01.032](https://doi.org/10.1016/j.physletb.2016.01.032). arXiv: [1512.01530](https://arxiv.org/abs/1512.01530) [[hep-ex](#)] (cit. on pp. 80, 82, 109).
- [162] ATLAS Collaboration. “Search for new phenomena in dijet events using 37 fb⁻¹ of pp collision data collected at $\sqrt{s} = 13$ TeV with the ATLAS detector”. In: *Phys. Rev. D* 96.5 (2017), p. 052004. DOI: [10.1103/PhysRevD.96.052004](https://doi.org/10.1103/PhysRevD.96.052004). arXiv: [1703.09127](https://arxiv.org/abs/1703.09127) [[hep-ex](#)] (cit. on pp. 80, 110).
- [163] Albert M Sirunyan et al. “Search for narrow and broad dijet resonances in proton-proton collisions at $\sqrt{s} = 13$ TeV and constraints on dark matter mediators and other new particles”. In: *JHEP* 08 (2018), p. 130. DOI: [10.1007/JHEP08\(2018\)130](https://doi.org/10.1007/JHEP08(2018)130). arXiv: [1806.00843](https://arxiv.org/abs/1806.00843) [[hep-ex](#)] (cit. on p. 80).
- [164] Albert M Sirunyan et al. “Search for new physics in dijet angular distributions using proton-proton collisions at $\sqrt{s} = 13$ TeV and constraints on dark matter and other models”. In: *Eur. Phys. J. C* 78.9 (2018), p. 789. DOI: [10.1140/epjc/s10052-018-6242-x](https://doi.org/10.1140/epjc/s10052-018-6242-x). arXiv: [1803.08030](https://arxiv.org/abs/1803.08030) [[hep-ex](#)] (cit. on pp. 80, 139).
- [165] M. Aaboud et al. “Search for low-mass dijet resonances using trigger-level jets with the ATLAS detector in pp collisions at $\sqrt{s} = 13$ TeV”. In: *Phys. Rev. Lett.* 121.8 (2018), p. 081801. DOI: [10.1103/PhysRevLett.121.081801](https://doi.org/10.1103/PhysRevLett.121.081801). arXiv: [1804.03496](https://arxiv.org/abs/1804.03496) [[hep-ex](#)] (cit. on pp. 80, 110, 139).

- [166] Vardan Khachatryan et al. “Search for narrow resonances in dijet final states at $\sqrt{s} = 8$ TeV with the novel CMS technique of data scouting”. In: *Phys. Rev. Lett.* 117.3 (2016), p. 031802. DOI: [10.1103/PhysRevLett.117.031802](https://doi.org/10.1103/PhysRevLett.117.031802). arXiv: [1604.08907](https://arxiv.org/abs/1604.08907) [[hep-ex](#)] (cit. on pp. [80](#), [139](#)).
- [167] Morad Aaboud et al. “Search for low-mass resonances decaying into two jets and produced in association with a photon using pp collisions at $\sqrt{s} = 13$ TeV with the ATLAS detector”. In: *Submitted to: Phys. Lett.* (2019). arXiv: [1901.10917](https://arxiv.org/abs/1901.10917) [[hep-ex](#)] (cit. on p. [80](#)).
- [168] Estia Eichten, Kenneth D. Lane, and John Womersley. “Finding low scale technicolor at hadron colliders”. In: *Phys. Lett.* B405 (1997), pp. 305–311. DOI: [10.1016/S0370-2693\(97\)00637-0](https://doi.org/10.1016/S0370-2693(97)00637-0). arXiv: [hep-ph/9704455](https://arxiv.org/abs/hep-ph/9704455) [[hep-ph](#)] (cit. on p. [80](#)).
- [169] Guido Altarelli, B. Mele, and M. Ruiz-Altaba. “Searching for New Heavy Vector Bosons in $p\bar{p}$ Colliders”. In: *Z. Phys.* C45 (1989). [Erratum: *Z. Phys.*C47,676(1990)], p. 109. DOI: [10.1007/BF01552335](https://doi.org/10.1007/BF01552335), [10.1007/BF01556677](https://doi.org/10.1007/BF01556677) (cit. on p. [80](#)).
- [170] A. G. Akeroyd et al. “Prospects for charged Higgs searches at the LHC”. In: *Eur. Phys. J.* C77.5 (2017), p. 276. DOI: [10.1140/epjc/s10052-017-4829-2](https://doi.org/10.1140/epjc/s10052-017-4829-2). arXiv: [1607.01320](https://arxiv.org/abs/1607.01320) [[hep-ph](#)] (cit. on p. [80](#)).
- [171] Daniel Abercrombie et al. “Dark Matter Benchmark Models for Early LHC Run-2 Searches: Report of the ATLAS/CMS Dark Matter Forum”. In: (2015). Ed. by Antonio Boveia et al. arXiv: [1507.00966](https://arxiv.org/abs/1507.00966) [[hep-ex](#)] (cit. on pp. [80](#), [91](#)).
- [172] *Search for dijet resonances in events with an isolated lepton using $\sqrt{s} = 13$ TeV proton-proton collision data collected by the ATLAS detector*. Tech. rep. ATLAS-CONF-2018-015. Geneva: CERN, 2018. URL: <https://cds.cern.ch/record/2621126> (cit. on p. [81](#)).
- [173] Morad Aaboud et al. “Measurement of the W^+W^- production cross section in pp collisions at a centre-of-mass energy of $\sqrt{s} = 13$ TeV with the ATLAS experiment”. In: *Phys. Lett.* B773 (2017), pp. 354–374. DOI: [10.1016/j.physletb.2017.08.047](https://doi.org/10.1016/j.physletb.2017.08.047). arXiv: [1702.04519](https://arxiv.org/abs/1702.04519) [[hep-ex](#)] (cit. on p. [82](#)).
- [174] *Search for resonances in the mass distribution of jet pairs with one or two jets identified as b-jets with the ATLAS detector with 2015 and 2016 data*. Tech. rep. ATLAS-CONF-2016-060. Geneva: CERN, 2016. URL: <https://cds.cern.ch/record/2206175> (cit. on p. [82](#)).
- [175] *Search for resonances below 1.2 TeV from the mass distribution of b-jet pairs in proton-proton collisions at $\sqrt{s}=13$ TeV with the ATLAS detector*. Tech. rep. ATLAS-CONF-2016-031. Geneva: CERN, 2016. URL: <https://cds.cern.ch/record/2161136> (cit. on p. [82](#)).
- [176] “Measurement of jet production properties at the CERN pp Collider”. In: *Physics Letters B* 144.3 (1984), pp. 283–290. ISSN: 0370-2693. DOI: [https://doi.org/10.1016/0370-2693\(84\)91822-7](https://doi.org/10.1016/0370-2693(84)91822-7). URL: <http://www.sciencedirect.com/science/article/pii/0370269384918227> (cit. on p. [82](#)).
- [177] G. Aad et al. “Search for New Particles in Two-Jet Final States in 7 TeV Proton-Proton Collisions with the ATLAS Detector at the LHC”. In: *Phys. Rev. Lett.* 105 (2010), p. 161801. DOI: [10.1103/PhysRevLett.105.161801](https://doi.org/10.1103/PhysRevLett.105.161801). arXiv: [1008.2461](https://arxiv.org/abs/1008.2461) [[hep-ex](#)] (cit. on p. [82](#)).

- [178] Georges Aad et al. “Search for New Physics in Dijet Mass and Angular Distributions in pp Collisions at $\sqrt{s} = 7$ TeV Measured with the ATLAS Detector”. In: *New J. Phys.* 13 (2011), p. 053044. DOI: [10.1088/1367-2630/13/5/053044](https://doi.org/10.1088/1367-2630/13/5/053044). arXiv: [1103.3864 \[hep-ex\]](https://arxiv.org/abs/1103.3864) (cit. on pp. [82](#), [141](#)).
- [179] Georges Aad et al. “Search for new phenomena in the dijet mass distribution using $p-p$ collision data at $\sqrt{s} = 8$ TeV with the ATLAS detector”. In: *Phys. Rev.* D91.5 (2015), p. 052007. DOI: [10.1103/PhysRevD.91.052007](https://doi.org/10.1103/PhysRevD.91.052007). arXiv: [1407.1376 \[hep-ex\]](https://arxiv.org/abs/1407.1376) (cit. on pp. [82](#), [111](#), [139](#)).
- [180] *Search for new light resonances decaying to jet pairs and produced in association with a photon or a jet in proton-proton collisions at $\sqrt{s} = 13$ TeV with the ATLAS detector*. Tech. rep. ATLAS-CONF-2016-070. Geneva: CERN, 2016. URL: <https://cds.cern.ch/record/2206221> (cit. on pp. [82](#), [109](#)).
- [181] *Search for light dijet resonances with the ATLAS detector using a Trigger-Level Analysis in LHC pp collisions at $\sqrt{s} = 13$ TeV*. Tech. rep. ATLAS-CONF-2016-030. Geneva: CERN, 2016. URL: <https://cds.cern.ch/record/2161135> (cit. on pp. [82](#), [109](#)).
- [182] Georgios Choudalakis and Diego Casadei. “Plotting the Differences Between Data and Expectation”. In: *Eur. Phys. J. Plus* 127 (2012), p. 25. DOI: [10.1140/epjp/i2012-12025-y](https://doi.org/10.1140/epjp/i2012-12025-y). arXiv: [1111.2062 \[physics.data-an\]](https://arxiv.org/abs/1111.2062) (cit. on p. [84](#)).
- [183] Frank J. Massey Jr. “The Kolmogorov-Smirnov Test for Goodness of Fit”. In: *Journal of the American Statistical Association* 46.253 (1951), pp. 68–78. DOI: [10.1080/01621459.1951.10500769](https://doi.org/10.1080/01621459.1951.10500769). eprint: <https://www.tandfonline.com/doi/pdf/10.1080/01621459.1951.10500769>. URL: <https://www.tandfonline.com/doi/abs/10.1080/01621459.1951.10500769> (cit. on p. [84](#)).
- [184] S. S. Shapiro and M. B. Wilk. “An Analysis of Variance Test for Normality (Complete Samples)”. In: *Biometrika* 52.3/4 (1965), pp. 591–611. ISSN: 00063444. URL: <http://www.jstor.org/stable/2333709> (cit. on p. [84](#)).
- [185] Georgios Choudalakis. “On hypothesis testing, trials factor, hypertests and the BumpHunter”. In: *Proceedings, PHYSTAT 2011 Workshop on Statistical Issues Related to Discovery Claims in Search Experiments and Unfolding, CERN, Geneva, Switzerland 17-20 January 2011*. 2011. arXiv: [1101.0390 \[physics.data-an\]](https://arxiv.org/abs/1101.0390) (cit. on pp. [84](#), [85](#), [120](#), [126](#)).
- [186] Dag J. Steinskog, Dag B. Tjøstheim, and Nils G. Kvamstø. “A Cautionary Note on the Use of the Kolmogorov–Smirnov Test for Normality”. In: *Monthly Weather Review* 135.3 (2007), pp. 1151–1157. DOI: [10.1175/MWR3326.1](https://doi.org/10.1175/MWR3326.1). eprint: <https://doi.org/10.1175/MWR3326.1>. URL: <https://doi.org/10.1175/MWR3326.1> (cit. on p. [85](#)).
- [187] Nornadiah Mohd Razali and Bee Yap. “Power Comparisons of Shapiro-Wilk, Kolmogorov-Smirnov, Lilliefors and Anderson-Darling Tests”. In: *J. Stat. Model. Analytics* 2 (Jan. 2011) (cit. on p. [85](#)).
- [188] E.S. Pearson and H.O. Hartley. *Biometrika Tables for Statisticians*. Biometrika Tables for Statisticians v. 2. Published for the Biometrika Trustees at the University Press, 1976. ISBN: 9780904653113. URL: <https://books.google.ca/books?id=vZEoAAAAYAAJ> (cit. on p. [85](#)).
- [189] *Cross-section measurements of the Higgs boson decaying to a pair of tau leptons in proton-proton collisions at $\sqrt{s} = 13$ TeV with the ATLAS detector*. Tech. rep. ATLAS-CONF-2018-021. Geneva: CERN, 2018. URL: <http://cds.cern.ch/record/2621794> (cit. on p. [85](#)).

- [190] Georges Aad et al. “Measurement of the top quark-pair production cross section with ATLAS in pp collisions at $\sqrt{s} = 7$ TeV”. In: *Eur. Phys. J. C* 71 (2011), p. 1577. DOI: [10.1140/epjc/s10052-011-1577-6](https://doi.org/10.1140/epjc/s10052-011-1577-6). arXiv: [1012.1792 \[hep-ex\]](https://arxiv.org/abs/1012.1792) (cit. on p. 85).
- [191] ATLAS Collaboration. *Standard Model Analysis Software Group (ASG)*. 2018. URL: https://twiki.cern.ch/twiki/bin/viewauth/AtlasProtected/StandardModelASG#Derivation_Details (visited on 05/13/2019) (cit. on p. 86).
- [192] S. Catani et al. “QCD”. In: *1999 CERN Workshop on standard model physics (and more) at the LHC, CERN, Geneva, Switzerland, 25-26 May: Proceedings*. 2000. arXiv: [hep-ph/0005025 \[hep-ph\]](https://arxiv.org/abs/hep-ph/0005025). URL: <http://weblib.cern.ch/abstract?CERN-TH-2000-131> (cit. on p. 87).
- [193] J. Chapman et al. “Challenges of the ATLAS Monte Carlo production during Run 1 and beyond”. In: *J. Phys. Conf. Ser.* 513 (2014), p. 032029. DOI: [10.1088/1742-6596/513/3/032029](https://doi.org/10.1088/1742-6596/513/3/032029) (cit. on p. 87).
- [194] *ATLAS Run 1 Pythia8 tunes*. Tech. rep. ATL-PHYS-PUB-2014-021. Geneva: CERN, 2014. URL: <http://cds.cern.ch/record/1966419> (cit. on pp. 88, 89).
- [195] *Summary of ATLAS Pythia 8 tunes*. Tech. rep. ATL-PHYS-PUB-2012-003. Geneva: CERN, 2012. URL: <https://cds.cern.ch/record/1474107> (cit. on p. 88).
- [196] Richard Corke and Torbjörn Sjöstrand. “Interleaved Parton Showers and Tuning Prospects”. In: *JHEP* 03 (2011), p. 032. DOI: [10.1007/JHEP03\(2011\)032](https://doi.org/10.1007/JHEP03(2011)032). arXiv: [1011.1759 \[hep-ph\]](https://arxiv.org/abs/1011.1759) (cit. on p. 88).
- [197] Andy Buckley et al. “General-purpose event generators for LHC physics”. In: *Phys. Rept.* 504 (2011), pp. 145–233. DOI: [10.1016/j.physrep.2011.03.005](https://doi.org/10.1016/j.physrep.2011.03.005). arXiv: [1101.2599 \[hep-ph\]](https://arxiv.org/abs/1101.2599) (cit. on p. 88).
- [198] Richard Corke and Torbjörn Sjöstrand. “Multiparton Interactions with an x-dependent Proton Size”. In: *JHEP* 05 (2011), p. 009. DOI: [10.1007/JHEP05\(2011\)009](https://doi.org/10.1007/JHEP05(2011)009). arXiv: [1101.5953 \[hep-ph\]](https://arxiv.org/abs/1101.5953) (cit. on p. 88).
- [199] Peter Skands, Stefano Carrazza, and Juan Rojo. “Tuning PYTHIA 8.1: the Monash 2013 Tune”. In: *Eur. Phys. J. C* 74.8 (2014), p. 3024. DOI: [10.1140/epjc/s10052-014-3024-y](https://doi.org/10.1140/epjc/s10052-014-3024-y). arXiv: [1404.5630 \[hep-ph\]](https://arxiv.org/abs/1404.5630) (cit. on p. 88).
- [200] S. Agostinelli et al. “GEANT4: A Simulation toolkit”. In: *Nucl. Instrum. Meth.* A506 (2003), pp. 250–303. DOI: [10.1016/S0168-9002\(03\)01368-8](https://doi.org/10.1016/S0168-9002(03)01368-8) (cit. on p. 88).
- [201] Coll ATLAS et al. *The simulation principle and performance of the ATLAS fast calorimeter simulation FastCaloSim*. Tech. rep. ATL-PHYS-PUB-2010-013. Geneva: CERN, 2010. URL: <https://cds.cern.ch/record/1300517> (cit. on p. 88).
- [202] *The new Fast Calorimeter Simulation in ATLAS*. Tech. rep. ATL-SOFT-PUB-2018-002. Geneva: CERN, 2018. URL: <https://cds.cern.ch/record/2630434> (cit. on pp. 88, 150).
- [203] Torbjörn Sjöstrand, Stephen Mrenna, and Peter Z. Skands. “A Brief Introduction to PYTHIA 8.1”. In: *Comput. Phys. Commun.* 178 (2008), pp. 852–867. DOI: [10.1016/j.cpc.2008.01.036](https://doi.org/10.1016/j.cpc.2008.01.036). arXiv: [0710.3820 \[hep-ph\]](https://arxiv.org/abs/0710.3820) (cit. on p. 89).
- [204] Anders Ryd et al. “EvtGen: A Monte Carlo Generator for B-Physics”. In: (2005) (cit. on p. 89).

- [205] Richard D. Ball et al. “Parton distributions with LHC data”. In: *Nucl. Phys.* B867 (2013), pp. 244–289. DOI: [10.1016/j.nuclphysb.2012.10.003](https://doi.org/10.1016/j.nuclphysb.2012.10.003). arXiv: [1207.1303](https://arxiv.org/abs/1207.1303) [hep-ph] (cit. on p. 89).
- [206] Stefano Frixione, Paolo Nason, and Carlo Oleari. “Matching NLO QCD computations with Parton Shower simulations: the POWHEG method”. In: *JHEP* 11 (2007), p. 070. DOI: [10.1088/1126-6708/2007/11/070](https://doi.org/10.1088/1126-6708/2007/11/070). arXiv: [0709.2092](https://arxiv.org/abs/0709.2092) [hep-ph] (cit. on p. 90).
- [207] Hung-Liang Lai et al. “New parton distributions for collider physics”. In: *Phys. Rev.* D82 (2010), p. 074024. DOI: [10.1103/PhysRevD.82.074024](https://doi.org/10.1103/PhysRevD.82.074024). arXiv: [1007.2241](https://arxiv.org/abs/1007.2241) [hep-ph] (cit. on p. 90).
- [208] Georges Aad et al. “Measurement of the Z/γ^* boson transverse momentum distribution in pp collisions at $\sqrt{s} = 7$ TeV with the ATLAS detector”. In: *JHEP* 09 (2014), p. 145. DOI: [10.1007/JHEP09\(2014\)145](https://doi.org/10.1007/JHEP09(2014)145). arXiv: [1406.3660](https://arxiv.org/abs/1406.3660) [hep-ex] (cit. on p. 90).
- [209] ATLAS Collaboration. *MuonTriggerPhysicsRecommendationsRel212017*. 2019. URL: <https://twiki.cern.ch/twiki/bin/view/Atlas/MuonTriggerPhysicsRecommendationsRel212017> (visited on 05/15/2019) (cit. on p. 92).
- [210] ATLAS Collaboration. *Egamma trigger recommendations for Run 2 data*. 2019. URL: <https://twiki.cern.ch/twiki/bin/view/Atlas/TrigEgammaRecommendations2015> (visited on 05/15/2019) (cit. on p. 92).
- [211] ATLAS Collaboration. *COMA Portal*. 2019. URL: <https://atlas-tagsservices.cern.ch/tagsservices/RunBrowser/index.html> (visited on 05/16/2019) (cit. on p. 93).
- [212] Fernando Monticelli, Moritz Backes, and Aranzazu Ruiz-Martinez. *Electron/photon trigger rate plots for ICHEP2016*. Tech. rep. ATL-COM-DAQ-2016-074. Geneva: CERN, 2016. URL: <https://cds.cern.ch/record/2195815> (cit. on p. 94).
- [213] Tetiana Hryn’ova et al. *Single electron trigger 2018 performance plots*. Tech. rep. ATL-COM-DAQ-2019-049. Geneva: CERN, 2019. URL: <https://cds.cern.ch/record/2668252> (cit. on p. 94).
- [214] Marcus Morgenstern and Mark Owen. *Muon trigger efficiency in early 2018 data taking*. Tech. rep. ATL-COM-DAQ-2018-047. Geneva: CERN, 2017. URL: <https://cds.cern.ch/record/2318500> (cit. on p. 94).
- [215] Morad Aaboud et al. “Electron efficiency measurements with the ATLAS detector using 2012 LHC proton–proton collision data”. In: *Eur. Phys. J.* C77.3 (2017), p. 195. DOI: [10.1140/epjc/s10052-017-4756-2](https://doi.org/10.1140/epjc/s10052-017-4756-2). arXiv: [1612.01456](https://arxiv.org/abs/1612.01456) [hep-ex] (cit. on p. 94).
- [216] *Selection of jets produced in 13TeV proton-proton collisions with the ATLAS detector*. Tech. rep. ATLAS-CONF-2015-029. Geneva: CERN, 2015. URL: <https://cds.cern.ch/record/2037702> (cit. on pp. 95, 96).
- [217] Julia Gonski. *Jet Cleaning in 2016 and the Event Level Cleaning Tool*. Tech. rep. ATL-COM-PHYS-2017-982. Geneva: CERN, 2017. URL: <https://cds.cern.ch/record/2272136> (cit. on p. 96).
- [218] Matteo Cacciari, Gavin P. Salam, and Gregory Soyez. “FastJet User Manual”. In: *Eur. Phys. J.* C72 (2012), p. 1896. DOI: [10.1140/epjc/s10052-012-1896-2](https://doi.org/10.1140/epjc/s10052-012-1896-2). arXiv: [1111.6097](https://arxiv.org/abs/1111.6097) [hep-ph] (cit. on p. 98).

- [219] *Tagging and suppression of pileup jets with the ATLAS detector*. Tech. rep. ATLAS-CONF-2014-018. Geneva: CERN, 2014. URL: <https://cds.cern.ch/record/1700870> (cit. on p. 98).
- [220] Georges Aad et al. “Performance of pile-up mitigation techniques for jets in pp collisions at $\sqrt{s} = 8$ TeV using the ATLAS detector”. In: *Eur. Phys. J. C* 76.11 (2016), p. 581. DOI: [10.1140/epjc/s10052-016-4395-z](https://doi.org/10.1140/epjc/s10052-016-4395-z). arXiv: [1510.03823](https://arxiv.org/abs/1510.03823) [hep-ex] (cit. on p. 98).
- [221] A. Hoecker et al. “TMVA - Toolkit for Multivariate Data Analysis”. In: *arXiv e-prints*, physics/0703039 (2007), physics/0703039. arXiv: [physics/0703039](https://arxiv.org/abs/physics/0703039) [physics.data-an] (cit. on p. 98).
- [222] D Adams et al. *Recommendations of the Physics Objects and Analysis Harmonisation Study Groups 2014*. Tech. rep. ATL-COM-PHYS-2014-451. Geneva: CERN, 2014. URL: <https://cds.cern.ch/record/1700874> (cit. on p. 99).
- [223] Morad Aaboud et al. “Measurement of differential cross sections and W^+/W^- cross-section ratios for W boson production in association with jets at $\sqrt{s} = 8$ TeV with the ATLAS detector”. In: *JHEP* 05 (2018), p. 077. DOI: [10.1007/JHEP05\(2018\)077](https://doi.org/10.1007/JHEP05(2018)077). arXiv: [1711.03296](https://arxiv.org/abs/1711.03296) [hep-ex] (cit. on p. 100).
- [224] Behnke, Olaf and others. *Data analysis in high energy physics*. Weinheim, Germany: Wiley-VCH, 2013. ISBN: 9783527410583, 9783527653447, 9783527653430. URL: <http://www.wiley-vch.de/publish/dt/books/ISBN3-527-41058-9> (cit. on pp. 101, 137, 139).
- [225] ATLAS collaboration. “Search for dijet resonances in events with an isolated lepton using $\sqrt{s} = 13$ TeV proton–proton collision data collected by the ATLAS detector”. In: (2018) (cit. on pp. 102, 110, 129, 150).
- [226] *Search for New Phenomena in Dijet Events using 139 fb^{-1} of pp collisions at $\sqrt{s} = 13$ TeV collected with the ATLAS Detector*. Tech. rep. ATLAS-CONF-2019-007. Geneva: CERN, 2019. URL: <https://cds.cern.ch/record/2668385> (cit. on p. 102).
- [227] B L Combridge, J Kripfganz, and J Ranft. “Hadron Production At Large Transverse Momentum And Qcd”. In: *Phys. Lett. B* 70.CERN-TH-2343. 2 (1977), pp. 234–8. DOI: [10.1016/0370-2693\(77\)90528-7](https://doi.org/10.1016/0370-2693(77)90528-7). URL: <https://cds.cern.ch/record/438781> (cit. on p. 110).
- [228] Karishma Sekhon, Ryan Christopher Edgar, and Dante Amidei. *SWiFt: Sliding Window Fit Method for Resonance Searches*. Tech. rep. ATL-COM-PHYS-2018-161. Geneva: CERN, 2018. URL: <https://cds.cern.ch/record/2305523> (cit. on pp. 110, 115).
- [229] T. Aaltonen et al. “Global Search for New Physics with 2.0 fb^{-1} at CDF”. In: *Phys. Rev. D* 79 (2009), p. 011101. DOI: [10.1103/PhysRevD.79.011101](https://doi.org/10.1103/PhysRevD.79.011101). arXiv: [0809.3781](https://arxiv.org/abs/0809.3781) [hep-ex] (cit. on p. 120).
- [230] Louis Lyons. “Open statistical issues in Particle Physics”. In: *Ann. Appl. Stat.* 2.3 (Sept. 2008), pp. 887–915. DOI: [10.1214/08-AOAS163](https://doi.org/10.1214/08-AOAS163). URL: <https://doi.org/10.1214/08-AOAS163> (cit. on p. 121).
- [231] Eilam Gross and Ofer Vitells. “Trial factors for the look elsewhere effect in high energy physics”. In: *Eur. Phys. J. C* 70 (2010), pp. 525–530. DOI: [10.1140/epjc/s10052-010-1470-8](https://doi.org/10.1140/epjc/s10052-010-1470-8). arXiv: [1005.1891](https://arxiv.org/abs/1005.1891) [physics.data-an] (cit. on p. 121).
- [232] F. James. “MINUIT Function Minimization and Error Analysis: Reference Manual Version 94.1”. In: (1994) (cit. on p. 130).

- [233] Georges Aad et al. “Improved luminosity determination in pp collisions at $\sqrt{s} = 7$ TeV using the ATLAS detector at the LHC”. In: *Eur. Phys. J. C* 73.8 (2013), p. 2518. DOI: [10.1140/epjc/s10052-013-2518-3](https://doi.org/10.1140/epjc/s10052-013-2518-3). arXiv: [1302.4393 \[hep-ex\]](https://arxiv.org/abs/1302.4393) (cit. on p. [134](#)).
- [234] Alexis Kalogeropoulos and Johan Alwall. “The SysCalc code: A tool to derive theoretical systematic uncertainties”. In: (2018). arXiv: [1801.08401 \[hep-ph\]](https://arxiv.org/abs/1801.08401) (cit. on p. [135](#)).
- [235] Torsten Paul Ake Akesson and others. *Search for New Phenomena in Dijet Events with the ATLAS Detector at $\sqrt{s} = 13$ TeV with the full 2015 dataset*. Tech. rep. ATL-COM-PHYS-2015-1205. Geneva: CERN, 2015. URL: <https://cds.cern.ch/record/2055242> (cit. on p. [135](#)).
- [236] T. Bayes. “An essay towards solving a problem in the doctrine of chances”. In: *Phil. Trans. of the Royal Soc. of London* 53 (1763), pp. 370–418 (cit. on p. [137](#)).
- [237] G. Cowan. *Statistical Data Analysis*. Oxford science publications. Clarendon Press, 1998. ISBN: 9780198501558. URL: <https://books.google.ca/books?id=ff8ZyW0nIJAC> (cit. on p. [137](#)).
- [238] Robert D. Cousins. “Why isn’t every physicist a Bayesian?” In: *Am. J. Phys.* 63 (1995), p. 398. DOI: [10.1119/1.17901](https://doi.org/10.1119/1.17901) (cit. on p. [139](#)).
- [239] A L Read. “Presentation of search results: theCLstechnique”. In: *Journal of Physics G: Nuclear and Particle Physics* 28.10 (2002), pp. 2693–2704. DOI: [10.1088/0954-3899/28/10/313](https://doi.org/10.1088/0954-3899/28/10/313). URL: <https://doi.org/10.1088/0954-3899/28/10/313> (cit. on p. [139](#)).
- [240] Frederik Beaujean et al. “BAT: The Bayesian analysis toolkit”. In: *J. Phys. Conf. Ser.* 331 (2011), p. 072040. DOI: [10.1088/1742-6596/331/7/072040](https://doi.org/10.1088/1742-6596/331/7/072040) (cit. on p. [142](#)).
- [241] S. V. Chekanov. “Imaging particle collision data for event classification using machine learning”. In: *Nucl. Instrum. Meth.* A931 (2019), pp. 92–99. DOI: [10.1016/j.nima.2019.04.031](https://doi.org/10.1016/j.nima.2019.04.031). arXiv: [1805.11650 \[hep-ph\]](https://arxiv.org/abs/1805.11650) (cit. on p. [146](#)).
- [242] S. V. Chekanov. “Machine learning using rapidity-mass matrices for event classification problems in HEP”. In: (2018). arXiv: [1810.06669 \[hep-ph\]](https://arxiv.org/abs/1810.06669) (cit. on p. [146](#)).
- [243] Meghan Frate et al. “Modeling Smooth Backgrounds and Generic Localized Signals with Gaussian Processes”. In: (2017). arXiv: [1709.05681 \[physics.data-an\]](https://arxiv.org/abs/1709.05681) (cit. on p. [146](#)).
- [244] S. Golchi and R. Lockhart. “A Bayesian Search for the Higgs Particle”. In: *ArXiv e-prints* (Jan. 2015). arXiv: [1501.02226 \[stat.AP\]](https://arxiv.org/abs/1501.02226) (cit. on p. [146](#)).
- [245] CMS Collaboration. “Measurement of the top quark mass in the dileptonic $t\bar{t}$ decay channel using the mass observables $M_{b\ell}$, M_{T2} , and $M_{b\ell\nu}$ in pp collisions at $\sqrt{s} = 8$ TeV”. In: *Phys. Rev. D* 96.3 (2017), p. 032002. DOI: [10.1103/PhysRevD.96.032002](https://doi.org/10.1103/PhysRevD.96.032002). arXiv: [1704.06142 \[hep-ex\]](https://arxiv.org/abs/1704.06142) (cit. on p. [146](#)).
- [246] Richard Hawkins et al. *Luminosity determination in pp collisions at $\sqrt{s} = 13$ TeV using the ATLAS detector at the LHC*. Tech. rep. ATLAS-COM-CONF-2019-036. Final version of run-2 13 TeV pp luminosity CONF note. Geneva: CERN, 2019. URL: <https://cds.cern.ch/record/2674889> (cit. on p. [149](#)).
- [247] Morad Aaboud et al. “Searches for heavy ZZ and ZW resonances in the $\ell\ell qq$ and $\nu\nu qq$ final states in pp collisions at $\sqrt{s} = 13$ TeV with the ATLAS detector”. In: *JHEP* 03 (2018), p. 009. DOI: [10.1007/JHEP03\(2018\)009](https://doi.org/10.1007/JHEP03(2018)009). arXiv: [1708.09638 \[hep-ex\]](https://arxiv.org/abs/1708.09638) (cit. on p. [150](#)).

- [248] Morad Aaboud et al. “Combination of searches for heavy resonances decaying into bosonic and leptonic final states using 36 fb^{-1} of proton-proton collision data at $\sqrt{s} = 13 \text{ TeV}$ with the ATLAS detector”. In: *Phys. Rev. D* 98.5 (2018), p. 052008. DOI: [10.1103/PhysRevD.98.052008](https://doi.org/10.1103/PhysRevD.98.052008). arXiv: [1808.02380](https://arxiv.org/abs/1808.02380) [[hep-ex](#)] (cit. on p. [150](#)).
- [249] Kyle Cranmer and Itay Yavin. *RECAST: Extending the Impact of Existing Analyses*. Tech. rep. arXiv:1010.2506. Comments: 13 pages, 4 figures. 2010. URL: <https://cds.cern.ch/record/1299950> (cit. on p. [150](#)).